Electro-Optic Methods for Longitudinal Bunch Diagnostics at FLASH

Dissertation

zur Erlangung des Doktorgrades
des Departments Physik
der Universität Hamburg

vorgelegt von

Bernd Richard Steffen
aus Marburg

Hamburg
2007

Gutachter der Dissertation	Prof. Dr. Peter Schmüser Prof. Dr. Klaus Sengstock
Gutachter der Disputation	Prof. Dr. Peter Schmüser Prof. Dr. Manfred Tonutti (RTWH Aachen)
Datum der Disputation	3. Juli 2007
Vorsitzender des Prüfungsausschusses	Dr. Hans Dierk Rüter
Vorsitzender des Promotionsausschusses	Prof. Dr. Günter Huber
Dekan der Fakultät für Mathematik, Informatik und Naturwissenschaften	Prof. Dr Arno Frühwald

Abstract

Precise measurements of the temporal profile of sub-picosecond electron bunches are of high interest for the optimization and operation of VUV and X-ray free electron lasers. In this thesis, the shortest electro-optic signals measured so far for electron bunch diagnostics are presented, reaching a time resolution of better than 50 fs (rms). The effects that introduce signal distortions and limit the time resolution are studied in numerical simulations for different electro-optic detection materials and techniques. The time resolution is mainly limited by lattice resonances of the electro-optic crystal.

Electro-optic signals as short as 54 fs (rms) are obtained with gallium phosphide (GaP) crystals in a crossed polarizer detection scheme using temporally resolved electro-optic detection. Measuring near crossed polarization, where the electro-optic signal is proportional to the velocity field of the relativistic electron bunch, the shortest obtained signal width is 70 fs (rms).

The electro-optic signals are compared to electron bunch shapes that are measured simultaneously with a transverse deflecting structure with 20 fs resolution. Numerical simulations using the bunch shapes as determined with the transverse deflecting cavity as input data are in excellent agreement with electro-optical signals obtained with GaP, both for temporally and spectrally resolved measurements. In the case of zinc telluride (ZnTe) the observed signals are slightly broader and significantly smaller than expected from simulations. These discrepancies are probably due to the poor optical quality of the available ZnTe crystals.

Zusammenfassung

Die präzise Messung des zeitlichen Profils von Elektronenpaketen mit einer Länge von weniger als einer Picosekunde ist für den Betrieb und die Optimierung von Freie-Elektronenlasern im VUV- und Röntgen-Bereich von großer Bedeutung. In dieser Arbeit werden die kürzesten Signale gezeigt, die bisher mit elektro-optischen Verfahren an einem Beschleuniger gemessen worden sind. Es wird eine Zeitauflösung von besser als 50 fs (rms) erreicht. Unterschiedliche Effekte, die bei verschiedenen elektro-optischen Detektionsverfahren zu Signalverformung und -verbreiterung führen, werden anhand von numerischen Simulationen für verschiedene elektro-optische Materialien untersucht. Die zeitliche Auflösung ist hauptsächlich durch die Gitterresonanz des elektro-optischen Kristalls begrenzt.

Mit Hilfe der zeitaufgelösten elektro-optischen Detektion mit Kristallen aus Galliumphosphid (GaP) können Signale mit einer Länge von 54 fs (rms) in einem Aufbau mit gekreuzten Polarisatoren gemessen werden. Bei fast gekreuzten Polarisatoren ist das elektro-optische Signal proportional zur elektrischen Feldstärke des vom relativistischen Elektronenpaket mitgeführten THz Pulses. In diesem Fall haben die kürzesten gemessenen Signale eine Breite von 70 fs (rms).

Die elektro-optischen Signale werden mit der Form eines Elektronenpakets verglichen, das parallel mit einem transversal ablenkenden Hochfrequenzresonator mit 20 fs Auflösung vermessen worden ist. Numerische Simulationen, die die mit dem seitlich ablenkenden Hochfrequenzresonator gemessene Form der Elektronenpakete als Eingangsdaten nutzen, stimmen sehr gut mit den Signalen der zeit- und spektralaufgelösten elektro-optischen Detektion überein, wenn mit GaP gemessen wird. Bei Kristallen aus Zinktellurid (ZnTe) sind die gemessenen Signale breiter und signifikant niedriger als von den Simulationen vorhergesagt wird. Diese Abweichungen können durch die schlechte optische Qualität des verwendeten ZnTe-Kristalls verursacht sein.

Contents

List of Figures

List of Tables

1. Introduction

Since its discovery in 1947 at the General Electric Research Laboratory [EMLP47] (Fig. 1.1) synchrotron radiation has become a powerful tool in many areas of science. The wide spectrum from microwaves to X-rays and the high brightness offer unique conditions for spectroscopy and X-ray crystallography. Since the radiation is emitted in very short pulses, typically less than a nanosecond, also time resolved measurements are possible. The major applications of synchrotron light today are in condensed matter physics, molecular biology, chemistry, material science and medicine.

First experiments were done in parasitic operation at circular accelerators primarily used for high-energy or nuclear physics using the synchrotron light emitted in bending magnets. The growing demand of synchrotron light sources led to both the con-

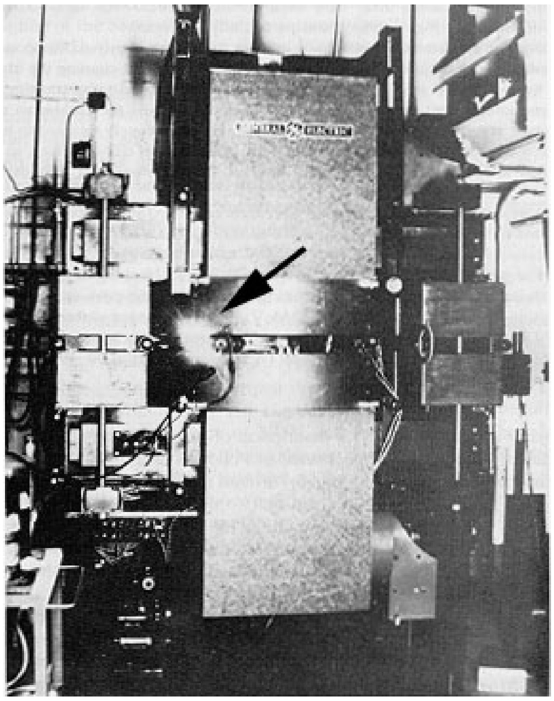

Figure 1.1.: Synchrotron light from the 70-MeV electron synchrotron at the General Electric Research Laboratory in Schenectady, New York, on April 24, 1947 [EMLP47].

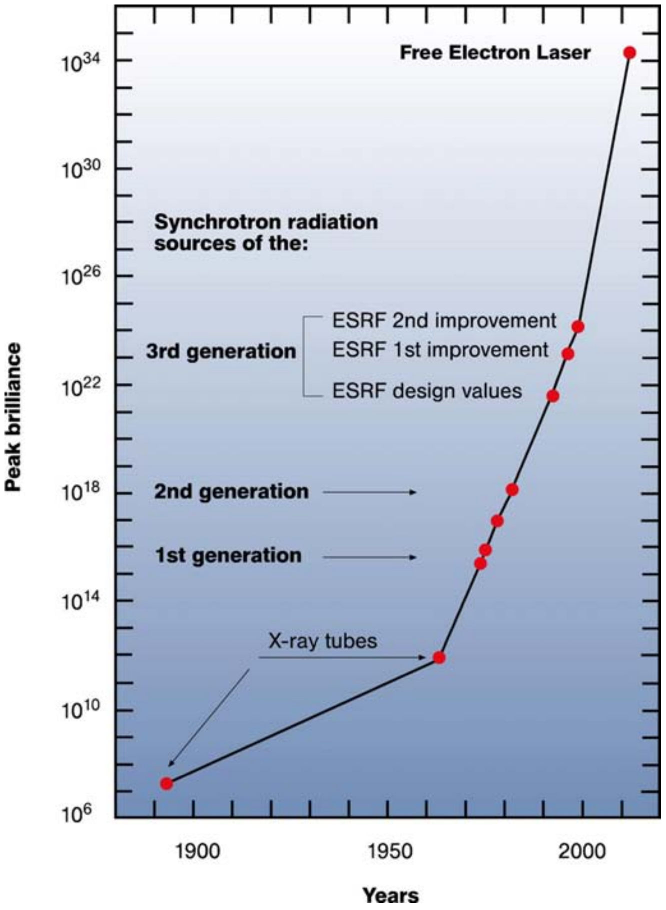

Figure 1.2.: History of the peak brilliance of X-ray light sources [DES07].

struction of dedicated accelerators – like the Synchrotron Radiation Source (SRS) at the Daresbury Laboratory – and the redesign of accelerators formerly used for high-energy physics – like the DORIS storage ring at DESY (so called second generation light sources). In the beginning these early dedicated facilities used bending magnets to produce synchrotron light. The use of magnetic insertion devices (wigglers and undulators) further increase flux and brightness of the radiation.

New storage rings with electron optics designed for a low emittance beam and long straight sections for undulators achieve an even higher brightness and also a considerable degree of spatial coherence (third generation light sources) [Rob01]. Modern light sources like the European Synchrotron Radiation Facility (ESRF) in Grenoble reach a peak brilliance (spectral brightness) of 10^{23}photons$/(\mathrm{s}\cdot\mathrm{mm}\cdot\mathrm{mrad}^2\cdot 0.1\%\Delta\lambda/\lambda)$ which is 10^{11} times more than in conventional X-ray tubes (Fig. 1.2).

One candidate for the next generation of light sources are free-electron lasers (FELs), accelerator based lasers, which use the accelerated electrons as gain media for the lasing process. Their peak brilliance which will be a factor of 10^8 higher than in third generation light sources and they offer also very short pulses (< 100 fs) and a high degree of spatial coherence.

For infrared FELs, like the Free-Electron Laser for Infrared eXperiments (FELIX) in the Netherlands, the electron bunches are injected into a resonator, consisting of two high-reflectivity mirrors around an undulator. The emitted spontaneous radiation is amplified on successive roundtrips in the resonator by synchronized electron bunches from the accelerator. In high-gain FELs, which are based on the principle of Self Amplified Spontaneous Emission (SASE), the spontaneous undulator radiation is amplified in a single pass through the undulator to the final intensity and no cavity mirrors are needed. Therefore these FELs can provide radiation in the vacuum ultra violet (VUV) and X-ray regime, where no high-reflectivity mirrors are available. Electron bunches of low emittance and extremely high local charge density are needed to reach laser saturation in a single pass through the undulator. To achieve this high charge densities at reasonable bunch charges of up to a few nC the electron bunches have to be very short. To prevent an emittance growth during the acceleration, usually the bunch length at the electron source is several picoseconds. During the acceleration in a linear accelerator the bunches are compressed in magnetic chicanes to 100 fs or less before they pass through the undulator.

Only few techniques allow to determine the bunch length with a sub-picosecond time resolution. Several techniques measure the spectral distribution or the autocorrelation of coherent transition (CTR), diffraction (CDR), or synchrotron (CSR) radiation to calculate the bunch profile from this data [LBB+03, MHB+05, DRS+06]. Bunch lengths as short as 90 fs (rms) could be determined [MHB+05], but only very recently a device has been presented that is capable of single-shot measurements of a CTR spectrum [DGR+05].

Streak cameras can measure the length of synchrotron or Cherenkov radiation pulses with a resolution of about 100 fs (rms) [HPSS01, UUKK98]. The use of a transverse deflecting RF structure (TDS) allows to quantify the bunch length with the best resolution of about 25 fs (rms) [ALL64, HBS+05]. Transverse deflecting structures are intrinsically destructive devices. They also have large infrastructure requirements and need significant beam line space, especially for high energetic beams. At the Free-Electron Laser in Hamburg (FLASH) at DESY the structure itself is 3.6 m long, compared to the requirement of about 0.2 to 1 m for CTR or electro-optical diagnostics.

The electro-optic (EO) diagnostic techniques offer the possibility to measure sub-picosecond bunches destruction-free and in a single shot. The underlying principle of these techniques is as follows: the THz pulse from CTR or the electric field co-propagating with the relativistic electron bunch induces a time dependent birefringence in an optically active crystal, and this optical anisotropy modulates the polarisation of a laser pulse. The conceptually simplest electro-optical diagnostic technique, electro-optic sampling, is not a single-shot measurement. It is frequently used to measure THz pulses from laser driven THz sources [WZ95, WZ97, LHS+99]. For electron bunch length diagnostic it was first applied at FELIX [OKY+99, YMG+00]. Single-shot electro-optic measurements with a chirped laser pulse (spectrally resolved EO detection) were first demonstrated at laser driven THz sources [JZ98, SJZ98] and later applied for electron bunch measurements at FELIX [Wil02] with a temporal resolution of about 175 fs (rms) and measured EO signals of 740 fs (rms). A second EO single-shot technique, the spatially resolved detection, uses a non-collinear geometry for the THz radiation and the probing laser beam [SWK+00]. EO signals widths of 120 fs (rms) could be measured at the Stanford Linear Accelerator Center (SLAC) [Cav05] and lately at DESY of 70 fs (rms) [ADS+06]. A third single-shot technique, temporally resolved EO detection, resolves the intensity of an electro-optically modulated probe pulse through an optical cross-correlation in a frequency doubling crystal, using a non-collinear geometry [JSM+03]. Just as in spatially resolved detection, a time-space mapping is achieved, but purely with optical pulses. Temporally resolved EO detection has been demonstrated at FELIX, reaching a minimum signal width of 150 fs (rms) [BJM+04]. All electro-optic detection techniques are described in detail in section 3.2.

FLASH has recently been upgraded to a maximum electron energy of 770 MeV, allowing to cover the wavelength range from 13 to 45 nm. The 1 nC electron bunches are generated in an RF-photocathode with an rms length of 4 ps and are rapidly accelerated to relativistic energies to reduce the emittance dilution due to internal Coulomb forces. At energies of 125 MeV resp. 380 MeV the bunches are longitudinally compressed to a narrow peak with an rms pulse length of $\sigma_t < 100$ fs which is followed by a longer tail.

Precise measurements of the temporal profile of the compressed electron bunches are essential for the optimization of the linac and a proper understanding of the bunch compression mechanism including subtle effects such as coherent synchrotron radiation.

In the framework of this thesis an electro-optical experiment for sub-ps, single-shot, destruction free longitudinal bunch profile measurements at FLASH is designed, set up and commissioned. The theoretical and experimental limits of the temporal resolution of spectrally and temporally resolved electro-optic detection are investigated and simulated numerically for different electro-optic crystals.

2. Theoretical background

The experiments described in this thesis use the electro-optic (EO) effect to reconstruct the time profile of electron bunches in the linear accelerator of the free electron laser in Hamburg (FLASH). A birefringence is induced in electro-optical active crystals by the Coulomb field of a relativistic electron bunch passing the crystal at a close distance. This birefringence is then probed by an ultrashort laser pulse. In this chapter the properties of the Coulomb field of a relativistic electron bunch traveling through the beam pipe of an accelerator and the physical background of the electro-optic effect (Pockels effect) will be described, followed by a description of the electro-optic detection techniques used in accelerators.

2.1. The Coulomb field of relativistic electron bunches

The electric field $\boldsymbol{E}$ of an electron at rest at $\boldsymbol{r} = (0, 0, 0)$ is spherically symmetric:

$$\boldsymbol{E}(\boldsymbol{r}) = \frac{q}{4\pi\varepsilon_0 r^2}\frac{\boldsymbol{r}}{r} \tag{2.1}$$

with the permittivity of free space ε_0 and the electron charge $q = -e$.

For accelerated electrons moving with a speed $v \approx c$ close to speed of light the electromagnetic field needs to be Lorenz transformed. It becomes longitudinally contracted and forms in the laboratory system a flat disc with an opening angle of $2/\gamma$ perpendicular to the direction of movement of the electron [Jac99].

The components of $\boldsymbol{E}$ are:

$$\begin{aligned}
E_x &= \frac{q\gamma}{4\pi\varepsilon_0} \cdot \frac{x}{(x^2 + y^2 + \gamma^2(z - vt)^2)^{3/2}} \\
E_y &= \frac{q\gamma}{4\pi\varepsilon_0} \cdot \frac{y}{(x^2 + y^2 + \gamma^2(z - vt)^2)^{3/2}} \\
E_z &= \frac{q\gamma}{4\pi\varepsilon_0} \cdot \frac{z - vt}{(x^2 + y^2 + \gamma^2(z - vt)^2)^{3/2}}
\end{aligned} \tag{2.2}$$

with the relativistic Lorenz factor $\gamma = \frac{1}{\sqrt{1-(v/c)^2}}$. At time $t = 0$ the field can be written in the following vector form:

$$\boldsymbol{E}(\boldsymbol{r}) = \frac{q\gamma}{4\pi\varepsilon_0} \cdot \frac{1-\beta^2}{(1-\beta^2 \sin^2\theta)^{3/2}} \frac{\boldsymbol{r}}{r^3} \tag{2.3}$$

where $\boldsymbol{r}$ is the radius vector from the electron to the observer, θ is the angle between $\boldsymbol{r}$ and the velocity vector $\boldsymbol{v}$ of the electron, and $\beta = v/c$.

Changing to a cylindrical coordinate system (r, z, φ) with $r = \sqrt{x^2 + y^2}$ and $\varphi = \arctan(y/x)$, the electric field of an electron moving with the constant speed v along the z-axis becomes (assuming that the electron is at $(0, 0, 0)$ at the time $t = 0$):

$$\begin{aligned} E_r(r,t) &= \frac{q\gamma}{4\pi\varepsilon_0} \cdot \frac{r}{(r^2+\gamma^2 v^2 t^2)^{3/2}} \\ E_\varphi(r,t) &= 0 \\ E_z(r,t) &= -\frac{q\gamma}{4\pi\varepsilon_0} \cdot \frac{vt}{(r^2+\gamma^2 v^2 t^2)^{3/2}} \end{aligned} \tag{2.4}$$

The frequency components $|\tilde{E}_r(r,\omega)|$ of this field seen by an observer at $z = 0$ in a distance r from the electron path, can be calculated using the Fourier transform $\mathcal{F}$ of the radial electric field:

$$\begin{aligned} \tilde{E}_r(r,\omega) &= \mathcal{F}\{E_r(r,t)\} = \frac{1}{\sqrt{2\pi}} \int_{-\infty}^{\infty} E_r(r,t) \exp(-i\omega t) \mathrm{d}t \\ E_r(r,t) &= \mathcal{F}^{-1}\{\tilde{E}_r(r,\omega)\} = \frac{1}{\sqrt{2\pi}} \int_{-\infty}^{\infty} \tilde{E}_r(r,\omega) \exp(i\omega t) \mathrm{d}\omega \end{aligned} \tag{2.5}$$

The Fourier transform is found to be [Jac99, CSS05c]:

$$\tilde{E}_r(r,\omega) = \frac{q\omega}{(2\pi)^{3/2}\varepsilon_0 \beta\gamma c^3} K_1\left(\frac{\omega}{\beta\gamma c} r\right) \tag{2.6}$$

The function K_1 is a modified Bessel function. The longitudinal field component is smaller than the radial component by a factor of $1/\gamma$ and can be neglected for highly relativistic electrons.

Assuming an electron bunch with an infinitesimally small radius and a longitudinal electron distribution $Q(t)$ moving along the z-axis the radial field becomes:

$$E_{r,Q}(r,t) = (E_r * Q)(r,t) \tag{2.7}$$

$$= \int_{-\infty}^{\infty} E_r(r, t-s) Q(t) \mathrm{d}s \tag{2.8}$$

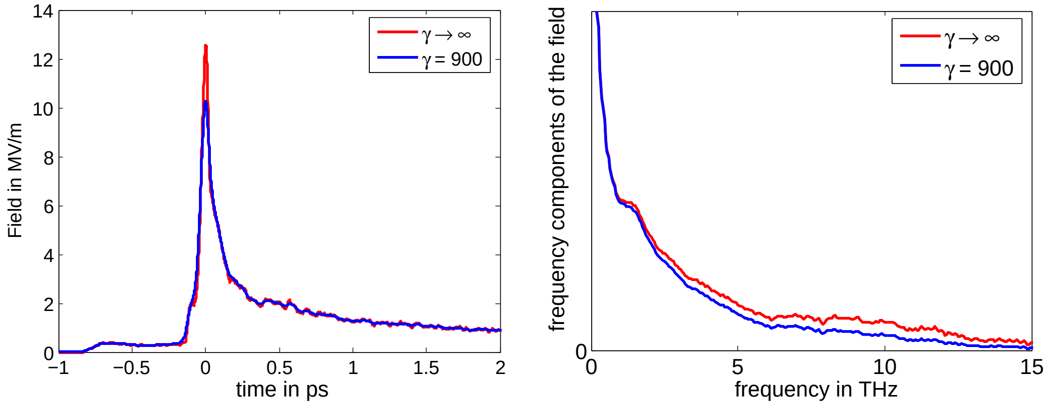

(a) (b)

Figure 2.1.: The radial electric field of a simulated charge distribution of a 450 MeV bunch at FLASH [Doh06a] after the last accelerating module at a distance of $r = 5$ mm (a, blue curve). The total charge is 500 pC. Fourier transform of the electric field at a distance $r = 5$ mm (b, blue curve). The red curves show the electric field of the simulated charge distribution for $\gamma \to \infty$ in time and frequency domain.

and the corresponding frequency components $|\tilde{E}_{r,Q}(\omega)|$ are:

$$\begin{aligned}\tilde{E}_{r,Q}(\omega) &= \mathcal{F}\{(E_r * Q)(t)\} &(2.9)\\ &= \mathcal{F}\{E_r(t)\} \cdot \mathcal{F}\{Q(t)\} &(2.10)\end{aligned}$$

Figure 2.1 shows the radial electric field created by the simulated charge distribution of a bunch at FLASH [Doh06a] at a distance of $r = 5$ mm from the axis (a) and also the corresponding Fourier transform (b). The total charge is 500 pC and the particle energy is 450 MeV. The small opening angle of $2/\gamma$ leads to a slight temporal broadening of the electric field pulse at a distance $r = 5$ mm, which results in a reduction of the high frequency parts of the electric field.

Due to the nonlinear compression of the electron bunches at FLASH (cf. 5.1.3), the bunches at the end of the accelerator have a sharp spike with a full width at half maximum (FWHM) duration in the order of 100 fs in their longitudinal charge distribution. This spike leads to frequency components of 10 THz and above.

2.2. Complex representation of the electric field of short laser pulses

For a mathematical description of short laser pulses it is useful to describe the electric field strength $E(t)$ of the pulse in time and frequency in a complex representation. This description is particularly useful to calculate the changes of the field during the propagation of the pulse in a dispersive material.

The temporal dependence of an optical laser pulse can be described by its electric field strength $E(t)$ in time domain or by the complex spectrum of its electric field strength $\tilde{E}(\omega)$ in frequency domain related through the complex Fourier transform ($\mathcal{F}$) [DR95]:

$$\tilde{E}(\omega) = \mathcal{F}\{E(t)\} = \frac{1}{\sqrt{2\pi}} \int_{-\infty}^{\infty} E(t) e^{-i\omega t} \mathrm{d}t = |\tilde{E}(\omega)| e^{i\Phi(\omega)} \tag{2.11}$$

$$E(t) = \mathcal{F}^{-1}\{\tilde{E}(\omega)\} = \frac{1}{\sqrt{2\pi}} \int_{-\infty}^{\infty} \tilde{E}(\omega) e^{i\omega t} \mathrm{d}\omega \tag{2.12}$$

where $|\tilde{E}(\omega)|$ is the spectral amplitude and $\Phi(\omega)$ is the spectral phase. In most cases the spectral amplitude will be centered around a mean frequency ω_0 and will have non-zero values only in a frequency interval $\Delta\omega \ll \omega_0$. In time domain it is convenient to introduce the carrier frequency ω_0 and to write $E(t)$ as:

$$E(t) = \mathcal{E}(t) e^{i\phi(t)} e^{i\omega_0 t} \tag{2.13}$$

where $\phi(t)$ is the time dependent phase, and $\mathcal{E}(t)$ is called the field envelope. It has to be emphasized that equation (2.13) is only useful if the bandwidth is a small fraction of the carrier frequency:

$$\frac{\Delta\omega}{\omega_0} \ll 1 \tag{2.14}$$

For that to be satisfied, the temporal variations of $\mathcal{E}(t)$ and $\phi(t)$ within an optical cycle $T_{\mathrm{opt}} = 2\pi/\omega_0$ have to be small. Then the slowly varying envelope approximation (SVEA) can be applied.

Standard laser pulse diagnostic devices like autocorrelators and spectrometers do not measure the electric field strength but the resulting intensities. The intensity profile $I(t)$ and the spectral intensity profile $S(\omega)$ can be calculated as:

$$I(t) = \frac{\varepsilon_0 c}{T_{\mathrm{opt}}} \int_{-T_{\mathrm{opt}}/2}^{+T_{\mathrm{opt}}/2} E^2(t+t') \mathrm{d}t' = \frac{\varepsilon_0 c}{2} \mathcal{E}^2(t) \tag{2.15}$$

$$S(\omega) = \frac{\varepsilon_0 c}{2} |\tilde{E}(\omega)|^2 \tag{2.16}$$

Usually the pulse duration and the spectral width are used to characterize short pulses. The pulse duration T_0 is commonly defined as the full width at half maximum (FWHM) of the intensity profile $I(t)$ and the spectral width $\Delta\omega$ as the FWHM of the spectral intensity profile $S(\omega)$.

2.2.1. Gaussian pulses

Gaussian laser pulses are commonly considered for simplicity in laser physics and have the convenient property that pulses with Gaussian profiles in time have Gaussian spectra as well. The concepts and definitions hold for other bunch shapes as well.

The temporal dependence of the field envelope of a Gaussian pulse is:

$$\mathcal{E}(t) = \mathcal{E}_0 \exp\left(-\frac{t^2}{2\sigma_\tau^2}\right) \tag{2.17}$$

and the intensity profile is:

$$I(t) = \frac{\varepsilon_0 c}{2}\mathcal{E}_0^2 \exp\left(-\frac{t^2}{\sigma_\tau^2}\right) \tag{2.18}$$

The FWHM is $T_0 = 2\sqrt{\ln 2}\sigma_\tau$. In the spectral domain the field envelope is:

$$\begin{aligned}\tilde{\mathcal{E}}(\omega) &= \mathcal{F}\{\mathcal{E}(t)\}\\ &= \mathcal{E}_0\sigma_\tau \exp\left(-\frac{\sigma_\tau^2}{2}(\omega-\omega_0)^2\right)\\ &= \mathcal{E}_{0,\omega} \exp\left(-\frac{(\omega-\omega_0)^2}{2\sigma_\omega^2}\right) \qquad (2.19)\end{aligned}$$

with

$$\begin{aligned}\mathcal{E}_{0,\omega} &= \mathcal{E}_0\sigma_\tau \quad \text{and} \qquad (2.20)\\ \sigma_\omega &= 1/\sigma_\tau = \frac{\Delta\omega}{2\sqrt{\ln 2}} \qquad (2.21)\end{aligned}$$

Here $T = 2\sqrt{\ln 2}\,\sigma_\tau$ and $\Delta\omega = 2\sqrt{\ln 2}\,\sigma_\omega$ will be used for FWHM duration and bandwidth, while σ_τ and σ_ω is used for the standard deviation of the Gaussian distribution of the electric field in time and frequency domain. In the laser literature also $\tau = \sqrt{2}\,\sigma_\tau$ is used. The field envelope of a Gaussian pulse becomes then $\mathcal{E}(t) = \mathcal{E}_0 \exp(-\frac{t^2}{\tau^2})$.

The temporal and spectral representations of the field are related through Fourier transformation. Therefore, the bandwidth σ_ω and the pulse duration σ_τ cannot vary independently from each other. There is a minimum duration-bandwidth product:

$$\sigma_\omega\sigma_\tau \geq c_B \tag{2.22}$$

where c_B is a numerical constant depending on the pulse shape. For Gaussian pulses $c_B = 1$. The equality holds for so called “Fourier limited” or “bandwidth limited” pulses, which have no frequency modulation (“chirp”) as described below.

2.2.2. Light propagation in dispersive materials

A plane wave traveling in z-direction in a medium with the relative permittivity ε_r and permeability μ_r can be written as

$$E(z,t) = E_0 e^{i(\omega t - kz)} \tag{2.23}$$

where $k = \omega\sqrt{\varepsilon\mu} = \omega\sqrt{\varepsilon_0\varepsilon_\mathrm{r}\mu_0\mu_\mathrm{r}}$ is the wave number of the plane wave in the medium, in which the wave is traveling in. In laser literature the wave number is also called the propagation constant although it is not constant in frequency. It can be written in any of the following forms:

$$k = \omega\sqrt{\varepsilon\mu} = \frac{\omega}{c'} = \frac{\omega n(\omega)}{c} = \frac{2\pi}{\lambda'} = \frac{2\pi n(\lambda)}{\lambda} \tag{2.24}$$

where c and λ are the velocity of light and the wavelength of the radiation in vacuum, $c' = c/n$ and $\lambda' = \lambda/n$ are the corresponding values in the medium, and $n = n(\omega)$ is the refractive index of the material.

Since the refractive index $n(\lambda)$ of optical glasses is often given in the form of the Sellmeier equation [Sch06c]:

$$n^2(\lambda) = 1 + \frac{B_1\lambda^2}{\lambda^2 - C_1} + \frac{B_2\lambda^2}{\lambda^2 - C_2} + \frac{B_3\lambda^2}{\lambda^2 - C_3} \tag{2.25}$$

with the constants $B_{1,2,3}$ and $C_{1,2,3}$. The following relations give the wave number k as a function of $n(\lambda)$ [DR95]:

$$\begin{aligned} k(\omega) &= \frac{\omega n(\omega)}{c} = \frac{2\pi n(\lambda)}{\lambda} \\ k' &= \frac{\mathrm{d}k}{\mathrm{d}\omega} = \frac{n(\omega)}{c_0} + \frac{\omega}{c_0}\frac{\mathrm{d}n}{\mathrm{d}\omega} = \frac{1}{c_0}\left(n(\lambda) - \lambda\frac{\mathrm{d}n}{\mathrm{d}\lambda}\right) \\ k'' &= \frac{\mathrm{d}^2k}{\mathrm{d}\omega^2} = \frac{2}{c_0}\frac{\mathrm{d}n}{\mathrm{d}\omega} + \frac{\omega}{c_0}\frac{\mathrm{d}^2n}{\mathrm{d}\omega^2} = \frac{\lambda}{2\pi c_0^2}\left(\lambda^2\frac{\mathrm{d}^2n}{\mathrm{d}\lambda^2}\right) \end{aligned} \tag{2.26}$$

2.2.3. Gaussian pulses in dispersive materials

In this section the propagation of a laser pulse in a linear, dispersive medium is treated. A linear medium in this context is any material with a linear response to the field of the light and dispersive means that the wave number $k(\omega)$ of the medium as a function of frequency is not proportional to ω. The polarization P of the material is proportional to the field strength E of the light and $\mathrm{d}k/\mathrm{d}\omega$ is not constant.

A laser pulse traveling through a material of length L acquires the phase shift

$$\Phi(\omega) = k(\omega)L \tag{2.27}$$

which does not change the spectral amplitude but leads to a change of the field envelope in time.

If the pulse has frequency components only in a narrow band around a center frequency ω_0 the wave number of a dispersive system can be expanded in a Taylor series about the center frequency ω_0:

$$k(\omega) = k_0 + k' \cdot (\omega - \omega_0) + \frac{1}{2}k'' \cdot (\omega - \omega_0)^2 \tag{2.28}$$

with $k_0 = k(\omega_0) = \omega_0 n(\omega_0)/c$, $k' = \mathrm{d}k/\mathrm{d}\omega|_{\omega=\omega_0}$ and $k'' = \mathrm{d}^2k/\mathrm{d}\omega^2|_{\omega=\omega_0}$.

The complex spectrum $\tilde{E}(\omega)$

$$\tilde{E}(\omega) = \mathcal{E}_0 \exp\left[-\frac{\omega - \omega_0}{2\sigma_\omega^2}\right] \tag{2.29}$$

of a Fourier limited Gaussian pulse enters a dispersive material with the wave number $k(\omega)$:

$$E(t) = \mathcal{E}_0 \exp\left[-\frac{t^2}{2\sigma_\tau^2} + i\omega_0 t\right] \tag{2.30}$$

After traveling through a length L of the material the spectrum $\tilde{E}(\omega, L)$ of the pulse will be the input spectrum multiplied by a frequency dependent phase factor:

$$\begin{aligned}
\tilde{E}(\omega, L) &= \tilde{E}(\omega) \exp\left[-ik(\omega)L\right] \\
&= \mathcal{E}_{0,\omega} \exp\left[-ik_0L - ik'L(\omega - \omega_0) - i\frac{k''L}{2}(\omega - \omega_0)^2 - \frac{(\omega - \omega_0)^2}{2\sigma_\omega^2}\right] \\
&= \mathcal{E}_{0,\omega} \exp\left[-\frac{1}{2}\left(\frac{1}{\sigma_\omega^2} + ik''L\right)(\omega - \omega_0)^2\right] \exp\left[-i\left(k_0L + k'L(\omega - \omega_0)\right)\right]
\end{aligned}$$

This can be written as:

$$\tilde{E}(\omega, L) = \mathcal{E}_{0,\omega} \exp\left[-\frac{1}{2\tilde{\sigma}_\omega^2}(\omega - \omega_0)^2\right] \exp\left[-i\left(k_0L + k'L(\omega - \omega_0)\right)\right] \tag{2.31}$$

with

$$\tilde{\sigma}_\omega^2 = \left(\frac{1}{\sigma_\omega^2} + ik''L\right)^{-1} = \frac{\sigma_\omega^2 - ik''L\sigma_\omega^4}{1 + k''^2L^2\sigma_\omega^4}$$

The Fourier transformation of $\tilde{E}(\omega, L)$ gives the electric field in time domain:

$$\begin{aligned} E(t,L) &= \frac{1}{\sqrt{2\pi}} \int_{-\infty}^{\infty} \tilde{E}(\omega, L) e^{i\omega t} \mathrm{d}\omega \\ &= \mathcal{E}_{0,\omega} \exp\left[i(\omega_0 t - k_0 L)\right] \frac{1}{\sqrt{2\pi}} \\ &\quad \cdot \int_{-\infty}^{\infty} \exp\left[-\frac{(\omega-\omega_0)^2}{2\tilde{\sigma}_\omega^2}\right] \exp\left[i(\omega-\omega_0)(t-k'L)\right] \mathrm{d}(\omega-\omega_0) \end{aligned} \tag{2.32}$$

The integral in equation (2.32) is a Fourier transformation of a Gaussian bunch of the form $\exp\left(\frac{1}{2}\tilde{\sigma}_\omega^2 t\right)$ with a shift in time by $t - k'L$. This leads to:

$$\begin{aligned} E(t,L) &= \mathcal{E}_{0,\omega} |\tilde{\sigma}_\omega| \exp\left[i(\omega_0 t - k_0 L)\right] \exp\left[-\frac{1}{2}\tilde{\sigma}_\omega^2 (t-k'L)^2\right] \\ &= \mathcal{E}_{0,\omega} \frac{\sigma_\omega}{\sqrt[4]{1+k''^2L^2\sigma_\omega^4}} \exp\left[-\frac{\sigma_\omega^2(t-k'L)^2}{2(1+k''^2L^2\sigma_\omega^4)}\right] \exp\left[i\frac{k'L\sigma_\omega^4}{2(1+k''^2L^2\sigma_\omega^4)}(t-k'L)^2\right] \\ &\quad \cdot \exp\left[i\omega_0(t-\frac{k_0}{\omega_0}L)\right] \\ &= \mathcal{E}_{0,\omega} \frac{\sigma_\omega}{\sqrt[4]{1+k''^2L^2\sigma_\omega^4}} \exp\left[-\frac{\sigma_\omega^2(t-k'L)^2}{2(1+k''^2L^2\sigma_\omega^4)}\right] \exp\left[i\frac{k'L\sigma_\omega^4}{2(1+k''^2L^2\sigma_\omega^4)}(t-k'L)^2\right] \\ &\quad \cdot \exp\left[i\omega_0(k'L-\frac{k_0}{\omega_0}L)\right] \exp\left[i\omega_0(t-k'L)\right] \end{aligned} \tag{2.33}$$

From the third exponent in equation (2.33) the phase of the carrier frequency ω_0 can be seen, which is delayed by the phase delay t_{ph} given by:

$$t_{\mathrm{ph}} = \frac{k(\omega_0)}{\omega_0} L = \frac{L}{v_{\mathrm{ph}}(\omega_0)} \tag{2.34}$$

with the phase velocity $v_{\mathrm{ph}} = \omega_0 / k(\omega_0)$. The forth exponent shows that the pulse envelope is delayed by the group delay time t_{g} given by:

$$t_{\mathrm{g}} = k'L = \frac{L}{v_{\mathrm{g}}(\omega_0)} \tag{2.35}$$

with the group velocity $v_{\mathrm{g}} = 1/k'$ which in general is different from v_{ph}. The pulse envelope remains Gaussian, but changes its width due to the effects of the group velocity dispersion k''. $k''L$ is also called *group delay dispersion* β. β is the chirp parameter in frequency domain, and is defined as:

$$\beta = \left.\frac{\mathrm{d}^2\Phi}{\mathrm{d}\omega^2}\right|_{\omega=\omega_0} = k''L \tag{2.36}$$

Since the constant delay of the pulse and the constant offset of the phase is of no importance for following, one can set $(t - k'L) \rightarrow t$ and $\omega_0(k'L - \frac{k_0}{\omega_0}L) \rightarrow 0$.
The equation (2.33) can also be written in the form:

$$E(t, L) = E_c(t) \quad = \quad \mathcal{E}_{0,c} \exp\left[-\frac{t^2}{2\sigma_{\tau,c}}\right] \exp\left[-i\frac{\alpha}{2}t^2 + i\omega_0 t\right] \tag{2.37}$$

with

$$\begin{aligned}
\mathcal{E}_{0,c} &= \frac{\mathcal{E}_{0,\omega}\sigma_\omega}{\sqrt[4]{1+\beta^2\sigma_\omega^4}} = \frac{\mathcal{E}_0}{\sqrt[4]{1+\beta^2\sigma_\omega^4}} = \frac{\mathcal{E}_0}{\sqrt[4]{1+\beta^2\sigma_\tau^{-4}}} \quad , \\
\sigma_{\tau,c} &= \frac{\sqrt{1+\beta^2\sigma_\omega^4}}{\sigma_\omega} = \sigma_\tau \sqrt{1+\beta^2\sigma_\tau^{-4}} \quad \text{and} \qquad (2.38) \\
\alpha &= -\frac{\beta\sigma_\omega^4}{1+\beta^2\sigma_\omega^4} = -\frac{\beta}{\sigma_\tau^4+\beta^2} \qquad (2.39)
\end{aligned}$$

From equations (2.38) and (2.39) follows:

$$\alpha = -\frac{\beta\sigma_\omega^2}{\sigma_{\tau,c}^2} = -\frac{\beta}{\sigma_\tau^2\sigma_{\tau,c}^2} \Leftrightarrow \alpha\sigma_{\tau,c}^2 = -\beta\sigma_\omega^2$$

From equation (2.38) follows:

$$\begin{aligned}
\frac{1}{\sigma_{\tau,c}^2} = \frac{\sigma_\omega^2}{1+\beta^2\sigma_\omega^4} \quad &\Rightarrow \quad \beta^2 = \frac{\sigma_\omega^2\sigma_{\tau,c}^2 - 1}{\sigma_\omega^4} = \sigma_t^2\sigma_{\tau,c}^2 - \sigma_t^4 \\
&\Rightarrow \quad |\beta| = \sqrt{\sigma_t^2\sigma_{\tau,c}^2 - \sigma_t^4} = \sigma_t^2\sigma_{\tau,c}^2\sqrt{\frac{1}{\sigma_t^2\sigma_{\tau,c}^2} - \frac{1}{\sigma_{\tau,c}^4}} \\
&\approx \sigma_t\sigma_{\tau,c} = \frac{T_0T_c}{4\ln 2} \quad \text{for} \quad \sigma_{\tau,c} \gg \sigma_t \qquad (2.40)
\end{aligned}$$

and:

$$\begin{aligned}
\alpha^2 &= \frac{\beta^2}{\sigma_\tau^4\sigma_{\tau,c}^4} = \frac{1}{\sigma_\tau^2\sigma_{\tau,c}^2} - \frac{1}{\sigma_{\tau,c}^4} \\
\Rightarrow |\alpha| &= \sqrt{\frac{1}{\sigma_t^2\sigma_{\tau,c}^2} - \frac{1}{\sigma_{\tau,c}^4}} \\
&\approx \frac{1}{\sigma_t\sigma_{\tau,c}} = \frac{4\ln 2}{T_0T_c} \approx \frac{1}{|\beta|} \quad \text{for} \quad \sigma_{\tau,c} \gg \sigma_\tau \qquad (2.41)
\end{aligned}$$

From equation (2.38) follows with equation (2.40):

$$\mathcal{E}_{0,c} = \sqrt{\frac{\sigma_\tau}{\sigma_{\tau,c}}}\mathcal{E}_0 \tag{2.42}$$

The pulse from equation (2.37) has a duration of $T_c = 2\sqrt{\ln 2}\,\sigma_{\tau,c}$ and shows a quadratic dependence ($-\frac{\alpha}{2}t^2$) of the phase in time. α is defined as $\alpha = -\mathrm{d}^2\phi/\mathrm{d}t^2|_{t=0}$ and is called the linear chirp parameter. With this definition the chirp parameter α is negative for an positive pulse (rising frequency: red-shifted frequencies arrive earlier than blue-shifted frequencies).

The time-varying phase shift of the sinusoidal signal within the Gaussian pulse is given by:

$$E(t) \propto \exp(i(\omega_0 t - \frac{\alpha}{2}t^2 + \varphi_0)) = \exp(i\varphi_i(t)) \tag{2.43}$$

with the total instantaneous phase of the field

$$\varphi_i(t) = \omega_0 t - \frac{\alpha}{2}t^2 + \varphi_0 \tag{2.44}$$

The instantaneous frequency ω_i is defined as the rate at which the total phase of the sinusoidal signal rotates. It becomes for the chirped Gaussian pulse:

$$\omega_i(t) = \frac{\mathrm{d}\varphi_i(t)}{\mathrm{d}t} = \omega_0 - \alpha t \tag{2.45}$$

and changes linearly in time. It can be used to calculate a time-frequency mapping of the pulse:

$$t(\omega_i) - t(\omega_0) = -\beta \cdot (\omega_i - \omega_0) \tag{2.46}$$

A bandwidth limited laser pulse acquires a chirp when passing through a dispersive material such as optical glass (Fig. 2.2). A positive chirp is acquired by a pulse passing through a dispersive material with a refractive index $n(\omega)$ with $\frac{\mathrm{d}n}{\mathrm{d}\omega} > 0$. Materials with $\frac{\mathrm{d}n}{\mathrm{d}\omega} > 0$ are called normal dispersive materials while $\frac{\mathrm{d}n}{\mathrm{d}\omega} < 0$ is called abnormal dispersion. For light at $\lambda = 800\,\mathrm{nm}$ all optical glasses have normal dispersion. To produce a negative chirp (or to cancel a positive chirp) optical setups like prism or grating stretchers (compressors) can be used.

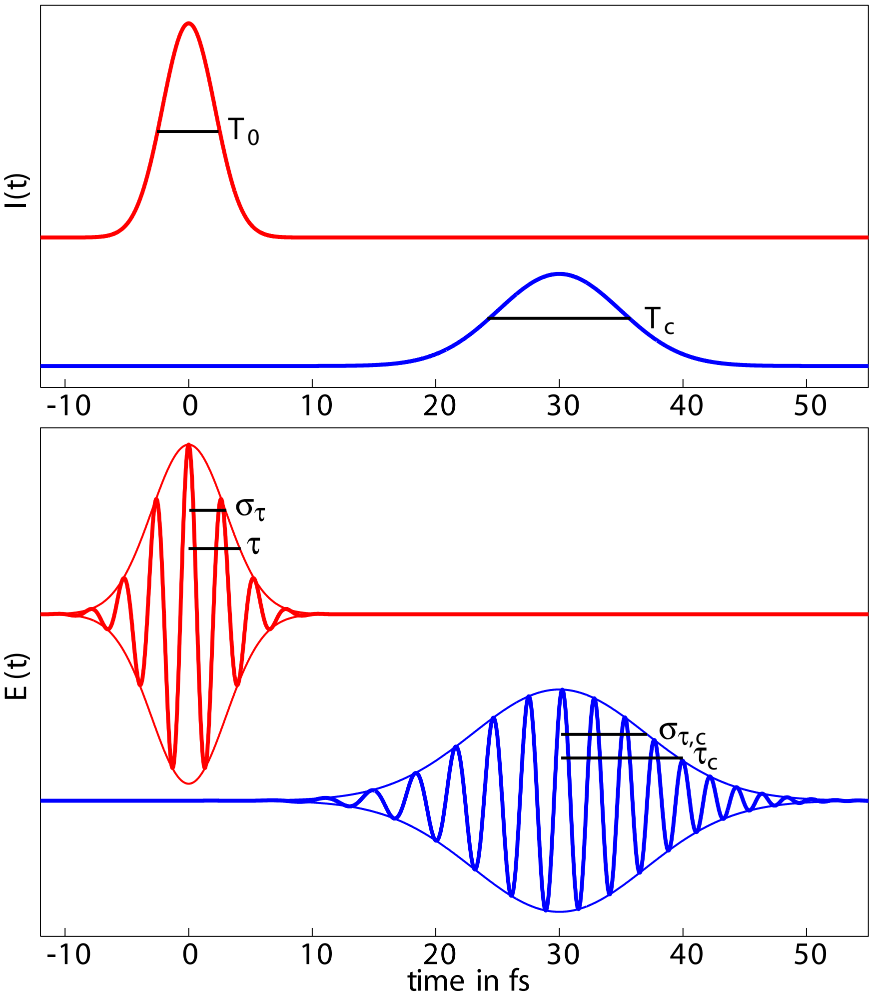

Figure 2.2.: Intensity (top) and electric field (bottom) of a Fourier limited laser pulse with $\lambda = 800\,\text{nm}$, $T_0 = 5\,\text{fs}$ (upper curve) and the field of the same pulse chirped to $T_c = 11.6\,\text{fs}$ by the propagation through $100\,\mu\text{m}$ of optical glass (SF11) (lower curve). The resulting linear chirp parameters are $\alpha = -0.0431\,\text{fs}^{-2}$ and $\beta = 18.9\,\text{fs}^2$.

2.3. Wave propagation in anisotropic crystals

The propagation of electromagnetic THz waves through optically active crystals leads to the linear electro-optic effect (Pockels effect), which is the basis of electro-optic detection techniques. In the following two sections the Pockels effect for a single frequency THz wave propagating through the crystal will be described. The modifications due to a THz pulse with a broad frequency spectrum will be discussed in chapter 4. The treatment follows mainly the references [YY84, BGG⁺03, Win04].

In an isotropic medium, the polarization $\boldsymbol{P}$ induced by an electric field $\boldsymbol{E}$ is always parallel to the electric field vector and related to the field by a scalar factor, the susceptibility. If the medium is anisotropic, the induced polarization is not necessarily parallel to the electric field, so the susceptibility is now a tensor. The relation between polarization and electric field can be written as (see e.g. [Jac99]):

$$P_i = \epsilon_0 \chi_{ij} E_j \tag{2.47}$$

The coefficients of the susceptibility tensor χ_{ij} depend on the choice of the coordinate system relative to the crystal lattice. It is always possible to find a system where χ_{ij} becomes a diagonal matrix with only three independent entries. The axes, whose choice makes the susceptibility tensor a diagonal matrix, are called the principal axes of the crystal. If the χ_{ii} are not all equal, the material will exhibit birefringence. Introducing the dielectric permittivity tensor

$$\epsilon_{ij} = 1 + \chi_{ij} \tag{2.48}$$

the relation

$$\boldsymbol{D} = \epsilon_0 \boldsymbol{E} + \boldsymbol{P} \tag{2.49}$$

can be written as

$$D_i = \epsilon_0 \sum_j \epsilon_{ij} E_j \tag{2.50}$$

In an anisotropic crystal, the phase velocity v_p of a plane electromagnetic wave

$$v_p = \frac{c}{\sqrt{\epsilon}} = \frac{c}{n} \tag{2.51}$$

depends on the direction of propagation and the direction of polarization. Along a given direction of propagation, two orthogonal optical axes $\boldsymbol{U}_s$ and $\boldsymbol{U}_f$ with different phase velocities and thus different refractive indices exist. The refractive indices of these two modes are commonly called n_s and n_f ('s' for slow and 'f' for fast).

In general, the polarization state of a wave entering the crystal with linear polarization will not remain invariant during the propagation through the crystal. Only if the polarization of the incident wave is parallel to one of the optical axes, its polarization state will remain unchanged. For any other direction of polarization, the field vector can be decomposed into two components parallel to the two optical axes of the crystal. As each propagates with a different phase velocity, a phase shift between both components and thus a change of polarization of the exiting wave relative to its initial state is induced.

2.3.1. The index ellipsoid

To find the indices of refraction n_s and n_f it is convenient to define the so-called *index ellipsoid*. The energy density of an electric field is given by:

$$w = \frac{1}{2}\boldsymbol{E} \cdot \boldsymbol{D} = \frac{1}{2} \cdot \sum_{i,j} E_i \epsilon_{ij} E_j \tag{2.52}$$

Changing to the coordinate system where the dielectric tensor is diagonal equation (2.52) can be rewritten as:

$$\frac{D_1^2}{\epsilon_1} + \frac{D_2^2}{\epsilon_2} + \frac{D_3^2}{\epsilon_3} = 2w \tag{2.53}$$

By defining a dimensionless vector

$$\boldsymbol{u} = \begin{pmatrix} u_1 \\ u_2 \\ u_3 \end{pmatrix} = \frac{\boldsymbol{D}}{\sqrt{2\epsilon_0 w}} \tag{2.54}$$

and introducing the main refractive indices

$$n_i = \sqrt{\epsilon_i}, \qquad i = 1, 2, 3 \tag{2.55}$$

equation (2.53) can be normalized. The result is

$$\frac{u_1^2}{n_1^2} + \frac{u_2^2}{n_2^2} + \frac{u_3^2}{n_3^2} = 1 \tag{2.56}$$

The main axes of the index ellipsoid have the length $2n_i$ and are parallel to the optical axes of the crystal. Defining the impermeability tensor by

$$\boldsymbol{\eta} = \boldsymbol{\epsilon}^{-1} \tag{2.57}$$

which form in the principal axis system of the crystal is

$$\boldsymbol{\eta} = \begin{pmatrix} \frac{1}{n_1^2} & 0 & 0 \\ 0 & \frac{1}{n_2^2} & 0 \\ 0 & 0 & \frac{1}{n_3^2} \end{pmatrix} \tag{2.58}$$

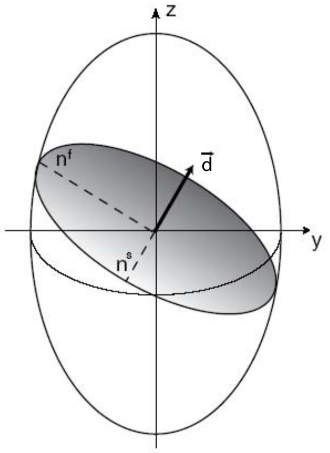

Figure 2.3.: The shaded ellipse is the intersection of the index ellipsoid with the plane normal to the direction of incidence ***d*** of the electromagnetic wave.

the equation of the index ellipsoid can be rewritten as

$$\boldsymbol{u} \cdot \boldsymbol{\eta} \cdot \boldsymbol{u} = 1 \tag{2.59}$$

Any plane through the origin of the index ellipsoid defines an intersecting ellipse (Fig. 2.3). The two axes of this intersecting ellipse are equal in length to 2 n_s and 2 n_f, where n_f and n_s are the two indices of refraction of material for light propagating perpendicular to this plane. These axes are parallel to two eigenvectors of the impermeability tensor $\boldsymbol{\eta}$.

2.3.2. The Pockels effect

An external electric field changes the properties of an optically active crystal. The refractive index becomes a function of the external field, which results in a change of the orientation and shape of the index ellipse.

For high electric fields the polarization becomes nonlinear in electric field strength and can be described by the following equation:

$$\boldsymbol{P} = \epsilon_0(\chi_e^{(0)}\boldsymbol{E} + \chi_e^{(1)}\boldsymbol{E}^2 + \chi_e^{(2)}\boldsymbol{E}^3 ...) \tag{2.60}$$

The linear susceptibility χ_e^0 induces the effects described in section 2.3. For weak electric fields all but the first term can be neglected. The second order susceptibility χ_e^1 induces a dependency of the refractive index on the electric field (linear electro-optical effect or Pockels effect). χ_e^2 leads to a dependency of the refractive index on the intensity of the electric field (quadratic electro-optical effect or Kerr effect).

As $\boldsymbol{\chi}$ and $\boldsymbol{\eta}$ are related by equations (2.48) and (2.57), the impermeability tensor also contains terms of higher order in the presence of a strong external electric field and can thus be expanded using a Taylor-expansion around $\boldsymbol{E} = 0$:

$$\eta_{ij} = \eta_{ij}(0) + r_{ijk}E_k + s_{ijkl}E_kE_l + \ldots \tag{2.61}$$

Here, r_{ijk} are the Pockels coefficients and s_{ijkl} the Kerr coefficients. For gallium phosphide (GaP) and zinc telluride (ZnTe) their order of magnitude is:

$$\begin{aligned} r_{ijk} &\approx 10^{-12}\frac{\mathrm{m}}{\mathrm{V}} \\ s_{ijkl} &\approx 10^{-21}\frac{\mathrm{m}^2}{\mathrm{V}^2} \end{aligned} \tag{2.62}$$

For these crystals, the Kerr effect can be neglected. The impermeability tensor thus becomes:

$$\boldsymbol{\eta}(\boldsymbol{E}) = \epsilon^{-1}\boldsymbol{I} + \boldsymbol{r} \cdot \boldsymbol{E} \tag{2.63}$$

where $\boldsymbol{I}$ is the identity matrix. Inserting this into equation (2.56) yields:

$$\boldsymbol{u} \cdot \boldsymbol{\eta}(\boldsymbol{E}) \cdot \boldsymbol{u} = \sum_{i,j=1,2,3} \left(\epsilon^{-1}\delta_{i,j} + \sum_{k=1,2,3} r_{ijk}E_k \right) u_i u_j = 1 \tag{2.64}$$

As the tensor $\boldsymbol{\eta}$ is symmetric ($r_{ijk} = r_{jik}$), it is convention to simplify the tensor by introducing the following nomenclature to contract the indices:

$(1,1) \rightarrow 1$	$r_{11k} \rightarrow r_{1k}$
$(2,2) \rightarrow 2$	$r_{22k} \rightarrow r_{2k}$
$(3,3) \rightarrow 3$	$r_{33k} \rightarrow r_{3k}$
$(2,3) \rightarrow 4$	$r_{23k} = r_{32k} \rightarrow r_{4k}$
$(1,3) \rightarrow 5$	$r_{13k} = r_{31k} \rightarrow r_{5k}$
$(1,2) \rightarrow 6$	$r_{12k} = r_{21k} \rightarrow r_{6k}$

(2.65)

2.3.3. Electro-optic effect in GaP and ZnTe

The symmetry of a crystal influences the number of independent elements of the matrix $\{r_{ijk}\}$. Crystals of the zinc blende structure (e.g. CdTe, GaAs, GaP, ZnS, ZnTe) are composed of two face-centered cubic lattices shifted by one quarter of the spatial diagonal and thus feature a high degree of symmetry. As a consequence, the matrix of Pockels coefficients has only one independent entry ($r_{41} = r_{52} = r_{63}$).

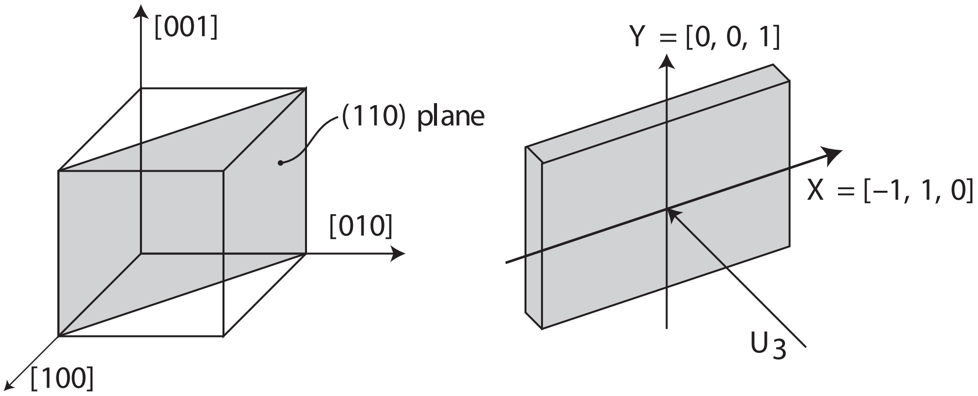

Figure 2.4.: The (110)-plane in which the used crystals are cut (a). The coordinate system (X,Y). The direction of incident of the THz radiation and the laser pulse are parallel to the vector $\boldsymbol{U}_3$ (b).

As GaP and ZnTe crystals are isotropic at vanishing electric field, $n_1 = n_2 = n_3 = n_0$ and owing to the high degree of symmetry, equation (2.59) assumes the following form:

$$\frac{1}{n_0^2}(u_1^2 + u_2^2 + u_3^2) + 2r_{41}(E_1u_2u_3 + E_2u_3u_1 + E_3u_1u_2) = 1 \tag{2.66}$$

To obtain the principal refractive indices a principal axis transformation has to be performed.

2.3.4. Determination of the main refractive indices

The crystals used in EO experiments are cut in the (110)-plane (Fig. 2.4, a). The THz radiation and the probe pulse propagate along the normal to this plane, therefore their electric field vectors lie in the (110)-plane.A new coordinate system (X, Y) is defined in this plane with

$$X = \frac{1}{\sqrt{2}}\begin{pmatrix} -1 \\ 1 \\ 0 \end{pmatrix} \quad \text{and} \quad Y = \begin{pmatrix} 0 \\ 0 \\ 1 \end{pmatrix} \tag{2.67}$$

Assuming perpendicular incidence to the XY-plane and an angle α of the electric field with respect to the X-axis, the components of the electric vector $\boldsymbol{E}_{\mathbf{THz}}$ of the THz radiation in the base system of the crystal lattice are

$$\boldsymbol{E}_{\mathbf{THz}} = E_{\text{THz}}\begin{pmatrix} -\frac{1}{\sqrt{2}}\cos\alpha \\ \frac{1}{\sqrt{2}}\cos\alpha \\ \sin\alpha \end{pmatrix} = E_{\text{THz},0}e^{-i\omega_{\text{THz}}t}\begin{pmatrix} -\frac{1}{\sqrt{2}}\cos\alpha \\ \frac{1}{\sqrt{2}}\cos\alpha \\ \sin\alpha \end{pmatrix} \tag{2.68}$$

with the amplitude $E_{\mathrm{THz},0}$ and the frequency ω_{THz} of the THz wave. Inserting this into equation (2.63) yields

$$\boldsymbol{\eta}(\boldsymbol{E}_{\mathrm{THz}}) = \frac{1}{n_0^2}\begin{pmatrix} 1 & 0 & 0 \\ 0 & 1 & 0 \\ 0 & 0 & 1 \end{pmatrix} + r_{41}E_{\mathrm{THz}} \begin{pmatrix} 0 & \sin\alpha & \cos\alpha/\sqrt{2} \\ \sin\alpha & 0 & -\cos\alpha/\sqrt{2} \\ \cos\alpha/\sqrt{2} & -\cos\alpha/\sqrt{2} & 0 \end{pmatrix} \tag{2.69}$$

To find the main refractive indices and the principal axes, the eigenvalues and eigenvectors of the tensor $\boldsymbol{\eta}$ have to be calculated. The eigenvalues can be evaluated to:

$$\begin{aligned} \lambda_{1,2} &= \frac{1}{n_0^2} - \frac{r_{41}E_{\mathrm{THz}}}{2}\left(\sin\alpha \pm \sqrt{1+3\cos^2\alpha}\right) \\ \lambda_3 &= \frac{1}{n_0^2} + r_{41}E_{\mathrm{THz}}\sin\alpha \end{aligned} \tag{2.70}$$

The normalized eigenvectors are:

$$\begin{aligned} \boldsymbol{U}_1 &= \tfrac{1}{2}\sqrt{1+\tfrac{\sin\alpha}{\sqrt{1+3\cos^2\alpha}}}\begin{pmatrix} -1 \\ 1 \\ \frac{2\sqrt{2}\cos\alpha}{\sqrt{1+3\cos^2\alpha}+\sin\alpha} \end{pmatrix} \\ \boldsymbol{U}_2 &= \tfrac{1}{2}\sqrt{1+\tfrac{\sin\alpha}{\sqrt{1+3\cos^2\alpha}}}\begin{pmatrix} 1 \\ -1 \\ \frac{2\sqrt{2}\cos\alpha}{\sqrt{1+3\cos^2\alpha}-\sin\alpha} \end{pmatrix} \\ \boldsymbol{U}_3 &= \tfrac{1}{\sqrt{2}}\begin{pmatrix} -1 \\ -1 \\ 0 \end{pmatrix} \end{aligned}$$

The main refractive indices are given by:

$$n_i = \frac{1}{\sqrt{\lambda_i}} \tag{2.71}$$

Taking into account that $r_{41}E_{\mathrm{THz}} \ll 1/n_0^2$ the result for the main refractive indices is:

$$\begin{aligned} n_1 &= n_0 + \tfrac{n_0^3 r_{41}E_{\mathrm{THz}}}{4}\left(\sin\alpha + \sqrt{1+3\cos^2\alpha}\right) \\ n_2 &= n_0 + \tfrac{n_0^3 r_{41}E_{\mathrm{THz}}}{4}\left(\sin\alpha - \sqrt{1+3\cos^2\alpha}\right) \\ n_3 &= n_0 - \tfrac{n_0^3 r_{41}E_{\mathrm{THz}}}{2}\sin\alpha \end{aligned}$$

Looking at the normalized eigenvectors it becomes obvious that the third principal axis is perpendicular to the (110) crystal plane. This is also the direction of incidence of the THz radiation. The vectors $\boldsymbol{U}_1$ and $\boldsymbol{U}_2$ are of course perpendicular to each other but $\boldsymbol{U}_1$ may enclose an angle ψ with the X-axis (the [-110] axis). This angle can be evaluated by using the scalar product of $\boldsymbol{U}_1$ and $\boldsymbol{X}$ and applying the relation $\cos(2\psi) = 2\cos^2\psi - 1$. This yields

$$\cos 2\psi = \frac{\sin\alpha}{\sqrt{1 + 3\cos^2\alpha}} \tag{2.72}$$

Care has to be taken in the evaluation of the vector $\boldsymbol{U}_2$ at the limit of $\alpha \to \pi/2$ as the normalization factor vanishes and the third component tends to infinity. The result is

$$\boldsymbol{U}_2\left(\frac{\pi}{2}\right) = \begin{pmatrix} 0 \\ 0 \\ 1 \end{pmatrix} \tag{2.73}$$

So for $\alpha = \pi/2$, the vectors $\boldsymbol{U}_1, \boldsymbol{U}_2$ point in the directions of X and Y, respectively.

The principal indices of refraction corresponding to the first two principal axes are n_1 and n_2. The according refractive index ellipse is shown in figure 2.5. The Ti:Sa laser beam of angular frequency ω is incident on the EO crystal along the eigenvector $\boldsymbol{U}_3$, so its electric vector $\boldsymbol{E}_{\text{laser}}$ lies in the (110) plane. In a crystal of the thickness d, the two components of $\boldsymbol{E}_{\text{laser}}$ along the principal axes $\boldsymbol{U}_1$ and $\boldsymbol{U}_2$ receive a relative phase shift of

$$\Gamma(\alpha) = \frac{\omega d}{c}(n_1 - n_2) = \frac{\omega d}{2c} n_0^3 r_{41} E_{\text{THz}} \sqrt{1 + 3\cos^2\alpha} \tag{2.74}$$

This equation will be used to evaluate the electro-optic measurements. In the following this phase shift will to referred to as 'phase retardation' or 'phase retardation parameter'. It is proportional to the electric field strength E_{THz} of the external field and depends on the angle α between the field vector and the X-axis. The dependence of ψ and Γ on the angle α is shown in figure 2.6. The maximal phase change is obtained for $\alpha = 0 \Rightarrow \psi = \pi/4$. The main refractive indices and the relative phase shift are plotted in figure 2.6 as a function of the angle α between the electric vector $\boldsymbol{E}_{\text{THz}}$ of the THz field and the X-axis. The larger index corresponds to a slower speed of the light, the smaller index to a faster speed. Hence, it is customary to designate the refractive indices also by $n_\text{s} = n_1$, $n_\text{f} = n_2$.

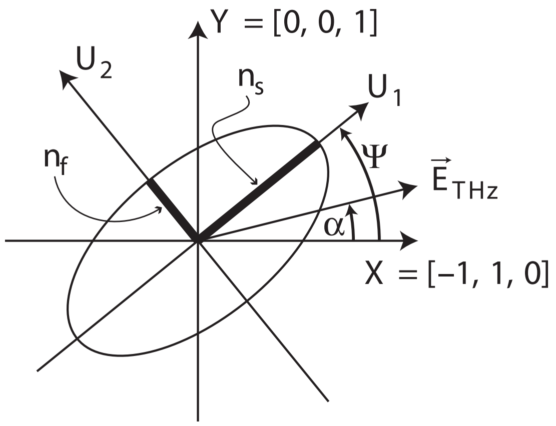

Figure 2.5.: The refractive index ellipsoid projected into the (110) plane of the EO crystal. The electric field vector $\boldsymbol{E}_{\mathrm{THz}}$ encloses an angle α with the X=[-110]-axis of the crystal while the angle between the long half axis of the ellipse and the X axis is given by $\psi(\alpha)$. Both the THz radiation and laser pulse impinge along the normal to the (110) plane, given by the unit vector $\boldsymbol{U}_3 = (-1/\sqrt{2}, -1/\sqrt{2}, 0)$.

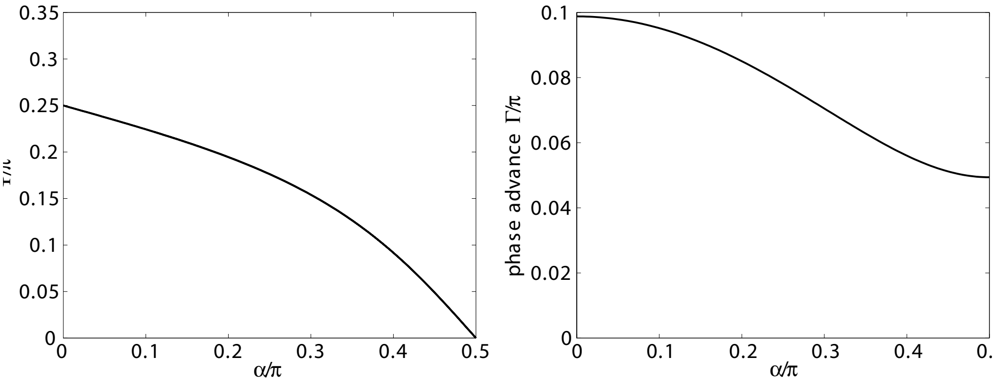

(a)

(b)

Figure 2.6.: The angle ψ between the first principal axis of the refractive index ellipsoid and the X axis as a function of the angle α between the electric vector $\boldsymbol{E}_{\mathrm{THz}}$ of the THz field and the X axis (a). The retardation parameter Γ, i.e. the relative phase shift between the two orthogonal components of the laser field $\boldsymbol{E}_{\mathrm{laser}}$, plotted as a function of α (b). The curve is computed for a ZnTe crystal of d=500 µm thickness and a THz field $E_a = 10^6$ V/m. From [CSS+05a].

3. Experimental methods in electro-optic measurements of THz pulses

3.1. Electro-optic detection schemes

The transverse electric field of a relativistic electron bunch (cf. 2.1) passing with the speed c at a close distance from the EO crystal corresponds to a transient THz pulse traveling through the crystal. The transverse electric field of the bunch has a radial polarisation, but at the position of the laser beam at a difference r from the electron beam, the field can be approximated as a linearly polarized field E_{THz}. The linearly polarized THz pulse induces birefringence in the EO crystal with an orientation of the optical axes, which depends on the angle α between the electric field vector of the THz radiation E_{THz} and the [-1,1,0] axis of the EO crystal. If a linear polarized optical probe pulse E_{laser} passes through the crystal, the different refractive indices n_{s} and n_{f} (Eq. (2.74)) will lead to a phase retardation between the two components of the electric field of the probe pulse parallel to the optical axes.

The relative phase retardation between the two components is given by equation (2.74). The phase shift reaches a maximum at $\alpha = 0$, when the field vector of the THz radiation is parallel to the X-axis of the EO crystal (Fig. 2.6):

$$\Gamma_{\max} = \frac{n_0^3 r_{41} E_{\mathrm{THz}} \omega}{c} d \tag{3.1}$$

The effect of the phase retardation on the polarization of the probe laser pulse depends on the direction of polarization relative to the optical axes of the EO crystal. This can be understood by assuming a laser pulse polarized parallel to one of the optical axes. In this case, the state of polarization remains unchanged, and there is no measurable signal on a detector. At any other orientation the phase retardation leads to an elliptical polarization. A polarization of the laser pulse, which is rotated by 45° relative to the optical axes of the crystal has two components parallel to the optical axes that are of equal amplitude. This leads to the maximum effect of the induced birefringence on the polarization of the laser (Fig. 3.1).

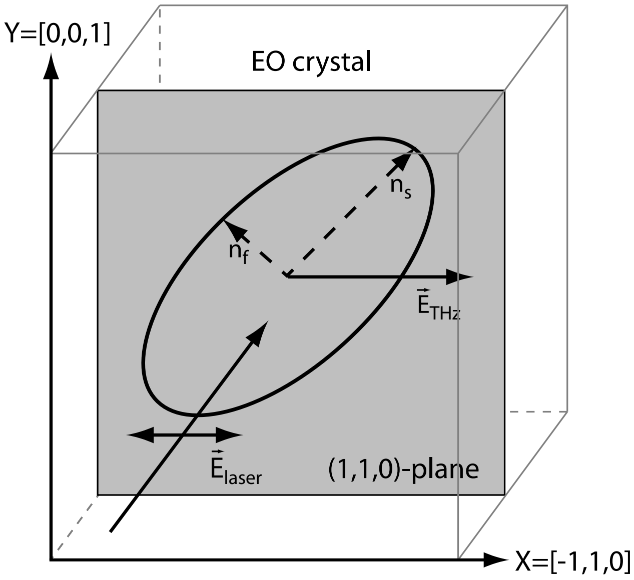

Figure 3.1.: Geometry leading to the largest electro-optical effect. The THz field is incident perpendicular to the (110) plane and is linearly polarized parallel to the [-110] axis. The probe pulse is incident perpendicular to the (110) plane as well and is linearly polarized parallel to the [-110] axis.

3.1.1. Principles of signal detection

The Ti:Sa laser beam with electric vector $\boldsymbol{E}_{\text{laser}}$ impinges along the normal to the XY-plane (cf. 2.3.4) coinciding with the principal axis $\boldsymbol{U}_3$. The propagation of a polarized light ray can be described using the Jones calculus, see e.g. [YY84]. Laser light with a horizontal or vertical polarization is represented by the vectors

$$\boldsymbol{E}_{\text{h}} = E_{\text{laser}} \begin{pmatrix} 1 \\ 0 \end{pmatrix} \quad \text{or} \quad \boldsymbol{E}_{\text{v}} = E_{\text{laser}} \begin{pmatrix} 0 \\ 1 \end{pmatrix} \tag{3.2}$$

The rotation of the polarization plane can be described by the matrix

$$\boldsymbol{R}(\phi) = \begin{pmatrix} \cos\phi & -\sin\phi \\ \sin\phi & \cos\phi \end{pmatrix} \tag{3.3}$$

The Jones matrix of a quarter-wave plate is:

$$\boldsymbol{Q} = \exp(+i\pi/4) \cdot \begin{pmatrix} 1 & 0 \\ 0 & -i \end{pmatrix} \tag{3.4}$$

To describe the birefringent EO crystal with the indices $n_\mathrm{s}(\alpha) = n_1(\alpha), n_\mathrm{f}(\alpha) = n_2(\alpha)$ and thickness d in the principal axis coordinate system the following matrix is used:

$$\boldsymbol{EO}(\alpha) = \begin{pmatrix} \exp(-in_\mathrm{s}(\alpha)\omega d/c) & 0 \\ 0 & \exp(-in_\mathrm{f}(\alpha)\omega d/c) \end{pmatrix} \tag{3.5}$$

This matrix can be rewritten by separating out the average phase change $\phi = (n_\mathrm{s} + n_\mathrm{f})\,\omega d/c$:

$$\boldsymbol{EO}(\alpha) = \begin{pmatrix} \exp(-i\Gamma(\alpha)/2) & 0 \\ 0 & \exp(+i\Gamma(\alpha)/2) \end{pmatrix} \cdot e^{-i\phi} \tag{3.6}$$

Here, $\Gamma(\alpha)$ is given by equation (2.74). As only intensities are calculated, the overall phase factor $\exp(-i\phi)$ can be omitted in the following.

To calculate the electric field strength after the EO crystal the field of the laser beam $\boldsymbol{E}_\mathrm{laser}$ is rotated into the principle axis system of the EO crystal, then passed through the crystal, and finally rotated back to the laboratory (X,Y) system. Mathematically this results in the following product of matrices:

$$\begin{aligned} &\boldsymbol{R}(-\psi(\alpha)) \cdot \boldsymbol{EO}(\alpha) \cdot \boldsymbol{R}(\psi(\alpha)) \cdot \boldsymbol{E}_\mathrm{laser} \\ &= \begin{pmatrix} e^{-i\Gamma/2}\cos^2(\psi) + e^{i\Gamma/2}\sin^2(\psi) & (e^{-i\Gamma/2} - e^{i\Gamma/2})\sin(\psi)\cos(\psi) \\ (e^{-i\Gamma/2} - e^{i\Gamma/2})\sin(\psi)\cos(\psi) & e^{-i\Gamma/2}\sin^2(\psi) + e^{i\Gamma/2}\cos^2(\psi) \end{pmatrix} \cdot \boldsymbol{E}_\mathrm{laser} \\ &= \begin{pmatrix} \cos(\Gamma/2) - i\sin(\Gamma/2)\cos(2\psi) & -i\sin(\Gamma/2)\sin(2\psi) \\ -i\sin(\Gamma/2)\sin(2\psi) & \cos(\Gamma/2) + i\sin(\Gamma/2)\cos(2\psi)) \end{pmatrix} \cdot \boldsymbol{E}_\mathrm{laser} \\ &= \begin{pmatrix} 1 & 0 \\ 0 & 1 \end{pmatrix} \cos(\Gamma/2) - i \begin{pmatrix} \cos(2\psi) & \sin(2\psi) \\ \sin(2\psi) & -\cos(2\psi)) \end{pmatrix} \sin(\Gamma/2) \cdot \boldsymbol{E}_\mathrm{laser} \end{aligned} \tag{3.7}$$

The angle $\psi(\alpha)$ is the angle between the principal axis of the index ellipsoid and the X-axis (Fig. 2.5) and can be calculated from equation (2.72) to:

$$\psi = \frac{1}{2}\arccos\left(\frac{\sin\alpha}{\sqrt{1 + 3\cos^2\alpha}}\right) \tag{3.8}$$

3.1.2. Crossed polarizer setup

In the simplest electro-optical detection setup, usually referred to as the crossed polarizer setup, a horizontally polarized laser beam is passed through the EO crystal and a vertical polarizer in front of the detector.

To calculate the electric field strength E_det at the detector, the electric field vector of the horizontally polarized laser beam $\boldsymbol{E}_\mathrm{h}$ is multiplied with the rotated matrix of the EO crystal (Eq. (3.7)), and the vertical polarized component is selected by multiplying it with $\begin{pmatrix} 0 & 1 \end{pmatrix}$:

$$\begin{aligned} E_{\mathrm{det}} &= \begin{pmatrix} 0 & 1 \end{pmatrix} \cdot \boldsymbol{R}(-\psi) \cdot \boldsymbol{EO}(\alpha) \cdot \boldsymbol{R}(\psi) \cdot E_{\mathrm{laser}} \begin{pmatrix} 1 \\ 0 \end{pmatrix} \\ &= -iE_{\mathrm{laser}} \sin(2\psi(\alpha)) \sin\left(\frac{\Gamma(\alpha)}{2}\right) \end{aligned} \tag{3.9}$$

The phase factor $-i = e^{-i\pi/2}$ drops out when intensities are calculated. At the detector the intensity I_{det} is given by:

$$I_{\mathrm{det}}(\alpha) = \frac{c\varepsilon_0}{2}|E_{\mathrm{det}}|^2 = \frac{c\varepsilon_0}{2}E_{\mathrm{laser}}^2 \sin^2(2\psi(\alpha)) \sin^2\left(\frac{\Gamma(\alpha)}{2}\right) \tag{3.10}$$

For $\alpha = 0 \rightarrow \psi = \pi/4$, which is the setting with the maximum EO effect, it is:

$$I_{\mathrm{det}} = \frac{c\varepsilon_0}{2}E_{\mathrm{laser}}^2 \sin^2\left(\frac{\Gamma}{2}\right) = \frac{c\varepsilon_0}{2}E_{\mathrm{laser}}^2 \sin^2\left(\frac{\omega d}{2c}n_0^3 r_{41} E_{\mathrm{THz}}\right) \tag{3.11}$$

For $\Gamma \ll 1$ the intensity is proportional to E_{THz}^2. The residual birefringence of the EO crystal caused by imperfections and mechanical stress can be compensated by a quarter-wave plate between the EO crystal and the analyzer.

Due to imperfect polarization of the input beam, uncompensated residual birefringence, scattering in the crystal, and imperfect polarization in the analyzer, the intensity at the detector in the absence of a THz pulse cannot be eliminated completely. This leads to a background signal $s_{\mathrm{bg}}I_{\mathrm{laser}}$ proportional to the laser intensity $I_{\mathrm{laser}} = \frac{c\varepsilon_0}{2}E_{\mathrm{laser}}^2$, which has to be added to I_{det}:

$$I_{\mathrm{det}} = \frac{c\varepsilon_0}{2}E_{\mathrm{det}}^2 + s_{\mathrm{bg}}I_{\mathrm{laser}} \tag{3.12}$$

3.1.3. Balanced detection

Inserting a quarter-wave plate between the EO crystal and the polarizer which optical axis is oriented 45° relative to the polarization direction of the incoming laser beam the electric field at the detector becomes:

$$E_{\mathrm{det,v}} = E_{\mathrm{laser}} \begin{pmatrix} 0 & 1 \end{pmatrix} \cdot \boldsymbol{R}(-\pi/4) \cdot \boldsymbol{Q} \cdot \boldsymbol{R}(\pi/4) \cdot \boldsymbol{R}(-\psi) \cdot \boldsymbol{EO}(\alpha) \cdot \boldsymbol{R}(\psi) \cdot \begin{pmatrix} 1 \\ 0 \end{pmatrix} \tag{3.13}$$

If no THz field is present this setup will lead to a circularly polarized laser pulse after the quarter-wave plate and the field at the detector becomes $E_{\mathrm{det,v}} = \sqrt{2}E_{\mathrm{laser}}$. Assuming again an angle $\alpha = 0 \rightarrow \psi = \pi/4$, the field and the intensity at a detector (e.g. a photodiode) with a THz field present becomes:

$$\begin{aligned} E_{\mathrm{det,v}} &= \frac{E_{\mathrm{laser}}}{\sqrt{2}}(\cos(\Gamma/2) - \sin(\Gamma/2)) && (3.14) \\ I_{\mathrm{det,v}} &= \frac{c\varepsilon_0}{2} E_{\mathrm{v}}^2 + s_{\mathrm{bg}} I_{\mathrm{laser}} \\ &= \frac{c\varepsilon_0}{2} \frac{E_{\mathrm{laser}}^2}{2} |\cos(\Gamma/2) - \sin(\Gamma/2)|^2 + s_{\mathrm{bg}} I_{\mathrm{laser}} \\ &= \frac{I_{\mathrm{laser}}}{2}(1 - \sin\Gamma) + s_{\mathrm{bg}} I_{\mathrm{laser}} && (3.15) \end{aligned}$$

For $\Gamma \ll 1$ the intensity I_{det} is proportional to E_{THz} but on a large background ($E_{\mathrm{THz}}^2/2$).

Using a polarizing beamsplitter like a Wollaston prism or a beamsplitter cube with access to both polarizations the horizontal component can simultaneously be measured:

$$\begin{aligned} E_{\mathrm{det,h}} &= E_{\mathrm{laser}} \begin{pmatrix} 1 & 0 \end{pmatrix} \cdot \boldsymbol{R}(-\pi/4) \cdot \boldsymbol{Q} \cdot \boldsymbol{R}(\pi/4) \cdot \boldsymbol{R}(-\psi) \cdot \boldsymbol{EO}(\alpha) \cdot \boldsymbol{R}(\psi) \cdot \begin{pmatrix} 1 \\ 0 \end{pmatrix} \\ &= \frac{E_{\mathrm{laser}}}{\sqrt{2}}(\cos(\Gamma/2) + \sin(\Gamma/2)) && (3.16) \\ I_{\mathrm{det,h}} &= \frac{I_{\mathrm{laser}}}{2} |\cos(\Gamma/2) + \sin(\Gamma/2)|^2 + s_{\mathrm{bg}} I_{\mathrm{laser}} \\ &= \frac{I_{\mathrm{laser}}}{2}(1 + \sin\Gamma) + s_{\mathrm{bg}} I_{\mathrm{laser}} && (3.17) \end{aligned}$$

which makes a balanced detector setup possible.

The intensity difference seen by the balanced detector is:

$$I_{\mathrm{det,h}} - I_{\mathrm{det,v}} = I_{\mathrm{laser}} \sin\Gamma \qquad (3.18)$$

For reasonable THz fields of up to $10^7\,\frac{\mathrm{V}}{\mathrm{m}}$, the phase retardation Γ is $\ll 1$. Since the balanced detector signal is linear in the electric field E_{THz} of the THz pulse, it is therefore much larger than the signal of the crossed-polarizer setup which is proportional to Γ^2. However, to use the advantage of this higher signal, a detector is needed, which does not saturate at half of the laser power transmitted through the EO crystal.

3.1.4. Measuring near crossed polarization

Balanced detection is not always possible, particularly in the single shot detection schemes discussed later. At crossed polarization, however, the electro-optic signal depends quadratic on the electric field of the THz pulse and a small residual birefringence of the EO crystal or slight misalignments of the wave plate or the polarizers can result in large errors in the acquired field strength. Therefore, an extended version of the crossed polarizer setup is studied here, where a half-wave plate is introduced between the quarter-wave plate and the analyzer.

The matrix of a half-wave plate is:

$$\boldsymbol{H} = \boldsymbol{Q}^2 = \exp(+i\pi/2) \cdot \begin{pmatrix} 1 & 0 \\ 0 & -1 \end{pmatrix} \tag{3.19}$$

For a horizontally polarized laser field $\boldsymbol{E}_{\text{laser}}$ going through the setup consisting of the EO crystal ($\boldsymbol{EO}$) rotated by an angle α relative to the vertical plane, a quarter-wave plate ($\boldsymbol{Q}$) rotated by ϕ, a half-wave plate ($\boldsymbol{H}$) rotated by θ and a vertical polarizer the output laser field can be calculated by multiplication of the corresponding Jones matrices:

$$\begin{aligned} E_{\text{det}}(\theta, \phi, \Gamma) &= \begin{pmatrix} 0 & 1 \end{pmatrix} \cdot \boldsymbol{R}(-\theta) \cdot \boldsymbol{H} \cdot \boldsymbol{R}(\theta) \cdot \boldsymbol{R}(-\phi) \cdot \boldsymbol{Q} \cdot \boldsymbol{R}(\phi) \cdot \\ & \qquad \boldsymbol{R}(-\psi) \cdot \boldsymbol{EO}(\alpha) \cdot \boldsymbol{R}(\psi) \cdot \begin{pmatrix} 1 \\ 0 \end{pmatrix} E_{\text{laser}} \end{aligned}$$

Assuming again an angle $\alpha = 0 \rightarrow \psi = \pi/4$, the field and the intensity at a detector (e.g. a photodiode) with a THz field present becomes[1]:

$$\begin{aligned} E_{\text{det}}(\theta, \phi, \Gamma) &= \frac{E_{\text{laser}}}{\sqrt{2}} \left[\cos(2\theta)\sin(\Gamma/2) - \sin(2\phi - 2\theta)\cos(\Gamma/2)\right. \\ & \quad \left. -i\left(\sin(2\theta)\cos(\Gamma/2) + \cos(2\phi - 2\theta)\sin(\Gamma/2)\right)\right] && (3.20) \\ I_{\text{det}}(\theta, \phi, \Gamma) &= \frac{c\varepsilon_0}{2} |E_{\text{det,v}}|^2 + s_{\text{bg}} I_{\text{laser}} \\ &= \frac{I_{\text{laser}}}{2} \left[1 - \cos(\Gamma - 2\phi + 4\theta)\cos^2\phi + \cos(\Gamma + 2\phi - 4\theta)\sin^2\phi\right] \\ & \quad + s_{\text{bg}} I_{\text{laser}} && (3.21) \end{aligned}$$

For the two special cases $\phi = 0$ or $\theta = 0$ this results in:

$$\begin{aligned} I_{\text{det}}(\theta, 0, \Gamma) &= \frac{I_{\text{laser}}}{2} \left[1 - \cos(\Gamma + 4\theta)\right] + s_{\text{bg}} I_{\text{laser}} && (3.22) \\ & \text{and} \\ I_{\text{det}}(0, \phi, \Gamma) &= \frac{I_{\text{laser}}}{2} \left[1 - \cos(\Gamma - 2\phi)\cos^2\phi + \cos(\Gamma + 2\phi)\sin^2\phi\right] \\ & \quad + s_{\text{bg}} I_{\text{laser}} && (3.23) \end{aligned}$$

The normalized signal intensity as a function of the phase retardation Γ is plotted in figure 3.2. For rotation angles of the quarter-wave plate which are not multiples of $\pi/4$, the amplitude of the $\cos^2$-oscillation is slightly lower than 1, reaching a minimum of about 0.85 for $\phi = \pi/8$ or odd multiples thereof. A rotation of the half-wave plate

---

[1] Calculated with Mathematica 5.0, Wolfram Research

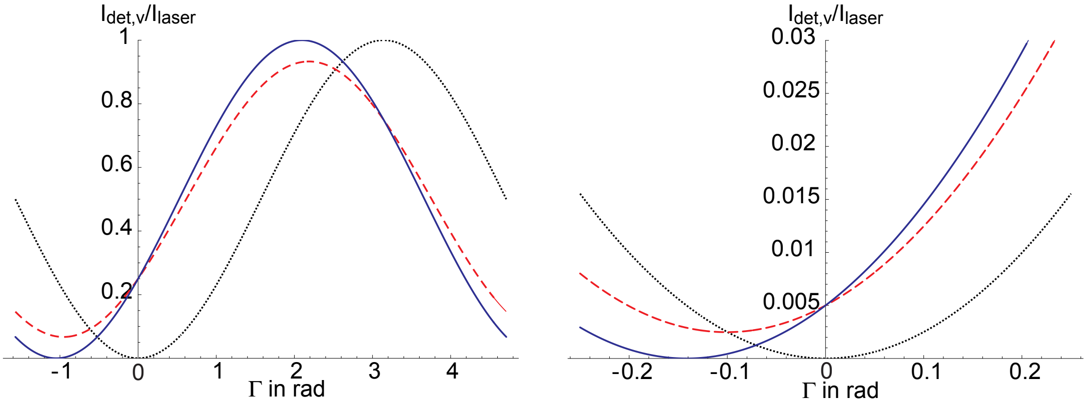

(a) $\phi = -\pi/8 = -22.5° = -393$ mrad, $\theta = 0$ (dashed line); $\phi = 0$, $\theta = 15° = 262$ mrad (solid line); $\phi = 0$, $\theta = 0$ (dotted line)

(b) $\phi = -2.9° = -50$ mrad, $\theta = 0$ (dashed line); $\phi = 0$, $\theta = 2° = 35$ mrad (solid line); $\phi = 0$, $\theta = 0$ (dotted line)

Figure 3.2.: Normalized signal intensity as a function of the phase retardation Γ for different settings of the wave plates ($s_{\mathrm{bg}} = 0$).

alone shifts the $\cos^2$-oscillation of the signal intensity in Γ but the amplitude of the oscillation remains 1. Since $\Gamma \ll 1$ for most EO measurements, a steep slope of $I_{\mathrm{det}}(\theta, \phi, \Gamma)$ at $\Gamma \approx 0$ is preferable. The steepest slope is achieved for $\phi = \pi/4$ as used in the balanced detection setup or for $\theta = \pi/8$, respectively. However, these settings lead to a background signal for $\Gamma = 0$ of $I_{\mathrm{laser}}/2$, which is only acceptable for balanced detectors. If a balanced detection in not possible, the background signal $I_{\mathrm{det}}(\theta, \phi, 0)$ will need to be small enough to not saturate the detector. Figure 3.2 shows the calculated EO signal intensity as a function of the phase retardation for two settings of the wave plates that lead to the same background of $0.005 \cdot I_{\mathrm{laser}}$. For one of these settings only the quarter-wave plate is rotated, for the other one only the half-wave plate. The slope of $I_{\mathrm{det}}(\theta, \phi, \Gamma)$ is steeper for the later one, which is also true for any other choice of the background value between $0 < I_{\mathrm{laser}} < 1$.

A small rotation of the half-wave plate also leads to an almost linear dependence of the intensity change on the phase retardation for small Γ. Expanding equation 3.22 into a Taylor series for $\Gamma = 0$ limited to the second order of Γ results in:

$$\begin{aligned} I_{\mathrm{det}}(\theta, 0, \Gamma) &\approx \frac{I_{\mathrm{laser}}}{2}\left[1 - \cos(4\theta) + \sin(4\theta)\Gamma + \frac{1}{2}\cos(4\theta)\Gamma^2\right] + s_{\mathrm{bg}} I_{\mathrm{laser}} \\ &\approx I_{\mathrm{laser}}\, 2\theta\Gamma\left(1 + \frac{\Gamma}{8\theta}\right) + \left(4\theta^2 + s_{\mathrm{bg}}\right) I_{\mathrm{laser}} \quad \text{for} \quad 4\theta \ll 1 \\ &\approx I_{\mathrm{laser}}\, 2\theta\Gamma + \left(4\theta^2 + s_{\mathrm{bg}}\right) I_{\mathrm{laser}} \quad \text{for} \quad \Gamma \ll 8\theta \qquad (3.24) \end{aligned}$$

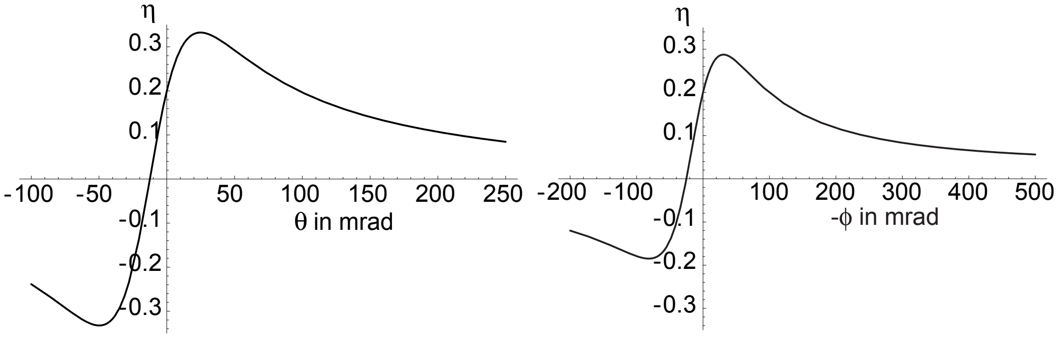

(a) (b)

Figure 3.3.: Modulation depth η vs. the angle θ of the half-wave plate (a) and ϕ of the quarter-wave plate (b) for $\Gamma = 0.1$ and $s_{\mathrm{bg}} = 0.005$.

Defining a modulation depth η of the signal [JSCZ99]:

$$\eta(\theta, \phi, \Gamma) = \frac{I_{\mathrm{det}}(\theta, \phi, \Gamma) - I_{\mathrm{det}}(\theta, \phi, 0)}{I_{\mathrm{det}}(\theta, \phi, \Gamma) + I_{\mathrm{det}}(\theta, \phi, 0)} \tag{3.25}$$

settings that maximize the modulation depth and therefore optimize the signal to noise ratio can be found. Figure 3.3 shows the modulation depth η vs. the angle θ of the half-wave plate and the angle ϕ of the quarter-wave plate, respectively, for $\Gamma = 0.1$ and $s_{\mathrm{bg}} = 0.005$, which are reasonable (worst case) assumptions for the EO measurements at crossed polarization described in this thesis. The modulation depth assumes its largest value of ≈ 0.33 for a rotation of the half-wave plate of $\theta \approx 25\,\mathrm{mrad} \approx 1.4°$. For small Γ ($\Gamma < 2\sqrt{s_{\mathrm{bg}}}$), the optimum value of θ is determined mostly by s_{bg} and varies only slowly with Γ. It has to be kept in mind that the part of the background caused by the detector noise does not scale with the laser intensity. This leads to a smaller relative noise for larger signal intensities.

It can be concluded that the quarter-wave plate should be used exclusively to compensate for a residual birefringence of the EO crystal while the half-wave plate is used to choose the proper background value and slope of $I_{\mathrm{det}}(\Gamma)$.

3.2. Electro-optic techniques used in electron accelerators

Bunch diagnostics by electro-optic sampling can be done by using either the Coulomb field of the electron bunch or the coherent transition radiation (CTR) produced by the electron bunch passing through a screen. The following section gives an overview over the techniques used to sample the time structure of the Coulomb field and transfer it to a measurable signal. For a detailed description of a setup that uses CTR refer to [Win04].

3.2.1. Electro-optic sampling using a variable delay

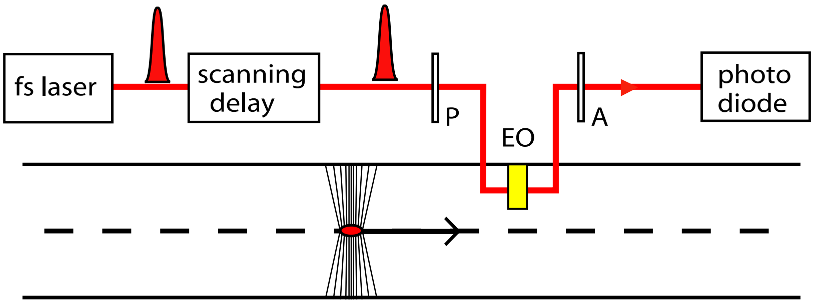

Figure 3.4.: Schematic drawing of an electro-optic sampling setup using a crossed polarizer setup. The laser pulse passes through the polarizer P and the EO crystal in the beampipe, where the polarization becomes elliptical in the presence of an electrical field. The analyzer A turns the elliptical polarization into an intensity change which is detected by the photo diode. The analyzer A may be a polarizer or a combination of a quarter wave plate to compensate the residual birefringence of the crystal and a polarizer. Changing the delay of the laser pulse, a different position along the longitudinal position of the Coulomb field can be probed for each electron bunch.

The conceptually simplest way to measure the transient Coulomb field of an electron bunch passing by the electro-optic crystal is to sample the induced birefringence with an ultra short laser pulse and change the temporal offset between the electron bunch and the laser pulse for consecutive data points (Fig. 3.4). The EO crystal is mounted in the beam pipe of an accelerator with the surface perpendicular to the electron beam axis and the edge of the crystal a few millimeters away from it. When the electron bunch passes by the crystal, the Coulomb field enters the crystal and travels through it inducing birefringence. Due to this birefringence, a laser pulse acquires a polarization change that can be measured. By changing the optical delay for each electron bunch a different position along the longitudinal position of the Coulomb field can be probed by the laser. This setup is usually referred to as Electro-Optic Sampling (EOS).

The detection of the signal can be done either by a crossed polarizer setup or by a balanced detector. Since the full energy of a laser pulse is used to probe a narrow slice of the charge distribution, only a low pulse energy of few nJ or less is needed.

Electro-optic sampling is frequently used to measure THz pulses from laser driven THz sources [WZ95, WZ97, LHS$^+$99]. These sources deliver THz pulses at a high repetition rate (kHz to MHz). Laser and THz pulses are intrinsically synchronized since the laser pulses are split and one part drives the THz pulse and the other part is used to sample it. Here the temporal resolution is limited by the length of the laser pulse and the material properties of the electro-optic crystal, which will be discussed in section 4.4.

It was first applied to measure the transient Coulomb field of an electron bunch in an accelerator at FELIX [OKY$^+$99, YMG$^+$00]. For bunch length diagnostics the main limit in temporal resolution is the arrival time jitter between the electron bunches and the laser pulses at the electro-optic crystal. Since this technique probes only a single slice of the charge distribution per electron bunch it relies on a charge distribution that is stable in its shape and arrival time over many bunches.

3.2.2. Spectrally resolved electro-optic detection

Spectrally encoded electro-optic detection (EOTD) can be used to measure the longitudinal charge distribution of an electron bunch in a single shot. Instead of passing the short laser pulse directly through the electro-optic crystal, the pulse is stretched in a dispersive material (or a grating stretcher) before it is sent to the crystal to a length significantly longer than the electron bunch. In the dispersive material the pulse acquires a frequency chirp due to the frequency dependent refractive index $n(\omega)$. The instantaneous frequency of the resulting chirped pulse is now lower than the central frequency in the leading part and higher in the tailing part. To a first approximation the instantaneous frequency varies linearly in time, so that a modulation of the laser pulse in time will cause the same modulation in the spectrum and the frequency-time correlation can be calculated according to equation (2.46).

Traveling through the EO crystal in parallel with the THz pulse of the Coulomb field the laser pulse acquires a modulation of the polarization state, which can be transferred into an intensity modulation by a polarizer. This intensity modulation can be retrieved measuring the spectrum of the laser pulse using a spectrometer with an attached CCD

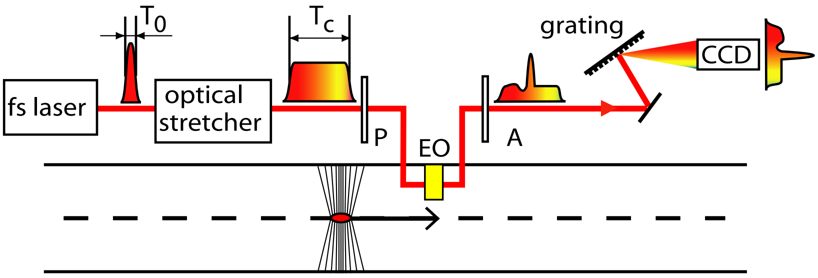

Figure 3.5.: Schematic drawing of a spectrally encoded electro-optic detection setup. The chirped laser pulse passes through the polarizer P and the EO crystal in the beampipe, where the polarization becomes elliptical. The ellipticity of the polarization is proportional to the electric field of the electron bunch and has the same temporal structure. The analyzer A turns the elliptical polarization into an intensity modulation. The longitudinal charge distribution gets encoded in the spectrum of the laser pulse, which can be detected using a spectrometer. The analyzer A may be a polarizer or a combination of wave plates and a polarizer, depending on the detection scheme.

camera (Fig. 3.5).

Since the laser pulse energy is now spread over several hundred pixels of the CCD camera either a higher laser pulse energy or an intensified CCD camera is needed.

A severe drawback of the spectrally encoded electro-optic detection is the signal distortion due to frequency mixing. A part of the laser spectrum experiences a frequency shift due to frequency mixing with the spectral components of the THz pulse [JBM+06]. Very short electron bunches or very short structures in the charge distribution lead to contributions at high frequencies in the Fourier transform of the resulting THz pulse. The resulting shifts in the laser spectrum can lead to a significant change in the frequency-time correlation of the laser pulse (Equ. 2.46), if the chirp of the laser pulse is large. In the measured spectrum the shifted spectral components cannot be distinguished from the original spectrum. Therefore the transformation from the spectral to the temporal distribution of the modulated laser pulse using the calculated frequency-time correlation leads to an artificial broadening of the signal and to distortions in its shape. For Gaussian bunch shapes the shortest THz pulse duration T_{lim} that can be measured without significant distortion is about [JBM+06]

$$T_{\mathrm{lim}} \approx 2.6\sqrt{T_0 T_c} \tag{3.26}$$

where T_c is the FWHM of the chirped probe pulse duration and T_0 is the FWHM of the duration of the unchirped probe pulse.

These unwanted artifacts in the case of short bunches can be avoided by choosing the chirp low enough to measure the fastest modulations without distortion, which are allowed by the material properties of the EO crystal. For a detailed numerical study of this effect see section 4.4.

Single-shot electro-optic measurements with a chirped laser pulse (spectrally resolved EO detection) were first demonstrated at laser driven THz sources [JZ98, SJZ98] and later applied for direct electron bunch measurements at FELIX [Wil02] with a temporal resolution of about 400 fs and measured EO signals of 1.7 ps.

3.2.3. Temporally resolved electro-optic detection

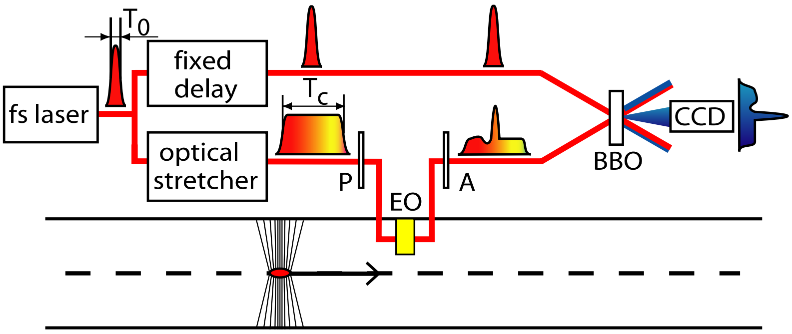

Figure 3.6.: Schematic drawing of a temporally encoded electro-optic detection setup. The short laser pulse is split into two parts: One part is stretched to several ps and sent through the polarizer P and the EO crystal in parallel with the Coulomb field of the electron bunch. The second part remains unstretched. In the EO crystal the stretched laser pulse acquires an elliptic polarization with an ellipticity which is proportional to the electric field of the electron bunch and has the same temporal structure. The analyzer A turns the elliptical polarization into an intensity modulation, which is then sampled by the short pulse in a single-shot cross-correlator.

One possibility to avoid the risk of distortion of the EO signal is not to measure the spectrum of the modulated laser pulse but to measure its time structure directly [JSM+03]. For the temporally encoded electro-optic detection the short laser pulse is split into two parts, where one part, called the EO beam, is stretched and sent through the EO crystal and the analyzing polarizer to a cross-correlator. The second part of the pulse, the gate beam, is used to sample the EO beam in the correlator (Fig. 3.6).

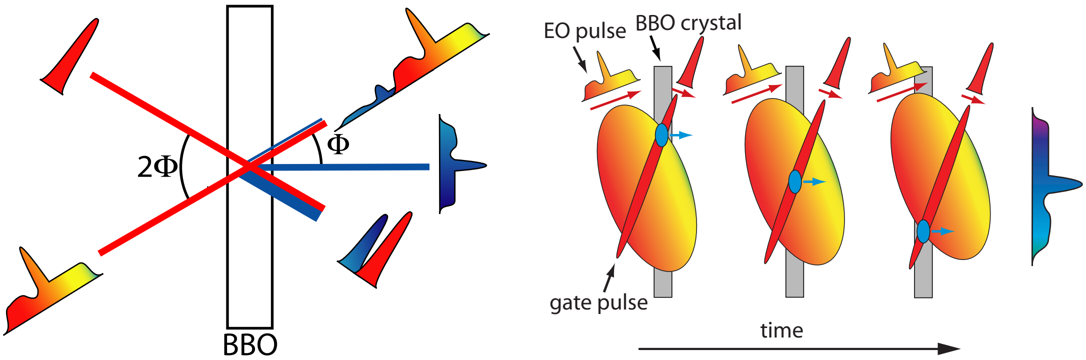

(a) The several ps long, modulated EO pulse and the short gate pulse are crossed in the BBO crystal under an angle of 2Φ. The SHG light originating from the overlap of both beams leaves the crystal along the bisecting line between the two beam paths and is therefore separated from the SHG light generated from each of the two beams individually.

(b) Since the two beams are expanded and they cross under a crossing angle of 2Φ, the short gate pulse overlaps with different temporal slices of the EO pulse at different spatial positions of the BBO crystal. Thus the temporal modulation of the EO pulse is transfered to spatial distribution of the SHG light which can by imaged to a camera.

Figure 3.7.: Schematic drawing of a single shot optical cross-correlator

The cross-correlator uses the technique of non-collinear second-harmonic generation (SHG) with expanded beam profiles [SGRB87]. The two beams are expanded to about 10 mm diameter and crossed in a SHG crystal with a crossing angle of 2Φ (Fig. 3.7(a)). When the pulses overlap spatially and temporally in the SHG crystal, a part of the pulse energy is converted into light of the double frequency of the incoming light. This light leaves the crystal along the bisecting line between the two beam paths and its intensity I_{SHG} is proportional to the product of the intensities of the two incoming pulses I_{gate} and I_{EO}:

$$I_{\mathrm{SHG}} \propto I_{\mathrm{gate}} I_{\mathrm{EO}} \tag{3.27}$$

The SHG light generated from each individual beam leaves the crystal collinear with the original beam and is proportional to the square of its intensity I_{gate}^2 or I_{EO}^2.

Since the beams are expanded and they cross in an angle, different longitudinal (temporal) slices of the long pulse from the EO beam overlap at different positions along the horizontal dimension of the SHG crystal with the short gate pulse (Fig. 3.7(b)). The spatial distribution of the SHG light intensity $I_{\mathrm{SHG}}(x)$ from the crystal is proportional to a convolution of the intensities of the two beams

$$I_{\mathrm{SHG}}(x) \propto \int_{-\infty}^{+\infty} I_{\mathrm{EO}}(t+\tau) I_{\mathrm{gate}}(t-\tau)\mathrm{d}t \tag{3.28}$$

can be imaged to an ICCD camera [SGRB87] The temporal resolution of this detection scheme depends on the duration of the gate beam, the thickness of the SHG crystal, the spatial resolution of the imaging system, and the camera. Using a Ti:Sa laser pulse of 30 fs FWHM duration and a 300 µm thick β-barium borate (BBO) crystal a resolution of better than 100 fs can be reached. Due to the low efficiency of the SHG process a pulse energy of several 100 µJ is needed, which requires an amplified laser system.

Temporally resolved electro.optic detection (EOTD) has been first demonstrated at FELIX, reaching a signal width of 330 fs [BJM+04].

3.2.4. Spatially resolved electro-optic detection

A third electro-optical technique to measure longitudinal charge distribution of an electron bunch in a single shot encodes the charge distribution in the transverse profile of a short laser pulse that is then detected with a camera. It was first demonstrated at laser induces THz sources [SWK+00]. For accelerator applications signals widths of 270 fs could be measured at SLAC [Cav05] and of 160 fs at DESY [ADS+06] with spatially resolved electro-optic detection.

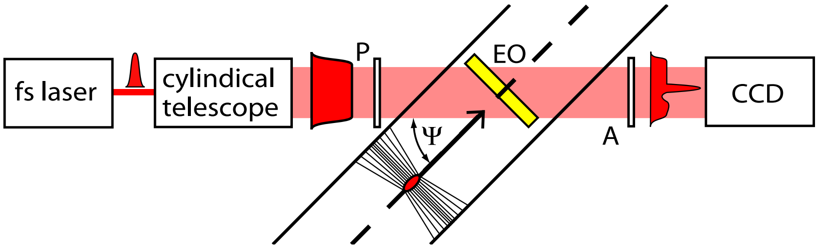

Figure 3.8.: Schematic drawing of a spatially encoded electro-optic detection setup. The electron bunch is traveling in a plane above the laser beam and the EO crystal. The horizontally expanded laser pulse passes through the polarizer P and the EO crystal in the beampipe. Since the laser hits the EO crystal under an angle, different spatial components of the laser pass through the crystal at different times and acquire a different elliptical polarization. The analyzer A turns the spatial modulation of the polarization into a spatial intensity modulation which is detected by the CCD camera.

As in the setups described above (cf. 3.2.1 - 3.2.3), the electron bunch passes by the EO crystal perpendicular to its surface, but here the path of the laser pulses is not parallel to the path of the electron bunches any more. Assuming the electron path is horizontal and the EO crystal is mounted below it, the laser beam lies in a horizontal plane through the EO crystal and encloses an angle Ψ with the vertical projection of the electron path to this plane. The laser beam focused to a horizontal line of the width

Δx at the crystal. Since one side of the laser pulse arrives earlier at the EO crystal than the other by a time difference

$$\Delta t = \frac{\Delta x}{c} \tan(\Psi) \tag{3.29}$$

and the Coulomb field enters the crystal over the whole surface simultaneously, the time profile of the Coulomb field is encoded into the spatial profile of the laser which can be measured by imaging the line focus at the crystal to a camera.

4. Numerical studies

In this chapter numerical studies on the electro-optic effect in zinc telluride (ZnTe) and gallium phosphide (GaP) are presented. Sections 4.1, 4.2 and 4.6 have been previously published in a similar form as a TELSA report in [CSS$^+$05b]. The frequency dependence is taken into account both of the complex index of refraction in the THz and the optical regime and of the electro-optic coefficient. Using the available experimental data on the refractive index $n(f)$ and the extinction coefficient $\kappa(f)$ in the THz regime, the coupling of this ultrashort THz pulse into the EO crystal and its propagation in the material is calculated. The frequency dependence of the complex refractive index $n(f) + i\kappa(f)$ leads to a pulse broadening and to distortions of the pulse shape, which may become severe for very short bunches. In particular high-frequency oscillations develop in the EO crystal. The propagation and broadening of the laser pulse is also considered. Ideally, the laser pulse and the THz pulse should move with the same speed through the EO crystal to obtain the best time resolution and a maximum signal in the EOS system. The group velocity mismatch constitutes a strong limitation and is investigated in detail.

The main limitation for the shortest time structure, which can be resolved, is given by transverse optical (TO) lattice oscillations. The lowest TO frequency amounts to 5.3 THz for ZnTe and 11 THz for GaP. Near a resonance the refractive index is rapidly changing with frequency and it is therefore basically impossible to achieve equal group velocities of the THz and the laser pulse. Obviously, GaP is better suited to measure very short pulses owing to its higher TO frequency. The disadvantage is that the electro-optic coefficient of GaP is about a factor of eight lower than that of ZnTe.

4.1. Electro-Optic Properties of ZnTe and GaP

4.1.1. Refractive index

4.1.1.1. Visible and infrared light

The index of refraction for visible and infrared light has been measured both for ZnTe [Mar64, War91] and GaP [PPY76, AS83, SVC85]. A useful parametrization

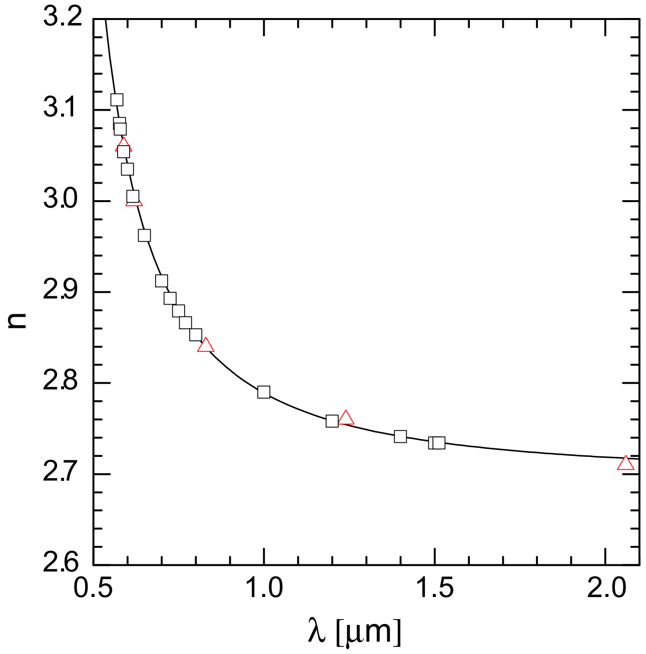

Figure 4.1.: The refractive index of ZnTe for visible and infrared light. Squares: experimental data [War91], triangles: experimental data [Mar64], solid curve: fit according to equation (4.1).

for ZnTe is [Mar64]

$$n(\lambda) = \sqrt{4.27 + \frac{3.01\lambda^2}{\lambda^2 - 0.142}} \tag{4.1}$$

where λ is the photon wavelength in µm. The optical refractive index of GaP is described by a similar expression derived from the data of [AS83, SVC85][1]

$$n(\lambda) = \sqrt{2.680 + \frac{6.40\lambda^2}{\lambda^2 - 0.0903279}} \tag{4.2}$$

The refractive indices of ZnTe and GaP are respectively plotted in Fig. 4.1 and Fig. 4.2 as a function of the wavelength in µm.

4.1.1.2. THz range

For frequencies far below the optical regime the complex dielectric function $\varepsilon(f)$ of a non-conducting crystal can be written in the form [Bar64]:

$$\varepsilon(f) = \varepsilon_{el} + \sum_j \frac{S_j f_j^2}{f_j^2 - f^2 - i\Gamma_j f} \tag{4.3}$$

---

[1] A parametrization in terms of the photon energy has been published by Pikhtin et al. [PPY76].

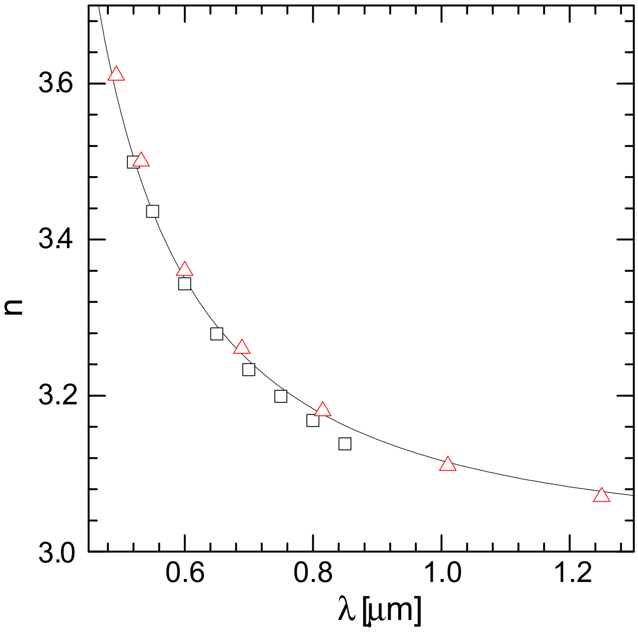

Figure 4.2.: Refractive index of GaP for visible and infrared light. The experimental data are indicated by squares [SVC85] resp. triangles [AS83], solid curve: fit according to equation (4.2).

where the first term is the contribution from the bound electrons and the second term is the contribution from lattice oscillations, which are treated as damped harmonic oscillators. The coefficient ε_{el} is constant in the THz frequency range. The sum extends over all lattice oscillations, which couple to the electromagnetic field. The quantities f_j, Γ_j and S_j are the eigenfrequency, damping constant and oscillator strength of the lattice oscillation j. For the electro-optic crystals ZnTe and GaP, a good description of $\varepsilon(f)$ in the THz regime is obtained by restricting the sum to the lowest transverse-optical (TO) lattice oscillation:

$$\varepsilon(f) = \varepsilon_{el} + \frac{S_0 f_0^2}{f_0^2 - f^2 - i\Gamma_0 f} \tag{4.4}$$

The complex index of refraction is given by taking the square root:

$$n(f) + i\kappa(f) = \sqrt{\varepsilon(f)} \tag{4.5}$$

In figures 4.3 and 4.4 the published experimental data for ZnTe and GaP on the real and imaginary part of the refractive index are plotted as a function of frequency. For ZnTe a variation can be observed up to 25% between the data from Ref. [GZM+99] and those from Ref. [War91]. Thus, two different sets of fitting parameters were used.

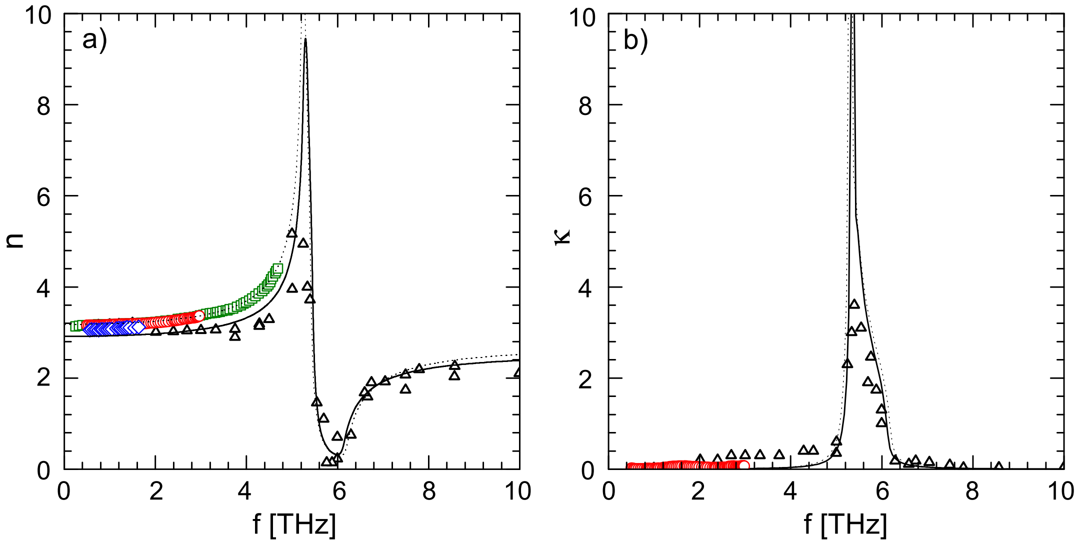

Figure 4.3.: Real part $n(f)$ (a) and imaginary part $\kappa(f)$ (b) of the refractive index of ZnTe in the THz range. The resonance at 5.3 THz is due to the excitation of a transverse optical (TO) lattice oscillation. The square symbols □ are experimental data taken from Ref. [GZM⁺99], the triangles △ from Ref. [War91], the diamonds ◇ from Ref. [HHMT73] and the circles ○ from Ref. [SWJ01]. The curves are fits of the experimental data using the formulas and the parameters shown in the text.

For Ref. [GZM⁺99] the parameters:

$$\text{ZnTe}: \ \varepsilon_{el} = 7.4\,, \quad f_0 = 5.3\ \text{THz}, \quad S_0 = 2.7\,, \quad \Gamma_0 = 0.09\ \text{THz} \tag{4.6}$$

were used, while for Ref. [War91] they were:

$$\text{ZnTe}: \ \varepsilon_{el} = 6.5\,, \quad f_0 = 5.35\ \text{THz}, \quad S_0 = 2.0\,, \quad \Gamma_0 = 0.09\ \text{THz} \tag{4.7}$$

For the simulations in the following sections we consider the first set of parameters.

The corresponding parameters used for GaP are:

$$\text{GaP}: \ \varepsilon_{el} = 8.7\,, \quad f_0 = 10.98\ \text{THz}, \quad S_0 = 1.8\,, \quad \Gamma_0 = 0.02\ \text{THz} \tag{4.8}$$

A second parameterization for the refractive index is given by [LHS⁺99]:

$$n(f) = \sqrt{\varepsilon_{el} \cdot \left[1 + \frac{f_{\text{LO}}^2 - f_{\text{TO}}^2}{f_{\text{TO}} - f^2 - i\Gamma_0 f}\right]} \tag{4.9}$$

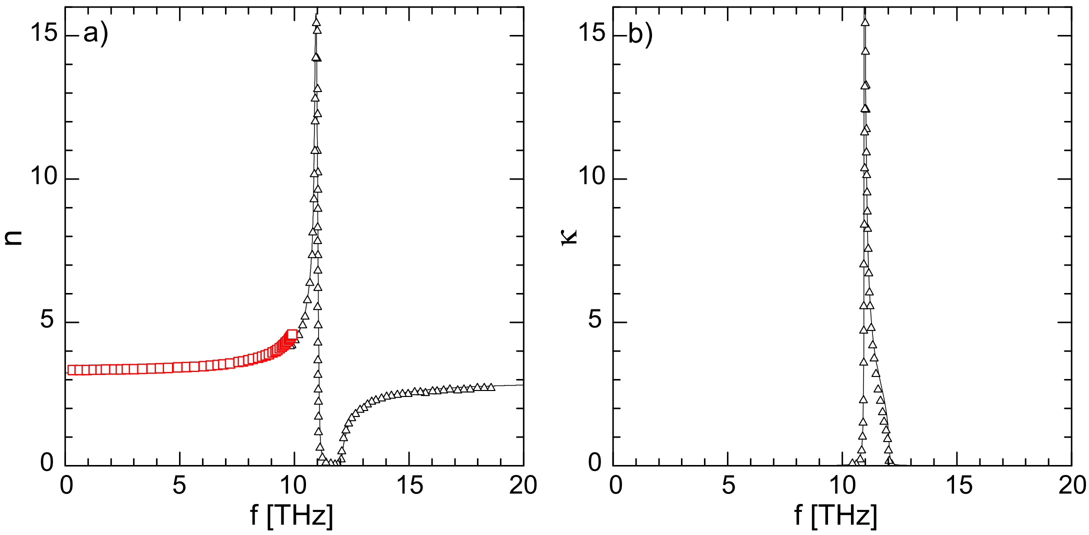

Figure 4.4.: $n(f)$ (a) and $\kappa(f)$ (b) for GaP. Here the lowest transverse optical (TO) lattice resonance is at 11 THz. The triangles △ are experimental data taken from Ref. [KS60], the squares □ from Ref. [WZ97]. The curves are fits of the experimental data using the formulas and the parameters shown in the text.

where f_{TO} and f_{LO} are the frequencies of the first transverse and longitudinal lattice oscillations with the following parameters for ZnTe and GaP:

$$\text{ZnTe}: \ \varepsilon_{el} = 6.7\,, \quad f_{\mathrm{TO}} = 5.31 \text{ THz}, \quad f_{\mathrm{LO}} = 6.18 \text{ THz}, \quad \Gamma_0 = 0.09 \text{ THz} \quad \text{and} \tag{4.10}$$

$$\text{GaP}: \ \varepsilon_{el} = 9.075\,, \quad f_{\mathrm{TO}} = 11.02 \text{ THz}, \quad f_{\mathrm{LO}} = 12.09 \text{ THz}, \quad \Gamma_0 = 0.129 \text{ THz} \tag{4.11}$$

However, the resulting deviations are small and for the simulations presented here only the parameters given in (4.6) and (4.8) are used.

4.1.2. Electro-optic coefficient

The electro-optic coefficient r_{41} is also influenced by lattice oscillations. It can be written as a function of frequency in the form [FH66]

$$r_{41}(f) = d_E \left(1 + \frac{C f_0^2}{f_0^2 - f^2 - i\Gamma_0 f}\right) \tag{4.12}$$

with the following parameters for ZnTe:

$$\text{ZnTe}: \ d_E = 4.25 \cdot 10^{-12} \text{ m/V}\,, \ C = -0.07\,, \ f_0 = 5.3 \text{ THz}\,, \ \Gamma_0 = 0.09 \text{ THz} \tag{4.13}$$

The value of C has been taken from Ref. [LHS$^+$99]. Figure 4.5 shows the frequency dependence of r_{41} of ZnTe given by equation (4.12). The very small value of r_{41} at 30 THz, reported in Ref. [Kam68], is in gross disagreement with other data [TA71] and the values found in the visible range [SJ66]. A possible reason for this discrepancy might be the low resistivity value of $\rho \approx 10^3\ \Omega$ m of the sample of Ref. [Kam68] comared with $\rho \approx 4 \times 10^6\ \Omega$ m in Ref. [SJ66] and of $\rho \approx 10^7\ \Omega$ m in Ref. [TA71]. For this reason the data point from Ref. [Kam68]is disregarded. The experimental data are too scarce and imprecise to derive a frequency dependence of r_{41}. On the other hand, due to the low piezoelectric constant of ZnTe [BJS63, SJ66], the value of the constant C is expected to be small, so that the high frequency value $r_{41}(\infty)$ should not differ appreciably from the low frequency value $r_{41}(0)$. For the simulations therefore a constant value of $r_{41}(f) = 4.0 \cdot 10^{-12}$ m/V is assumed. It was verified that no significant change in the simulated EO signal is observed if instead of a constant r_{41} the frequency dependence given by equation (4.12) is used.

The literature values on r_{41} for GaP are collected in figure 4.6. In the following sections we use for GaP the frequency dependence given in equation (4.12) with the following parameters:

$$\text{GaP}: \; d_E = 1 \cdot 10^{-12}\ \text{m/V},\; C = -0.53\,,\; f_0 = 10.98\ \text{THz},\; \Gamma_0 = 0.02\ \text{THz} \qquad (4.14)$$

Leitenstorfer et al. [LHS$^+$99] suggests $C = -0.53$, $f_0 = f_{\mathrm{TO}} = 11.02$ THz and $\Gamma_0 = 0.129$ THz.[2]

---

[2] Note however, that in Ref. [LHS$^+$99] equation (4.12) is incorrectly cited from Ref. [FH66] with the imaginary part having the opposite sign.

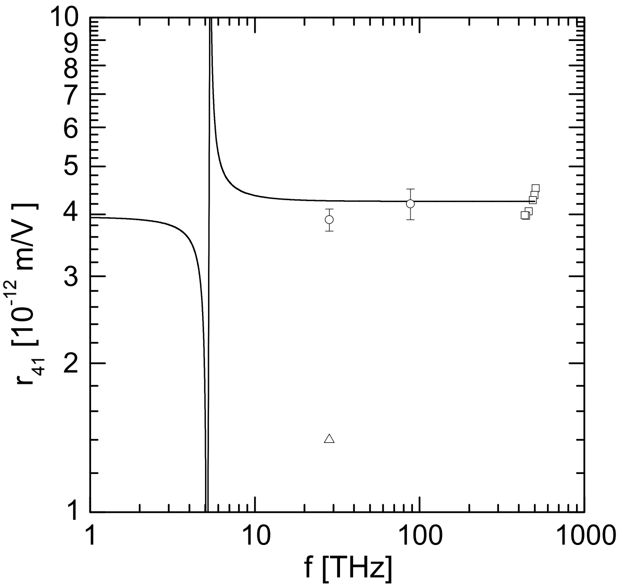

Figure 4.5.: Real part of the EO coefficient $r_{41}(f)$ of ZnTe. The square symbols □ are experimental data taken from Ref. [SJ66] ($\rho \approx 4 \times 10^6 \Omega$ m), the circles ∘ from Ref. [TA71] ($\rho \approx 10^7 \Omega$ m), the triangle △ from Ref. [Kam68] ($\rho \approx 10^3 \Omega$ m). The curve is obtained using equation (4.12) with the parameters shown in the text.

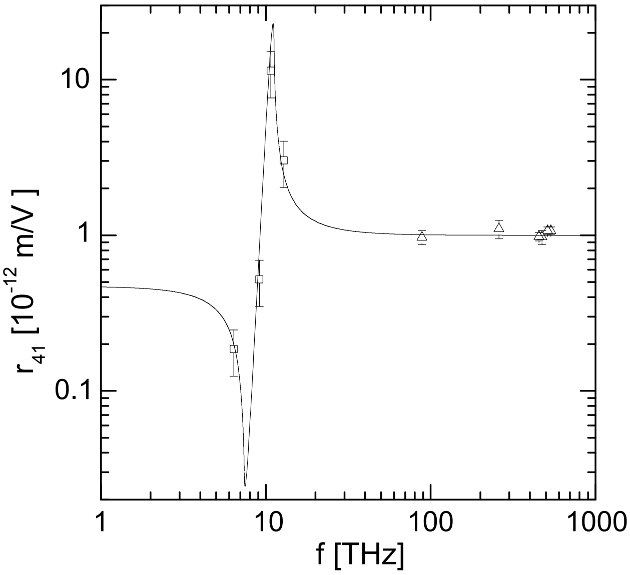

Figure 4.6.: Real part of the EO coefficient $r_{41}(f)$ for GaP. The square symbols □ are experimental data taken from Ref. [FH66], the triangles △ from Ref. [NT68]. The curve is a fit of the experimental data using equation (4.12) with the parameters shown in the text.

4.2. Propagation of the THz and Laser Pulses

4.2.1. Phase and group velocities

The refractive indices n of ZnTe and GaP decrease with increasing wavelength in the optical regime. In the THz region below the lowest TO lattice resonance n increases with the frequency. The short THz and Ti:Sa laser pulses propagate with the group velocity

$$v_g = \frac{c}{n}\left(1 + \frac{\lambda}{n}\frac{\mathrm{d}n}{\mathrm{d}\lambda}\right) = \frac{c}{\left(n + f\frac{\mathrm{d}n}{\mathrm{d}f}\right)} \qquad (4.15)$$

which is in both cases lower than the phase velocity of the contributing harmonic waves. The phase and group velocities of ZnTe and GaP are shown in figure 4.7 as a functions of frequency. For comparison also the optical group velocity at $\lambda = 0.8$ µm is plotted ($v_g = 0.309\,c$ for ZnTe and $v_g = 0.280\,c$ for GaP). While at low frequency the THz pulse propagates with a somewhat higher speed than the laser pulse, there is a growing mismatch in the velocities when one approaches the lattice resonance of 5.3 THz in ZnTe and 11 THz in GaP.

4.2.2. Electro-optic response function

For ideal electro-optic sampling conditions the THz pulse and the laser pulse should propagate at the same speed. The difference in speed leads to a reduced time resolution.

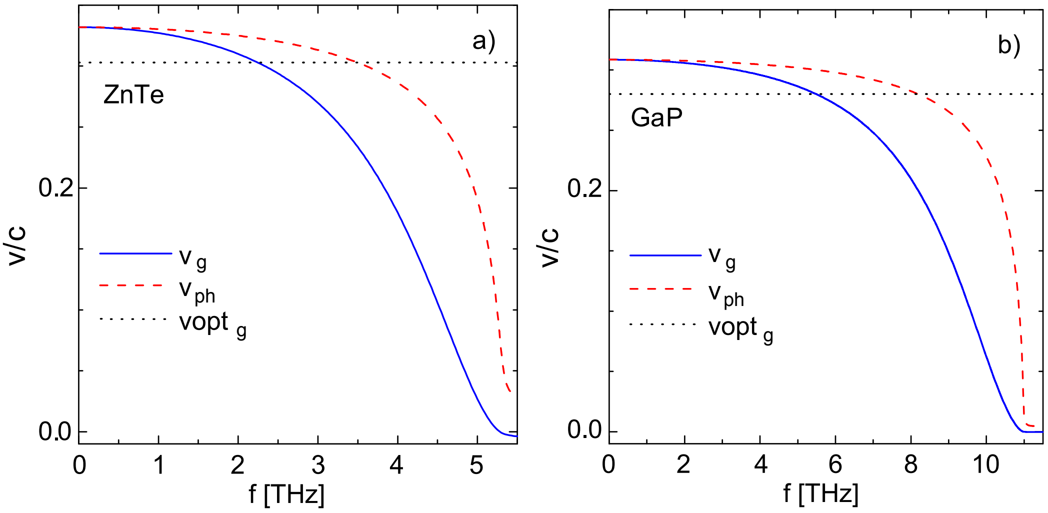

Figure 4.7.: Phase velocity and group velocity of ZnTe (a) and GaP (b) in the THz range. The velocities have been divided by c. The group velocity of optical radiation at 0.8 µm is shown as a dotted line.

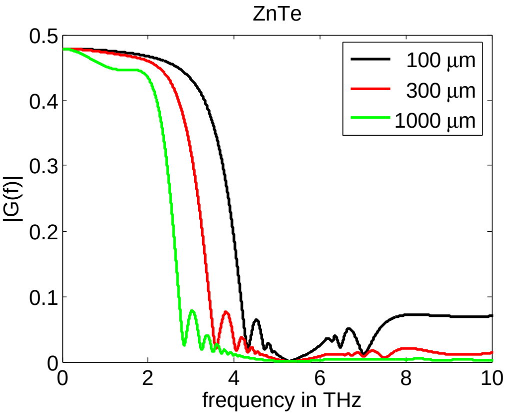

Figure 4.8.: EO response function of ZnTe for crystal thickness of 100 µm, 300 µm and 1000 µm.

It is customary to characterize the electro-optic efficiency by a response function which depends on the THz frequency f and the crystal thickness d:

$$\begin{aligned} G(f,d) &= \frac{2}{1+n(f)+i\kappa(f)}\,\frac{1}{d}\int_0^d\int_{-\infty}^{\infty}\exp[i(kz-2\pi f\,t]\delta(z-v_g t)\,\mathrm{d}t\,\mathrm{d}z \\ &= \frac{2}{1+n(f)+i\kappa(f)}\,\frac{1}{d}\int_0^d \exp\left[i\,2\pi f\,z\left(\frac{1}{v_{\mathrm{ph}}(f)}-\frac{1}{v_{\mathrm{g}}}\right)\right]\mathrm{d}z \end{aligned} \tag{4.16}$$

where $v_{\mathrm{ph}}(f)$ is the phase velocity at the THz frequency f and v_{g} is the optical group velocity at the laser wavelength. The factor

$$A_{trans}(f) = \frac{2}{1+n(f)+i\kappa(f)} \tag{4.17}$$

is the frequency-dependent transmission coefficient for the transition of the THz electric field from vacuum into the EO crystal[3]. The EO response function of ZnTe is shown in Fig. 4.8 for different crystal thicknesses from 100 µm to 1 mm. The minima in the response function result from the fact that the phase slippage between the laser pulse and THz waves of these frequencies over the full crystal thickness is a multiple of 2π. Therefore, the phase retardation Γ caused by the positive half cycle of the THz waves is compensated by the phase retardation of equal amplitude but of opposite sign caused by the negative half cycle. It is obvious that high THz frequencies can only be reached in sufficiently thin crystals. The lattice resonance sets an upper limit of about 4.5 THz to the accessible frequency range.

---

[3] Some authors include the EO coefficient $r_{41}(f)$ in the definition of the response function, given then by $G(f,d)\cdot r_{41}(f)$. This function is referred to as the effective response function in this thesis.

Gallium phosphide permits to increase the frequency range. A fairly thin crystal ($d \leq 100$ µm) should be used to exploit this capability (Fig. 4.9). At too large thickness, for example $d = 300$ µm, GaP reaches only about 3 THz and is therefore inferior to ZnTe with its much larger EO coefficient r_{41}. The figures 4.8 and 4.9 suggest to use a ZnTe crystal thickness $d \approx 200 - 300$ µm as a compromise between high-frequency response and signal amplitude. For GaP the thickness should be about 100 µm to detect signals with frequencies up to 7.5 THz, where $|r_{41}(f)|$ of GaP approaches zero. For crystals thicker than about 200 µm the absolute value of the response function approaches zero due to the velocity mismatch at frequencies lower than 7.5 THz. The small EO signal amplitude is then an unavoidable consequence. The simulations discussed below are therefore mainly based on a ZnTe crystal of 300 µm and a GaP crystal of 100 µm thickness.

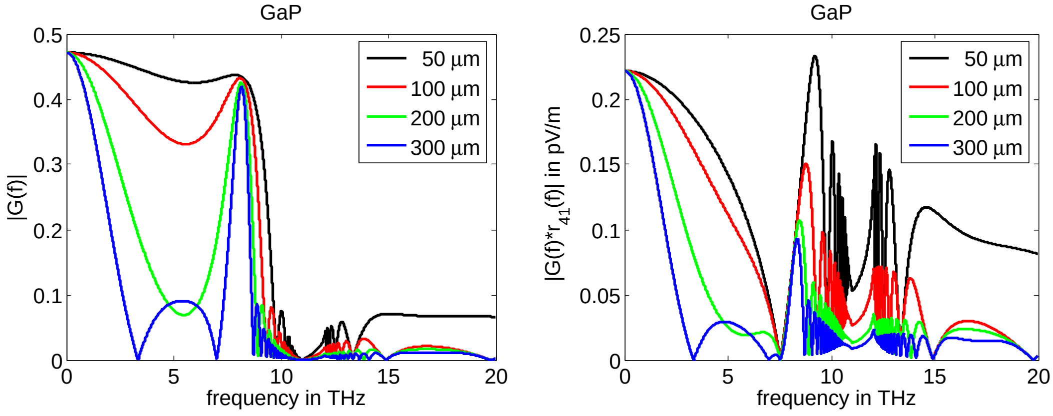

(a) (b)

Figure 4.9.: (a) EO response function of GaP for a crystal thickness of 50 µm, 100 µm, 200 µm and 300 µm. (b) The effective response function $G \cdot r_{41}$.

4.2.3. Propagation and distortion of a Gaussian THz pulse in the EO crystal

Instead of using the EO response function a more physical approach is used in this and the next section in which both the THz pulse and the optical laser pulse are propagated as wave packets through the EO crystal. This also allows to study the influence of the broadening of the laser pulse within the EO crystal on the detected signal. The best insight into the physics of electro-optic sampling is provided by studying Gaussian THz pulses of well-defined width such as Gaussian electron bunches at relativistic energies ($\gamma > 1000$). Realistic bunch shapes for the FLASH accelerator will be discussed in section 4.4.3.

A cylindrical coordinate system ($r = \sqrt{x^2 + y^2}, \varphi, z$) with the relativistic beam moving in the z direction is. The longitudinal charge distribution in the electron bunch of charge Q_0 is described by a Gaussian of variance $\sigma_z = c\sigma_t$. The line charge density is then

$$\rho(z,t) = \frac{Q_0}{\sqrt{2\pi}\sigma_z} \exp\left(-\frac{(z-ct)^2}{2\sigma_z^2}\right) \tag{4.18}$$

For highly relativistic electrons with a Lorentz factor $\gamma > 1000$ the electric field of the bunch is concentrated in a flat disk perpendicular to the direction of motion (cf. 2.1). The field has mainly a radial component and can be approximated as

$$E_r(r,z,t) = \frac{\rho(z,t)}{2\pi\varepsilon_0 r} \tag{4.19}$$

Let the EO crystal be located at $z = 0$ at a distance r_0 from the beam axis. The electric field at the position of the crystal has the time dependence

$$E_r(t) = E_0 \exp\left(-\frac{t^2}{2\sigma_t^2}\right) \quad \text{with} \quad E_0 = \frac{Q_0}{2\pi\varepsilon_0 r_0 \sqrt{2\pi} c\sigma_t} \tag{4.20}$$

$F_E(f)$ is the Fourier transform of the electric field pulse, which in this special case can be computed analytically, or for more complicated charge distributions, by an FFT (Fast Fourier Transform) algorithm. At the interface between the accelerator vacuum and the EO crystal, some fraction of the incident wave is reflected, and the remaining part is transmitted into the dielectric crystal. The amplitude transmission coefficient depends on frequency and is given by the expression

$$A_{\text{trans}}(f) = \frac{2}{n(f) + i\kappa(f) + 1} \tag{4.21}$$

The Fourier component of the transmitted electric field pulse is

$$F_{\text{trans}}(f) = F_E(f)\frac{2}{n(f) + i\kappa(f) + 1} \tag{4.22}$$

To propagate the THz pulse inside the EO material we subdivide the crystal into ten thin slices of thickness $\delta = d/10$. The Fourier component at slice j is given by

$$F_{\text{slice } j}(f) = F_{\text{trans}}(f) \exp\left(i\frac{2\pi f}{c} n(f) d_j - \frac{2\pi f}{c} \kappa(f) d_j\right) \tag{4.23}$$

where $d_j = (j + 0.5)\delta$ is the depth of slice j. The phase propagation is determined by the refractive index $n(f)$, and the attenuation by the extinction coefficient $\kappa(f)$. The

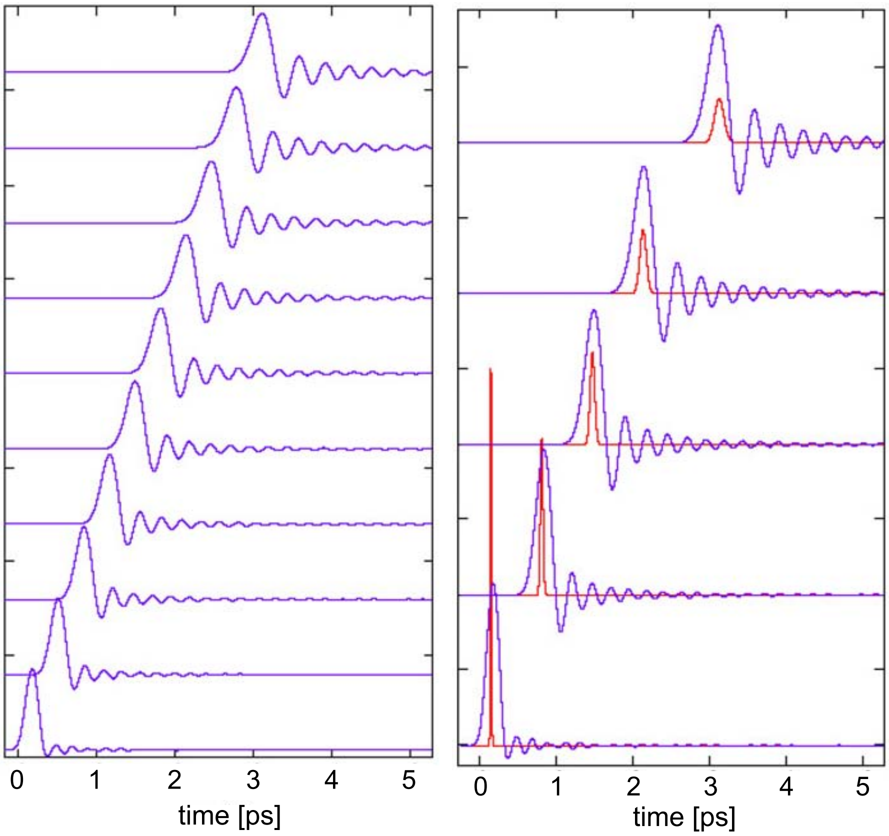

(a) (b)

Figure 4.10.: (a) The propagation of a Gaussian THz pulse with initial variance of $\sigma_t = 67$ fs ($\sigma_z = 20$ µm) in a 300 µm thick ZnTe crystal. The time profiles are plotted in the ten 30 µm thick slices of the crystal. (b) The propagation of a Gaussian THz pulse and of a Gaussian Ti:Sa laser pulse in a 300 µm thick ZnTe crystal. The time profiles are plotted at selected positions in the crystal.

time profile of the pulse at slice j is then simply obtained by applying the inverse FFT to equation (4.23):

$$E_j^{\mathrm{THz}}(t) = \mathcal{F}^{-1}\left\{F_{\mathrm{trans}}(f)\exp\left(i\,\frac{2\pi f}{c}\,n(f)d_j - \frac{2\pi f}{c}\,\kappa(f)d_j\right)\right\} \tag{4.24}$$

The time profile of the THz pulse at 10 positions inside a 300 µm thick ZnTe crystal is illustrated in figure 4.10. The pulse width increases with increasing depth in the crystal, and the oscillations gradually develop. These high frequency oscillations lag behind the main pulse since the THz refractive index grows approaching the lattice resonance at 5.3 THz (Fig. 4.3).

Also the Ti:Sa laser pulse changes its shape when it traverses the EO crystal, because the optical refractive index has a nonlinear dependence on the wavelength (Figs. 4.1 and 4.2). Assuming a Gaussian distribution for the intensity

$$I_{\mathrm{laser}}(t) \propto \exp\left(-\frac{t^2}{2\sigma_0^2}\right) \tag{4.25}$$

with a bandwidth-limited FWHM duration of $\Delta t = 2\sqrt{2\ln 2}\sigma_0 = 15$ fs for the Ti:Sa laser used in the EO experiment a growth of the variance is expected with increasing depth in the EO crystal [Mes04]

$$\sigma(z) = \sigma_0 \sqrt{1 + \left(\frac{z}{L_{\mathrm{char}}}\right)^2} \tag{4.26}$$

with a characteristic length

$$L_{\mathrm{char}} = \frac{\Delta t^2}{4\ln 2 \frac{\mathrm{d}}{\mathrm{d}\omega}(v_g^{-1})} \tag{4.27}$$

which is $L_{\mathrm{char}} = 30$ µm in ZnTe and $L_{\mathrm{char}} = 42$ µm in GaP. Figure 4.10 shows the THz and laser pulses at selected positions inside the 300 µm thick ZnTe crystal. The laser pulse moves at a lower speed than the THz pulse[4] and due to the nonlinear dispersion its width increases.

The detrimental effects of group velocity mismatch and pulse distortion are of course reduced by choosing a thinner crystal, but at the price of a lower detector signal.

4.2.4. Phase retardation and balanced detector signal

4.2.4.1. Without laser pulse broadening

In the previous section the shape of the THz pulse was computed in the 10 thin slices of the EO crystal and the relative timing with respect to the laser pulse[5]. Equation (2.74) will now be applied to calculate the retardation parameter Γ for each slice. The angle between the electric vector of the THz field and the crystallographic axis [-1,1,0] is chosen as $\alpha = 0$. To be accurate, also the frequency dependence of the EO coefficient r_{41} must be considered. This is done by multiplying the Fourier component of the propagated THz pulse (Eq. (4.23)) with $r_{41}(f)$, and by applying then the inverse FFT.

---

[4] The frequency components of a THz pulse with $\sigma_t = 67$ µm are predominantly below 2 THz. According to Fig. 4.7 the THz pulse has therefore a higher group velocity than the laser pulse.

[5] The slice thickness has to be chosen small enough, so that the shift between THz and laser pulse within a slice can be neglected. Increasing the number of slices from 10 to 20 has a negligible effect on the computed EO signal.

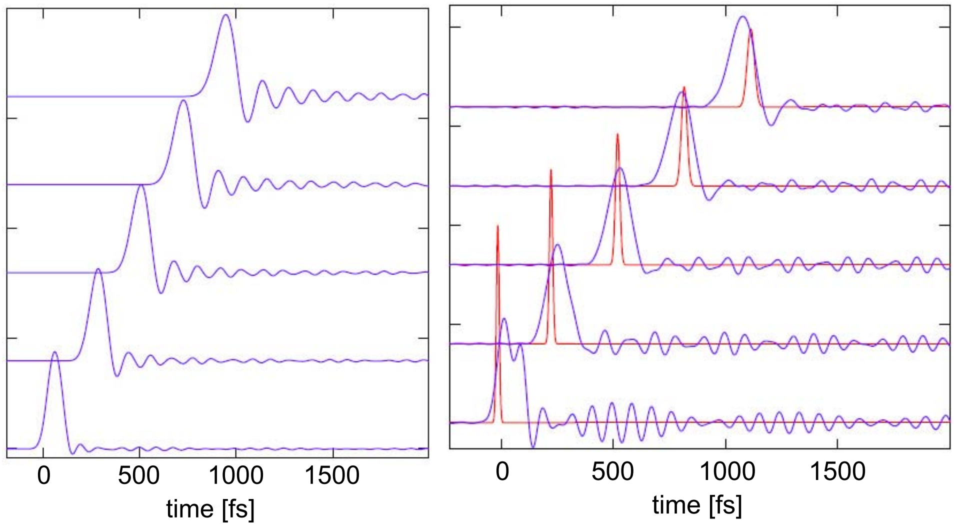

(a)

(b)

Figure 4.11.: (a) The propagation of a Gaussian THz pulse (variance $\sigma_t = 33$ fs) in a 100 µm thick GaP crystal at selected positions. (b) Same as in (a) but the frequency dependence of r_{41} is taken into account according to equation (4.28). The broadening of a Gaussian Ti:Sa laser pulse is also shown.

The *effective* electric THz pulse in slice j is therefore given by:

$$E_j^{\text{eff}}(t) = \mathcal{F}^{-1}\left\{F_{\text{trans}}(f)\exp\left(i\,\frac{2\pi f}{c}\,n(f)d_j - \frac{2\pi f}{c}\,\kappa(f)d_j\right)\cdot r_{41}(f)\right\} \tag{4.28}$$

Since for ZnTe the frequency dependence of r_{41} is disregarded, these pulses have the same shapes as shown in figure 4.10. For a GaP crystal the propagation of an *effective* Gaussian THz pulse (Eq.(4.28)) with initial variance of $\sigma_t = 33$ fs in a 100 µm thick crystal is shown in figure 4.11.

Approximating for the time being the laser pulse by a delta function, the phase retardation Γ_j generated in slice j is proportional to the electric field amplitude $E_j(t_{j,laser})$ at the arrival time of the laser pulse in slice j:

$$\Gamma_j = \frac{2\pi}{\lambda_0}\,n_0^3\,\delta\,E_j^{\text{eff}}(t_{j,\text{laser}}) \tag{4.29}$$

This time is

$$t_{j,\text{laser}} = d_j/v_{\text{g}} + \tau \tag{4.30}$$

where a variable time delay τ is allowed between THz and laser pulse. The total phase retardation accumulated in the EO crystal can be computed as a sum over the contributions of each slice:

$$\Gamma(\tau) = \sum_j \Gamma_j(\tau) = \frac{2\pi}{\lambda_0} n_0^3 \, \delta \sum_j E_j^{\mathrm{eff}} \left(d_j / v_{\mathrm{g}} + \tau \right) \tag{4.31}$$

In the actual EOS experiment the delay τ is varied in small steps to scan the THz pulse.

4.2.4.2. With laser pulse broadening

The next refinement is to incorporate the laser pulse broadening. According to equation (4.26) the rms width of the laser pulse in slice j is:

$$\sigma_j = \sigma_0 \sqrt{1 + \left(\frac{d_j}{L_{\mathrm{char}}} \right)^2} \tag{4.32}$$

The overlap of the THz and laser pulses in each slice is computed by a convolution integral:

$$\Gamma(\tau) = \frac{2\pi}{\lambda_0} n_0^3 \, \delta \sum_j \left[\int E_j^{\mathrm{eff}}(d_j / v_{\mathrm{g}} + t) \, \frac{1}{\sqrt{2\pi}\, \sigma_j} \exp\left(-\frac{(t-\tau)^2}{2\sigma_j^2} \right) \mathrm{d}t \right] \tag{4.33}$$

The signal in the balanced diode detector is proportional to $\sin(\Gamma(\tau))$ (Eq. (3.18)). Figure 4.12 shows the expected balanced diode detector signal as a function of the relative delay τ between the THz and the laser pulse. The computations have been made for a 500 µm thick ZnTe crystal and a THz pulse with $\sigma_t = 67$ fs. The influence of laser pulse broadening in the rather thick EO crystal is visible but not significant. For thinner crystals it can be neglected so it is legitimate to use equation (4.31) to compute the phase retardation parameter Γ.

The total phase retardation can also be computed from the EO response function (Figs. 4.8 and 4.9) in the following way:

$$\Gamma(\tau) = \frac{2\pi}{\lambda_0} n_0^3 \, d \cdot \mathcal{F}^{-1}\{F_E(f) G(f,d) r_{41}(f)\} \tag{4.34}$$

When the number of slices inequation (4.31) tends to infinity, the sum goes over into an integral. Then the pulse propagation method is mathematically equivalent to the response function method. A comparison with the pulse propagation method is made in figures 4.13. There is a well agreement at small crystal thickness. Differences are only visible for thick crystals and are mainly caused by the laser pulse broadening, which is not taken into account in the response function method.

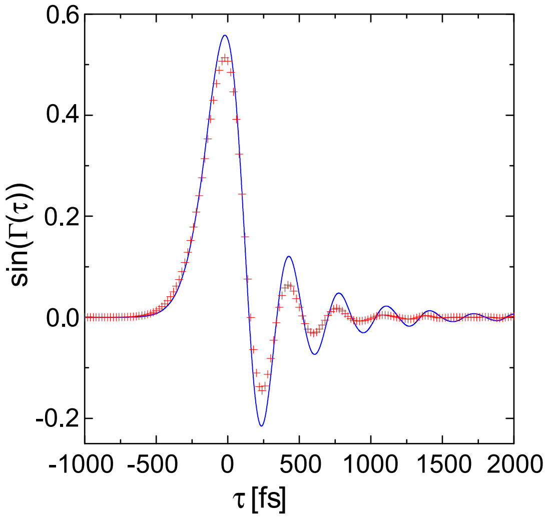

Figure 4.12.: Signal in the balanced diode detector for a 500 µm thick ZnTe crystal, which is placed at a distance $r_0 = 14$ mm from the electron beam. Bunch charge $Q = 0.2$ nC, rms bunch length $\sigma_t = 67$ fs. $\sin\Gamma(\tau)$ is plotted as a function of the relative delay τ between the THz and the laser pulse. Continuous blue curve: delta-function like laser pulse (Eq. (4.31)). Crosses: laser pulse broadening taken into consideration (Eq. (4.33)).

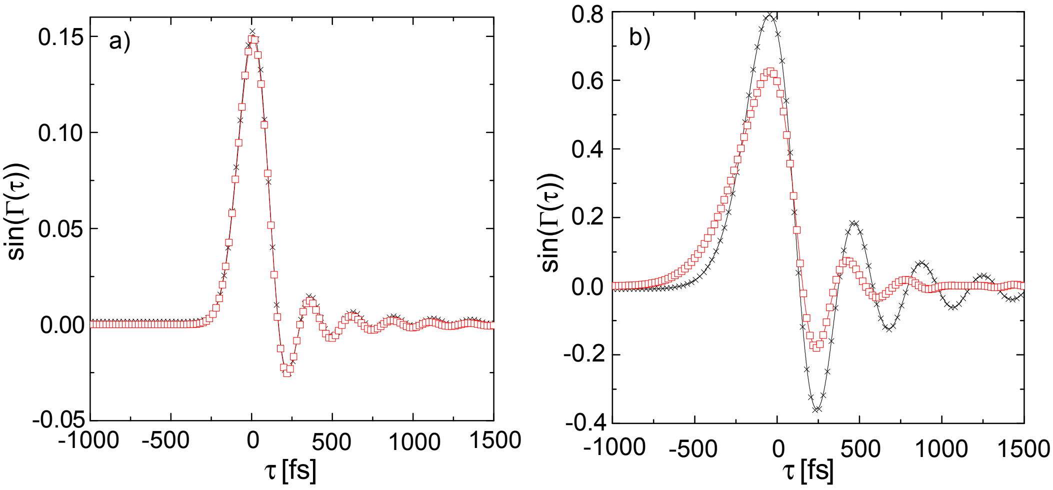

(a) (b)

Figure 4.13.: The balanced detector signal of ZnTe computed with the pulse propagation method (squares), taking into account the laser pulse broadening, in comparison with the response function method (crosses). Bunch charge $Q_0 = 0.2$ nC, rms bunch length $\sigma_t = 67$ fs. (a): Crystal thickness of 100 µm. (b): Crystal thickness of 800 µm.

4.3. Quality of Gaussian bunch shape determination by EO sampling

Although the electron bunches at the FLASH accelerator are usually not of Gaussian shape, Gaussian electron pulses of various width are well suited to study the broadening and distortion of the THz pulse due to the frequency dependencies of the transfer function G and the electro-optic coefficient r_{41} because it is easy to recognize distortion of the shape and calculate the amount of the broadening.

For the calculations in this and the following sections equation (4.34) is used to calculate the phase retardation. To prevent a significant pulse broadening due to the opening angle of the field of relativistic electrons the distance between the electron beam and the laser spot on the EO crystal is chosen as $r_0 = 1$ mm and the Lorenz factor is taken as $\gamma = 1000$. This leads to an rms pulse length for a single electron of $\sigma_t \approx 2$ fs. The bunch charge is chosen $Q_0 = 10$ pC to prevent a phase retardation of $\Gamma \geq \pi$. All calculations are done for a balanced detector setup. From the EO signal (proportional to $\sin(\Gamma)$) the phase retardation $\Gamma(t)$ is calculated, which is independent of the used detection setup. However, it has to be kept in mind that for the crossed polarizer setup the sign of Γ cannot be resolved since here the signal is proportional to $\sin^2(\Gamma/2)$. For convenience the bunch charge is chosen positive leading to positive field in the THz pulse and positive Γ. For an (electron) bunch with negative charge the electric field and therefore Γ would change its sign.

Note that in the calculations any time jitter between the electron bunch and the laser pulse is neglected.

4.3.1. Pulse broadening and distortion

Figure 4.14 shows the predicted phase retardation determined with EO sampling with a 300 μm thick ZnTe crystal induced by the field of a Gaussian electron bunch with a variance of $\sigma_t = 150\,\text{fs}$ and $\sigma_t = 50\,\text{fs}$, respectively. For a better comparison the expected phase retardation Γ_{ideal} for a frequency independent response function $G_{\text{ideal}} \equiv G(0) \cdot r_{41}(0)$ is plotted as well. Γ_{ideal} is proportional to the original THz pulse and is not broadened or distorted. The field of the 150 fs long bunch is well reproduced without any pulse broadening and almost any distortion. However, the field of the short bunch is broadened by a factor of about 1.7 and shows a shape distortion in the form of strong oscillations following the main peak. The frequency spectrum of these oscillations peaks around 3.8 THz, i.e. in the region where the refractive index exhibits a strong rise towards the lattice resonance at 5.3 THz. This rise of the refractive index leads to a large phase mismatch between the laser light and the field components above 3.5 THz. In a 300 μm thick ZnTe crystal this phase mismatch leads to small value of

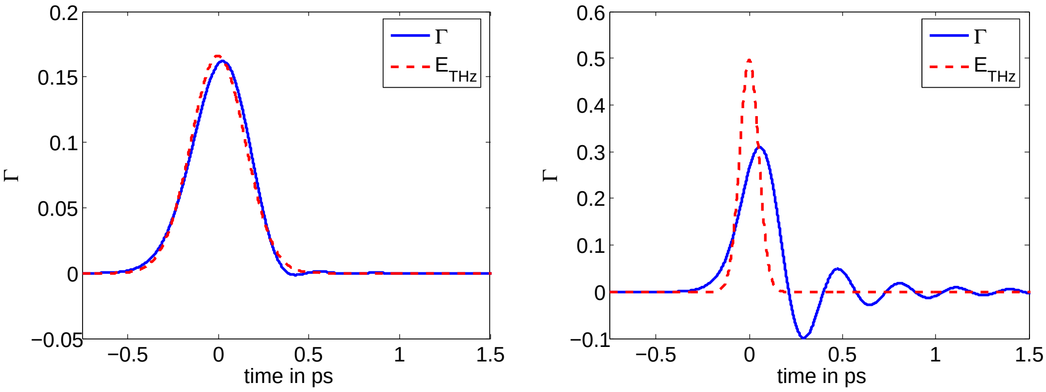

(a) (b)

Figure 4.14.: Predicted phase retardation Γ as determined with EO sampling with a 300 µm thick ZnTe crystal for a long THz pulse E_{THz} ($\sigma_t = 150\,\mathrm{fs}$, a) and a short THz pulse ($\sigma_t = 50\,\mathrm{fs}$, b).

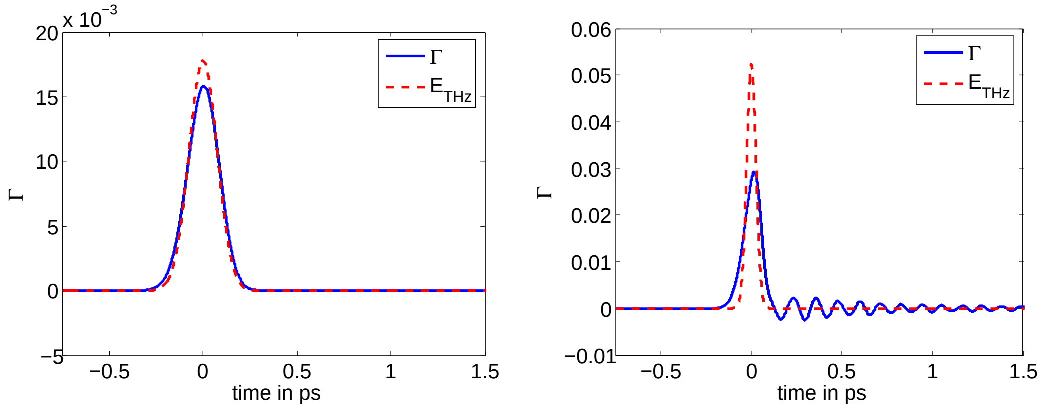

(a) (b)

Figure 4.15.: Predicted phase retardation Γ for EO sampling with a 100 µm thick GaP crystal for a long THz pulse E_{THz} ($\sigma_t = 75\,\mathrm{fs}$, a) and a short THz pulse ($\sigma_t = 25\,\mathrm{fs}$, b).

the response function at 3.6 THz (Fig. 4.8) and hence to a small electro optic signal. At 3.9 THz the phase mismatch sums up a 1.5 wavelengths leading to a better electro-optic effect and a small peak in the response function.

Since the lowest TO lattice resonance of GaP is at 11 THz, this material should support the measurement of shorter bunches. Figure 4.15 shows the predicted phase retardation for EO sampling with a 100 µm thick GaP crystal induced by two Gaussian electron bunches with a rms length of $\sigma_t = 75\,\mathrm{fs}$ and $\sigma_t = 25\,\mathrm{fs}$, respectively. The 75 fs long bunch is well reproduced without significant broadening or distortions. A 25 fs

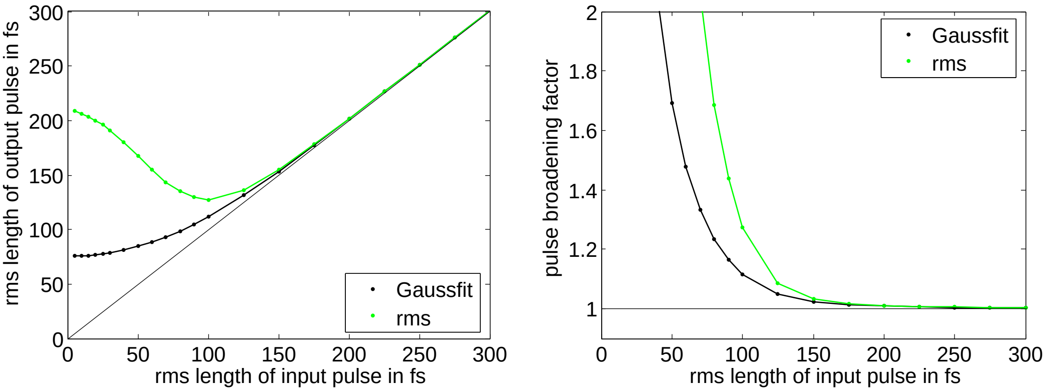

(a) (b)

Figure 4.16.: Pulse broadening in a 300 µm thick ZnTe crystal as predicted for EO sampling. Length of the EO signal (a) and pulse broadening factor (b) as a function of the electron bunch length.

long bunch results in a broadened peak followed again by strong oscillations, here at a frequency of 8.8 THz. This results from a peak in the effective response function $G \cdot r_{41}$, which is located between 7.5 THz where the electro-optic coefficient r_{41} approaches zero and 9.3 THz where the phase mismatch leads to a vanishing response function.

4.3.2. Limits on the measurable electron bunch length and time resolution

To distinguish between pulse broadening and other shape distortions the length of the resulting phase retardation signal is determined in two different ways. Firstly, a Gaussian of a variance σ_1 is fitted to $\Gamma(\tau)$. Secondly, the variance of the entire $\Gamma(\tau)$ signal is calculated as:

$$\sigma_2 = \sqrt{2} \cdot \sqrt{\frac{\int \Gamma(\tau)^2 \, \tau^2 \mathrm{d}\tau}{\int \Gamma(\tau)^2 \mathrm{d}\tau} - \frac{\int \Gamma(\tau)^2 \, \tau \mathrm{d}\tau}{\int \Gamma(\tau) \mathrm{d}\tau}} \tag{4.35}$$

For a Gaussian $\Gamma(\tau)$ pulse both variances agree: $\sigma_1 = \sigma_2$. A pulse broadening results in a $\sigma_1 = \sigma_2$ greater than σ_t of the input electron bunch. Any distortion of the pulse shape leads to an increase of σ_2 compared to σ_1: $\sigma_2 > \sigma_1 \geq \sigma_t$.

Figure 4.16a shows the resulting pulse length σ_1 and σ_2 as a function of the electron bunch length σ_t for a 300 µm thick ZnTe crystal. For long bunches $\sigma_t \geq 150$ fs, there is no significant deviation between σ_1 and σ_2. For bunches shorter than 125 fs σ_2 rises rapidly to $\sigma_2 = 2.8\,\sigma_1$ at $\sigma_t = 5$ fs. The length determined by a fitted Gaussian σ_1 decreases for shorter bunch lengths, reaching $\sigma_1 \approx 75$ fs for $\sigma_t \leq 30$ fs. The variance σ_2 decreases for shorter bunch lengths reaching a minimum of $\sigma_2 = 128$ fs at

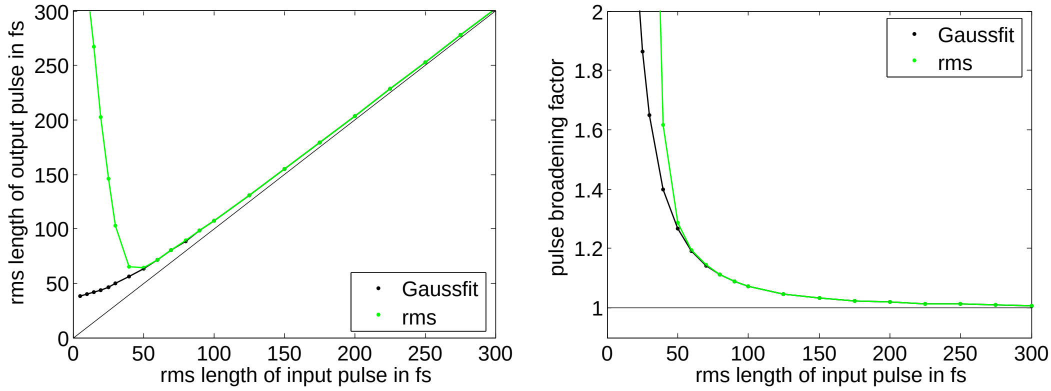

(a)

(b)

Figure 4.17.: Pulse broadening in a 100 µm thick GaP crystal as predicted for EO sampling. Length of the EO signal (a) and pulse broadening factor (b) as a function of the electron bunch length.

$\sigma_t = 100$ fs and rises again for shorter bunch length to $\sigma_2 = 208$ fs at $\sigma_t = 5$ fs. The pulse broadening factor (σ_1/σ_t) is smaller than 1.2 for bunches longer than $\sigma_t = 80$ fs (Fig. 4.16b). Note however, that at pulse length $\sigma_t < 150$ fs already a significant distortion of the pulse shape takes place.

For a 100 µm thick GaP crystal the variances σ_1 and σ_2 agree well for bunches with $\sigma_t \geq 50$ fs (Fig 4.17). For bunches with $\sigma_t < 50$ fs the variance of $\Gamma(\tau)$ rises very rapidly with decreasing pulse length σ_t to $\sigma_2 > 200$ fs for $\sigma_t < 20$ fs, while σ_1 decreases to $\sigma_1 > 40$ fs for $\sigma_t < 10$ fs. The pulse broadening factor (σ_1/σ_t) is below 1.2 for bunch length $\sigma_t \geq 60$ fs.

From this data it can be concluded that a 300 µm thick ZnTe crystal allows the measurement of bunches with $\sigma_t > 100$ fs with reasonably small distortions and pulse broadening. Using a 100 µm thick GaP crystal the measurement of bunches with $\sigma_t > 50$ fs can be expected without distortions except some pulse broadening for pulsed shorter than 100 fs. For bunches shorter than 100 fs for ZnTe and 50 fs for GaP strong oscillations are expected due to a resonant amplification of the Fourier components of the bunch in the vicinity of the TO crystal lattice oscillation frequency.

Theoretically the distortions in the phase retardation signal can be corrected by a division of the Fourier spectrum of the phase retardation signal $\Gamma(\tau)$ by the effective response function to reconstruct the THz field:

$$E_{\text{reconstructed}}(t) \propto \mathcal{F}^{-1}\left\{\frac{\mathcal{F}\{\Gamma(t)\}}{G(f)\cdot r_{41}(f)}\right\} \tag{4.36}$$

However, this requires a very good knowledge of the effective response function $G(f)\cdot r_{41}(f)$ and particularly a very good signal-to-noise ratio of the measured signal. The

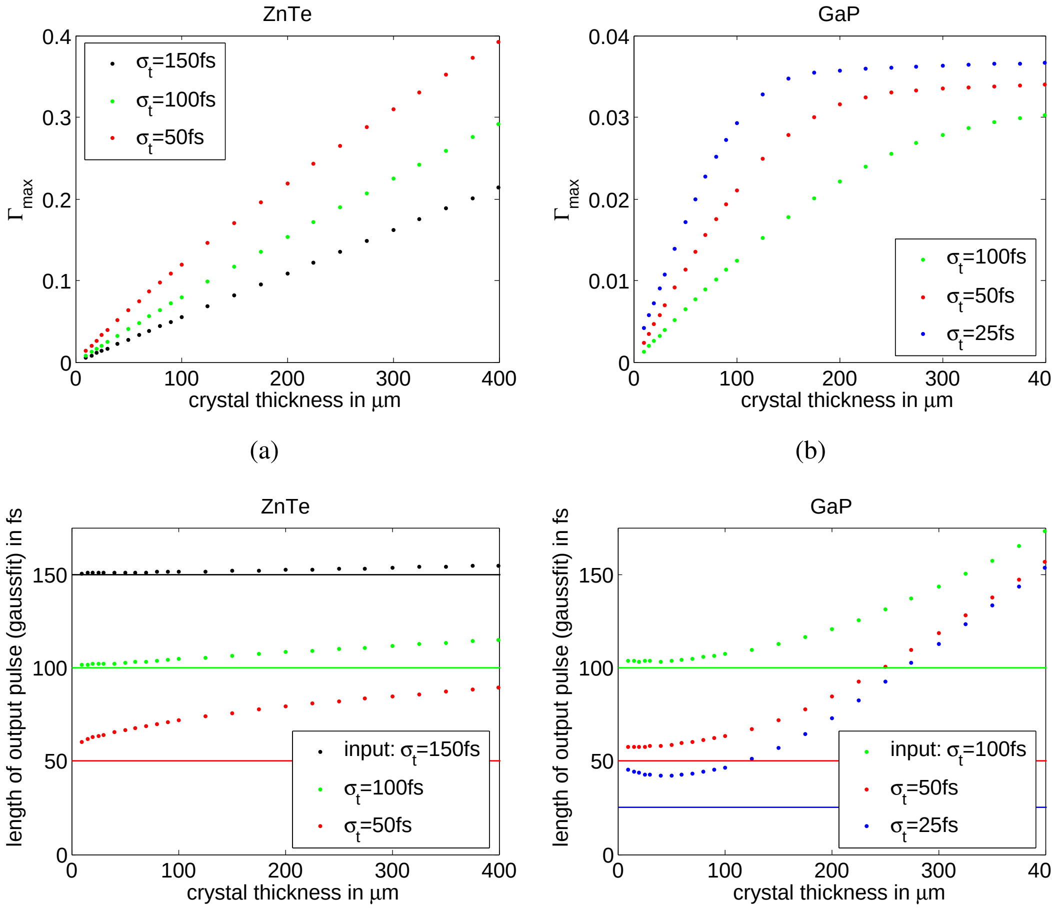

(a) (b)

(c) (d)

Figure 4.18.: Dependence of the maximal detected phase retardation (a+b) and the length of the output signal σ_1 (c+d) for different crystal thicknesses for ZnTe (a+c) and GaP (b+d). The length of the incident electron bunches σ_t are shown as solid lines of the accordant color.

division is impossible for frequencies where $G(f)$ or r_{41} approach zero, and therefore the reconstruction of the field will become incorrect for THz pulses with non-vanishing Fourier components at these frequencies. The required signal-to-noise ratio has not been reached for EO measurements of short electron bunches at accelerators, but the reconstruction of the THz pulse for frequencies above the lattice resonance has been done in pump-probe experiments with very thin (≈ 10 μm) crystals [LHS+99].

4.3.3. Dependence of the EO signal on the crystal thickness

Ideally, the phase retardation $\Gamma(\tau)$ should be directly proportional to the thickness d of the EO crystal. In reality this is true for slowly varying fields or very thin crystals. For short pulses the strong dispersion of the EO crystal for frequencies close to the lattice resonances and the phase mismatch between laser pulse and the THz components of the electric field pulse lead to a slower than linear rise of the phase retardation with d and eventually to a saturation (Fig. 4.18). For ZnTe the saturation is reached at a crystal thickness of about 4 mm, for GaP already at 150 µm to 300 µm as a function of the electron bunch length σ_t.

Due to the dispersion the length of the phase retardation signal grows considerably towards larger thickness. To preserve a good time resolution the GaP crystal thickness should therefore not exceed $d = 100$ µm by a large amount. However, going to $d = 50$ µm or less does not really improve the resolution but only leads to much smaller signals.

4.4. Simulation of temporally and spectrally resolved EO detection with chirped laser pulses

The code used to simulate the temporally and spectrally resolved EO detection with chirped laser pulses consists of three main parts. The first part calculates the field of the (horizontally polarized) chirped laser pulse $\boldsymbol{E}_{\mathrm{c,laser}}$. The second part calculates the radial electric field $E_{\mathrm{THz}}(Q(t), r_0, \gamma)$ of a electron bunch of an arbitrary longitudinal electron distribution $Q(t)$ at distance r_0 to the bunch path and the resulting phase retardation $\Gamma(t)$ for a given EO crystal. The third part than calculates the electric field $\boldsymbol{E}_{\mathrm{out,laser}}$ of the laser pulse after the EO crystal and a quarter- and a half-wave plate. The rotation angles ϕ of the quarter-wave plate and θ of the half-wave plate can be set to arbitrary values. From the vertically polarized component of this field the temporal and spectral intensity is calculated. For the reason of simplicity the orientation of the THz field to the EO crystal is assumed to be $\alpha = 0$. Note that the simulations presented here do not include any resolution limits, noise of the detectors, or residual birefringence of the EO crystal.

The code uses equation (2.17) and (2.13) to calculate the field of a Fourier limited Gaussian laser pulse with a duration of $T_p = 15$ fs. This pulse is then propagated through a dispersive medium (cf. 2.2.3). Unless otherwise explicitly stated,the dispersive medium consists of 100 mm of strongly dispersive glass type SF11 and 15 mm of glass type BK7 accounting for the vacuum windows and the lenses used in the transfer line (cf. 5.2.3). This results in a chirped laser pulse of a duration of $T_c = 3.63$ ps

(FWHM of the intensity). To find the proper time scale for the spectrally resolved detection, the instantaneous frequency $\omega_i(t)$ is determined by fitting sinusoidal functions locally to $E_{\mathrm{c,laser}}$. To the resulting values of $\omega_i(t)$ a second order polynomial is fitted, thereby also nonlinear dispersion is accounted for.

Equations (2.5) and (2.8) are used to calculate the radial electric field $E_{\mathrm{THz}}(Q(t), r_0, \gamma)$ of a electron bunch of an arbitrary longitudinal electron distribution Q and electron energy at distance r_0 to the bunch path. The resulting phase retardation $\Gamma(t)$ for a given EO crystal is then calculated using equations (4.16) and (4.34) with the parameters given in section 4.1. In equation (4.34) the variable delay τ between laser and THz pulse is replaced by the absolute time t.

The vertically polarized component of $\boldsymbol{E}_{\mathrm{out,laser}}(t)$ can now be calculated using equation (3.20) with $E_{\mathrm{c,laser}}(t)$ and $\Gamma(t)$. $E_{\mathrm{out,laser}}(\omega)$ is the Fourier transform of $E_{\mathrm{out,laser}}(t)$ according to equation (2.11). The resulting temporal intensity $I(t)$ and spectral intensity $S(\omega)$ is calculated using equations (2.15) and (2.16).

The retrieved phase retardation $\Gamma_{\mathrm{retrieved}}$ can now be calculated using the inversion of equation (3.20) restricted to $2\phi - 4\theta \leq \Gamma \leq \pi + 2\phi - 4\theta$ and compared to expected phase retardation from an ideal EO crystal with a frequency independent effective response function where $\Gamma \propto E_{\mathrm{THz}}$.

4.4.1. Quality of bunch shape determination by temporally and spectrally resolved detection

In this section various longitudinal profiles for the electron bunches are assumed (Gaussian, Gaussian with exponential tail, a theoretically predicted longitudinal bunch profile in FLASH and a profile measured with the transverse deflecting structure). It is studied how well the electric field profile of the charge distributions can be recovered by temporally and spectrally resolved EO detection.

For the calculations with Gaussian bunch shapes the same parameters as in section 4.3 are used ($r_0 = 1$ mm, $\gamma = 1000$, $Q_0 = 10$ pC). For the calculations with other bunch shapes a bunch charge of $Q_0 = 0.5$ nC, an electron energy of ≈ 450 MeV ($\gamma = 900$) and a distance between the electron beam and the laser spot on the EO crystal of $r_0 = 5$ mm is chosen, which are typical parameters for EO measurements at FLASH.

4.4.2. Gaussian bunch shape

Figures 4.19 and 4.20 show the predicted phase retardation for temporally and spectrally resolved detection for a 150 fs and a 50 fs long bunch using a 300 μm thick ZnTe

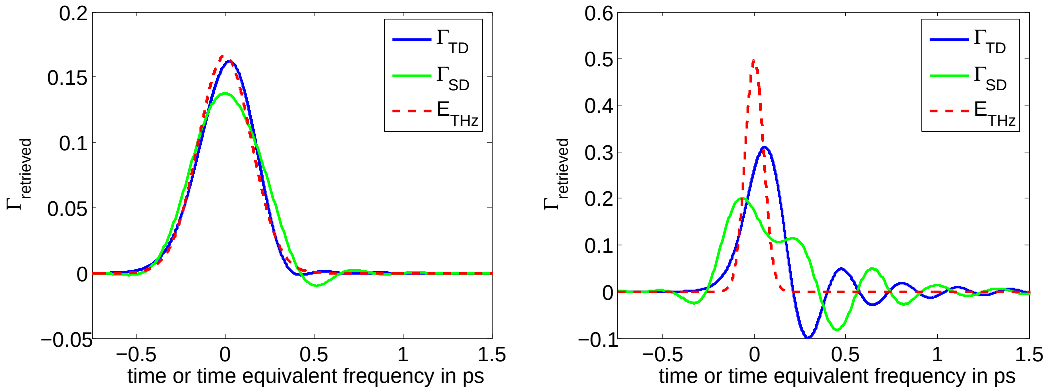

(a)

(b)

Figure 4.19.: Expected phase retardation signal $\Gamma_{\text{retrieved}}$ for temporally and spectrally resolved detection with a 300 µm thick ZnTe crystal for a long THz pulse E_{THz} (σ_t = 150 fs, a) and a short THz pulse (σ_t = 50 fs, b).

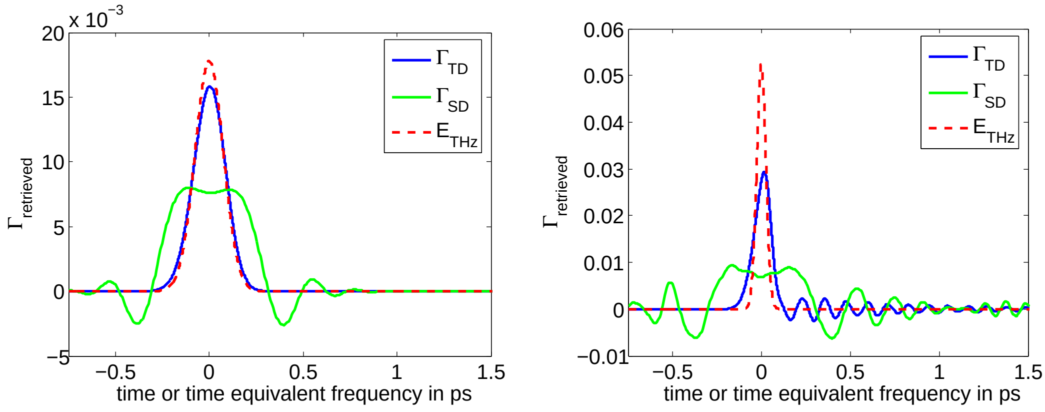

(a)

(b)

Figure 4.20.: Expected phase retardation signal $\Gamma_{\text{retrieved}}$ for temporally and spectrally resolved detection with a 100 µm thick GaP crystal for a long THz pulse E_{THz} (σ_t = 75 fs, a) and a short THz pulse (σ_t = 25 fs, b).

crystal and for a 75 fs and a 25 fs long bunch using a 100 µm thick GaP crystal, respectively. The phase retardation signal expected for temporally resolved detection is identically to the phase retardation expected for the EO sampling technique (Figs. 4.14 and 4.15) except a negligible broadening in the case of the EO sampling due to the length of the laser pulse. The simulated data for the spectrally decoded data show strong additional shape distortions and pulse broadening due to frequency mixing between the frequency components of the laser pulse $E_{\text{c,laser}}(\omega)$ and the frequency components of effective THz pulse (see section 3.2.2).

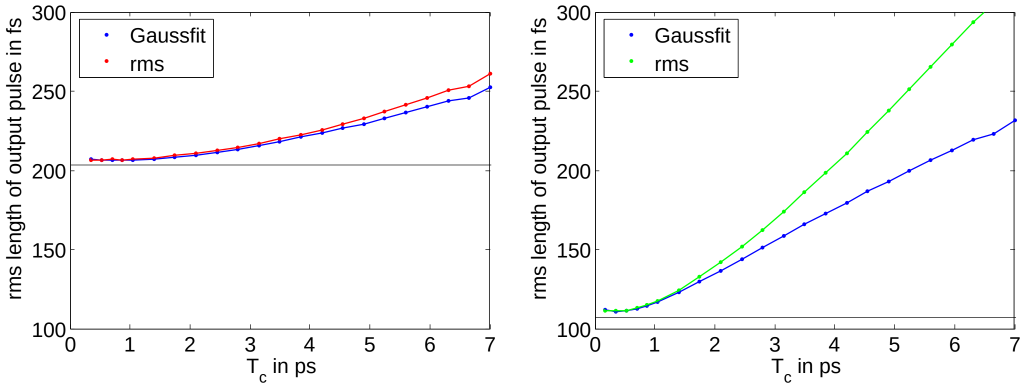

(a)

(b)

Figure 4.21.: Pulse broadening at spectrally resolved EO detection due to frequency mixing: predicted width of the output pulse as function of T_c for a 200 fs long (a) and a 100 fs long (b) THz pulse for a 100 µm tick GaP crystal (T_0 = 15 fs). The black line shows the pulse length σ_1 predicted for temporally resolved detection for comparison.

The shortest THz pulse, which is reproduced with moderate shape distortions and pulse broadening due to frequency mixing depends on the chirp of the laser pulse. For the used chirped laser pulse with $T_c = 3.6$ ps the shortest THz pulse, which correctly reproduced is about $\sigma_{t,\mathrm{lim}} = 250$ fs. The following equation published by Jamison et al. [JBM+06] is supported by this simulations:

$$\begin{aligned} T_{\mathrm{lim}} &= 2\sqrt{2\ln 2}\sigma_{\mathrm{lim}} \approx 2.6\sqrt{T_0 T_c} \\ \Rightarrow \sigma_{t,\mathrm{lim}} &\approx 1.1\sqrt{T_0 T_c} \end{aligned} \tag{4.37}$$

A comparison of the pulse length σ_1 and σ_2 predicted for different input pulse length σ_t as a function of T_c is shown in figure 4.21. A 200 fs long bunch is reproduced with a small pulse broadening ($\lessapprox$ 10%) using a laser pulse with $T_0 = 15$ fs chirped to 4 ps, while T_c needs to be smaller than 1 ps to reproduce a 100 fs bunch.

4.4.3. Other bunch shapes

Theoretical studies of the present bunch compression scheme at the FLASH linac predict a longitudinal bunch shape consisting of a Gaussian with an exponential tail [Li01, GSSY04]. Figure 4.22 shows the expected phase retardation from a 300 µm thick ZnTe and a 100 µm thick GaP crystal for a bunch shape with the following

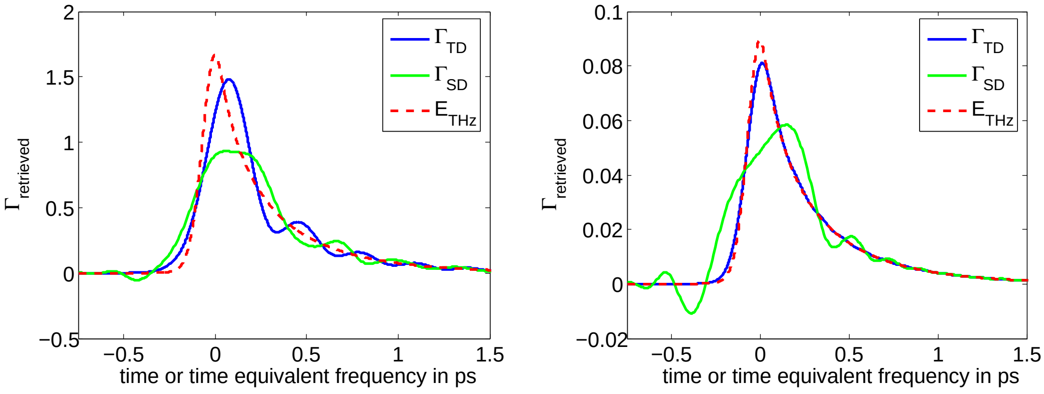

(a) (b)

Figure 4.22.: Expected phase retardation signal $\Gamma_{\text{retrieved}}$ for temporally and spectrally resolved detection of a Gaussian bunch with exponential tail according to equation (4.38) with a 300 µm thick ZnTe crystal (a) and a 100 µm thick GaP crystal (b).

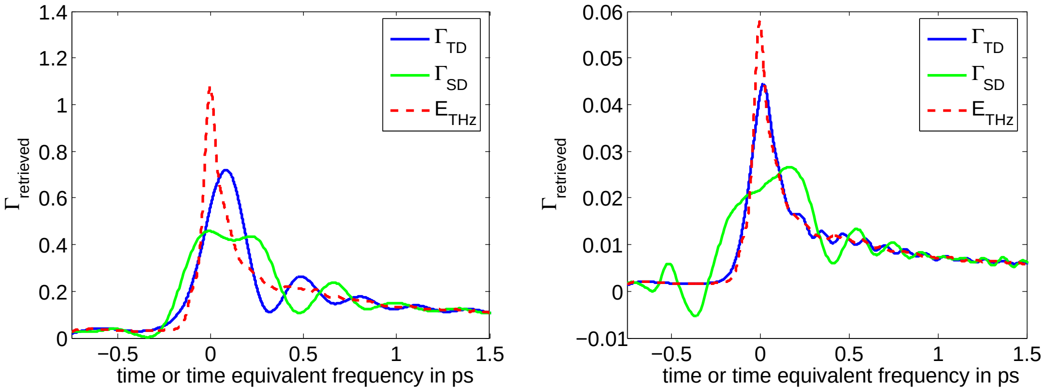

(a) (b)

Figure 4.23.: Expected phase retardation signal $\Gamma_{\text{retrieved}}$ for temporally and spectrally resolved detection of a simulated charge distribution of a bunch at FLASH [Doh06a] with a 300 µm thick ZnTe crystal (a) and a 100 µm thick GaP crystal (b).

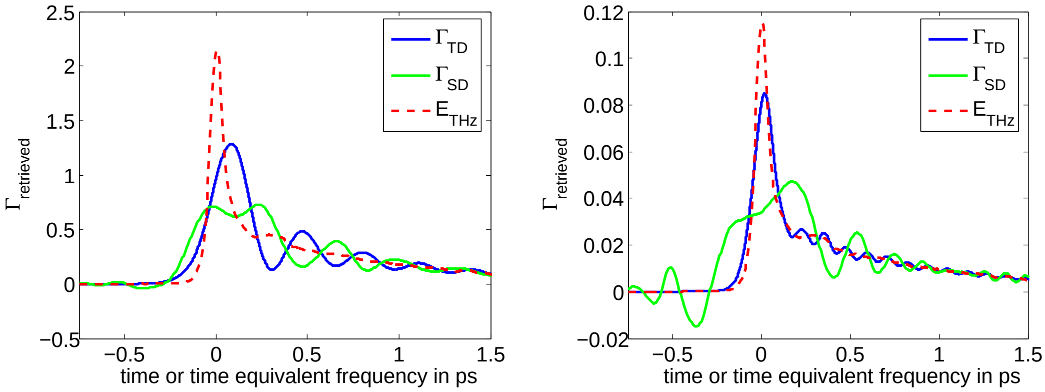

(a) (b)

Figure 4.24.: Expected phase retardation signal $\Gamma_{\mathrm{retrieved}}$ for temporally and spectrally resolved detection using a 300 µm thick ZnTe crystal (a) and a 100 µm thick GaP crystal (b) of a charge distribution of a bunch measured at FLASH with the transverse deflecting structure [Röh06].

electron distribution:

$$Q(t) = \begin{cases} \exp(-\frac{t^2}{2\sigma_t^2}) & \text{for } t < t_1 \\ \frac{A\exp(-t/\tau_1)}{\sqrt{(t+t_0)/\tau_1}} & \text{for } t > t_1 \end{cases} \tag{4.38}$$

where the following parameters are used:

$$A = 0.47,\ \sigma_t = 66.7\ \mathrm{fs},\ t_1 = 8.9\ \mathrm{fs},\ \tau_1 = 500\ \mathrm{fs},\ t_0 = 100\ \mathrm{fs} \tag{4.39}$$

A second study uses the programs ASTRA [Flö04] and elegant [Bor00] for the generation and transport of the electron distribution through the linac [DFK$^+$04, Doh06b]. The resulting longitudinal electron distribution and THz pulse of a 450 MeV bunch at FLASH after the last accelerating module is shown in figure 2.1, the expected phase retardation in figure 4.23 [Doh06a].

The THz pulse shown in figure 4.24 is calculated for a bunch distribution measured with the transverse deflecting structure (TDS, see section 5.3.1).

The predicted phase retardation signal for temporally resolved detection using a 100 µm thick GaP crystal reproduces well the THz pulse for all three charge distributions. Only a moderate broadening of the leading peak can be observed and some small oscillations following the peak in cases of the later two charge distributions. For spectrally resolved detection using a 15 fs laser pulse chirped to $T_c = 3.6$ ps, frequency mixing of the frequency components of the laser pulse $E_{\mathrm{c,laser}}(\omega)$ and the frequency components of effective THz pulse leads to a strong broadening and distortion of the leading peak. It is not possible to determine a pulse length from this data, but a position (arrival time) of the peak can still be determined. Only for laser pulses with $T_c \lesssim 500$ fs the SD signal can reproduce the THz pulse without strong distortions.

For temporally resolved detection using a 300 µm thick ZnTe crystal the predicted phase retardation signal shows a large broadening and additional distortions for all three charge distributions. Frequency mixing leads to additional distortions for spectrally resolved detection. However, they are less severe as in the case of temporally resolved detection because the length of the effective THz pulse is longer in the ZnTe crystal than in GaP.

4.5. Additional sources of signal broadening

Apart from the resolution limitations due to the material properties of the electro-optical material (cf. 4.2.2) and the intrinsic limits of the detection technique (cf. 4.4), other sources of signal broadening described in this section have to be taken into account.

While the THz pulse travels perpendicular to the surface through the crystal, the laser beam is inclined by 6° (cf. 5.2.4 and Fig. 5.11). The right part of the laser (seen in the direction of the laser beam) arrives earlier at the crystal surface than the left part. Therefore the phase retardation resulting from the interaction of the THz pulse laser field in the crystal is not distributed perpendicular to the direction of travel of the laser but tilted by 6°. When the laser is focused again, this tilt leads to a broadening of the signal by $\sigma_{\mathrm{angle}} = \tan(6^\circ)\,\sigma_{\mathrm{x,laser}}/c \approx 350\ \mathrm{fs/mm}/\sigma_{\mathrm{x,laser}}$, where $\sigma_{\mathrm{x,laser}}$ is the transverse variance of the laser beam in the direction of the tilt. The effect can be included in the simulations by a convolution of the calculated phase retardation (in time domain) with a Gaussian of variance σ_{angle}. The resulting *effective* phase retardation parameter Γ_{eff} is then used in equation (3.20) instead of Γ (Fig. 4.25(a)).

A second effect, which leads to a broadening of the signal in temporally resolved detection is the dispersion of the laser pulse in dispersive material the laser passes after the EO crystal. For the EO setup at FLASH this is the vacuum window where the laser leaves the beam pipe, two wave plates, thin film polarizers and the cylindrical lens which focuses the laser to the BBO crystal (cf. 5.2.4). This effect can be calculated as described in section 2.2.3 (Fig. 4.25(b)).

Finally the detector resolution has to be taken into account. For temporally resolved detection the resolution of the cross-correlator is determined by the length of the gate laser pulse, the phase matching properties and the thickness of the BBO crystal and the optical resolution of the imaging system and the camera. The total resolution of the cross-correlator is $\sigma_{\mathrm{det}} \approx 35$ fs. For spectrally resolved detection the resolution of the spectrometer with the used camera is $\sigma_\lambda = 0.3$ nm (cf. 5.2.4). For the used

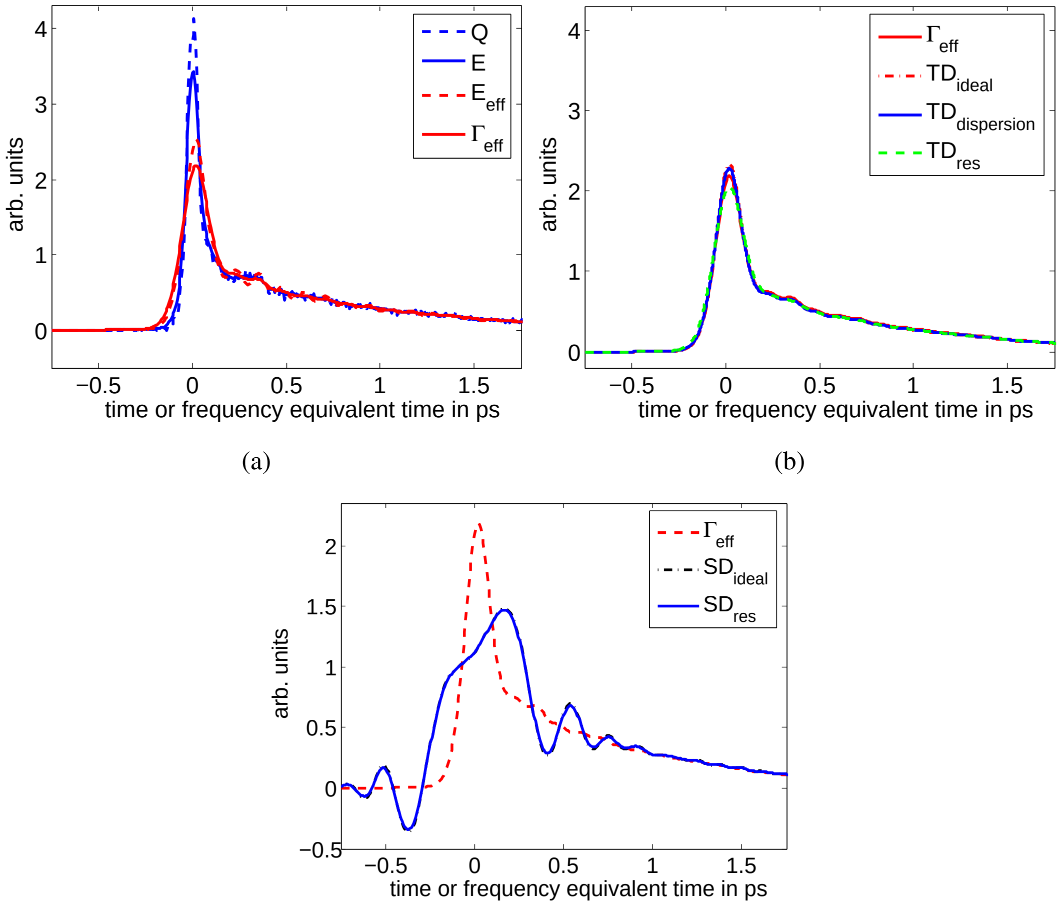

(a)

(b)

(c)

Figure 4.25.: Charge distribution of an electron bunch, the field and the phase retardation signal for temporally and spectrally resolved detection using a 100 µm thick GaP crystal as expected for a measurement near zero optical transition ($\phi = 0$, $\theta = 4°$). As the input for the simulation a charge distribution measured with the transverse deflecting structure [Röh06] was used.

(a): The measured charge distribution, the resulting field in 5 mm distance, the phase retardation parameter due to the GaP material properties and the effective phase retardation Γ_{eff} broadened due to the inclination angle of 6°.

(b): The background subtracted and normalized temporally resolved detection signal (TD) as expected directly after the EO crystal, at the position of the BBO crystal broadened due to dispersive optical elements and including the resolution of the cross-correlator.

(c): Γ_{eff} and the background subtracted and normalized spectrally resolved detection (SD) signal with and without taking a limited spectrometer resolution into account. The effective phase retardation is shown for comparison.

laser beam chirped to $T_c = 3.6$ ps this is equivalent to $\sigma_{\text{det}} \approx 30$ fs. The effect of the detector resolution can be calculated by convolving the temporal or spectral intensity at the detector with a Gaussian of variance σ_{det} (Fig. 4.25(c)).

4.6. Multiple reflections in the EO crystal

The THz pulse can undergo a reflection at the exit surface of the crystal, move back, and after a second reflection at the front surface, move again through the crystal in forward direction. This is sometimes referred to as the Fabry-Perot effect. The double-reflected pulse will be scanned by the laser if the laser pulse is delayed by the travel time $2d/v_{\text{THz}}$. The Fourier transform of the double-reflected THz pulse, just behind the front surface of the EO crystal, is given by

$$F_{\text{double}}(f) = F_{\text{trans}}(f) A_{\text{ref}}^2 \exp\left(i\frac{2\pi f}{c} n(f)\,(2d) - \frac{2\pi f}{c}\kappa(f)\,(2d)\right) \tag{4.40}$$

where $A_{\text{ref}} = [1 - n(f) - i\kappa(f)]/[1 + n(f) + i\kappa(f)]$ is the amplitude reflection coefficient. These Fourier components are propagated through the crystal in the same manner as was applied for the direct THz pulse (cf. 4.1). The phase retardation signal in Fig. 4.26 shows the direct signal, and after the delay of $2d/v_{\text{THz}}$, the signal from the double-reflected THz pulse. This second signal has an amplitude of about 25% of the first peak, mainly due to the reflection coefficient, which enters quadratically. The next reflection will produce a pulse at twice the delay but with a signal amplitude of only a few per cent of the main peak. This and even higher-order reflections will be lost in the noise, so it is not necessary to sum up the Fabry-Perot effect in a geometric series.

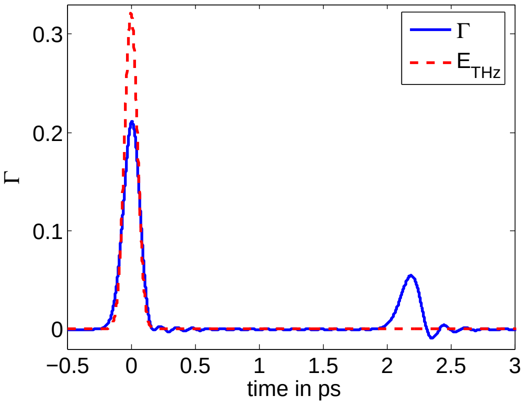

Figure 4.26.: The balanced detector signal of a Gaussian THz pulse with $\sigma_t = 50$ fs, $Q_0 = 0.1$ nC in a 100 µm thick GaP crystal. Both the direct and the double-reflected pulse are shown.

Also the laser pulse will undergo multiple reflections in the EO crystal. A coincidence of the double-reflected laser pulse with the direct THz pulse leads to a signal appearing artificially earlier than the THz pulse in EO sampling and spectrally resolved detection. In temporally resolved detection the double-reflected laser pulse contributes to the signal from the unreflected laser pulse with some attenuation due to the double reflection. If the double-reflected laser pulse coincides with the double-reflected THz pulse a contribution to the detector signal is found at the position of the first main peak. This contribution is small since not only the THz pulse but also the laser pulse is attenuated by the double reflection broadened due to the dispersion in the crystal. The effects can be avoided altogether if a wedge-shaped EO crystal is used. The EO crystal then acts like a prism and deflects the direct laser beam by an angle of $(n-1)\alpha$, where α is the wedge angle and n the refractive index for laser light. The double-reflected laser beam will leave the EO crystal at a deflection angle of $(3n-1)\alpha$ and can therefore be easily separated from the direct laser beam. However, that the wedge angle does not eliminate the multiple reflections of the THz pulse. The reason is that the electric field carried by the electron bunch is not well collimated like the Ti:Sa laser beam, but extends over the whole EO crystal.

5. Experimental setup

5.1. The FLASH accelerator and free electron laser

The free electron laser in Hamburg (FLASH) has recently been upgraded to a maximum electron energy of 770 MeV allowing to cover the wavelength range from 13 to 45 nm [TES02]. The free electron laser (FEL) is based on the principle of self amplified spontaneous emission (SASE), which opens the way to powerful FELs in the x-ray regime. Electron bunches of extremely high local charge density are needed to achieve laser saturation in the undulator magnet.

The FLASH linear accelerator and free electron laser consists of three main parts: the RF-photoinjector, the superconducting linac including the bunch compressors, and the undulators.

This section describes the different components of FLASH with a special emphasis

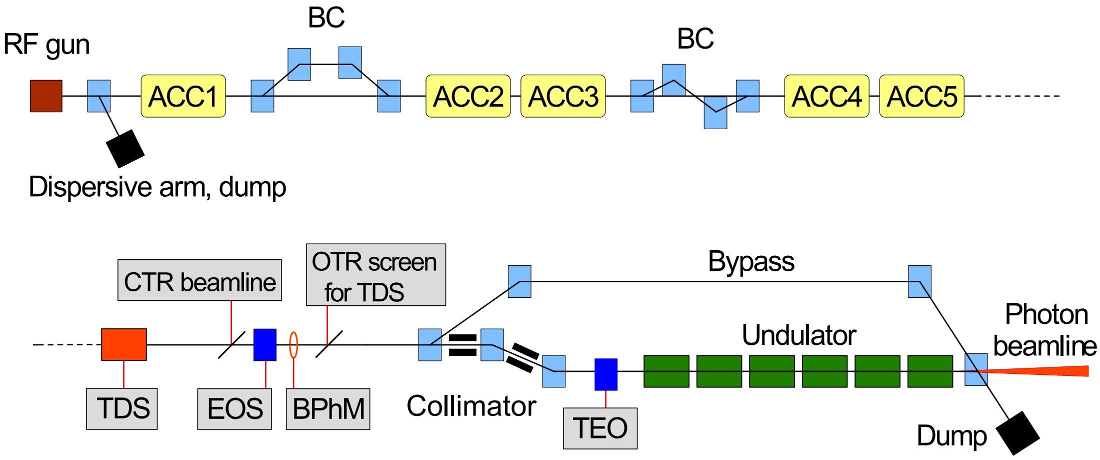

Figure 5.1.: Schematic layout of FLASH at DESY. The beam is accelerated to a maximum energy of 770 MeV in five acceleration modules ACC1 to ACC5 containing eight superconducting cavities each. The two bunch compression stages are denoted by BC. The accelerator is followed by a diagnostic section and the undulator to create the FEL radiation. Abbreviations for the experiments in the diagnostic section are explained in the text.

on the effects influencing the longitudinal electron bunch profile, followed by a brief overview of the user facility for experiments with the FEL radiation. A schematic overview of FLASH is shown in Fig. 5.1.

5.1.1. The photoinjector gun

A laser driven radio frequency (RF) photo-cathode gun is used to produce the high current electron bunches with small transverse emittance and a small energy spread as they are needed for the operation of a SASE-FEL [SCG+02, FP02].

A high power Nd:YLF laser generates a series of pulses at a wavelength of 1047 nm. The pulses are twice frequency doubled in two nonlinear crystals to reach a wavelength of 262 nm with a pulse energy of up to 50 μJ and a pulse duration of 4 ps (rms). This beam is focused on a cesium telluride (Cs_2Te) cathode, where the pulses liberate electrons due to photo emission. The cathode is placed inside a $1\frac{1}{2}$-cell normal conducting copper RF structure operated at 1.3 GHz with a maximal accelerating gradient of up to 42 MV/m on the cathode. The high gradient is needed to rapidly accelerate the electrons to relativistic energies to reduce the emittance dilution due to internal Coulomb forces. One solenoid coil is placed around the RF cavity to produce a longitudinal magnetic field of 0.163 T along the axis of the cavity. A small bucking coil at the back of the cathode is used to cancel the field at the cathode surface. This field forces the accelerated electrons to spiraling trajectories to further reduce the effects of the internal Coulomb forces. This way it is possible to achieve a bunch charge of 0.5 to 1 nC with a normalized transverse emittance of only a few micrometers.

The electron bunches leave the gun with an energy of about 4.5 MeV per electron and an rms bunch length of about 4 ps and are injected into the first accelerating module.

5.1.2. The accelerator modules

The electrons are accelerated by alternating electric fields stored in resonant RF cavities. The cavities used at the FLASH accelerator are superconducting nine cell cavities developed for the TESLA[1] collider project [RSTW01]. The cavities are made from pure niobium and are operated at 2 K cooled with liquid helium (Fig. 5.2).

The nine-cell cavities (Fig. 5.2) are excited at 1.3 GHz at their π-mode, where the electric field along the cavity axis is parallel to the axis and its amplitude varies sinusoidal with the resonant frequency f. Since the resonant frequency f depends mainly on the diameter of the cavity, the length of the resonating cells $L = \frac{1}{2}\frac{c}{f}$ can be chosen such that a relativistic particle with speed $v \approx c$ needs half a period of the resonating

---

[1] teraelectronvolt energy superconducting linear accelerator

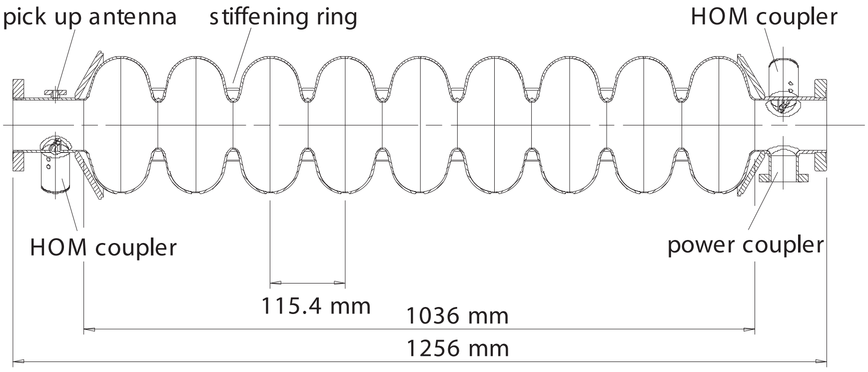

Figure 5.2.: Cross section of a superconducting RF cavity installed in the FLASH linac [Aun00]. The power coupler is connected by a wave guide to the klystron. Higher-order mode (HOM) couplers remove resonant fields of higher order, a pick-up antenna is used to measure the field.

frequency to pass the cell. An electron entering the cell at the zero crossing of the electric field is accelerated along the full length of the cell and leaves the cell when the electric field strength changes its sign. In multi-cell cavities excited at their π-mode neighboring cells have a phase offset of π so that an electron entering the first cell at the zero crossing of the electric field is accelerated along the full length of the cavity. This phase setting, where the electron has the maximum possible energy gain, is usually referred to as *on crest acceleration*, for all other phases the electron gains less energy (*off crest acceleration*) or even loses energy (*deceleration*).

The FLASH linac consists of five accelerating modules containing eight cavities each. The applied accelerating gradients vary between 12 and 25 MV/m. The electrons can be accelerated to energies of 380 to 770 MeV. The installation of a sixth module is planned to increase the maximum energy. The photoinjector and the modules are powered by three 5 MW klystrons and one 10 MW klystron. The first 5 MW klystron drives the gun, the second module ACC1, the third one drives modules ACC2 and ACC3 and the 10 MW klystron drives the modules ACC4 and ACC5. The amplitude and phase of the accelerating fields in the cavities are controlled by adjusting amplitude and phase of the individual klystrons. Each nine-cell cavity in the modules is equipped with a pick-up antenna to measure its field. The calculated vector sum is used to regulate phase and amplitude of module ACC1 and the module groups ACC2-3 and ACC4-5. The phase and amplitude of the field in the normal conducting gun is calculated from the measured input from the klystron and reflected electric field from the gun.

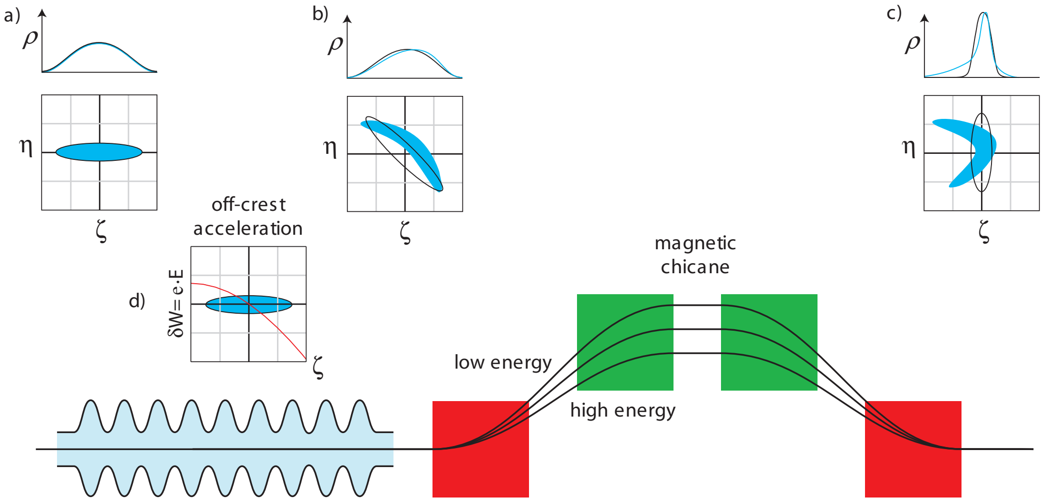

Figure 5.3.: Schematic drawing of a bunch compressor. The off-crest acceleration introduces a correlated energy spread. The phase space is sheared by the magnetic chicane. Symbols: δW: energy gain of a particle, η: particle energy relative to reference particle, ζ: relative longitudinal position inside the bunch, ρ: longitudinal charge density, E: electric field.
a) The particle distribution as a function of ζ and as a function of W and ζ before the acceleration. b) The particle distribution after off-crest acceleration. c) The particle distribution behind the magnetic chicane. The peak current is increased. The black ellipse shows linear compression, the blue shape the effects of non-linear compression. d) The energy gain in the accelerating cavity as a function of relative longitudinal position.
Adapted from [Isc03].

5.1.3. Bunch compression

The SASE-FEL process requires electron bunches with high peak currents of several kA. This currents cannot be directly produced in the injector gun, because the resulting high repulsive space change forces would lead to an unwanted emittance growth. To reach these high peak currents the 4 ps long electron bunches from the injector gun with peak currents of about 100 A are longitudinally compressed after further acceleration at energies of 125 MeV and 380 MeV. At this highly relativistic energies the magnetic forces compensate the electric forces of the space charge. For the compression magnetic chicanes are used where electrons with different energies have different path lengths through the chicane so that an electron bunch with an energy distribution correlated with the longitudinal position can be compressed in length.

Shifting the phase of the first accelerating module away from the on-crest phase leads to a stronger acceleration of the electrons in the tail of the bunch than the electrons in the head: an energy chirp is imposed on the bunch. In the following magnetic chicane the higher energetic electrons in the tail of the bunch are less bended by the dipole magnets and travel on a shorter trajectory through the chicane, allowing them to catch up with the leading electrons (Fig. 5.3).

Since the bunch length covers a non-negligible part of the RF wavelength – 4 ps corresponds to about 2° of an 1.3 GHz oscillation – and the accelerating field has a sinusoidal time dependency, the energy chirp is not linear. This leads to a nonlinear compression and results in a longitudinal charge distribution, which is not Gaussian any more but has a short leading spike followed by a longer tail. To reduce these nonlinearities and also other distorting effect like coherent synchrotron radiation, the compression can be distributed among several bunch compressors at different energies.

At FLASH the energy chirp is imposed on the bunch by an acceleration at about 8° off crest in the first accelerating module. The bunch with an energy of 125 MeV is then partially compressed in a C-type magnetic chicane and further accelerated to 380 MeV by two modules operated on crest. The second bunch compressor is a S-type magnetic chicane further compressing the bunch to its final shape with a leading spike of about 100 fs length with a peak current of several kA and a low current tail of several ps (Fig. 5.4).

A comprehensive description of the FLASH bunch compression system and simulations of the resulting charge distributions can be found in [LPS02, FP02, Doh06b]

5.1.4. The diagnostic and collimation section

The last acceleration module is followed by a section holding several experiments for bunch diagnostics to measure the longitudinal charge distribution, coherent transition radiation (CTR), slice emittance and the bunch arrival time. This experiments include the transverse deflecting structure (TDS), the CTR beam line, the electro-optical beam phase monitor, and the timing electro-optical experiment (TEO), which are described in section 5.3.

A small dispersive section with collimators is inserted to protect the following undulator magnets from radiation damage. Copper apertures in front of the dispersive section remove most of the beam halo, while apertures in the dispersive section remove electrons from the dark current which have a different energy than the bunch. Otherwise these electrons would be lost in the narrow beam pipe of the undulator and increase the radiation load of the permanent magnets.

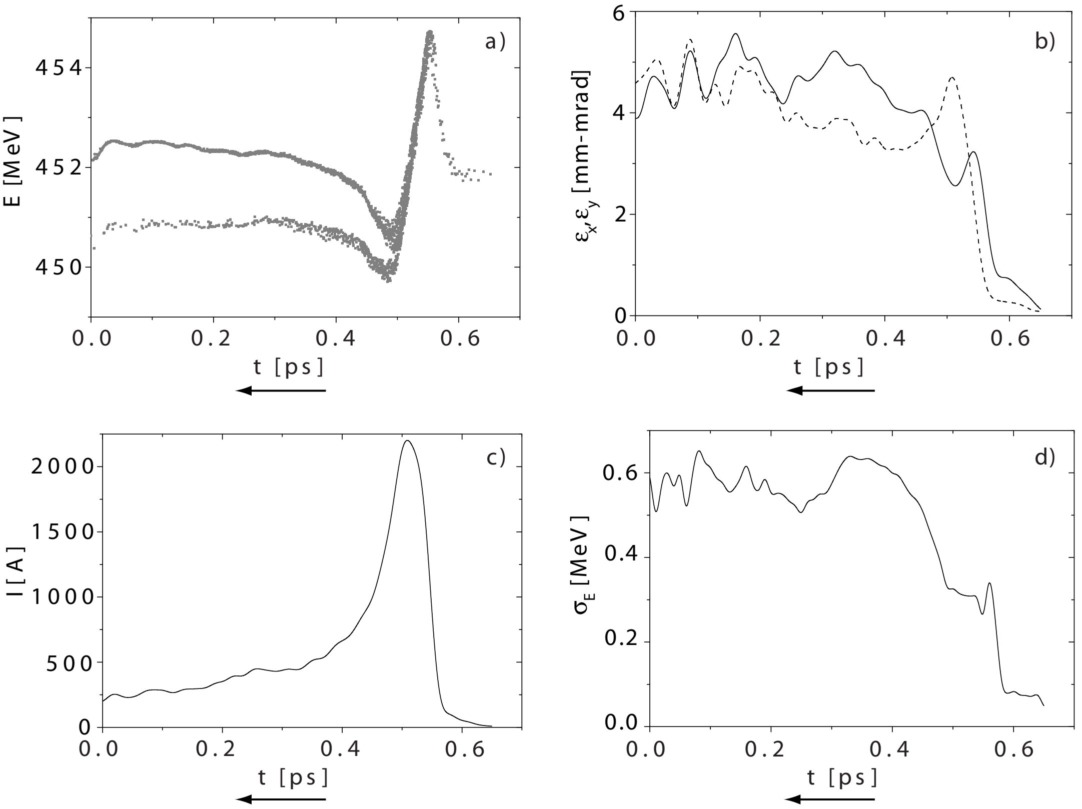

Figure 5.4.: Example for the expected phase space distribution, current, slice emittance and slice energy spread along the bunch at the undulator entrance. Bunch charge is 1 nC. Bunch head is at the right side. Note the reversed direction of time axis. From [SSY04]

5.1.5. The undulator section

The undulator system consists of six magnets each 4.5 m long. The undulator magnets create on the beam axis a sinusoidal field in vertical direction with a period of 27.3 mm and a peak induction of 0.46 T, leading to a horizontal oscillation of the electron beam (Fig. 5.5).

Between the segments quadrupole magnets are installed to focus the beam as well as diagnostic tools, such as beam position monitors (BPM) and wire scanners to measure position and transverse shape of the electron beam. Achieving a perfect overlap of the electron beam with the radiation field generated inside the undulator is mandatory for the FEL process. Therefore, the utmost care has been taken in aligning all the elements. An excellent field quality has been achieved in the undulator modules so that the expected rms deviations of the electrons from the ideal orbit should be less

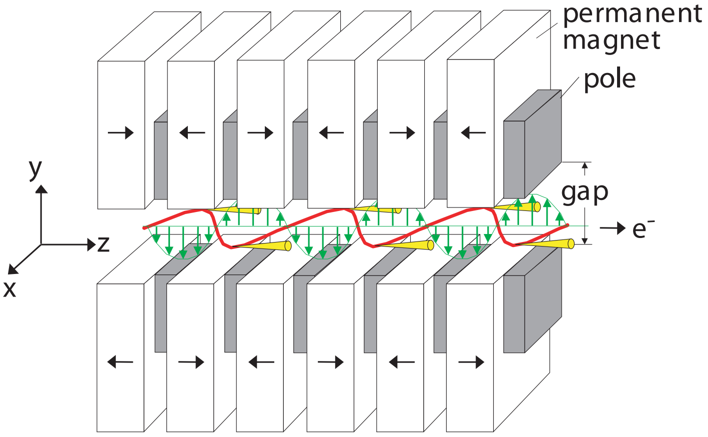

Figure 5.5.: Arrangement of the magnets in the undulator that creates a sinusoidal field on the beam axis [FP99]. The electron beam oscillation is not to scale.

than 10 μm [Ayv06].

Following the undulators a dipole magnet bends the electron beam to an underground beam dump while the FEL radiation continues through a section with photon diagnostic to the experimental hall with the user beam lines.

5.1.6. The FLASH experimental area

The FLASH experimental hall provides five beam lines for user experiments. Two beam lines are equipped with monochromators for measurements with different spectral components of the FEL beam. For pump-probe experiments pulses from an optical laser synchronized to the FEL radiation pulses can be distributed to the end station of all beam lines. Either 50 fs long pulses with 3 nJ pulse energy at 800 nm from a Ti:Sa oscillator or 120 fs long pulses with 20 µJ at 800 nm from an optical parametric amplifier are available.

The properties of the FEL pulses are listed in table 5.1.

5.1.7. Synchronization and timing

The various timing signals for FLASH are derived from a master oscillator frequency of $f = 9.027775$ MHz, which is the 144th sub-harmonic of the RF field of the accelerating cavities of 1.2999996 GHz. For special devices like the injector laser, the laser for the electro-optic experiment or the pump-probe laser in the FEL experimental hall, other harmonics of 9.03 MHz are generated by the master oscillator as well and distributed to the experiments, namely 108.33 MHz and 81.25 MHz.

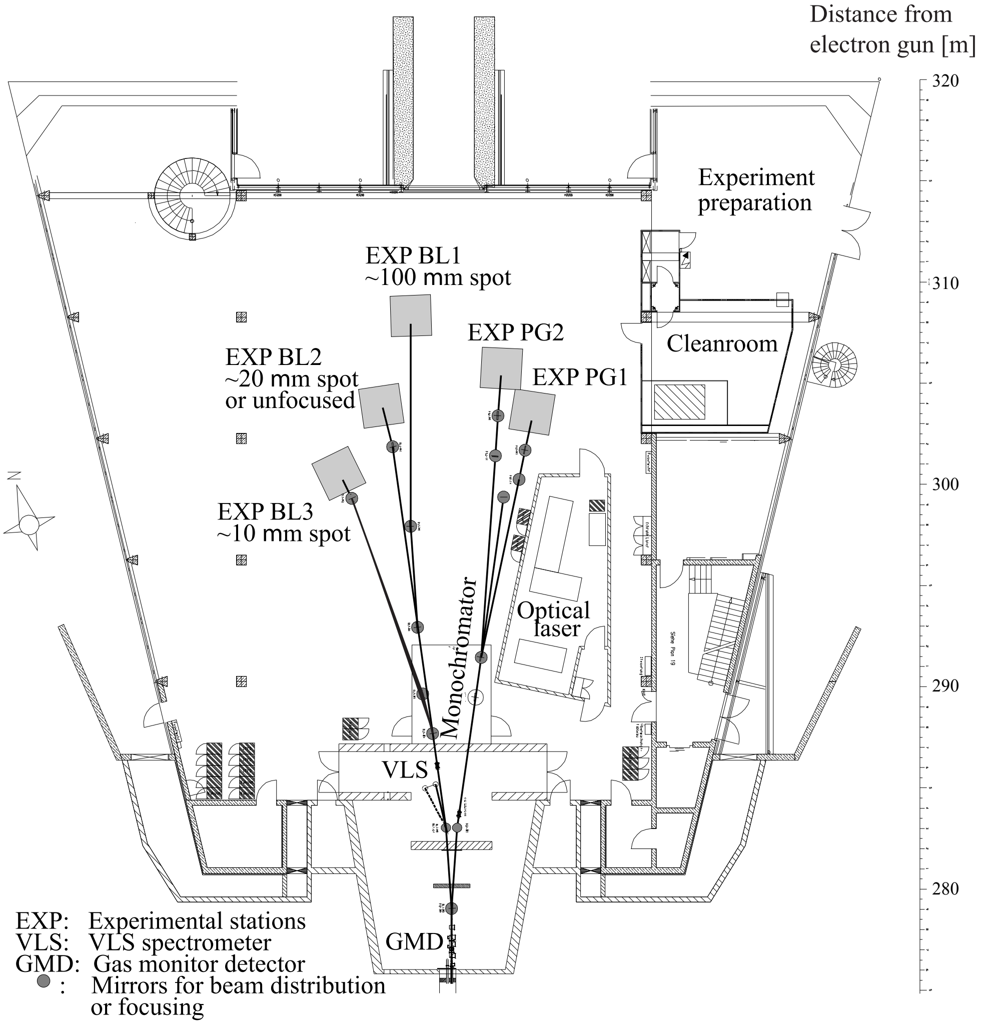

Figure 5.6.: The FLASH experiment hall. From [HAS06].

Due to the design of the accelerating modules, the cryogenic cooling system and the RF power generation, the accelerator is run in a pulsed mode with a usable accelerating period of 800 μs and a repetition frequency of 2, 5 or 10 Hz. During the accelerating period a train of up to 800 electron bunches with a spacing of 1 μs or multiples thereof can be accelerated. These bunch trains are also referred to as *macropulses*.

An overview of the bunch timing at FLASH is given in figure 5.7.

Table 5.1.: Properties of the FEL pulses

Parameter	Measured value
wavelength (1st harmonic)	13 … 47 nm
pulse length	10 … 50 fs
pulse energy	5 … 200 µJ
peak power	up to 5 GW
spectral width	0.5 … 1 % (FWHM)
intensity in 3rd harmonic	0.5 % of fundamental
peak brilliance	$10^{29} \ldots 10^{30} \frac{\text{photons}}{\text{s} \cdot \text{mm}^2 \cdot \text{mrad}^2 \cdot 0.1\% \Delta\lambda}$
angular divergence	300 µrad
beam diameter at experiments	0.01 … 5 mm
pulses per macropulse	1 … 800

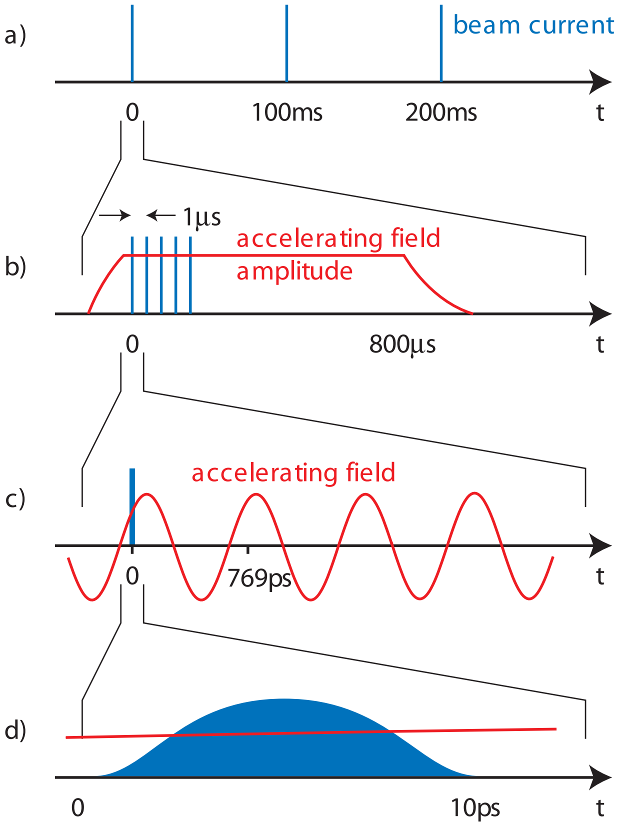

Figure 5.7.: Timing in the FLASH linac. a) The macropulses are separated by 100 to 500 ms. b) Detailed view of a macropulse: the envelope of the accelerating field has a flat top of up to 800 µs. The electron bunches are spaced by multiples of 1 µs. c) The accelerating RF field has a frequency of 1.3 GHz, corresponding to a period of 769 ps. d) An electron bunch with a length of 5 ps FWHM is shown. Drawings are not to scale. From [Isc03].

5.2. The setup of the electro-optic experiment

The electro-optic experiment at FLASH consists of a 18 m^2 laser laboratory outside the accelerator tunnel, a laser transfer line to the tunnel and an optical table inside the tunnel (Fig. 5.8). The laser laboratory is temperature stabilized to 20 ±1°C and holds the optical table with the laser systems (cf. 5.2.1) and laser diagnostic equipment, the synchronization electronics for the lasers (cf. 5.2.2) and the electronics and computers to control motorized optics, the synchronization electronics, data acquisition devices and accelerator settings. From the optical table in the laboratory the laser beam is sent trough a 17 m long, evacuated transfer line (cf. 5.2.3) into the accelerator tunnel. There a second optical table holds the vacuum chamber (cf. 5.2.4) with the electro-optic crystals (cf. 5.2.6) and the optics for the detection setup.

The following section gives a description of the parts of the experiment including information of the used components and materials.

5.2.1. Laser systems

The laser used for electro-optic sampling and spectrally encoded EO detection is a FemtoSource Compact20 titanium-sapphire (Ti:Sa) oscillator from Femtolasers, Vienna, Austria. It is pumped with 3.5 W cw laser beam at 532 nm from a diode pumped, frequency doubled Nd:YVO_4 laser (Verdi-V5 from Coherent Inc., Santa Clara, California). The oscillator delivers 15 fs (FWHM) long pulses of up to 4 nJ pulse energy at a repetition frequency of 81.25 Hz. The emitted bandwidth is up to 65 nm (FWHM) with a center wavelength of 803 nm.

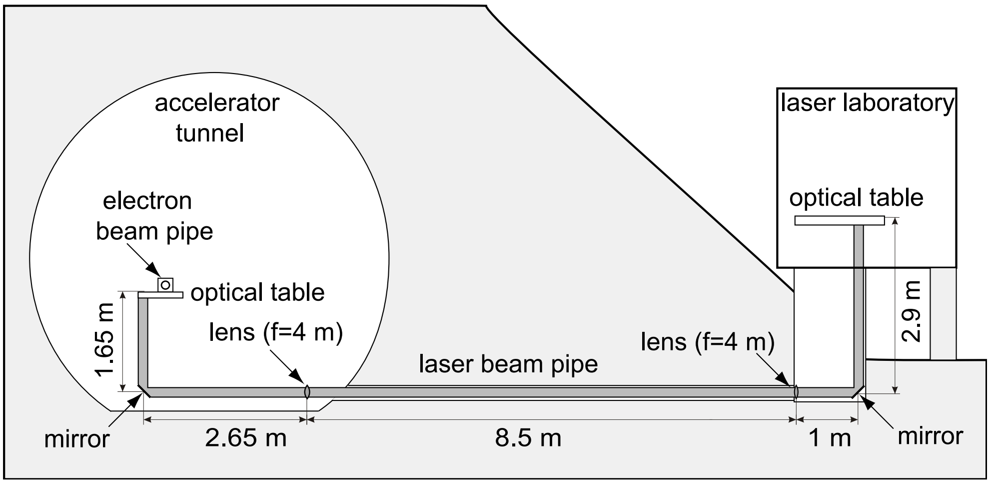

Figure 5.8.: Schematic cross section off the EO laser laboratory and the FLASH accelerator tunnel

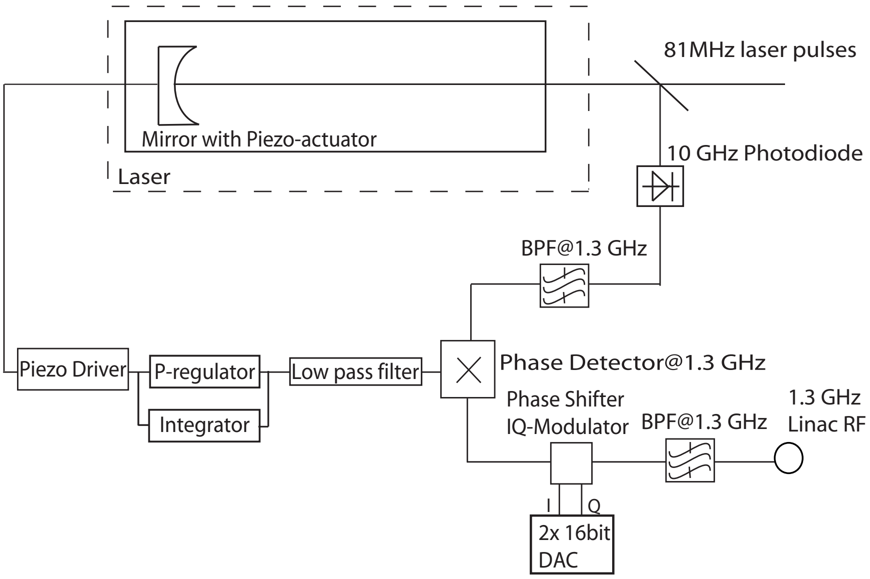

Figure 5.9.: Schematics of the setup used to synchronize the TiSa oscillator to the RF. The laser repetition frequency is 81 MHz. The 16$^{\text{th}}$ harmonic of the laser frequency is phase-locked to the 1.3 GHz radio frequency of the linac.

The second laser system, used especially for the temporally encoded EO detection, is a Ti:Sa seed oscillator (FemtoSource Pro HP, Femtolasers) and amplifier (Omega Pro, Femtolasers) borrowed from FOM Institute for Plasma Physics 'Rijnhuizen', Nieuwegein, The Netherlands. The amplifier delivers 30 fs (FWHM) long pulses of 1 mJ pulse energy at a repetition frequency of 1 kHz. The emitted bandwidth is 30 nm (FWHM) with a center wavelength of 795 nm.

5.2.2. The synchronization of the lasers to the linac RF

All EO detection techniques require a precise synchronization between the used laser and the accelerator RF. The accuracy of the synchronization sets an upper limit on the possible resolution of the EO sampling technique as well as the resolution of the electron bunch arrival time measurements with other EO techniques.

The repetition frequencies of both Ti:Sa oscillators are locked to the 1.3 GHz master frequency of the accelerator using a single-loop phase-locked-loop (PLL). A beam splitter directs a part of laser pulses to a 10 GHz photo diode (EOT-4000, EOT, USA). The 16th harmonic of the narrow photo diode signals is selected by a eighth-order bandpass filter (Integrated Microwave Inc., USA), amplified and fed to one port of a 1.3 GHz phase detector (HMC-439, Hittite, USA). The other port of the phase detector is connected to the 1.3 GHz signal from the master oscillator. The error signal of the

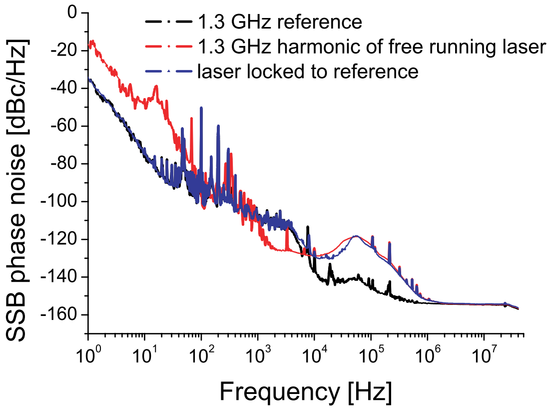

Figure 5.10.: Phase noise of the 1.3 GHz reference signal, the free running oscillator and the oscillator locked to the reference. From [WIK+05]

1.3 GHz phase detector is then fed back to the piezo-controlled end mirror of the laser resonator. The regulation of the laser repetition rate is done via a PI controller. The phase shift of the laser pulses with respect to the linac RF is accomplished by a vector modulator (HMC497LP4, Hittite, USA), shifting the phase of the linac RF before the phase detector in programmable steps. The synchronization scheme is shown in figure 5.9.

A frequency analysis of the phase detector error signal permits to determine the stability of the synchronization circuit. A phase noise measurement of phase detector error signal is shown in figure 5.10. From these data a residual time jitter of 65 fs (rms) in a bandwidth of 31 mHz up to the Nyquist frequency (40 MHz) is derived. The relative jitter between the electron bunches and the linac RF is not included. Alternatively the remaining time jitter can be measured by an RF monitoring system independently of the locking PLL. The phase noise measured with an independent RF monitoring system working at 10.4 GHz leads to the same time jitter. A more comprehensive description of the synchronization scheme and the measurements of its accuracy can be found in [WIK+05].

5.2.3. The transfer line

The laser laboratory is connected to the accelerator tunnel by a 16.7 m long evacuated laser beam pipe to transport the laser beam into the tunnel. The optics in the transfer line consists of two remotely controlled mirrors and two identical lenses with focal lengths of $f = 4$ m. An approximate $f - 2f - f$ imaging setup is realized to image the exit of the optical table in the laser laboratory to the entrance of the optical table in the accelerator tunnel in order to minimize the effect of vibrations and movement of

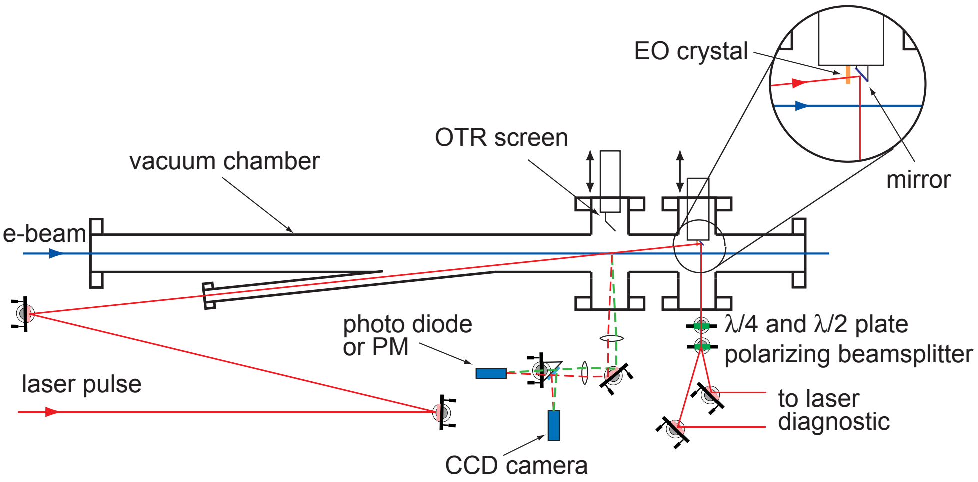

Figure 5.11.: Schematic drawing of the EOS setup in the accelerator tunnel. An OTR screen can be moved into the e-beam to adjust the relative timing between the laser pulses and the electron bunches with ≈ 200 ps precision.

the outer table on the beam stability at the EO setup in the tunnel. An exact $f-2f-f$ imaging setup is not possible due to the limited access to the 8.5 m long part of the beam pipe passing through the radiation shielding of the accelerator (Fig. 5.8).

The laser transfer line and the imaging system has proven to be very stable. Neither short-term nor long-term motions of the laser spot position on the electro-optic crystal are observed.

The two vacuum windows and the two lenses contained in the transfer line add up to 6 mm Kodial and 6 mm BK7 glass. This introduces additional dispersion to the laser pulse, which has to compensated with SF11 prism compressors for the EO sampling and the temporally resolved detection to reach the shortest possible laser pulse length at the EO or the BBO crystal, respectively. For the spectrally resolved detection the additionally introduced chirp does not need to be compensated but it has to be taken into account when calculating the pulse length of the chirped laser pulse at the EO crystal.

5.2.4. The optical setup in the accelerator tunnel

Inside the linac tunnel two level optical table is installed which holds on the lower level the vacuum chamber (Fig. 5.11) and on the upper level the detector optics (Fig. 5.12). The vacuum chamber includes the electron beam pipe with an inner diameter of 65 mm, an input port for the laser, two exit ports for laser and optical transition radiation (OTR), two ports to mount the movable holders for the EO crystals, and an

OTR screen and a viewport to survey the laser beam on the EO crystal (from above, not seen in figure 5.11). Two EO crystals can be mounted vertically separated at the holder. The laser beam can be steered to either of the crystals allowing measurements with two different crystals without opening the vacuum chamber. The length of the full chamber is 1.2 m.

The laser beam is injected into the beam pipe at an angle of 6° relative to the e-beam. Thereby, a mirror upstream of the crystal is avoided which would disturb the Coulomb field of the electron bunches. A spherical mirror ($f = 1.5$ m) is used to focus the laser on the EO crystal. Behind the crystal a mirror reflects the laser beam to the detector optics outside the vacuum chamber.

The OTR screen can be moved into the e-beam path to measure the relative timing between the laser pulses and the electron bunches. The screen reflects OTR pulse and the laser light to a photomultiplier (PM) or a fast photo diode. A simultaneous measurement of both pulses can be used to adjust the relative timing between the pulses with approx. 200 ps precision before starting an EO measurement.

The detection optics outside the vacuum chamber is shown in figure 5.12. For schematic drawings of the different EO detection techniques refer to figures 3.4 to 3.6 in section 3.2.1.

5.2.4.1. Electro-optic sampling using a scanning delay

For electro-optic sampling only a small part of the setup is used (Fig. 5.12(c)). The laser pulse coming from the transfer line is passed through a polarizer and is sent to the EO crystal in the vacuum chamber. After the vacuum chamber the pulses pass through a quarter- and a half-wave plate and are reflected to a Wollaston prism by a remotely controlled flip mirror. The two orthogonal polarized beams are coupled into multi-mode fibers leading to the laser laboratory.

The fibers are connected to a 650 MHz balanced diode detector (New Focus 1607-AC-FC). For measurements at or near zero optical transmission (at or close to the crossed polarizer setup, cf. 3.1.2 and 3.1.4) only one diode of the balanced diode detector is used. The detector signal is measured and stored by a 1 GHz oscilloscope (Wavemaster, LeCroy). To scan the longitudinal bunch profile, the vector modulator of the laser to RF synchronization is used to vary the relative delay between the 1.3 GHz reference signal and the laser pulse in 20 fs to 100 fs steps. The EO sampling technique samples over many successive bunches and therefore depends critically on a low jitter in the arrival time of the bunches at the EO crystal and on a reproducible, stable electron bunch shape. Moreover, the synchronization between the femtosecond laser and the 1.3 GHz master oscillator of the linac RF must be very precise.

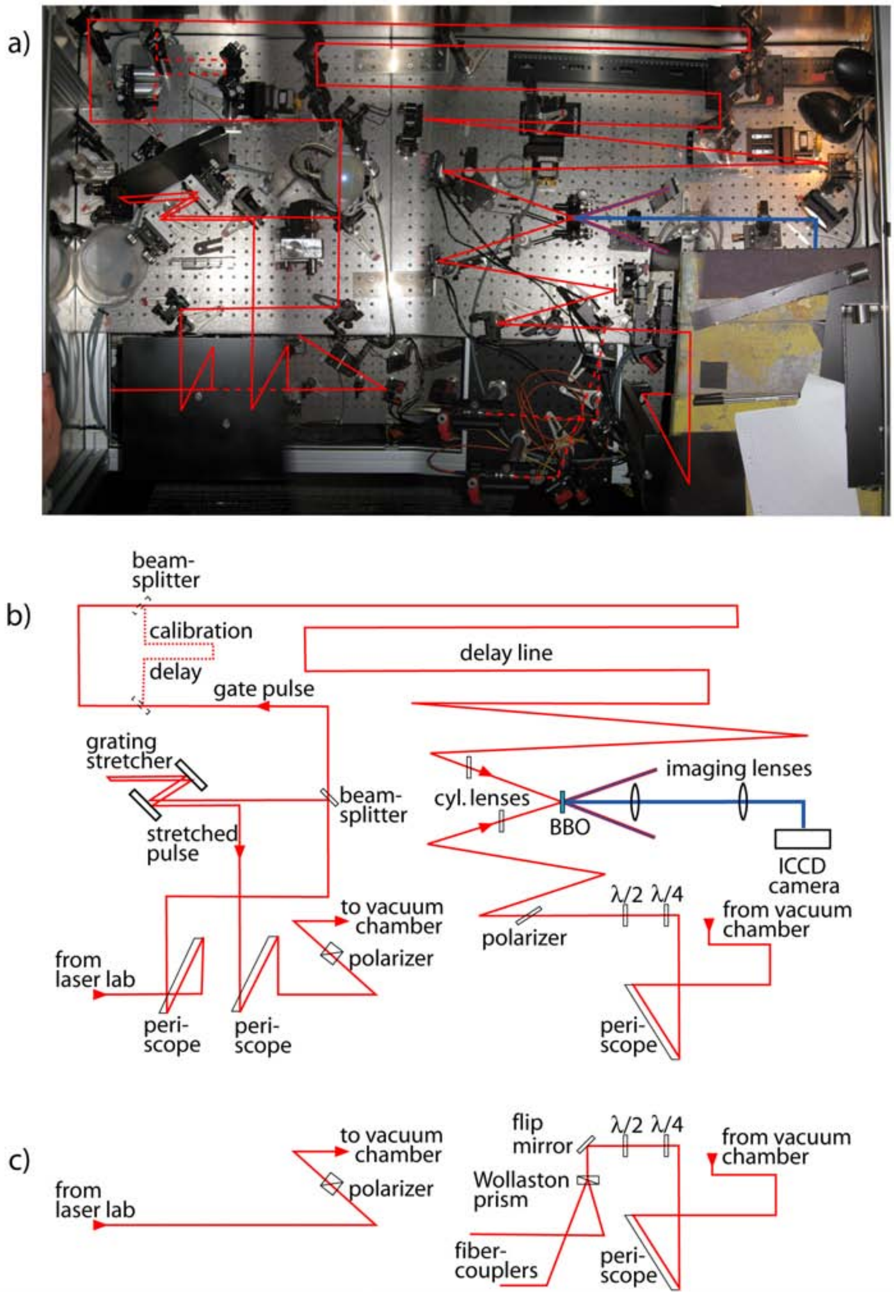

Figure 5.12.: a) Photography of the electro-optic setup in the accelerator tunnel with the laser beam path. b) Laser beam path for the temporally resolved EO detection. The beam splitters of the calibration delay line can be removed once the time calibration has been done. c) Laser beam path for the spectrally resolved EO detection and EO sampling. Mirrors are not shown in the drawing.

5.2.4.2. Spectrally resolved electro-optic detection

For the spectrally resolved electro-optic detection the pulse is stretched by SF11 glass blocks or by a SF11 prism stretcher in the laser lab resulting in a linearly chirped pulse of several picoseconds length. The setup in the tunnel is the same as for EO sampling, but the fibers are connected to a spectrometer (SpectraPro 150, Acton Research) located outside the linac tunnel. For measurements at or near zero optical transmission (at or close to the crossed polarizer setup) only one fiber is used, the second fiber can be used as reference to normalize the spectrum measured at the first fiber. All measurements presented in this thesis were measured at or near zero optical transmission and the normalization was done with background and reference data measured prior to the measurements. The image of the spectrum is recorded with a gated intensified camera (PCO DicamPro with an S25 photo cathode or Andor DH720-18F-03).

The PCO camera is fully integrated in the accelerator control and data acquisition (DAQ) system and single shot spectra of each bunch can be taken and stored with the full 5 Hz repetition rate of the accelerator. The integration in the DAQ system also provides the possibility to synchronize and compare the measured data to other bunch diagnostic and accelerator data.

The spectrometer was calibrated using the first order argon and the second and third order mercury lines of a low pressure mercury arc lamp with argon carrier gas (Oriel Model 6035) between 730 nm and 866 nm [BD00]. The resolution was found to be better than $\sigma_\lambda = 0.3$ nm (rms).

5.2.4.3. Temporally resolved electro-optic detection

To change the setup to temporally resolved detection a mirror is inserted remotely controlled into the laser beam path to steer the beam via a periscope to the second level of the optical table (see Fig. 5.12(b)). Here, the laser pulse is split into two parts of equal intensity. The first part is sent to a grating stretcher and stretched to about 20 ps (FWHM). The stretched pulse is then transfered back to the lower level and reflected to the EO crystal in the vacuum chamber by a second remotely controlled mirror following the same path as the laser for the spectrally resolved measurements. After the quarter- and half wave-plates the pulse passes the (now removed) flip-mirror used to steer the laser to the spectral decoding setup and is polarized by a thin film polarizer. The horizontally polarized component is focused by a cylindrical lens (f = 100 mm) to a thin line of about 100 µm in height and 20 mm in width on a β-barium borate (BBO) crystal. The second part of the split pulse, called the gate pulse, is sent to the BBO crystal via a set of delay lines to ensure that the optical paths of the two pulses from the beam splitter to the BBO crystal are of equal length. The gate beam is partially focused with a cylindrical lens (f = 200 mm) to a line of about 1 mm in

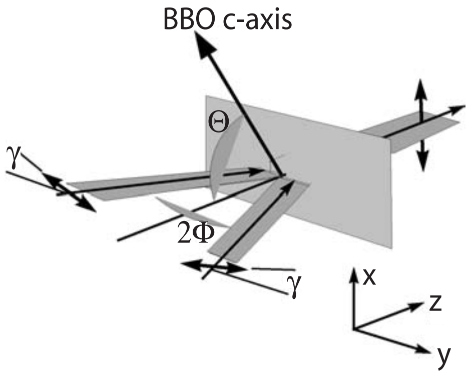

Figure 5.13.: BBO crystal and beam geometry of the non-collinear SHG used for the temporally resolved measurements. The vertical (x) dimension of the beams is not shown. From [JSM+03].

height and 20 mm in width on the BBO crystal. Focusing the two beams was necessary to increase the pulse intensity available for second harmonic generation (SHG). The angle of incidence of the beams on the BBO crystal is $\Phi = \pm 19°$.

The BBO crystal is 300 µm thick and 15 mm wide, with the crystal axis $\Theta = 45°$ from the normal. For the crystal axis and beam geometry (Fig. 5.13), type I SHG phase matching of the 800 nm and 400 nm beams leads to the following relationship between angle of incidence Φ and crystal angle Θ:

$$\cos^2\Theta = \left(\frac{n_{E,400}^2 n_{O,400}^2}{n_{O,800}^2 - \sin^2\Phi} - n_{O,400}^2\right) \cdot \frac{1}{n_{E,400}^2 - n_{O,400}^2} \tag{5.1}$$

The BBO axis was tuned to the correct phase-matching angle by tilting the crystal around the y-axis, while maintaining the symmetry of the incident beams with respect to the crystal axis. For the geometry used here, the 800 nm polarization should strictly be rotated to an angle $\gamma \approx 10°$ from the horizontal (Fig. 5.13) to be in the ordinary polarization [JSM+03]. However, in practice the beams were used with horizontal polarization.

The generated 400 nm second harmonic radiation was imaged onto a gated intensified camera (PCO DicamPro with S20 phothocathode) by two lenses ($f_1 = 100$ mm, $f_2 = 200$ mm), with the BBO crystal laying in the image plane and with an image magnification of 2. Since the active area of the camera is 18 mm wide, only $a = 9$ mm of the BBO crystal width could be used. For some measurements a second set of lenses ($f_1 = 75$ mm, $f_2 = 250$ mm) was used increasing the magnification to 3.3 ($a = 5.4$ mm).

With an angle of incidence $\Phi = 19°$, this leads to a temporal window of the measurements of $t = 2a\sin\Phi/c \approx 19$ ps and a conversion factor of about 15 fs/pixel at the

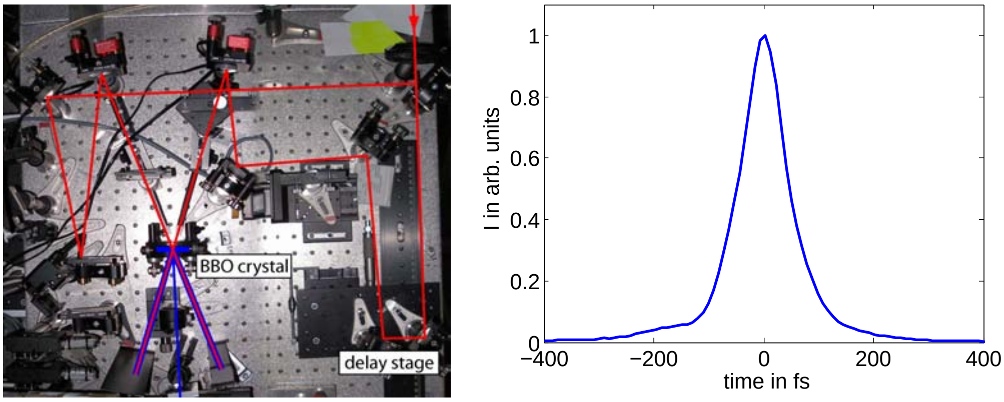

(a) Setup for the autocorrelation measurement

(b) Autocorrelation signal of the gate pulse averaged over 50 pulses.

Figure 5.14.: Setup for the autocorrelation measurement and the autocorrelation signal of the gate pulse

1280 pixel wide camera image ($t \approx 11.4$ ps and a conversion factor of 9 fs/pixel for the second set of lenses). The camera is equipped with a short-pass filter (2 mm thick BG39, Schott AG) to block stray light at the fundamental wavelength.

The resolution of the imaging system (two lenses and camera) was tested in the laboratory with a sine test pattern (M-19 Transition Sine Pattern, Applied Image, Rochester, NY) at the position of the crystal illuminated with blue light of 400 nm wavelength. Two lines could be separated for up to 40 lines/mm corresponding to an resolution of better than 25 µm at the crystal or 3.2 camera pixels. This limits the time resolution of the setup to about $3.2\ \text{pixel} \cdot 15\ \text{fs/pixel} = 48$ fs leading to a σ_{camera} of ≈ 20 fs. The resolution of the cross-correlator setup is determined by the length of the gate laser pulse, the phase matching properties and the thickness of the BBO crystal and the optical resolution of the imaging system and the camera. The total resolution of the cross-correlator estimated to be $\sigma_{\text{det}} \approx 35$ fs.

For a test of the time resolution of the cross-correlator, the gate beam was split into two parts and these two parts were spatially and temporally overlapped in the BBO crystal in the same geometry as in the TD experiment (Fig. 5.14(a)). The signal traces acquired by the camera show now the autocorrelation function of the gate pulse including the resolution limitations of the BBO crystal and the optical system that images the BBO to the camera (Fig. 5.14(b)). The measured width of the autocorrelation signal is 44 ± 8 fs (rms). This width sets an upper limit to the resolution of the cross-correlator and it agrees well with the estimated resolution $\sigma_{\text{det}} \approx 35$ fs (cf. 4.5). It includes the effects of the duration of the gate pulse, the phase miss-match in the BBO and the finite resolution of the imaging system. The real resolution is be slightly better, as the contribution of the gate pulse duration to the autocorrelation function is $\sqrt{2}$ times higher than to the resolution of the detection system.

Moving the delay stage by a defined distance, one pulse is delayed by a known time ΔT and the corresponding shift of the autocorrelation function is observed. The from the observed shift a time calibration constant of 9.98 fs/pixel can be determined, which is in good agreement with the value of 9 fs/pixel calculated from the crossing angle of the laser pulses before.

For precise time calibration an additional delay line with beam splitters was introduced in the setup (calibration delay in Fig. 5.12). A set of two beam splitters can be moved by a remotely controlled stage into the path of the gate beam. The first beam splitter splits the beam into two parts of equal intensity. One part follows the old path, the other one is sent through a remotely controlled delay line to the second beam splitter as well, where it is recombined with the first part of the beam. The path through the delay line is of almost the same length as the beam path around it with a slight offset Δt, which can be varied with the remotely controlled delay line. The gate pulse is now split into two pulses separated by a variable time delay Δt. The EO pulse is sampled by each of the two pulses leading to two signals from the same electron bunch in one camera image. Varying the delay Δt by a known amount allows a time calibration of the camera images, which is independent of the arrival time jitter of the electron bunch. The delay can be varied by more than 10 ps with an accuracy of better than 50 fs. The position of the signal can be determined with an accuracy of less than 100 fs. This leads to an calibration error of less than 1%. Time calibration measurements are shown in section 6.3.3.

5.2.5. The electro-optic setup at the CTR beam line

Next to the EO setup in the accelerator tunnel a beam pipe is installed, which reflects pulses of coherent transition radiation (CTR) from a transition radiation screen in the electron beam pipe to a laboratory next to the EO laboratory. The beam line was designed for spectral measurements of CTR with wavelengths from 7 µm to several millimeters. A more comprehensive description of the CTR beam line and the spectral measurements done and planned at this beam line is given in section 5.3.2 and in [CSS05c, CSSS06].

In a first proof of principle experiment the time structure of CTR pulses was measured with the spectrally resolved EO technique. The CTR leaves the evacuated beam pipe through a low-density polyethylene (LDPE) window and is vertically polarized and focused to a EO crystal by a toroidal mirror ($f = 123$ mm) via an indium-tin oxide (ITO) beam combiner. The laser pulses are transfered from the EO laboratory to the optical table in the CTR laboratory. The pulses are vertically polarized and are sent

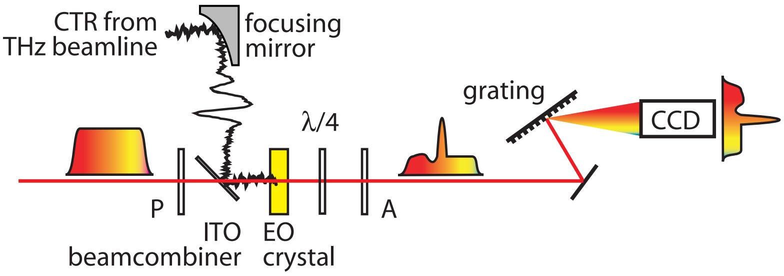

Figure 5.15.: Schematic drawing of the setup for spectrally resolved measurements at the CTR beam line. The CTR is focused onto the EO crystal via the ITO beam combiner. The chirped laser pulse passes through the polarizer P, the ITO beam combiner, and the EO crystal, where the polarization becomes elliptical. The ellipticity of the polarization is proportional to the electric field of the CTR and has the same temporal structure. The analyzer A turns the elliptical polarization into an intensity modulation. The longitudinal charge distribution gets encoded in the spectrum of the laser pulse, which can be measured using a spectrometer. The quarter wave plate is used to compensate residual birefringence of the EO crystal.

through the beam combiner to the EO crystal. After the crystal a quarter-wave plate and a polarizer are inserted before the beam is coupled into a multi-mode fiber leading to the spectrometer and the intensified gated camera as described above (Fig 5.15).

5.2.6. The electro-optic crystals used in the experiments

For the measurements a number of gallium phosphide (GaP) and zinc telluride (ZnTe) crystals with different thicknesses and from different suppliers were used. Some of the crystals are wedge-shaped to be able to do measurements passing the laser trough the EO crystals at different thicknesses and to prevent multiple reflections of the laser pulse in the crystal (Fig. 5.16). They are used with the thin edge pointing towards the electron beam. All crystals are cut in the (110)-plane. In the electron beam pipe they were mounted with the [-110]-axis pointing to the center of the beam pipe. Figure 5.17 shows two GaP crystals glued to a crystal holder ready to be mounted in the accelerator beam pipe.

A list of the EO crystals used for the measurements presented in this thesis is given in table 5.2. A number of these crystals were tested at the Strathclyde Terahertz to Optical Pulse Source (TOPS, University of Strathclyde, Glasgow, Scotland) with EO sampling measurements with laser induced THz pulses (cf. 6.1).

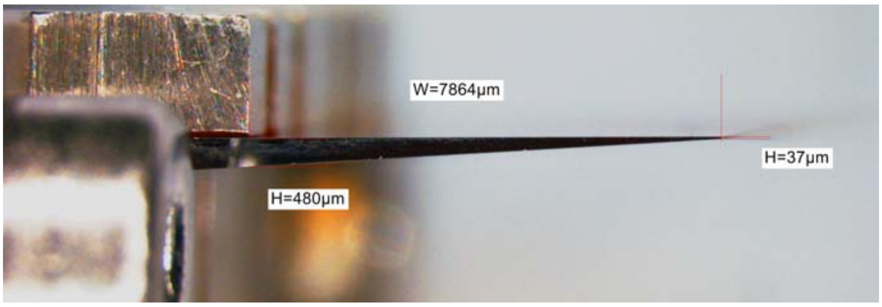

(a) Wedged ZnTe crystal of 37 µm at the top edge and 480 µm at the bottom

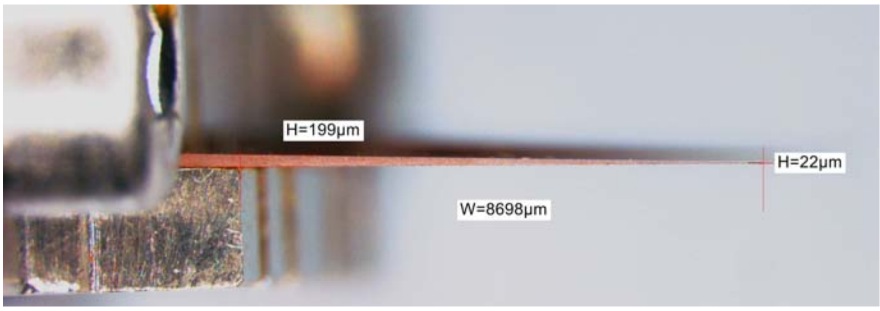

(b) Wedged GaP crystal of 22 µm at the top edge and 199 µm at the bottom

Figure 5.16.: Side view of the wedge-shaped EO crystals

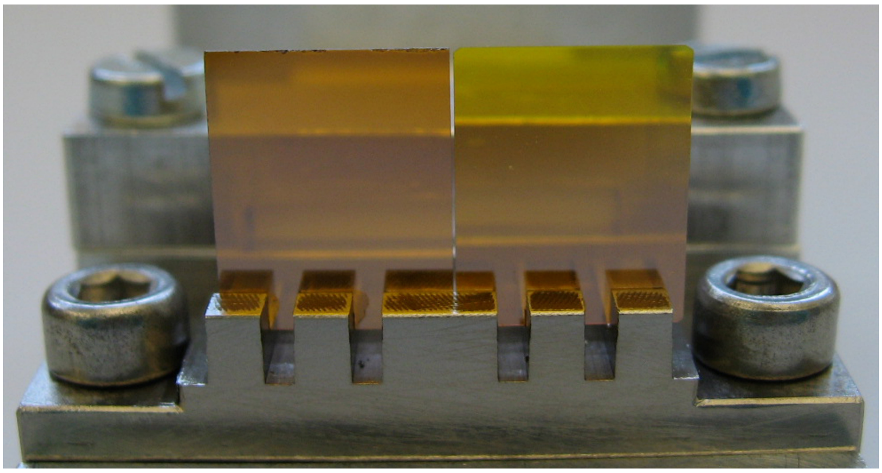

Figure 5.17.: GaP crystals in holder. Left a 185 µm thick flat crystal, right a wedged crystal of 20 µm at the top edge, 200 µm at the bottom.

Table 5.2.: The electro-optic crystals used for the experiments described in this thesis

No.	Material	Thickness	Supplier
1	flat GaP	175 µm	Moltech, Berlin
2	wedge-shaped GaP	25 to 250 µm	Moltech, Berlin
3	flat ZnTe	185 µm	Moltech, Berlin
4	wedge-shaped ZnTe	40 to 300 µm	Princeton Scientific Corp., NY, USA
5	flat ZnTe	300 µm	eV-Products, PA, USA
6	flat ZnTe	300 µm	Princeton Scientific Corp., NY, USA
7	flat ZnTe	500 µm	borrowed from FOM Institute for Plasma Physics ’Rijnhuizen’, NL
8	flat ZnTe	500 µm	Ingcrys Laser Systems, UK
9	flat ZnTe	4 mm	Ingcrys Laser Systems, UK
10	flat ZnTe	5 mm	borrowed from FOM, NL

5.3. Other longitudinal bunch diagnostics and bunch arrival time measurements at FLASH

Apart from the EO experiment described in this thesis several other diagnostic devices and experiments are used to measure the longitudinal bunch shape and the bunch arrival time at FLASH. This section concentrates on devices able to measure in the sub-picosecond regime as they are installed after the second bunch compressor. Measurements with time resolutions of hundreds of femtoseconds or above and techniques averaging over many bunches are completely omitted here, i.e. streak camera [Gri06] or autocorrelation [Frö05, GS06] measurements of coherent synchrotron radiation at the first bunch compressor or RF-phase monitors.

Four setups for longitudinal bunch shape diagnostic and bunch arrival time measurements are implemented in the diagnostic section between the second bunch compressor and the undulator (Fig. 5.1). The transverse deflecting RF structure (TDS) measures the longitudinal bunch profile with a resolution down to 15 fs (rms) by applying a time dependent vertical streak to the electron bunch and measuring the vertical bunch profile afterward. From the net deflection of the bunch also an arrival time can be derived (cf. 5.3.1). Single shot spectral of coherent transition radiation (CTR) can be measured at the CTR beam line described in section 5.3.2. From this data the longitudinal form factor and thus the charge distribution can be derived [Sch06b]. The timing electro-optical experiment (TEO) described in section 5.3.3 uses spatially resolved electro-optical detection (cf. 3.2.4) to measure bunch shape and arrival time down to a resolution of 70 fs (rms) [ADS+06]. The electro-optic beam phase monitor (BPhM) measures the arrival time of the electron bunch with a resolution of 20 to 50 fs using a pulsed fiber laser to sample the zero-crossing of the signal of an RF beam pickup [LHL+06]. Due to the limited bandwidth of the system the BPHM measures the arrival time of the 'center of charge' of the bunch and cannot provide any information on the bunch shape.

5.3.1. The transverse deflecting RF structure

The principle of the transverse deflecting RF structure (TDS) has been demonstrated at SLAC in 1964 [ALL64]. The temporal profile of the electron bunch is transferred to a transverse streak on a view screen by a rapidly varying electromagnetic field, analogous to the sawtooth voltage in conventional oscilloscope tubes.

The TDS was built and used for particle separation at SLAC under the name LOLA IV. It has been installed and commissioned at FLASH in cooperation between SLAC and DESY. The TDS is a 3.6 m long traveling wave structure operated at 2.856 GHz in which a combination of electric and magnetic fields produces a time-

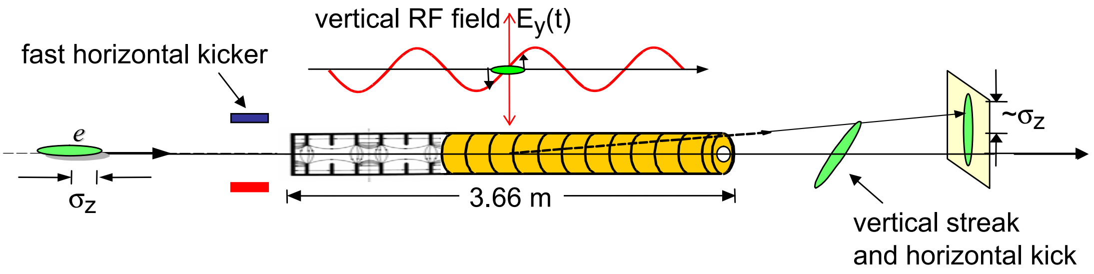

Figure 5.18.: Scheme of the operating principle of the transverse deflecting structure. Adapted from [Sch06a].

dependent transverse kick for the electrons. The bunches pass the TDS near zero crossing of the RF field and receive little or no net deflection but are transversely streaked in the vertical direction. Time calibration is achieved by measuring the net deflection for RF phase settings different from zero crossing. With a fast kicker magnet, this bunch is deflected horizontally towards an optical transition radiation (OTR) screen viewed by a CCD camera (Fig. 5.18). Since the fill-time of the TDS is less than a microsecond, a single bunch out of a train can be streaked leaving the other bunches in the train unaffected. The measured bunch is destroyed, prohibiting the characterization of bunches that are needed further downstream of the accelerator.

The time resolution of a TDS can reach 15 fs (rms) [HBS$^+$05] if the electron beam optics is optimized to yield the smallest possible beam spot on the view screen, and as such the diagnostic itself must be considered part of the accelerator optics design. For the beam optics used during standard accelerator operation the beam size is bigger and therefore resolution is limited to about 50 fs (rms).

TDS measurements in combination with a scan of the focusing strength of a quadrupole in front of the TDS allow to determine parameters of longitudinal slices of the electron bunch like the slice emittance [RBH$^+$05], while measurements in combination with an OTR screen in the dispersive section after the TDS can reveal the time-energy correlation of the bunch [RGHS06].

5.3.2. The coherent transition radiation beam line

The relativistic electrons of the bunch radiate electromagnetic waves whenever their Coulomb field is subjected to changes: synchrotron radiation due to directional changes in the bending sections or transition and diffraction radiation when the field enters regions of changing dielectric properties. For wavelengths of the radiation longer than the distance of two electrons, these electrons radiate 'in phase' or coherently, the intensity of this coherent radiation scales with the square of the number of

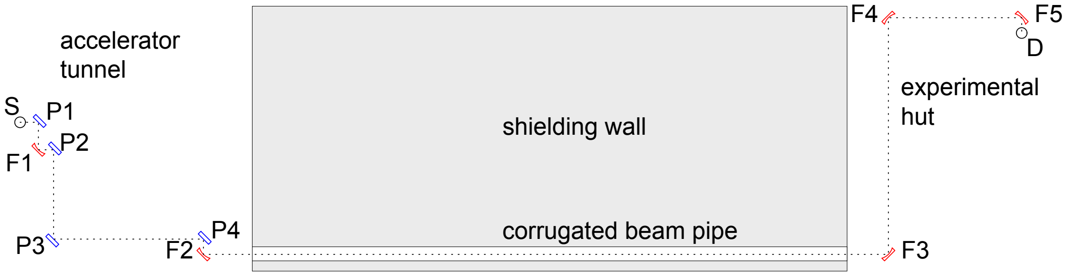

Figure 5.19.: Layout of the CTR beam line with transition radiation screen S, five focusing mirrors F1 to F5, four plane mirrors P1 to P4, and detector D. The sketch is somewhat simplified. In reality, the optical path between the mirrors F1 and P2 and between F4 and F5 is perpendicular to the plane of the drawing. Thereby, the polarization of the radiation is rotated by 90°. From [CSSS06].

contributing electrons and can be a massive effect. More precisely, the radiated power per frequency interval can be written as [Sch06b]:

$$\frac{\mathrm{d}U}{\mathrm{d}\omega} \propto N^2 |F_{\mathrm{long}}(\omega)|^2 \; T(\omega, \gamma, r_{\mathrm{beam}}, \Theta, \mathrm{source}) \tag{5.2}$$

where $F_{\mathrm{long}}(\omega) = \mathcal{F}\{\rho(t)\}$ is the longitudinal form factor of the bunch (the Fourier transform of the longitudinal charge distribution $\rho(t)$) and T summarizes all other, potentially complex, properties of the radiation source [Sch06b].

From spectrally resolved measurements of the intensity of the emitted coherent transition radiation information about the longitudinal form factor and thus the charge distribution can be obtained. Although only the magnitude of the form factor can be measured, the charge distribution can be reconstructed within certain limitations using the Kramers-Kroning relation to determine the phase (see e.g. [GS06]).

The coherent transition radiation beam line has been designed to transport diffraction and transition radiation from a screen in the electron beam pipe of FLASH to the outside of the accelerator tunnel in order to facilitate longitudinal bunch diagnostic with high resolution interferometric and spectroscopic devices outside the tunnel in a laboratory environment. The beam line is located after the last accelerating module right in front of the EO setup. It was designed to image the radiation from the screen to the laboratory 20 m away using nine gold coated mirrors, five of them focusing (Fig. 5.19). The beam line transports wavelength from the optical regime (above approx. 500 nm, limited by the gold coating of the mirrors) to several millimeters. It is evacuated to less than 0.1 mbar to eliminate absorption from humid air and it is separated from the vacuum in the electron beam pipe by a 0.5 mm thick chemical vapor deposition (CVD) diamond window, which has an excellent transmission over the full

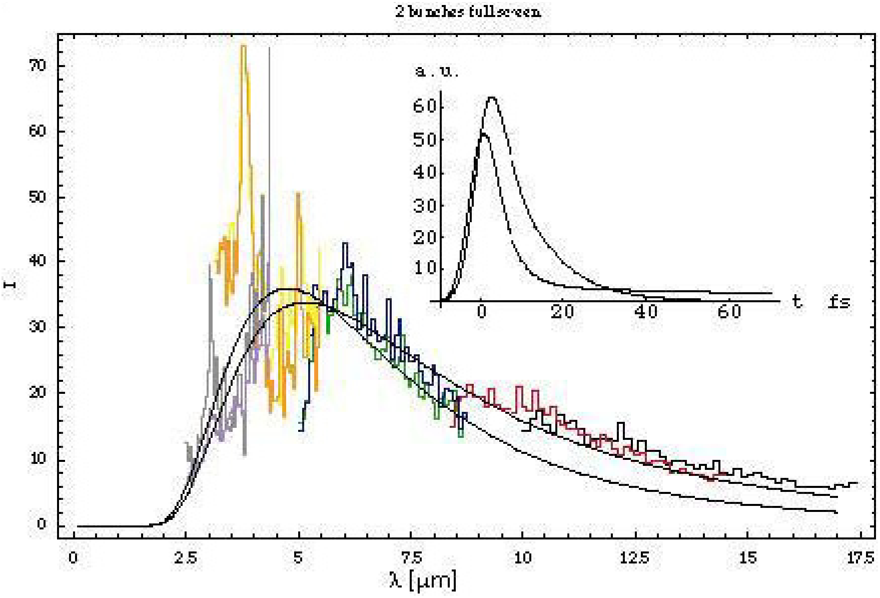

Figure 5.20.: Preliminary CTR spectrum and the corresponding bunch profiles. From [DGSS06].

bandwidth except a absorption band between 3 μm and 7 μm. A fast magnetic kicker is used to kick individual bunches to the screen, thus the measurements can run in parallel to normal accelerator operation. For a detailed description see [CSS05c, CSSS06].

Several spectrometer setups using transmission and reflective gratings have been developed and tested at the beam line including a 30 channel single shot spectrometer based on pyro-electric sensors [DGvdM$^+$06, DRS$^+$06]. For fully compressed bunches significant spectral intensity could be detected at wavelength as short as 2.5 μm. The preliminary data was used to estimate the time profile of the bunches suggesting bunches with a leading peak to be as short as 15 fs [DGSS06] (Fig. 5.20).

First time resolved measurements of CTR radiation were done using spectrally resolved EO detection leading to EO signals shorter than 500 fs (cf. 6.4.5).

5.3.3. Spatially resolved electro-optic detection: The timing electro-optical experiment

The main purpose of the timing electro-optical experiment (TEO) is to measure the pulse-to-pulse time jitter between the electron bunch directly before the undulator and the laser used for pump-probe experiments with the FEL photon pulses. For a detailed description see [vdBDF$^+$04, ADS$^+$06].

For pump-probe experiments a precise timing between the FEL and the optical laser pulses is mandatory and the time jitter should be ideally in the order of the duration of

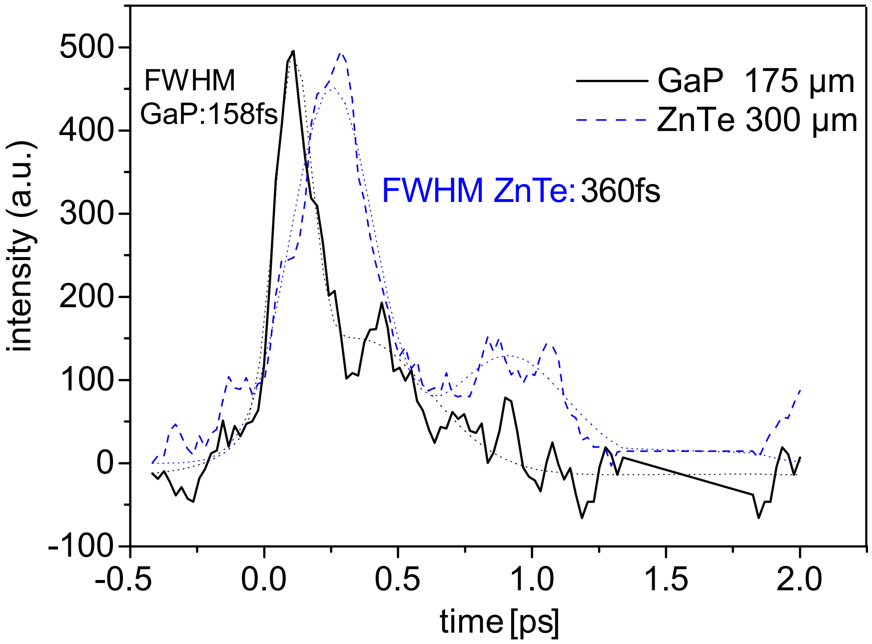

Figure 5.21.: Comparison between the TEO signals with GaP and ZnTe crystal. The temporal position of relative arrival is given by the rising edge. From [ADS⁺06].

the used pulses. It is however very demanding, if not impossible, to synchronize a laser to the FEL to a level of a few tens of femtoseconds particularly since the FEL process starts from statistical noise within the high current spike of the electron bunch. The TEO experiment uses an alternative approach and measures the relative arrival time between the pump-probe laser and the electron bunches for each individual electron pulse. Using the changes in the relative arrival time the exact time delay between the optical pump-probe pulse and the FEL photon pulse can be calculated and the data measured in pump-probe experiments can be properly corrected or binned.

The TEO experiment uses spatially resolved EO detection as described in section 3.2.4 with a 180 µm thick GaP crystal and a crossed polarizer setup. The laser pulses come from the Ti:Sa oscillator that also seeds an optical parametric amplifier used for the pump-probe experiments. The laser pulses are transported from the laser in the FLASH experimental area via a 160 m long polarization maintaining single mode glass fiber to the TEO setup inside the accelerator tunnel. The 50 fs (FWHM) long pulses from the oscillator are pre-chirped to about 350 ps by a grating stretcher to compensate for the dispersion in the glass fiber. The third order and higher order dispersion is compensated by a liquid crystal light modulator [vdB05]. The resulting pulse at the TEO setup is $T_0 = 100 \pm 10$ fs and the currently reached minimum width of the EO signal is 158 fs (FWHM) with a rise time of the leading edge of the signal of 100 fs (Fig. 5.21). The arrival time of the electron bunch to the laser pulse can be determined with a precision of better than 50 fs by fitting the leading edge [ADS+06].

5.3.4. The electro-optic beam phase monitor: Bunch arrival time measurements with fiber lasers

The electro-optic beam phase monitor (BPhM) employs a mode-locked erbium-doped fiber laser to sample the zero-crossing of an RF pulse from a beam pick-up. The laser produces pulses of $\approx$ 200 fs length at a wavelength of 1550 nm and is synchronized to the linac master oscillator. Currently timing systems are being developed based on mode-locked erbium-doped fiber lasers used as master oscillators [KBC+06, WCI+06]. Pulses from this timing system could be used directly for the BPhM, eliminating the need of a synchronization loop and the resulting additional time jitter.

The beam pick-up used for the measurements consists of a thin metal ring with an inner diameter of 34 mm and is installed in the FLASH accelerator right after the EO setup. With two feed-throughs mounted in opposite directions in the horizontal plane, the inductively shaped beam transient is coupled out. After about 30 m cable, the signal has a peak-peak voltage of more than 30 V and a bandwidth of more than 5 GHz. In the zero-crossing the slope is about 0.25 V/ps [LHL+06] (Fig. 5.22).

The RF signal and the laser pulses are fed into a 12 GHz commercially available electro-optical modulator (EOM), where the RF signal modulates the amplitude of the laser pulses: inside the EOM, the laser signal is split in two waveguides which traverse the electro-optic material $LiNBO_3$. The $LiNBO_3$ becomes birefringent when the RF signal of the beam pick-up is applied to the waveguides with opposite polarity, causing a phase shift between the laser light in the two waveguides. Recombining the two signals transfers this phase modulation into an amplitude modulation [LHL+06].

Sampling the RF signal close to the zero-crossing (approx. at 550 ps in Fig 5.22), the modulator converts changes of the electron bunch arrival time into an amplitude modulation of the laser pulses. This modulation can then be detected by a photo diode. Away from zero-crossing the phase shift between the laser light in the two waveguides can exceed π, leading to an over-rotation (Fig. 5.22). The resolution with which the arrival time can be detected is determined by the slope of the RF signal, the efficiency of the EOM, and the accuracy the laser pulse amplitude can be measured with. The resolution of the current setup is about 20 to 50 fs, not including the time jitter of the fiber laser synchronization to the RF master oscillator.

Due to the limited bandwidth of the system the BPhM cannot provide any information on the bunch shape. It measures the arrival time of the ’center of charge’ of the bunch and not of the leading spike, which lases in the undulator.

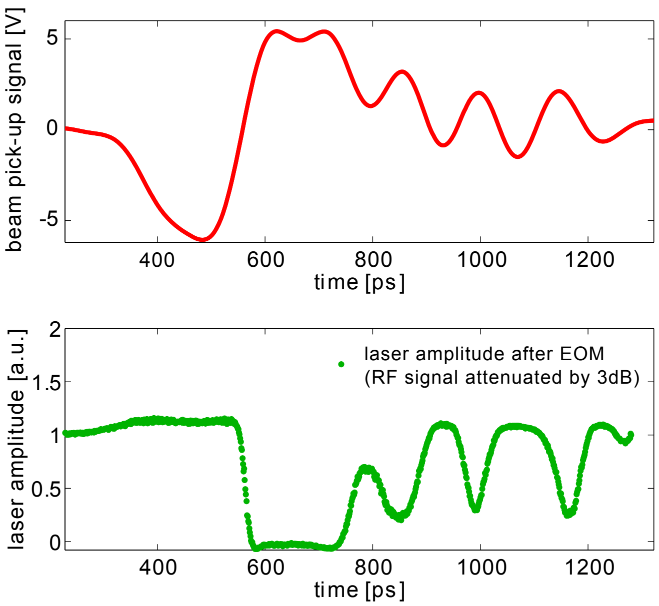

Figure 5.22.: top: Beam pick-up signal limited to 25 dBm. bottom: Measured laser amplitude at different sample positions along the beam pick-up signal. From [LHL+06].

Measurements of the arrival time using the beam phase monitor, the TEO setup and spectrally resolved electro-optic detection will be presented in section 6.4.2.2.

6. Electro-optic measurements

6.1. Characterization of the EO crystals

Several of the EO crystals used at the FLASH EO experiments were tested at the Terahertz to Optical Pulse Source (TOPS) at the University of Strathclyde, Glasgow, Scotland [Jar06]. The laboratory provides a user station for experiments with free-space propagating THz radiation. The sub-picosecond far-infrared pulses are generated from photo-conductive emitters (GaAs Austin switch) using a 1 kHz, 40 fs (FWHM) Ti:Sa laser. The photo-conductive switch is a 2 inch GaAs wafer with two electrodes separated horizontally by ≈ 45 mm. The voltage applied to the electrodes was 7 kV, and the switch was illuminated with 330 µJ, 40 fs (FWHM) Ti:Sa pulses. The emitted THz pulses reach energies of ≈ 1 µJ with a frequency range between 30 GHz and 2.5 THz. The pulses were focused onto the EO crystal to be tested. The induced birefringence was measured with EO sampling with a variable delay in a balanced detection setup (cf. 3.2.1). The laser pulses for the detection had a duration of 40 fs (FWHM) and a pulse energy of 100 nJ. For data acquisition a balanced diode detector and a lock-in amplifier were used. The delay between THz pulse and sampling laser pulse was varied in steps of 67 fs by a motorized delay stage.

The THz pulse shapes measured with a 175 µm thick GaP crystal and with a 185 µm ZnTe crystal agree well (Fig. 6.1(a)). The deviation for delays between 3.5 ps and 5 ps is due to the double reflection of the THz pulse inside the crystals. The measured pulse length of the THz pulse was 620 fs (FWHM). The amplitude of the signal measured with ZnTe is 2.36 times higher than the signal measured with GaP. Simulations for Gaussian THz pulses of a duration of 620 fs (FWHM) lead to an expected amplitude for the ZnTe crystal which is 6.7 times higher than the expected amplitude for the GaP crystal. For this pulse length no distortion of the pulse shape in neither of the two crystals can be expected from simulations.

Measurements with ZnTe crystals of different thicknesses between 185 µm and 5 mm show an increase in the amplitude of the EO signal and in the measured pulse length with larger thicknesses (Fig. 6.1(b)). The increase in amplitude is approximately linear for the three thinner crystals (185 µm, 300 µm and 500 µm), while the amplitudes for the 4 mm and 5 mm thick crystals reach only about 25% of the value

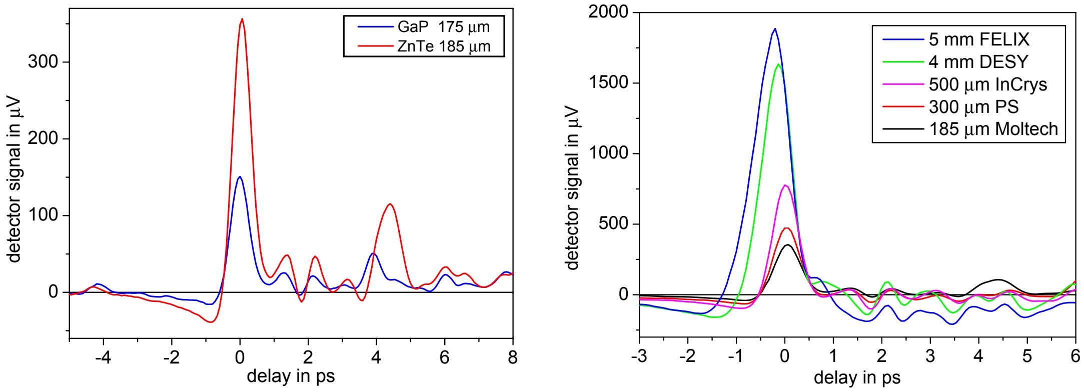

(a) (b)

Figure 6.1.: EO sampling measurements of laser induced THz pulses measured with a 185 µm thick ZnTe crystal and a 175 µm thick GaP crystal (a) and of ZnTe crystals of different thickness (b).

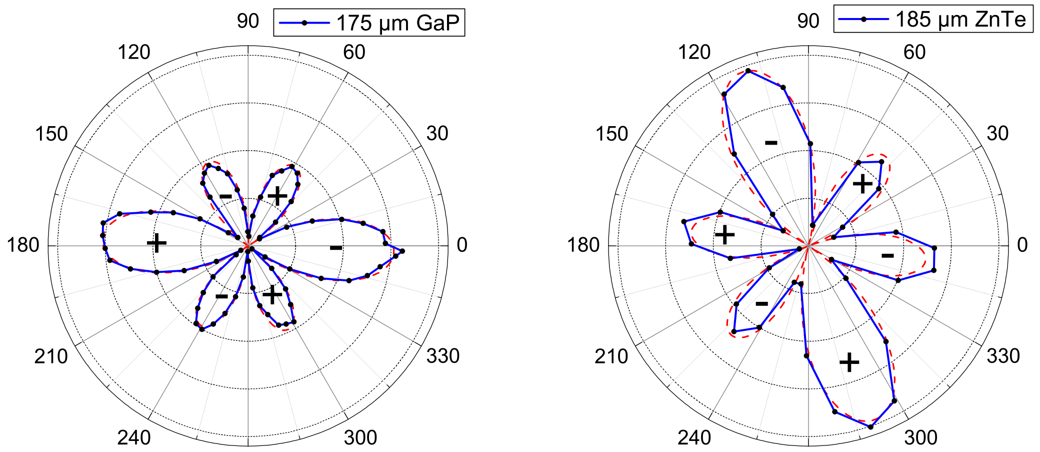

(a) 175 µm thick GaP crystal with [-1,1,0]-axis almost parallel to the crystal edge (-2.5° offset)

(b) 185 µm thick ZnTe crystal with [-1,1,0]-axis not parallel to the crystal edge (111° offset)

Figure 6.2.: Amplitude of the electro-optic signal as a function of crystal orientation. The THz pulse and the sampling laser pulse are horizontally polarized. The edge of the crystal is horizontally orientated at an angle of 0°. The dashed curve shows the expected angular dependence, rotated into the coordinate system of the (misaligned) crystal.

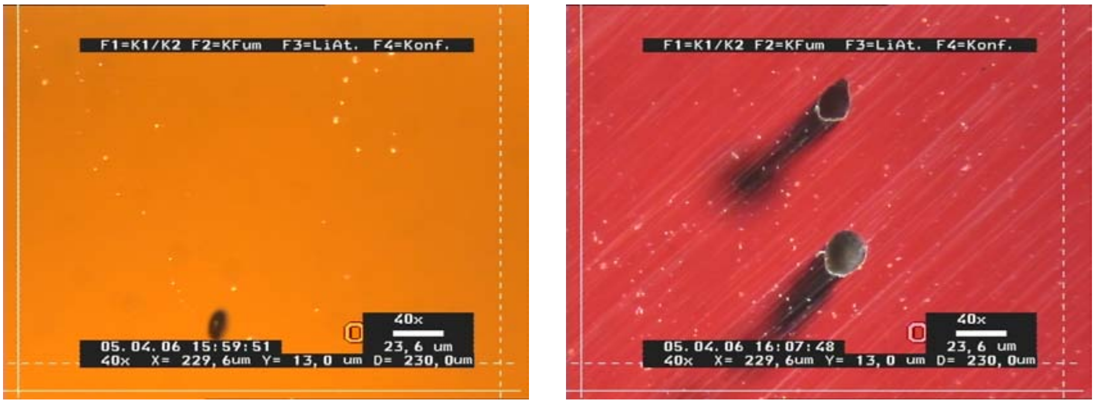

(a) 175 µm thick GaP crystal

(b) 185 µm thick ZnTe crystal

Figure 6.3.: Microscopic images of a GaP and a ZnTe crystal. The black structures are air bubbles embedded in the crystalline material. These inclusions are quite frequent in ZnTe crystals and only rarely found in GaP. The white lines are scratches from polishing.

expected from a linear continuation. Due to the increasing effect of the phase mismatch in thicker crystals an amplitude is calculated in the simulations for a 5 mm thick ZnTe crystal, which is 70% of the value expected from a linear continuation of the signal amplitudes for thin crystals. The measured pulse length increases from 620 fs (FWHM) for the 185 µm thick crystal, to 710 fs for the 4 mm crystal and to 820 fs for the 5 mm crystal. This is in good agreement with the signal width as expected simulations where a 620 fs Gaussian pulse is broadened to 770 fs and 805 fs (FWHM).

The lower optical quality of the available ZnTe crystals, particularly of the thick ones, in comparison to the GaP crystals (Fig. 6.3) may be one reason why the measured signal amplitudes are lower than the simulated ones. The background signal due to residual birefringence and scattering is compensated by the balanced detector, but the lower coupling efficiency into the detector may lead to a lower signal. However, this error can not be quantified since the signals for the individual diodes of the balanced diode detector were not measured. The lower signal for the thick crystals might be caused by the defocussing of the THz beam within the crystals which leads to lower electric field at the end of the crystal than at the front surface where the THz beam is focused. This effect was disregarded in the simulations. The effect can be neglected for crystals which are thinner than the Rayleigh length of the THz focus (approx. 3 mm in ZnTe for 1 THz with the used focusing optics), but it can lead to an average field strength in the 5 mm thick crystal which is only about 75% of the field strength in the thin crystals.

The orientation of the crystal axes was determined by measuring the electro-optic signal at zero time delay as a function of crystal orientation (Fig. 6.2). The EO crystal was rotated around the incident THz and laser beam direction, while the polarisation of THz and laser pulses were kept horizontally. All crystals show an angular dependence as calculated from equation (3.13). However, for the 185 µm thick ZnTe crystal the [-110]-axis was found to be rotated by 110° against the long edge of the crystal, making it impossible to mount it properly orientated in the accelerator beam pipe.

6.2. Spectrally resolved detection

6.2.1. Data analysis

All measurements presented in this chapter were done at or near crossed polarisation as described in section 3.1.2 and 3.1.4. The quarter wave plate was always set to $\phi = 0$. The angle θ of the half wave plate is quoted for every measurement. The angles $\phi = 0$ and $\theta = 0$ are defined by the crossed polarization settings, where minimum light is transmitted through the analyzing polarizer, this means that for $\phi = 0$ and $\theta = 0$ the residual birefringence of the EO crystal is already compensated as good as possible (cf. 3.1.4).

The raw data for spectrally resolved detection (EOSD) measurements are recorded as two dimensional camera images with the spectral information in horizontal axis (Fig. 6.4). The vertical width of the signal depends on the height of the entrance slit of the spectrometer and is of no interest. To acquire the electro-optical signal trace from this image several steps of binning, background subtraction and normalization have to be done. The vertical columns of the images are summed to obtain a one dimensional trace. To reduce the camera read-out noise only a 15 to 50 pixel high section of the images is used.

For a correct reconstruction of the phase retardation parameter Γ three different background traces are needed, which are all taken without electron beam.

Camera background The ”dark counts” of the camera are measured without laser pulses and the resulting trace is subtracted from all other traces including the following background measurements.

Background at crossed polarization Images are taken with laser pulses and with the wave plates set to crossed polarization ($\theta = 0$).

Normalization trace Here the images are taken with laser pulses at $\theta \neq 0$. Typically an angle of $\theta = 2^\circ$ is used. The data are used to calculate the spectral intensity at full transmission through the analyzing polarizer (at $\theta = \pi/4$). It cannot be measured directly, as the high intensity would drive the ICCD-camera into saturation and most likely also damage the camera. The normalization trace is calculated dividing the background trace at $\theta \neq 0$ by $(1 - \cos(4\theta))/2$.

All background images have to be taken with the same laser and camera settings (e.g. gain and exposure time) that are used for the EO measurements. The used background traces are the average from 10 to several 100 images.

From the EO data trace the camera background and the background at crossed polarisation is subtracted. The resulting trace is then divided by the averaged normalization

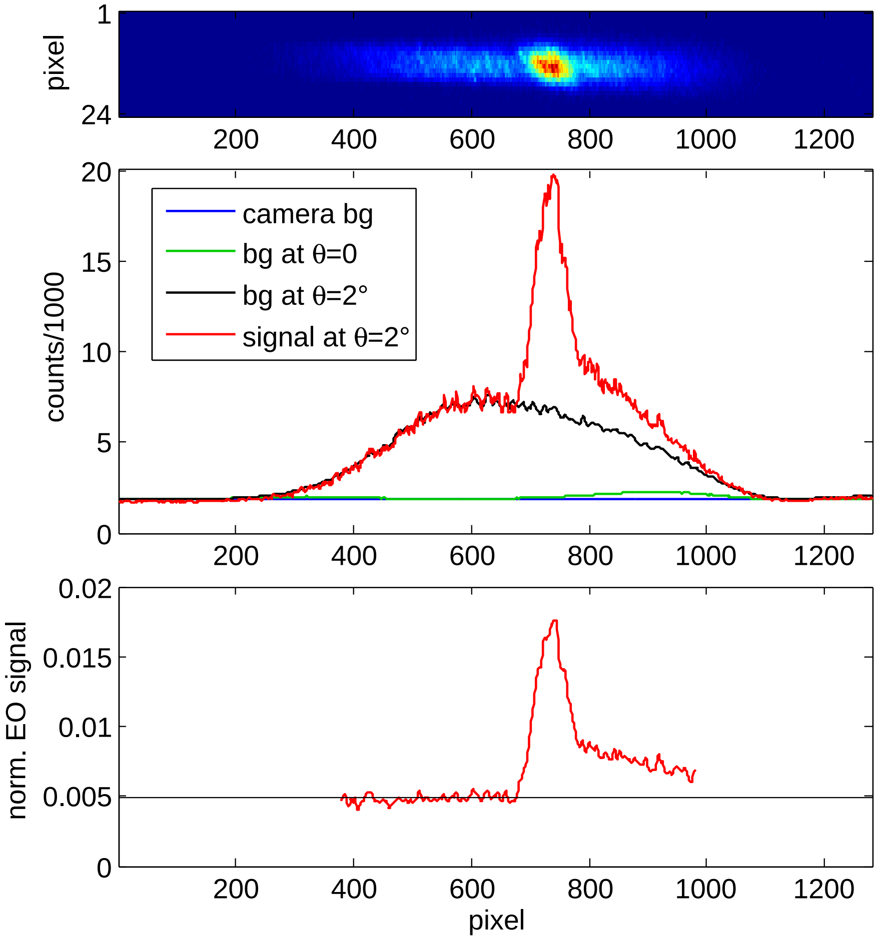

Figure 6.4.: Camera image of spectrally resolved EO signal (top), the corresponding signal trace and background traces (center) and the normalized EO signal trace in the usable range (bottom).

trace to get an EO signal trace which is independent of the laser spectrum. Due to the low intensity at the wings of the laser spectrum, the usable spectral range is restricted to about 1.5 to 2 times the FWHM of the laser spectrum. The useful time window is about 1.5 to 2 times the duration T_c of the chirped pulse.

All EO signal traces presented here are background subtracted and normalized unless otherwise explicitly mentioned.

The time-scale for the EO signal is calculated using the spectrometer calibration function and the instantaneous frequency $\omega_i(t)$ (Equ. (2.45)) of the chirped laser pulse (cf. 6.2.3).

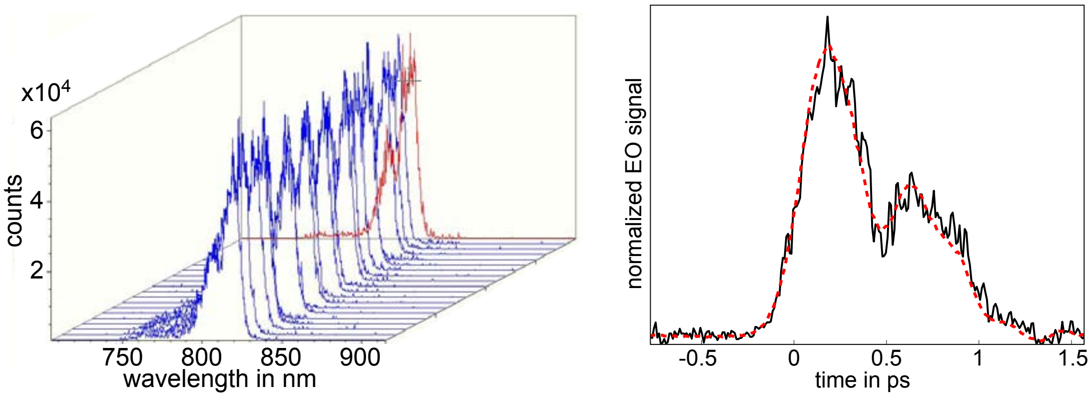

(a) Screen shot of a series of 20 bunches. Note that the leading edge of the bunch is at longer wavelength at the right side. Raw data, not background subtracted.

(b) Single SD trace. The dashed line shows the smoothed data used to determine signal width and arrival time. The leading edge of the bunch is at the left side.

Figure 6.5.: First spectrally resolved detection data measured in June 2005. Measured in a crossed polarizer configuration ($\theta = 0$) using a 300 µm thick ZnTe crystal. The laser pulses were chirped to 2 ps (FWHM).

6.2.2. Measurements of the longitudinal bunch shape

Zinc telluride

The first single-shot bunch profiles were recorded in June 2005 using a 300 µm thick ZnTe crystal and laser pulses chirped to $T_c = 2$ ps. The signals exhibit two peaks separated by $\approx$ 450 fs. The FWHM of the individual peaks is approx. 300 fs and 450 fs (Fig. 6.5). The signal to noise ratio of the raw data is about 10:1. The noise scales linearly with signal amplitude and is also seen in the normalization traces. The main part of the noise is caused by interferences among the different spectral components of the broadband laser pulse in the multi-mode fiber of a core diameter on 50 µm, guiding the light from the accelerator tunnel to the spectrometer. These can be suppressed using a single-mode fiber (core diameter approx. 5 µm), but at the price of a lower coupling efficiency and larger sensitivity to beam pointing fluctuations. The interferences generate noise frequencies higher than the lattice resonance of the electro-optical crystals. This noise can be reduced using Fourier-filters or smoothing algorithms like the Savitzky-Golay filter [SG64]. The EOSD data presented here were smoothed using a multi-pass, 5-point Savitzky-Golay filter (Fig. 6.5(b) and 6.7).

For optimally compressed electron bunches as used in SASE operation of FLASH, the EO signals measured at $\theta = 0$ with a 300 µm thick ZnTe crystal are shown in figures 6.6 and 6.20. The signals show a main peak of approx. 400 fs (FWHM) followed by a small tail with an additional peak 750 fs after the main peak reaching about 20 %

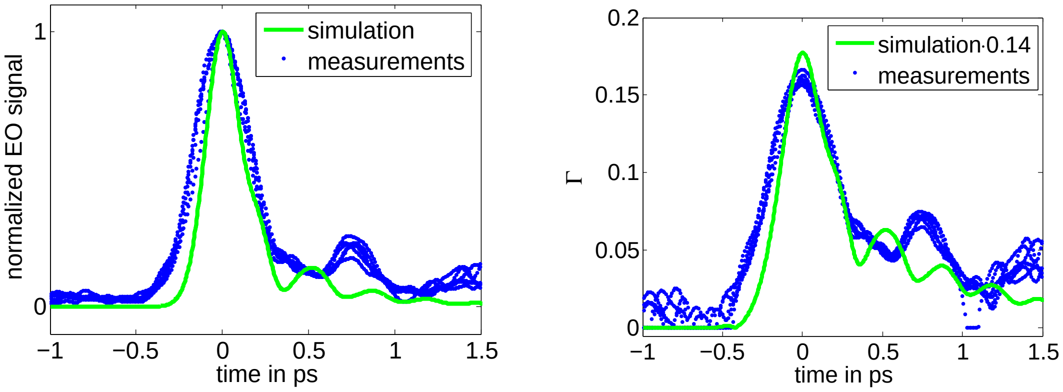

(a) Spectrally resolved EO data traces of compressed bunches and simulations for the corresponding parameters. The maximum signal is normalized to 1.

(b) Calculated phase retardation from the measurements shown in (a). The measured value is smaller than the expected by a factor of 0.14.

Figure 6.6.: Measured and simulated spectrally resolved EO signals of optimally compressed bunches. Measured with $\theta = 0$ using a 300 µm thick ZnTe crystal. The laser pulses with a bandwidth of 52 nm were chirped to 1.7 ps (FWHM).

of its amplitude.

In figure 6.6 a numerical simulation of the EO signal for a 300 µm thick ZnTe crystal is compared to the EO signals. For the simulation a longitudinal bunch profile of a compressed electron bunch as measured with the transverse deflecting structure (TDS, cf. 5.3.1) and the parameters of the setup and laser pulses corresponding to the presented measurements were used as input. The width of the simulated signal is 245 fs (FWHM), which is significantly narrower than the width of the measured signals. The oscillations in the simulated signal following the main peak are due to the frequency dependence of the response function (cf. 4.3). They are not seen in the measured signal. The bunch profile used for the simulation was not measured in parallel with the EO measurements but several days later with the same bunch charge and accelerator settings. This can result in slightly different bunch profiles.

The measured phase retardation is a factor of approx. 7 smaller than expected from simulations based on published material parameters (cf. 4.1). It is still a factor of 2.5 smaller than expected taking into account the lower EO response of the ZnTe crystal that was found in the measurements with laser induced THz radiation (cf. 6.1). A possible explanation of this discrepancy may be the poor optical quality of the ZnTe crystal or radiation damage from electron beam halo.

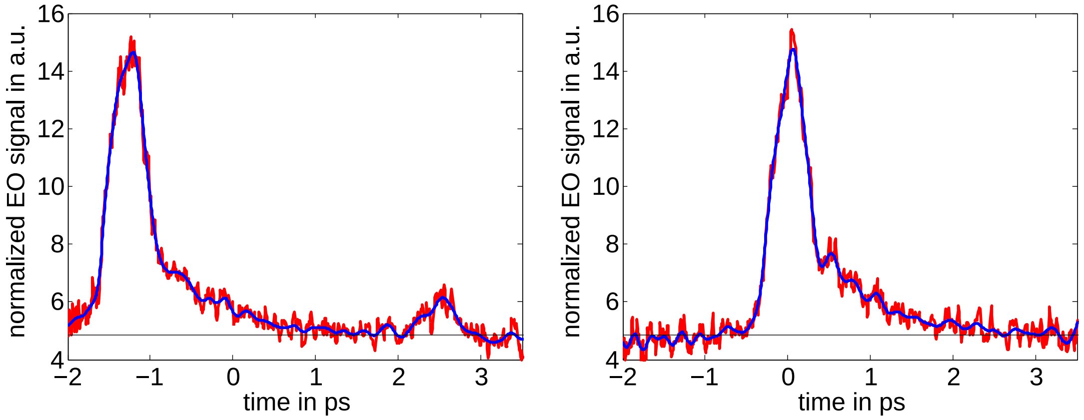

Figure 6.7.: Two typical EOSD measurements of compressed bunches, measured with $\theta = 2°$ using a 175 µm thick GaP crystal and laser pulses chirped to 3.6 ps (FWHM).

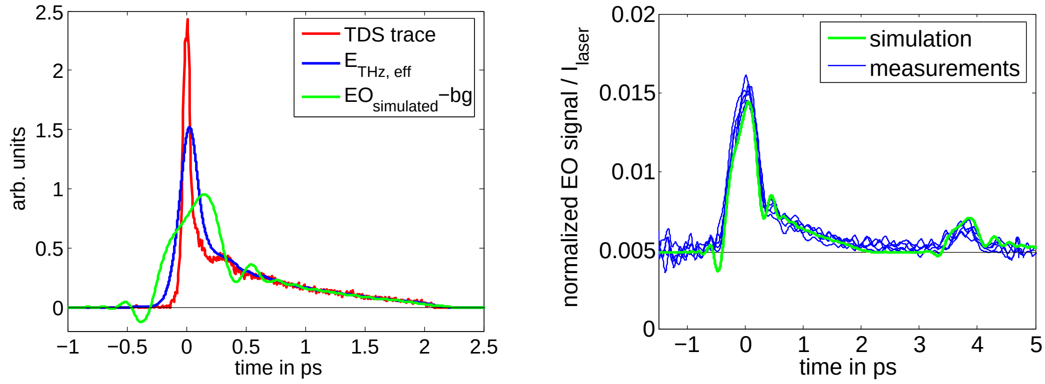

(a)

(b)

Figure 6.8.: EOSD measurements of compressed bunches (b) and simulations for the corresponding parameters (a). Measured with $\theta = 2°$ using a 175 µm thick GaP. The laser pulses were chirped to 3.6 ps (FWHM).

Gallium phosphide

Spectrally resolved EO measurements of compressed bunches using a 175 µm thick GaP crystal lead to a signal width of 500 ± 30 fs (FWHM) (Fig. 6.7). The half wave plate was set to $\theta = 2°$. At this setting the EO signal is linear in phase retardation within an error of a few percent and the signal to background ratio is about 2 : 1 (cf. 3.1.4). The time window of approx. $1.5 \cdot T_c = 5.4$ ps is large enough to see the signal from first internal reflection of the THz pulse within the crystal, leading to a second peak 3.8 ps after the main signal (Fig. 6.7(a)).

For a comparison with theoretical expectations the bunch shape as obtained with the transverse deflecting structure (TDS) is used as an input to a simulation of the EO process in GaP. The TDS pulse shape is shown in figure 6.8(a). The frequency dependent response function of the GaP crystal leads to a broadened effective THz pulse $E_{\mathrm{THz,eff}}$ at the EO crystal. The resulting pulse is too short to be accurately reproduced by spectrally resolved detection with a laser pulse chirped to 3.6 ps. Frequency mixing of the effective THz pulse and the laser pulse lead to an additional broadening of the EO signal (Fig 6.8(a)). In figure 6.8(b) the predicted EO signal is compared to the measured signal of five bunches. Excellent agreement is observed both in shape and magnitude, except for the very fast oscillations to frequency mixing in front and after the main peak due. These oscillations have amplitudes in the order of the signal noise and might be additionally reduced by a spectrometer resolution that is lower than assumed for the simulations (cf. 5.2.4.2). The excellent agreement between the measured and the simulated EO signals indicates that the published GaP material properties and the resulting effective response function are correct.

For the spectrally resolved EO detection, it can be concluded that the time resolution is limited mainly by the material properties of the ZnTe crystal to approximately 400 fs (FWHM) for measurements using a 300 µm thick ZnTe crystal and laser pulses chirped to 2 ps. For measurements using a 175 µm thick GaP crystal and laser pulses chirped to 3.6 ps the shortest measured signals were approximately 470 fs wide (FWHM), limited by the chirp of the laser pulses. However, to resolve signals down to the limit of approx. 200 fs (FWHM) given by the response function of a 175 µm thick GaP crystal, the duration of the chirped laser pulses would have to be below $T_c = 1$ ps for the used laser system with 63 nm spectral bandwidth (FWHM).

6.2.3. Time calibration for spectrally resolved detection

As mentioned above, the time-axis for the EO signal is calculated using the spectrometer calibration function and the correlation $\omega_i(t)$ between frequency and time in the chirped laser pulse (Equ. (2.46)). The frequency-time correlation and the pulse duration are determined from the known parameters of the laser pulses at the Ti:Sa oscillator and the dispersion of the optical elements in the laser path (cf. 2.2.3). Small changes of the spectral intensity of the oscillator pulses change the duration of the chirped pulses but have no influence on the time calibration as long as the pulse length at the oscillator is small compared to the pulse length of the chirped pulses. The optical elements in the laser path including the vacuum windows are equivalent to 15 mm BK7 glass. To achieve a sufficient duration of the chirped pulse SF11 glass blocks were added in the path of up to 100 mm total length.

Measurements of the relative arrival time between the electron bunches and the laser

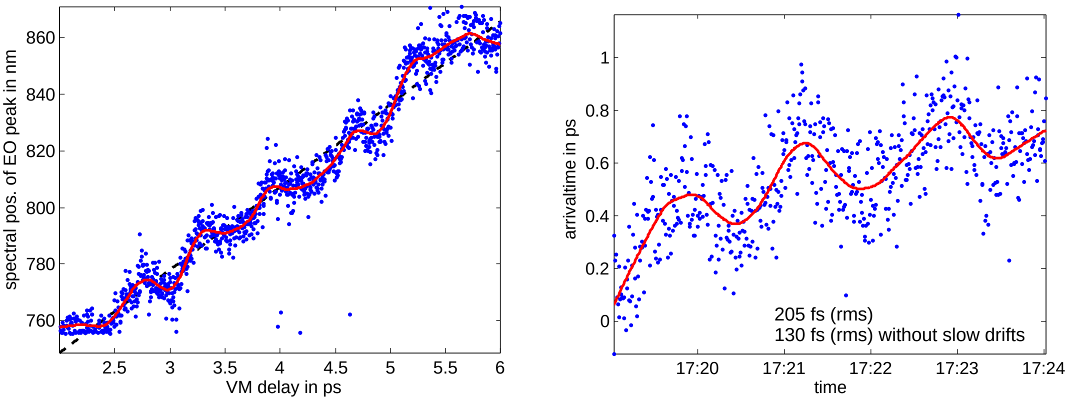

(a) Position of the EO peak in the laser spectrum. During the measurement the delay between the laser and the RF master oscillator was varied to check the time calibration. The dashed black line shows a linear fit with a slope of 29.2 nm/ps.

(b) Relative arrival time between the electron bunch and the laser pulse at the EO setup.

Figure 6.9.: Relative arrival time between the electron bunch and the laser pulse at the EO setup. The red line shows the slow drift. The oscillations with a period of 1 to 2 minutes are caused by temperature oscillations of the cooling water for the photoinjector gun, which were observed in spring 2005 when these measurements were done.

pulses at the EO setup offer the possibility to obtain the instantaneous frequency-time correlation of the chirped laser pulse according to equation (2.46). Hence the time calibration can be checked independently by measuring the position of the EO peak in the laser spectrum or the bunch arrival time for different delays of the laser pulses. For the data shown in figure 6.9(a) the delay of the laser pulses was changed in steps of 10 fs using the vector-modulator of the laser synchronization (cf. 5.2.2). Slow drifts of the acceleration parameters can lead to drifts of the arrival time (Fig. 6.9(b)), which limits the accuracy of this calibration test. The calibration factor of 29.2 nm/ps determined from a fit to the arrival time data (Fig. 6.9(a)) is in reasonable agreement with the calculated factor of 31 nm/ps.

Scanning the time delay between the laser pulses and the RF master oscillator, a superposition of the delay changes and the arrival time jitter of the electron bunches is measured (Fig. 6.9(a)). The slow drift during the 10 minutes needed for the scan over 4 ps was below 200 fs (Fig. 6.9(b)), as the fast jitter can be averaged for this measurement. This leads to a calibration accuracy of approx. 5%. The oscillations with a period of 1 to 2 minutes seen in figures 6.9(a) and 6.9(b) are caused by temperature oscillations of the cooling water for the photoinjector gun, which were observed in spring 2005 when these measurements were done.

6.3. Temporally resolved detection

6.3.1. Data analysis

The analysis of the raw data from temporally resolved detection (EOTD) measurements follows the same procedure as the spectrally resolved data (cf. 6.2.1). Due to space constraints, the line image of the second harmonic (SHG) light from the BBO crystal could not be aligned horizontally on the camera. The region of interest was adjusted accordingly becoming a rhomboid instead of a rectangle. In figure 6.10 the tilt of the image is exaggerated due to a non-uniform magnification.

The background at crossed polarization ($\theta = 0$) is caused mainly by stray SHG light from the gate beam.

Beam pointing instabilities of the laser amplifier lead to changes in the overlap of the gate pulse and the stretched pulse at the BBO crystal and cause intensity fluctuations of up to ±50%. For signal traces measured at $\theta \neq 0$ these fluctuations can be compensated by multiplying the signal trace with an intensity factor, which is determined from the section of the EO trace in front of the EO peak. In this part of the trace the amplitude should be equal to the averaged background at the given θ.

6.3.2. Measurements of the longitudinal bunch profile

All signals presented in this section were measured using GaP crystals, either a flat crystal of 175 µm or a wedge-shaped crystal at a thicknesses of 65 to 100 µm. At the outer edges of the BBO crystal the low intensity of the laser pulses leads to an increased signal to noise ratio, limiting the useful time window of the temporally resolved detection to approx. 15 ps (Fig. 6.10).

Figure 6.11 shows two EOTD signals of compressed electron bunches at $\theta = 1^\circ$ and $\theta = 0$. The EOTD trace measured at $\theta = 1^\circ$ shows a narrow spike ≈ 200 fs (FWHM) wide followed by a about 7 ps long decreasing tail. A second narrow spike appears 2.2 ps after the first spike, caused by the internal reflection of the THz pulse in the EO crystal. This signal is very similar to the predicted signal as shown in figures 4.23(b) and 4.24(b), but the signal from the tail is about 50% to 100% higher and longer than expected from simulations. The leading spike in EOTD traces taken at crossed polarization is shorter (< 150 fs) and the tail is less pronounced. In several data series no signal from the tail of the electron bunch is seen (i.g. Fig. 6.11(b)). This is most likely caused by slight misalignments of the wave plates by a few tenth of a degree which can lead to strong suppression of low signal intensities at crossed polarization settings.

A minimum width of less than 54 fs (rms, 120 fs FWHM) was found for crossed

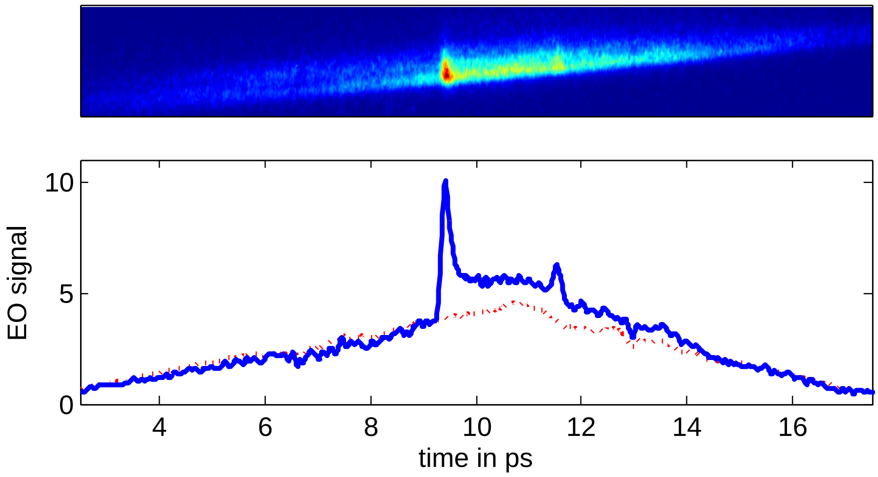

(a) $\theta = 1°$

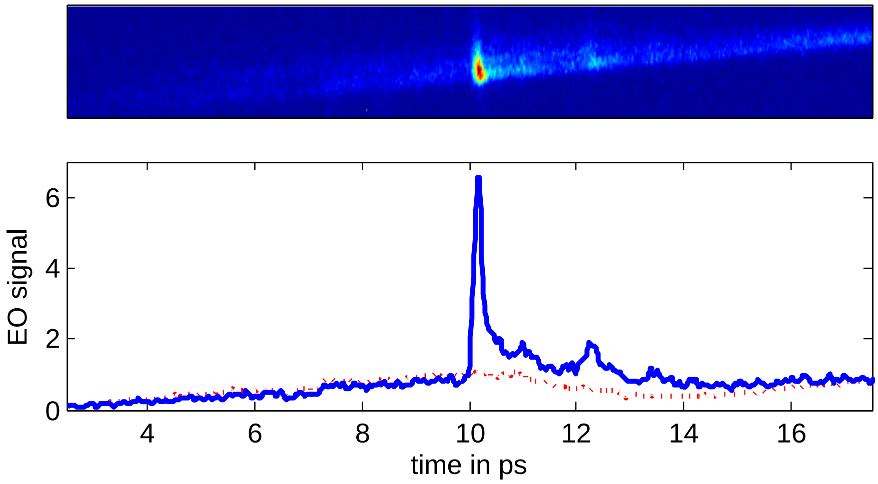

(b) $\theta = 0$

Figure 6.10.: Camera images of temporally resolved EO signals and the corresponding signal traces (solid line, raw data, only camera background subtracted) and traces without electron bunch present (dotted line). Measured at $\theta = 0$ (a) and $\theta = 1°$ (b) using a 100 µm GaP crystal.

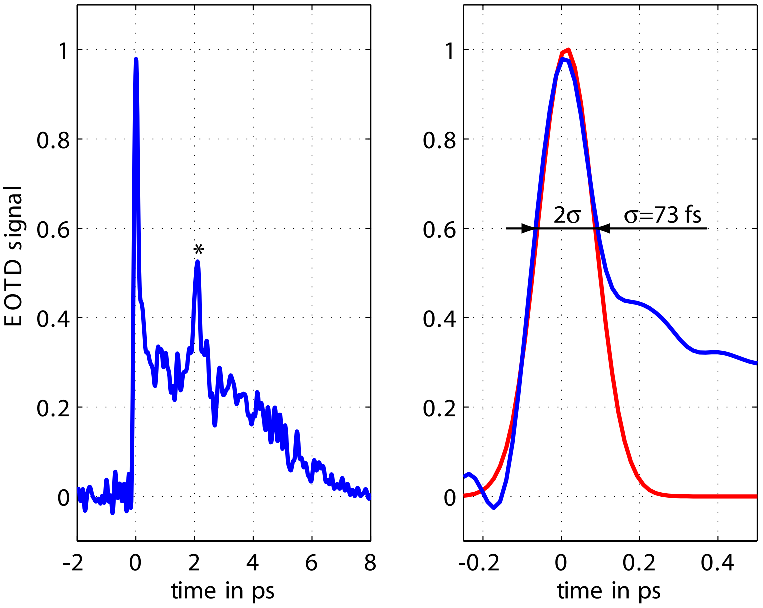

(a) $\theta = 1°$

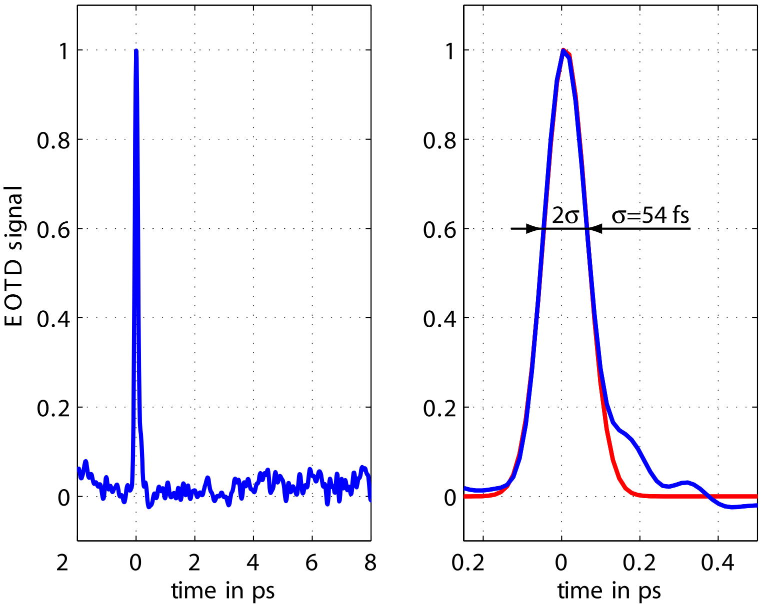

(b) $\theta = 0$

Figure 6.11.: EOTD signals of optimally compressed electron bunches using a 100 µm GaP crystal. The peak marked by an asterisk (*) is caused by the internal reflection of the THz pulse in the EO crystal. The right figures show the leading peak on an expanded time scale. The red line shows a Gaussian fit to the main peak.

polarizer settings and less than 73 fs (rms, 170 fs FWHM) for $\theta = 1°$. The rise time of the main peak from 10% to 90% of the maximum amplitude is 80 fs and 115 fs, respectively. The EO signal widths for measurements of compressed electron bunches at crossed polarization fluctuate between 120 fs and 190 fs (FWHM, see Fig.6.30(a)). When the half wave plate is set to $\theta = 1°$ the signal widths increases by about a factor of $\sqrt{2}$ to 150 fs to 260 fs as expected when changing from a quadratic dependence of the EO signal on the Coulomb field to an almost linear dependence (cf. 3.1.4).

6.3.2.1. Comparison to bunch shapes measured with other measuring techniques and numerical simulations

A number of EOTD traces have been taken in parallel with longitudinal bunch profile measurements with high temporal resolution using the transverse deflecting structure (TDS). Owing to space constraints, the EO experiment had to be mounted downstream of the TDS. Therefore it is not possible to observe the same electron bunch with EO experiment and the TDS, since the TDS deflects the bunch away from the EO crystal to an OTR screen. For this reason, the EO measurements were carried out on the second last bunch and TDS measurements on the last bunch in a pulse train of 2 to 21 bunches.

This data offer the possibility to use the TDS bunch profile as the charge distribution input for a numerical simulation and compare the calculated EOTD signal to the measured one. For the simulations shown in the following all broadening effects of the EOTD setup are taken into account (cf. 4.5).

An excellent agreement in shape and magnitude between the simulated and measured phase retardation is found for the main peak of the signal (Figs. 6.12 to 6.14). The deviation of the signal amplitude is about 20% to 30%, which is within the expected fluctuations due to changes in laser pulse power, electron bunch orbit and bunch charge. The peak width of the measured and simulated normalized phase retardation agrees with less than 10% deviation for most data traces. The EO signal from the bunch tail is almost doubled compared to the simulations. This effect is far less pronounced for bunch shapes without short structures of less than about 100 fs (rms, see Fig. 6.14). A possible explanation for this increased signal level following short peaks in the bunch profile are wake fields which are exited by the electron bunch upsteam of the EO crystal. These wake fields originate from the Coulomb field of the electron bunch which is diffracted and scattered from structures in the beam pipe like diffraction screens or viewports and especially from periodic structures like accelerating cavities or the TDS [ZWD04]. The wake fields follow the electron beam and since the electro-optical detection probes the electric field and not the charge distribution directly these wake fields are seen by EOTD but not in the TDS trace.

One series of measurements shows clear deviation of the measured phase retarda-

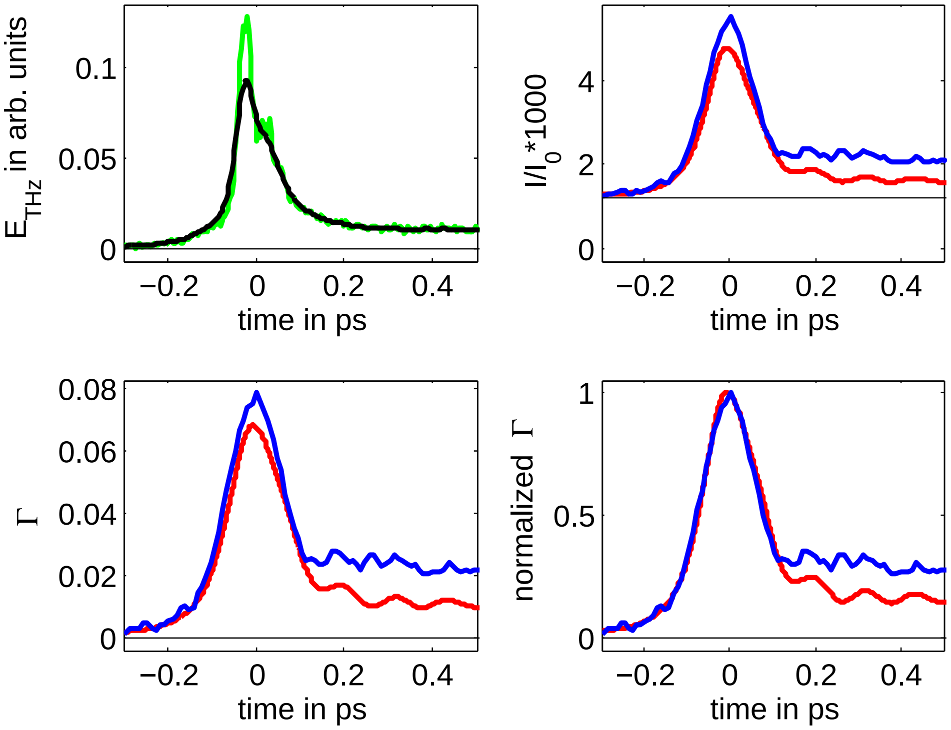

Figure 6.12.: TDS trace (green) of a compressed bunch and the field amplitude (black) at the EO crystal (top left). The corresponding simulated EO signal I and phase retardation Γ is shown in red, the measured data is shown in blue. Measured at $\theta = 1°$ using a 65 µm GaP crystal and a bunch charge of $Q_0 = 0.6$ nC.

tion from the simulated one (Fig. 6.15). The TDS traces show a 330 fs to 480 fs (FWHM) broad main peak with a slowly decaying tail. A narrow second peak of 70 fs to 100 fs width and smaller amplitude is situated in the rising edge of the main peak. The distance between the centers of the two peaks is 160 fs to 300 fs. In the simulated phase retardation signal the narrow peak causes a shoulder within the rising edge of the main peak. It is clearly visible if the two peaks are separated by more than 200 fs (Fig. 6.15(c) and 6.15(a)). This shoulder is not seen in the measured phase retardation even if the two peaks are separated by about 300 fs (Fig. 6.15(b)). Most likely this effect is caused by a systematic change of the bunch shape along the bunch train. This data series used the first bunch of the train for the EOTD and the second bunch for the TDS, while the other data is usually taken at the 10th and 11th bunch or later. Measurements of the arrival time of the bunches within one bunch train using the beam phase monitor (BPhM) show a systematic change of the arrival time relative to the linac RF for the first bunches (Fig. 6.16). The arrival time stabilizes after the fifth to

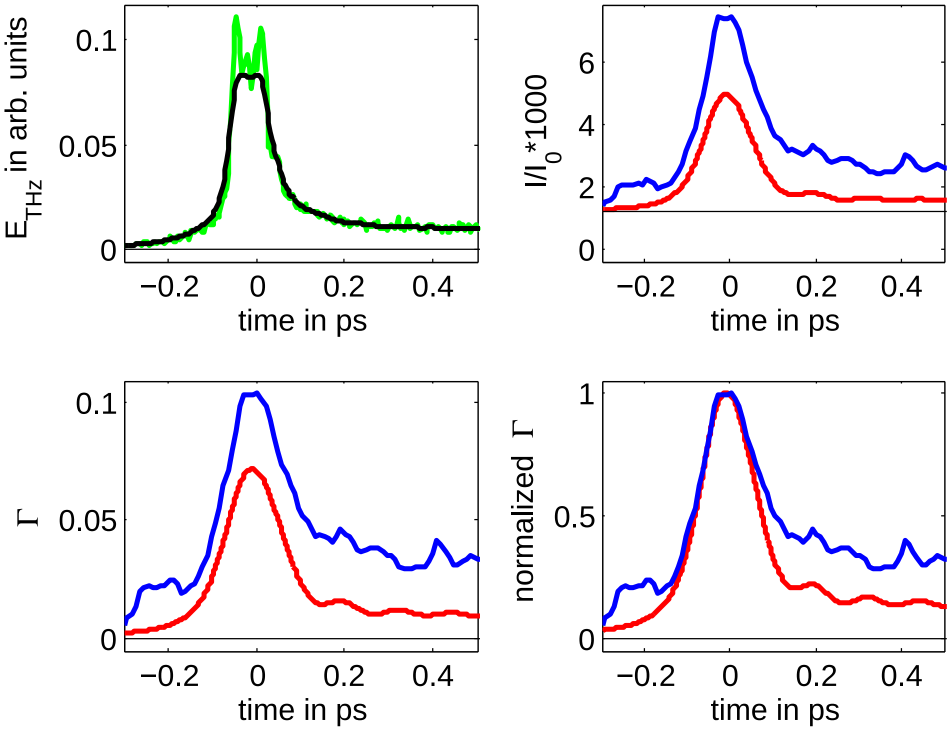

Figure 6.13.: TDS trace (green) of a compressed bunch and the field amplitude (black) at the EO crystal (top left). The corresponding simulated EO signal I and phase retardation Γ is shown in red, the measured data is shown in blue. Measured at $\theta = 1°$ using a 65 µm GaP crystal and a bunch charge of $Q_0 = 0.6$ nC. The width of the leading peak in Γ is 70 fs (rms).

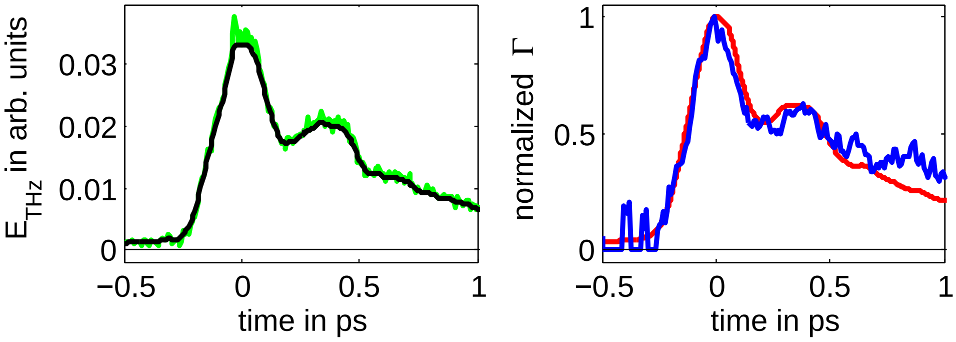

Figure 6.14.: TDS trace (green) of an overcompressed bunch ($\phi_{\mathrm{ACC1}} = 9.5°$) and the field amplitude (black) at the EO crystal (left) and the corresponding simulated (red) and measured (blue) phase retardation Γ (right). Measured at $\theta = 0$ using a 65 µm GaP crystal and a bunch charge of $Q_0 = 0.6$ nC.

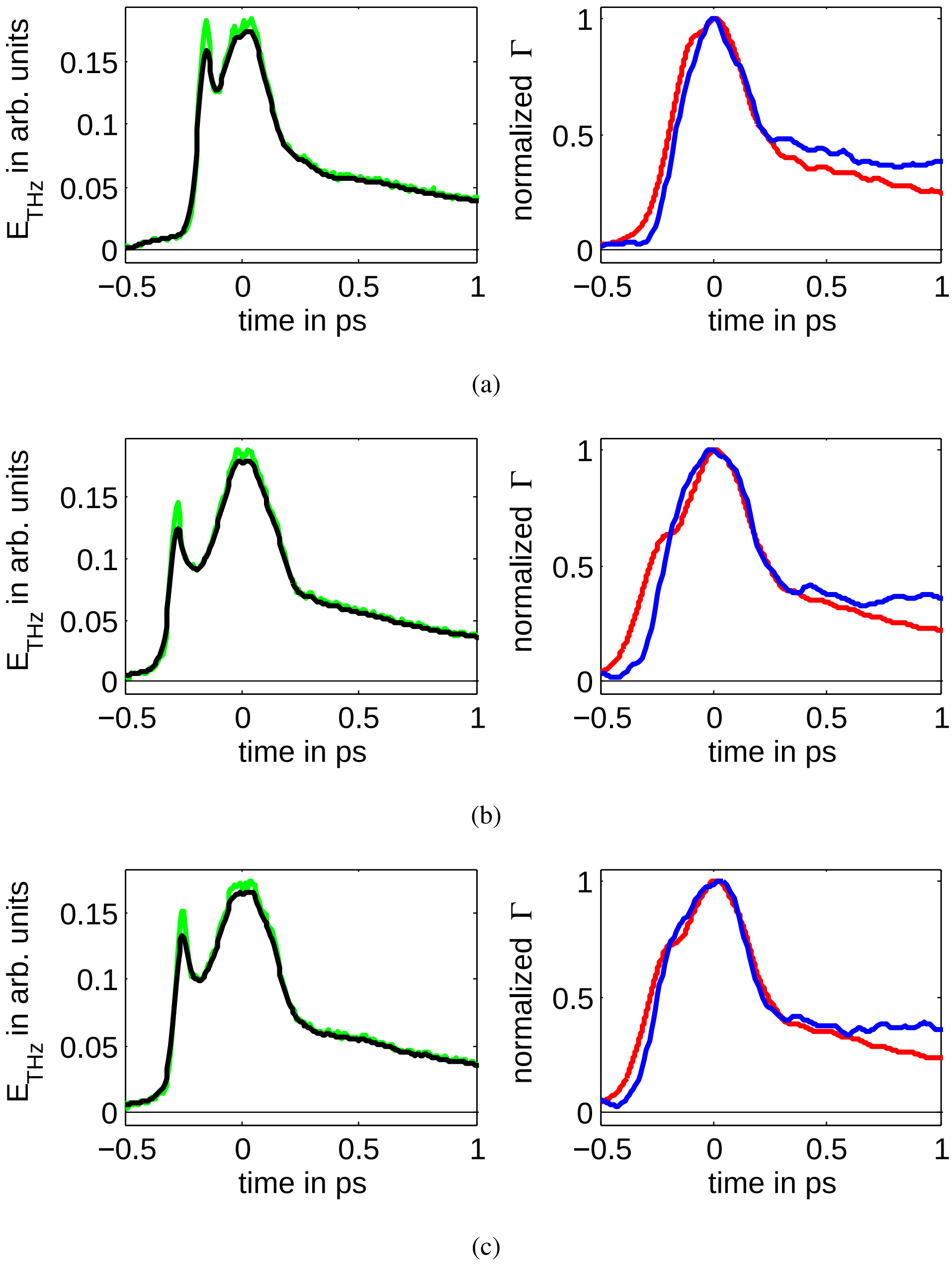

Figure 6.15.: TDS trace (green) of compressed bunches ($\phi_{\text{ACC1}} = 9.5°$) and the field amplitude (black) at the EO crystal (left) and the corresponding simulated (red) and measured (blue) phase retardation Γ (right). Measured at $\theta = 2°$ using a 175 µm GaP crystal and a bunch charge of $Q_0 = 0.8$ nC.

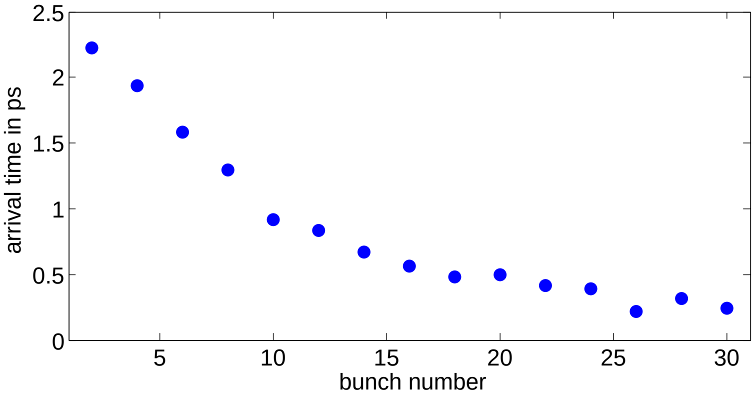

Figure 6.16.: Arrival time of the electron bunches within a bunch train. Measured with the beam phase monitor [Löh07]. Every second bunch is sampled in a 30 bunches long bunch train.

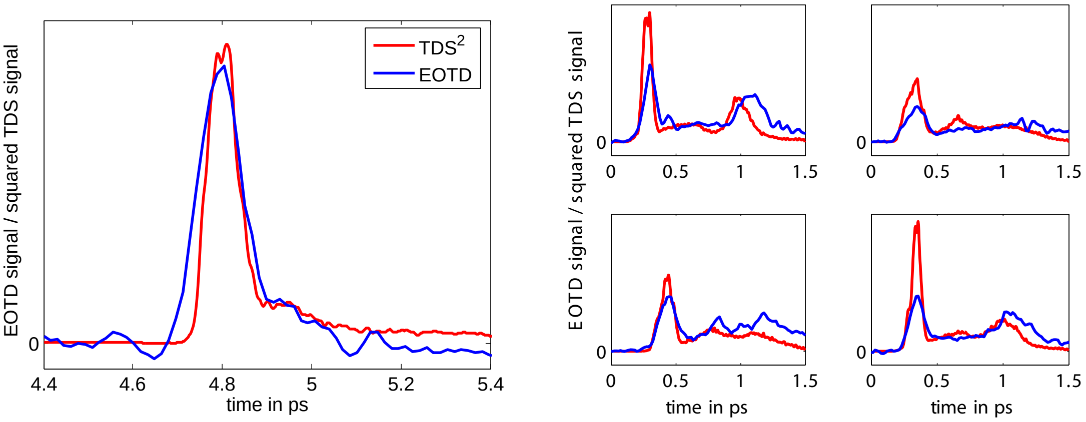

(a) Measured at optimum compression (ϕ_{ACC1} = 8°)

(b) Four consecutive bunches measured at overcompression (ϕ_{ACC1} = 11°)

Figure 6.17.: Comparison of the EOTD signal using a 100 µm thick GaP crystal and the bunch profile measured simultaneously with the transverse deflecting structure. The EO trace was measured at the first bunch of a bunch train, while the TDS trace was measured at the second bunch in the same bunch train.

10th bunch in the bunch train [Löh07]. The discrepancy between the TDS and EOTD data in figure 6.15 suggest that also the bunch shape can change significantly within the first bunches of a bunch train.

For series of simultaneous measurements with temporally resolved detection and with the TDS, the RF phase of the first accelerating module (ϕ_{ACC1}) was varied to produce very differently shaped electron bunches (cf. 6.4.1).

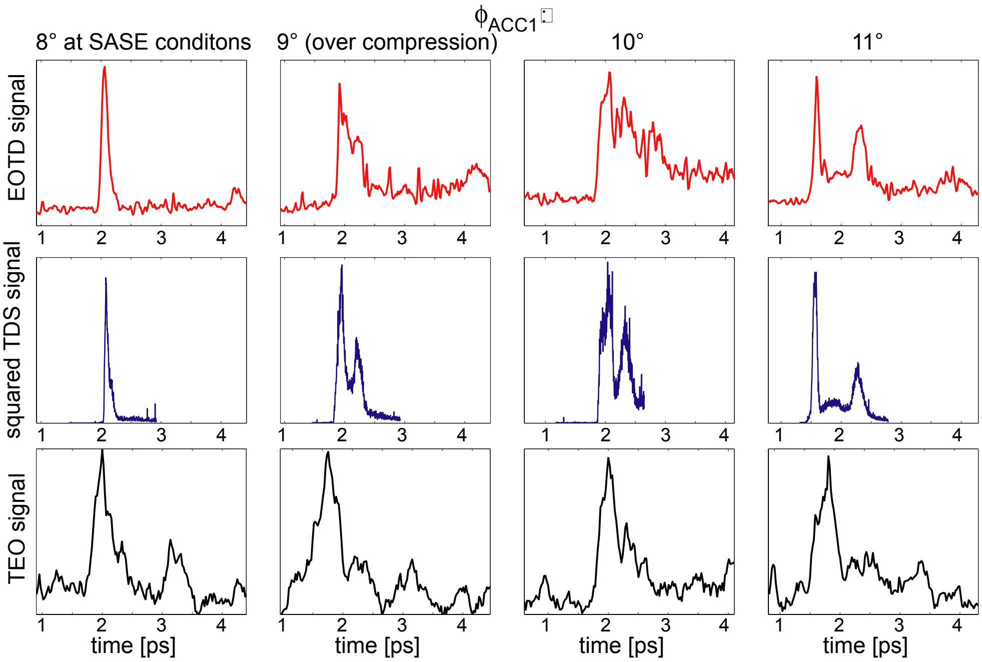

Figure 6.18.: Simultaneous measurements of the bunch profile with three different experiments for different settings of the RF phase of the first accelerating module. The upper row shows the signals measured with temporally resolved EO detection using a 100 µm thick GaP crystal. The middle row shows the squared signal of the transverse deflecting structure (TDS). The lower row shows the signal measured at the TEO experiment with spatially resolved EO detection using a 300 µm thick ZnTe crystal. The EO and TEO traces were measured at the first bunch of a bunch train, while the TDS trace was measured at the second bunch in the same bunch train.

In crossed polarizer geometry, the EO signal scales quadratically with the Coulomb field of the bunch while the TDS signal is linear in the field. For this reason the square of the TDS signal is plotted in the figure 6.17 and 6.18. The TDS and EOTD signals are in fair agreement except for a broadening and amplitude reduction of very short bunch structures. The width of the reconstructed Coulomb field pulses amounts to 100 fs (FWHM) for the TDS and to 170 fs for EOTD. Very short structures in the bunch profile lead to very high frequency components in the Coulomb field bunches which are suppressed due to the lattice resonance of the GaP crystal. This leads to a signal distortion and broadening. Note that the TDS measurement has been performed with the standard SASE beam optics in FLASH yielding a fairly large vertical beam size of 300 µm (rms) at the OTR screen. The time resolution of the TDS could be improved by tuning the accelerator optics for a minimum beam size at the OTR screen, however this would be incompatible with SASE operation of FLASH.

Apart from the EO experiment described here and the transverse deflecting structure (TDS), also the timing electro-optical experiment (TEO) can measure the longitudinal bunch shape with a sub-picosecond resolution (cf. 5.3). In parallel with the EOTD and TDS data shown in figure 6.18, also bunch profiles with spatially resolved detection at the TEO experiment were recorded. The TEO signal was measured at the same electron bunch as the EOTD signal. Some changes in the longitudinal beam profile are possible due to additional compression in the collimating chicane which is situated between the EO setup and the TEO experiment. The TEO signals are significantly broader. The temporal resolution is limited to about 400 fs (FWHM) due to the response function of the 300 μm thick ZnTe crystal. The low time resolution and the bad signal to noise ratio prohibits a reliable comparison of the bunch shapes, but a separation into two peaks is recognizable for larger ϕ_{ACC1}. Recently the ZnTe crystal at the TEO experiment has been replaced by a 175 μm thick GaP which improved the temporal resolution to 160 fs at a better signal to noise ratio (Fig. 5.21).

6.3.3. Time calibration for temporally resolved detection

For a precise time calibration of the temporally resolved detection (EOTD) setup the gate pulse was duplicated with a precisely adjustable time delay T as described in section 5.2.4.3. Each of the two gate pulses samples the stretched laser pulse. This leads to two peaks from the same electron bunch in the EOTD trace, which are separated in time. Varying the path length of the delay line by a known amount Δx leads to a precisely known change of the time delay between the two bunch signals by ΔT (Fig. 6.19). A slight misalignment of the mirrors of the delay line leads to a non-perfect overlap of the second laser pulse at the BBO crystal for small delays T. This has no influence on the accuracy of the calibration. The calibration constant was determined to be 15.93 ± 0.02 fs/pixel in good agreement with the value of 15 fs/pixel that was calculated from the crossing angle of the laser beams in the BBO crystal (cf. 5.2.4.3).

To improve the resolution of the optical setup imaging the SHG light from the BBO onto the camera a larger magnification was chosen for the later measurements (cf. 5.2.4.3) leading to a calibration constant for this magnification of 9.47 ± 0.11 fs/pixel, again in good agreement with the value of 9 fs/pixel that was calculated from the crossing angle.

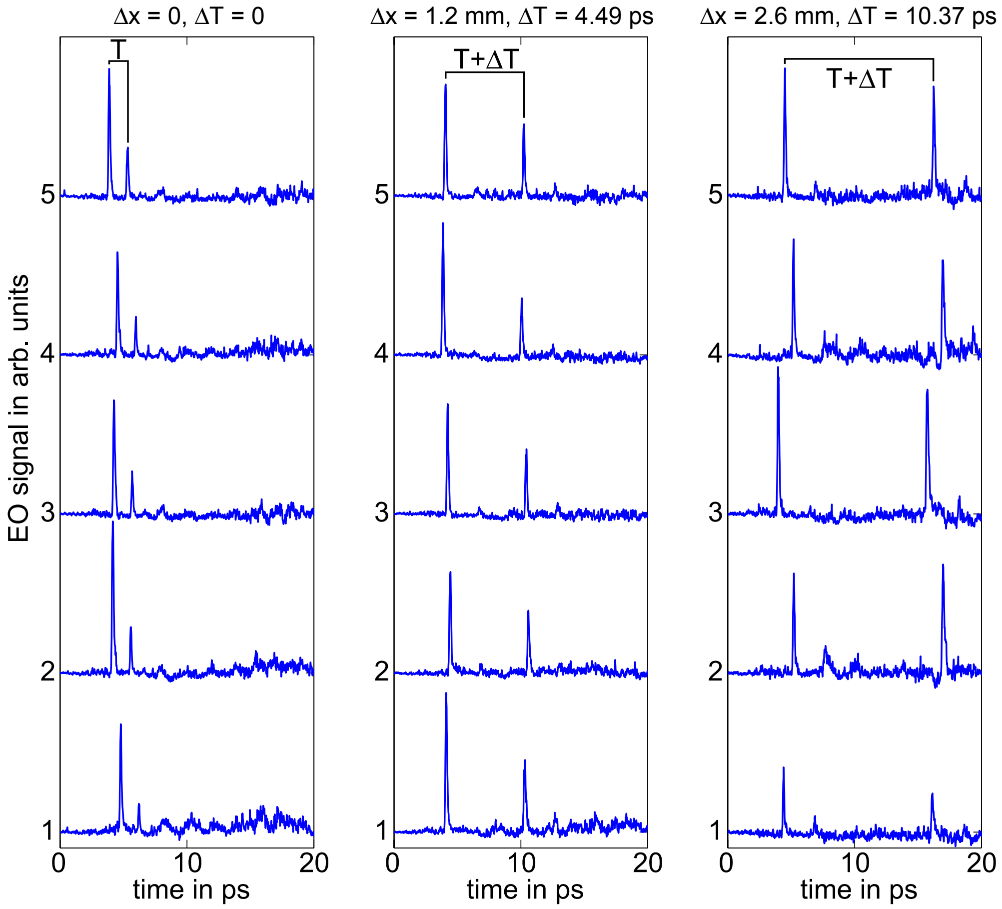

Figure 6.19.: Time calibration of the temporally resolved detection setup by duplicating the gate pulse. No background subtraction or normalization applied.

6.4. Applications

6.4.1. Bunch shape dependence on acceleration phase and bunch charge

Changing the RF phase in the first accelerating module (ϕ_{ACC1}) leads to a different compression of the electron bunch in the bunch compressors. At $\phi_{\mathrm{ACC1}} = 0$ the electron bunch is accelerated ”on crest”, leading to a maximum acceleration but no compression. For SASE-FEL operation of FLASH the first accelerating module is usually operated at $\phi_{\mathrm{ACC1}} = 8°$ leading to optimum compression (cf. 5.1.3).

For optimum compression ($\phi_{\mathrm{ACC1}} = 8°$) the signal shape is stable with some fluctuations in the arrival time (Fig. 6.20). The EO signal shows a main peak of 350 fs to 450 fs (FWHM) in width and a small additional peak 750 fs after the main peak, reaching 15% of its amplitude.

For bigger values of ϕ_{ACC1} a second peak splits off from the main peak at a distance of 300 to 650 fs. The temporal separation and the amplitude of the second peak increases with increasing RF phase. At $\phi_{\mathrm{ACC1}} = 12°$ the bunch has two peaks of approx. equal amplitude separated by about 650 fs (Fig. 6.21).

These data are in qualitative agreement with simulations of the compression process and with measurements using the transverse deflecting structure (TDS), where similar bunch shapes with double peaks were found at the same accelerator settings [HBS+05]. Simultaneous measurements of the bunch shape with EOTD are presented in section 6.3.2.1.

Figure 6.22 shows the EO signal and the calculated phase retardation for different bunch charges at $\phi_{\mathrm{ACC1}} = 10°$. The EO signal amplitude decreases with lower bunch charge. The area under the curves in figure 6.22(b) depends linear on the bunch charge (with a relative standard deviation of 5%) as expected from theory. Also the signal shape changes with different bunch charges. For the lowest charge (0.5 nC) the second peak is smaller compared to the first peak than for the bunches with higher charge. These changes in the signal shape for different bunch charges are probably caused by different longitudinal bunch profiles due to lower space charge effects in the injector area and in the bunch compressors at lower bunch charges.

6.4.2. Arrival time measurements

Apart from information on the bunch shape the single shot EO measurements can also deliver an arrival time of the electron bunch. The arrival time is derived from the position of the bunch signal in the EO trace. The fluctuations of the obtained arrival time are caused by three different sources: the arrival time fluctuations of the electron bunch

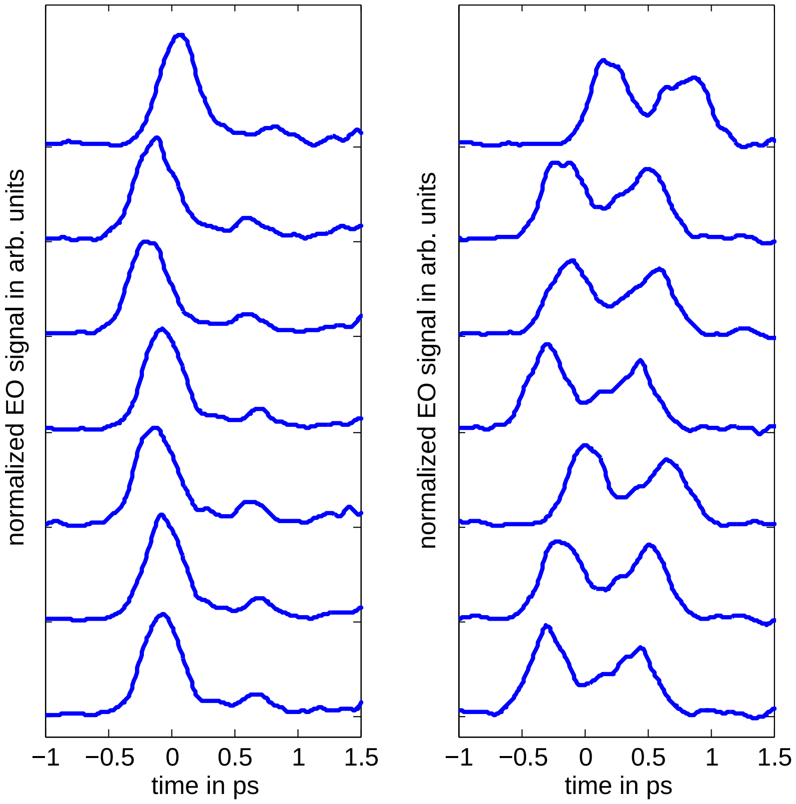

Figure 6.20.: Single shot EOSD measurements of 7 consecutive bunches at optimum compression (left, $\phi_{\mathrm{ACC1}} = 8°$) and at over-compression leading to double pulses (right, $\phi_{\mathrm{ACC1}} = 12°$). Measured with $\theta = 0$ using a 300 µm thick ZnTe crystal. The laser pulses were chirped to 2 ps (FWHM).

at the position of the EO crystal caused by fluctuations of the accelerator parameters, the time jitter of the laser pulse due to synchronization jitter between the Ti:Sa laser and the 1.3 GHz linac master oscillator, and the error of the arrival time detection in the EO signal.

The arrival time jitter of the electron bunches can be estimated from simulations and indirect measurements (Fig. 6.23) to approx. 150 fs (rms). The time jitter of the synchronization between the laser and the 1.3 GHz linac master oscillator of approx. 65 fs (rms) can be calculated from the phase noise measurement of phase detector error signal as described in section 5.2.2. The arrival time for compressed bunches is defined here as the time when the rising edge of the leading peak reaches half of the peak amplitude. It can be determined very accurately from a linear fit to the rising edge or from a Gaussian fit to the leading peak. For the Gaussian fit the slowly decaying tail of the bunch has to be excluded. The accuracy of both methods is estimated to be better than one tenth of the 10% to 90% rise time of the leading peak. The accuracy

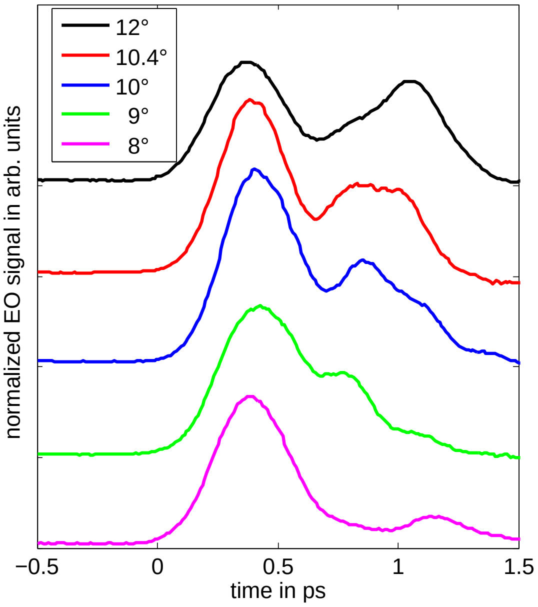

Figure 6.21.: EOSD signal for different settings of the RF phase ϕ_{ACC1} of the first accelerating module. Each line represents the average of 100 normalized and time-jitter corrected single shot traces. The data were taken at crossed polarization settings ($\theta = 0$) using a 300 µm thick ZnTe crystal at a bunch charge of 1 nC. The laser pulses were chirped to 2 ps (FWHM).

is hence about 25 fs for the spectrally resolved measurements. An experimental determination of the accuracy of the arrival time detection in the EO signal is not possible, since currently no other independent device exists at FLASH to measure the relative arrival time between the electron bunch and the EO laser pulses. The time jitter of the synchronization of approx. 65 fs (rms) and the arrival time jitter of the electron bunches of approx. 150 fs (rms) are by far bigger than the estimated accuracy of the arrival time detection in the EO signal.

Energy fluctuations of the bunches entering the first bunch compressor are a known source of arrival time jitter. Due to the energy dependence of the path length in the magnetic chicane (cf. 5.1.3), an energy jitter translates into a time jitter of the bunches after the bunch compressor. The energy fluctuations can be measured in the dispersive section of the bunch compressor, and the resulting time jitter can be calculated using the known longitudinal dispersion of the bunch compressor (Fig. 6.23). The energy jitter of 0.026% (rms) measured in the first bunch compressor results in a arrival time jitter of 155 fs (rms) and it is expected to be one of the major sources of time jitter. Other sources are the time jitter of the UV-laser pulses of the injector laser at the

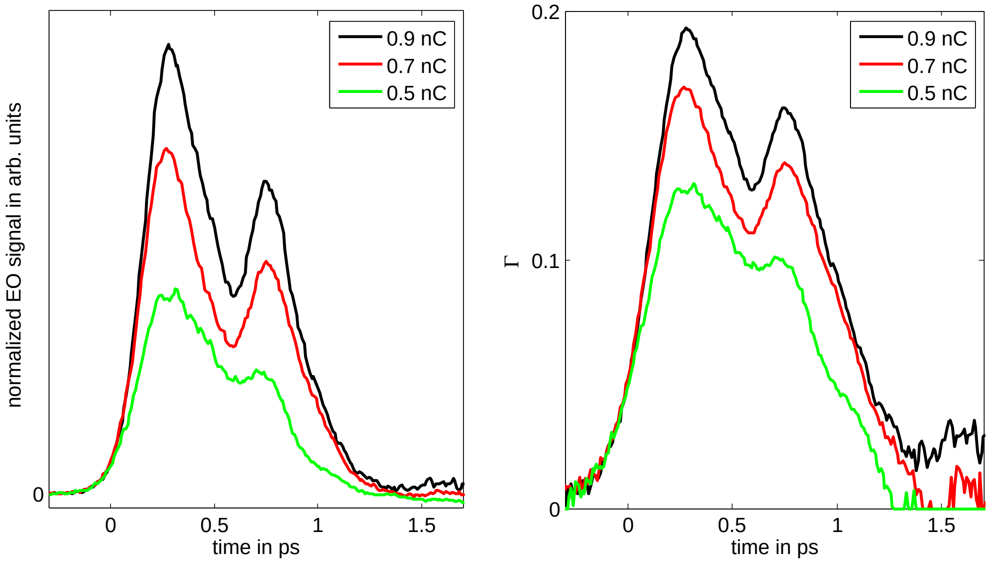

(a) EOSD signals as a function of bunch charge. Each line represents the average of 600 normalized and time-jitter corrected single shot traces. Measured at $\phi_{\mathrm{ACC1}} = 10°$ and $\theta = 0$ using a 300 µm thick ZnTe crystal. The laser pulses were chirped to 2 ps (FWHM).

(b) Phase retardation parameter calculated from the data shown in (a).

Figure 6.22.: EOSD signals as a function of bunch charge (a) and the calculated phase retardation (b).

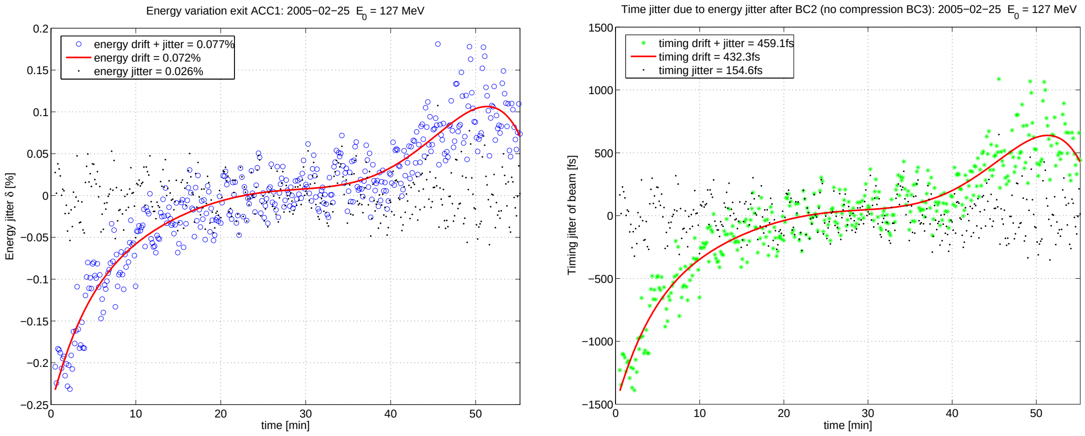

(a) Measured energy jitter

(b) Calculated time jitter

Figure 6.23.: Energy variation measured in the first bunch compressor and the time jitter calculated from the energy variation. From the FLASH electronic logbook [Sch05].

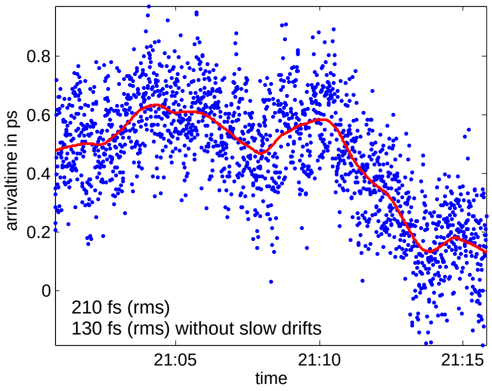

Figure 6.24.: Bunch arrival time at the EO crystal with respect to the 1.3 GHz reference frequency over a period of 15 minutes. The resulting rms time jitter is 130 fs without slow drifts (red line).

photocathode[1] and fluctuationes of the linac RF master oscillator.

6.4.2.1. Spectrally resolved detection

Bunch arrival times were recorded over periods between 15 minutes (Fig. 6.24) and 120 minutes (Fig. 6.25). Systematic drifts of several ps were observed, and in addition bunch-to-bunch time jitter in the order of 130 fs to 200 fs (rms), if slow drifts with time constants longer than approx. 30 seconds are removed. These numbers include the above mentioned 65 fs time jitter of the synchronization between the laser and the 1.3 GHz linac master oscillator.

Figure 6.25 shows the arrival time of the first bunch in the bunch train measured over two hours during normal accelerator operation. The FLASH accelerator is located inside the circular accelerator PETRA, which has a diameter of 730 m and serves as an injector for the electron-proton collider HERA. Between 18:50 and 19:00 the protons in the PETRA accelerator were accelerated and the dipole magnet current was increased. This causes changes of the external magnetic field of about 1 μT in the FLASH accelerator tunnel, due to time-dependent, uncompensated magnet currents of more than 800 A in the PETRA tunnel. Without activated orbit stabilization feedback, the resulting beam displacements of several hundred μm in the undulators were large enough to inhibit SASE amplification [KGHS06].The large fluctuations between 19:40 and 20:15 were caused by changes in the accelerator settings during machine tuning. They exceeded ±1.5 ps, leaving the time window, the spectrally resolved detection measurement can cover with laser pulsed chirped to approx. $T_c = 1$ ps.

The bunch arrival time depends linear on small changes of the RF phase ϕ_{ACC1}. For

---

[1] However, this time jitter is reduced by the bunch compression.

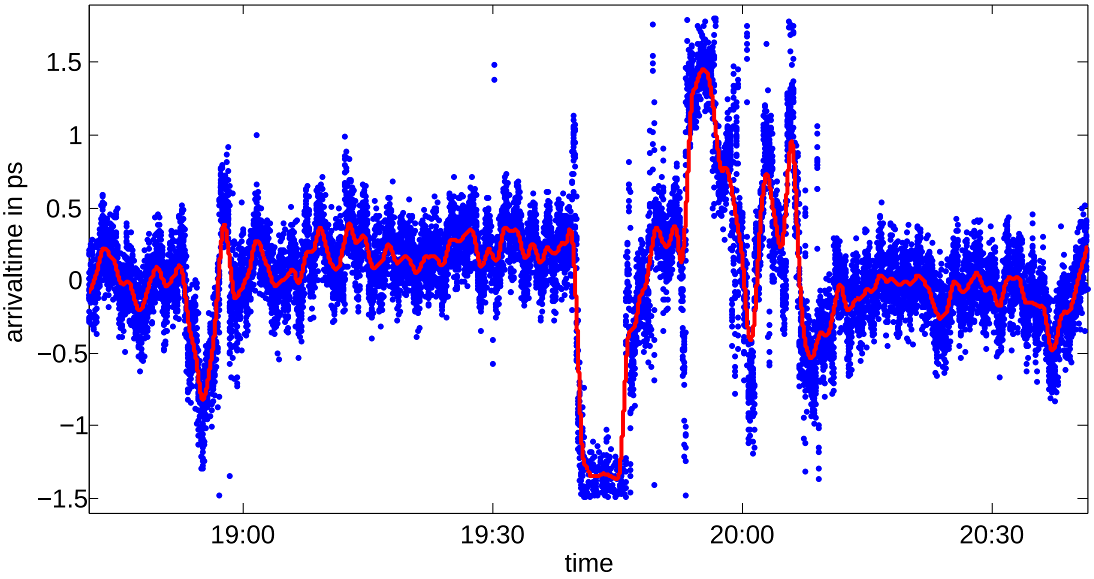

Figure 6.25.: Arrival time of the electron bunch at the EO experiment measured during SASE tuning. The red line shows the slow drift.

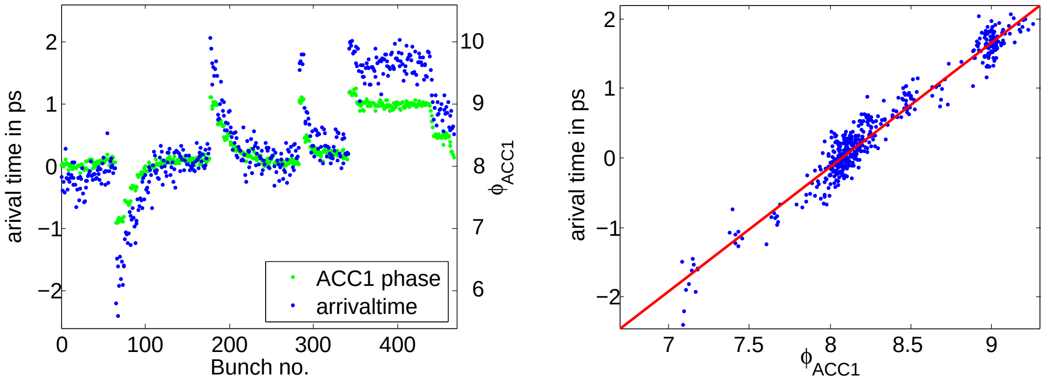

(a) Variation of ϕ_{ACC1} and the corresponding arrival time for a sequence of 450 bunches

(b) Arrival time to ϕ_{ACC1} correlation. The slope is 1.79 ps/degree.

Figure 6.26.: Arrival time dependence on the relative phase of the first accelerating module (ϕ_{ACC1})

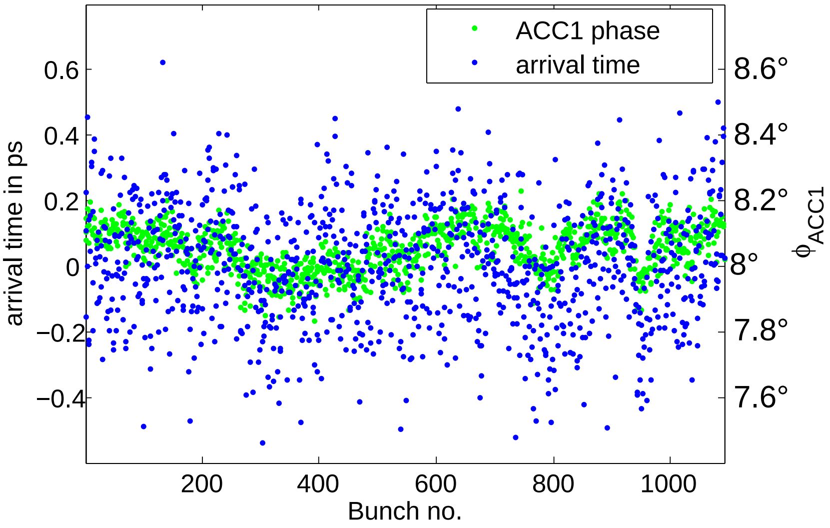

Figure 6.27.: Arrival time jitter and the jitter of ϕ_{ACC1}

a measurement of this dependence ϕ_{ACC1} was changed by ±1° around its value for optimum compression. A linear fit leads to a correlation constant of 1.79 ps arrival time change per degree change of ϕ_{ACC1} (Fig. 6.26).

An arrival time measurement without changes in ϕ_{ACC1} the arrival time jitter was $\sigma_1 = 182$ fs (rms, Fig. 6.27). The measured jitter of ϕ_{ACC1} during this time was 0.07° (rms, including the measurement error), which corresponds to an energy jitter of 0.017% and an arrival time jitter of $\sigma_2 = 127$ fs. Correcting the measured arrival time by the arrival time change calculated from the jitter of ϕ_{ACC1} leads to a reduced arrival time jitter of $\sigma_3 = 167$ fs. Assuming that the sources of the time jitter are uncorrelated, the different contributions to the measured time jitter σ_1 should add quadratically. It is possible to calculate the contribution of the jitter of ϕ_{ACC1} to the arrival time jitter of the electron bunch using the following relations:

$$\begin{aligned} \sigma_2^2 &= \sigma_{21}^2 + \sigma_{22}^2 \\ \sigma_1^2 &= \sigma_b^2 + \sigma_{21}^2 + \sigma_{\mathrm{EO}}^2 \\ \sigma_3^2 &= \sigma_b^2 + \sigma_{22}^2 + \sigma_{\mathrm{EO}}^2 \end{aligned} \tag{6.1}$$

where σ_{21} is the contribution of the ϕ_{ACC1} jitter to σ_2 and σ_{22} the contribution of the measurement error of ϕ_{ACC1}. σ_b summarizes the bunch arrival time jitter from all other accelerator parameters except ϕ_{ACC1}, and $\sigma_{\mathrm{EO}} \approx 65$ fs is the jitter of the EO laser synchronization. Solving equations 6.1 leads to:

$$\begin{aligned}
\sigma_{21}^2 &= \frac{1}{2}\left(\sigma_2^2 + \sigma_3^2 - \sigma_1^2\right)\\
\sigma_{22}^2 &= \frac{1}{2}\left(\sigma_2^2 + \sigma_1^2 - \sigma_3^2\right)\\
\sigma_{\mathrm{b}}^2 &= \sigma_1^2 - \sigma_{\mathrm{EO}}^2 - \sigma_{21}^2
\end{aligned}$$

From this equations one calculates an arrival time jitter of $\sigma_{21} = 103$ fs due to a ϕ_{ACC1} jitter of 0.058° and an arrival time jitter from other sources of $\sigma_{\mathrm{b}} = 135$ fs. The contribution of measurement error of ϕ_{ACC1} to σ_2 is $\sigma_{22} = 73$ fs and the corresponding measurement error is 0.041°.

6.4.2.2. Comparison with other methods

The pickup antenna which is used for the beam phase monitor (cf. 5.3.4) is mounted 50 cm downstream of the EO experiment. The two experiments are separated by a drift space without any magnets or other dispersive elements, which could introduce a time jitter. This offers the opportunity to compare the arrival time of the electron bunches measured with both setups and to distinguish between measurement uncertainties and real electron bunch arrival time jitter (Fig. 6.28).

It is justified to assume that the time jitter for the EO laser synchronization σ_{EO}, the BPhM laser synchronization σ_{PM} and the real arrival time of the electron bunch σ_{b} are uncorrelated. The square of the arrival time jitter σ_1 measured with spectrally resolved detection and σ_2 measured with the BPhM should be the sum of the squared laser synchronization time jitter and the squared arrival time jitter of the electron bunch:

$$\begin{aligned}
\sigma_1^2 &= \sigma_{\mathrm{EO}}^2 + \sigma_{\mathrm{b}}^2\\
\sigma_2^2 &= \sigma_{\mathrm{PM}}^2 + \sigma_{\mathrm{b}}^2
\end{aligned}$$

The square of the time jitter of the difference of the two measurements σ_3 is the sum of the squared laser synchronization time jitter of the two lasers:

$$\sigma_3^2 = \sigma_{\mathrm{EO}}^2 + \sigma_{\mathrm{PM}}^2$$

Therefore, all three time jitters can be calculated from the arrival time jitter measured with EOSD σ_1, the one measured with the BPhM σ_2 and the time jitter of the difference of the two measurements σ_3:

$$\begin{aligned}
\sigma_{\mathrm{EO}}^2 &= \frac{1}{2}\left(\sigma_1^2 + \sigma_3^2 - \sigma_2^2\right)\\
\sigma_{\mathrm{PM}}^2 &= \frac{1}{2}\left(\sigma_2^2 + \sigma_3^2 - \sigma_1^2\right)\\
\sigma_{\mathrm{b}}^2 &= \frac{1}{2}\left(\sigma_1^2 + \sigma_2^2 - \sigma_3^2\right)
\end{aligned}$$

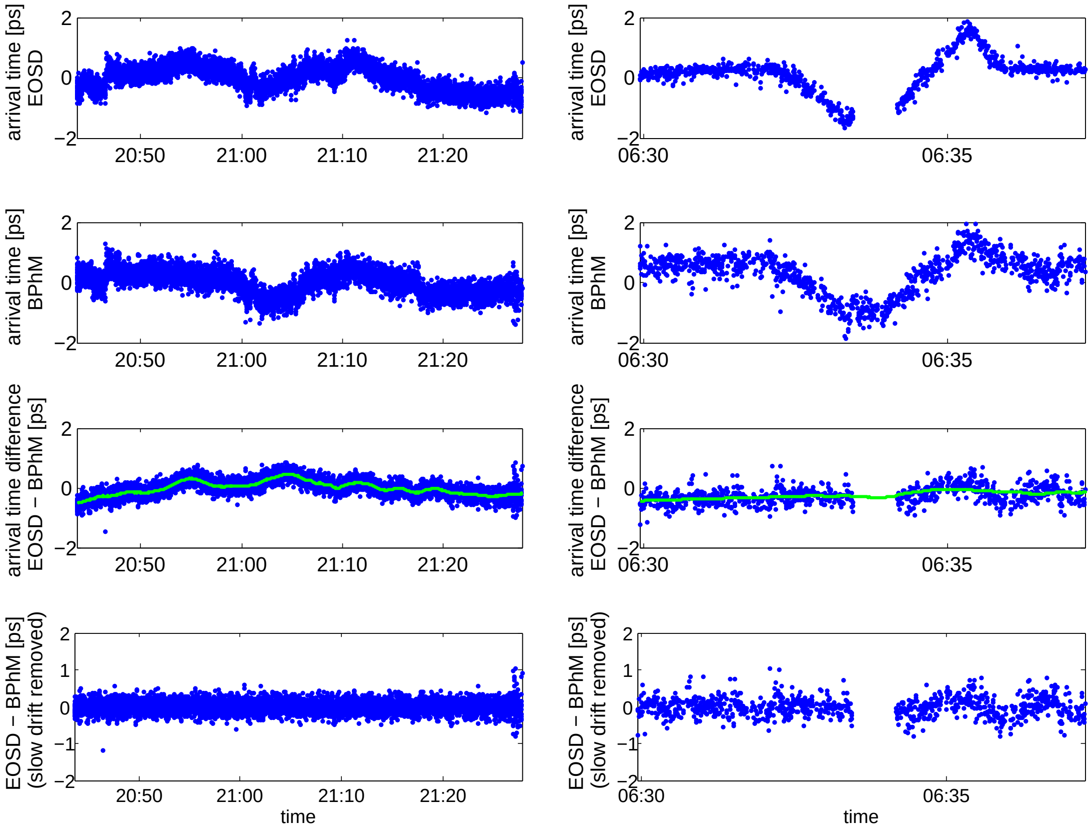

(a) Arrival time measured during undisturbed accelerator operation

(b) Increased arrival time change induced varying the ACC1 phase ϕ_{ACC1}.

Figure 6.28.: Arrival time measured with spectrally resolved detection using a 175 µm thick GaP crystal (top) and with the beam phase monitor (second row from the top). The difference between the arrival time measured with the two methods is shown in the third row including slow drifts (green line) and in the bottom row excluding the slow drifts.

Two data series of approx. 50 minutes (≈ 15000 bunches) each were measured in parallel with spectrally resolved detection and the beam phase monitor. One of these series is shown in figure 6.28(a). The results are summarized in table 6.1. For both experiments slow drifts with a time constant of more than 1 min. have been removed. To cross check the time calibration of the two experiments, an arrival time change of about ±2 ps has been induced by varying the ACC1 phase ϕ_{ACC1} (Fig, 6.28(b)). The resulting time jitter is 150 to 200 fs for the beam phase monitor and 60 to 80 fs (rms) for the spectrally resolved detection, which is in good agreement with the values measured for the EOSD laser synchronization of 65 fs and the expected resolution of

Table 6.1.: Rms arrival time jitter measured with EO spectrally resolved detection or the beam phase monitor and the calculated laser synchronization jitter and electron bunch arrival time jitter.

	Aug. 27 / 2006	Sept. 18 / 2006	expected from other measurements
σ_1	196 fs	201 fs	
σ_2	270 fs	242 fs	
σ_3	218 fs	159 fs	
σ_{EO}	81 fs	60 fs	65 fs
σ_{PM}	202 fs	147 fs	
σ_{b}	179 fs	192 fs	≈ 150 fs

the detection method of approx. 25 fs. The synchronization of the fiber laser for the BPhM is currently being revised to improve its performance [Löh06]. The jitter of the electron bunch arrival time is 180 fs and 190 fs (rms) for the two measurements series.

6.4.2.3. Temporally resolved detection

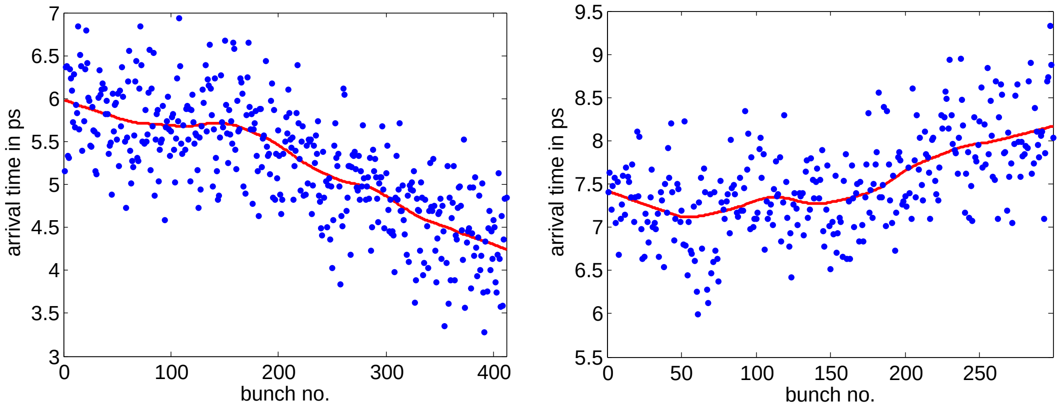

(a) (b)

Figure 6.29.: Arrival time of the electron bunch at the experiment measured with temporally resolved detection. The measured rms time jitter is 460 fs (a) and 450 fs (b) without slow drifts limited by the jitter of the amplified laser system. Including slow drifts the rms time jitter is 700 fs (a) and 565 fs (b).

The synchronization accuracy of the amplified laser system used for temporally resolved detection is worse than the one of the oscillator used for spectrally resolved

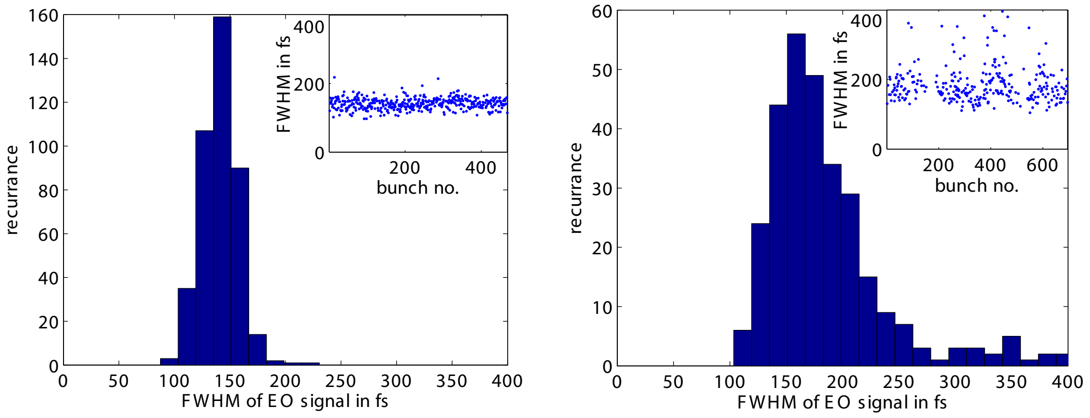

(a)

(b)

Figure 6.30.: EOTD signal width measured at crossed polarization. (a): Measured bunch length when the compression feedback for the RF phase of the first accelerating module was running. (b) Measured bunch length 10 min after the feedback had been switched off.

detection, mainly due to mechanical resonances between several Hz and several kHz, which can be exited by acoustic noise. Efforts have been taken to improve the mechanical stability of the laser housing and the optics, but the time jitter of the laser could not suppressed to below ≈ 450 fs (rms). This limits the usefulness of arrival time measurements with temporally resolved detection using the current laser amplifier as the time jitter of the laser system is bigger than the fast time jitter of the accelerator for standard operation (Fig. 6.29).

6.4.3. Performance of the bunch compression feedback

At the FLASH accelerator a feedback system is used to stabilize the bunch compression. The intensity of coherent diffraction radiation (CDR), which depends critically on the bunch shape, is measured after the first bunch compressor. The signal is used to control the RF phase ϕ_{ACC1} of the first accelerating module keeping the CDR signal constant. For a series of EOTD measurements the compression feedback was switched off leading to increased fluctuations in the electron bunch shape. After the feedback was switched off for several minutes the FWHM of the EO signal increased from 158 ± 15 fs (FWHM) to 181 ± 34 fs (Fig. 6.30). These data were taken at crossed polarisation. The temporal width of the phase retardation is a factor of $\sqrt{2}$ wider.

Setting the RF phase of the first accelerating module slightly (approx. 0.2°) beyond maximum compression leads to only a slight over compression but to strongly fluctuating bunch shapes (Fig. 6.31). The EO signals show either a single peak or two peaks

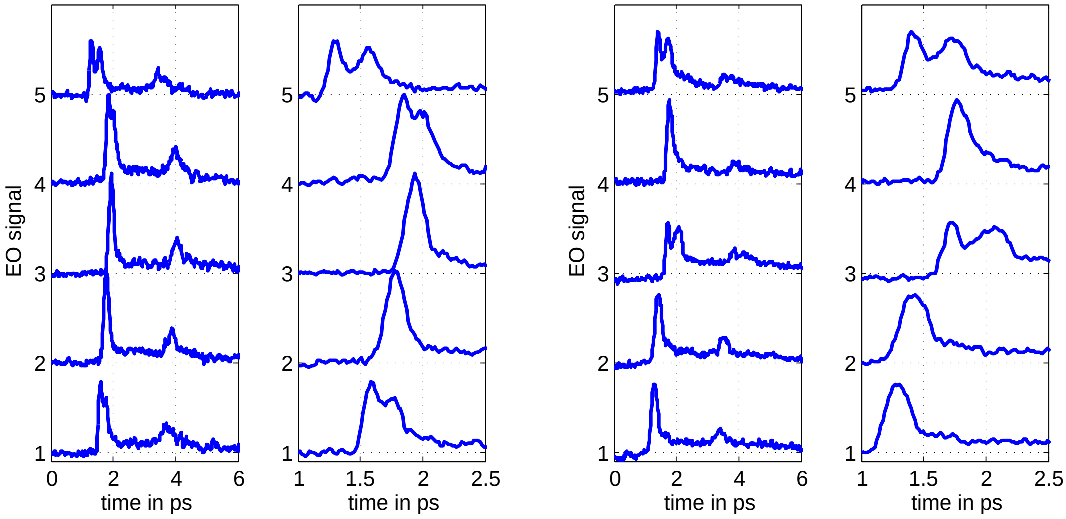

(a) $\theta = 0$

(b) $\theta = 1°$

Figure 6.31.: EOTD traces of slightly overcompressed bunches without compression feedback at $\theta = 0$ (a) and $\theta = 1°$ (b). The right figures show the leading peak on an enlarged time scale. Measured using a 100 µm thick GaP crystal.

separated by up to 500 fs. The smallest distance of two peaks which could still be clearly discriminated was 130 fs.

6.4.4. Dependence of the EO signal on the electron beam orbit

The amplitude and direction of the electric field $\boldsymbol{E}_{\mathrm{THz}}$ at the EO crystal depend on the horizontal and vertical distance Δx and Δy between the electron beam orbit and the laser spot on the EO crystal. The distance r between the electron beam and the laser spot is

$$r = \sqrt{\Delta x^2 + \Delta y^2} \tag{6.2}$$

leading to a field amplitude

$$E_{\mathrm{THz}}(r) \propto \frac{1}{r} = \frac{1}{\sqrt{\Delta x^2 + \Delta y^2}} \tag{6.3}$$

The angle α between the (horizontal) [-1,1,0]-axis of the EO crystal and the electric field vector is

$$\alpha = \arccos\left(\frac{\Delta x}{\sqrt{\Delta x^2 + \Delta y^2}}\right) \tag{6.4}$$

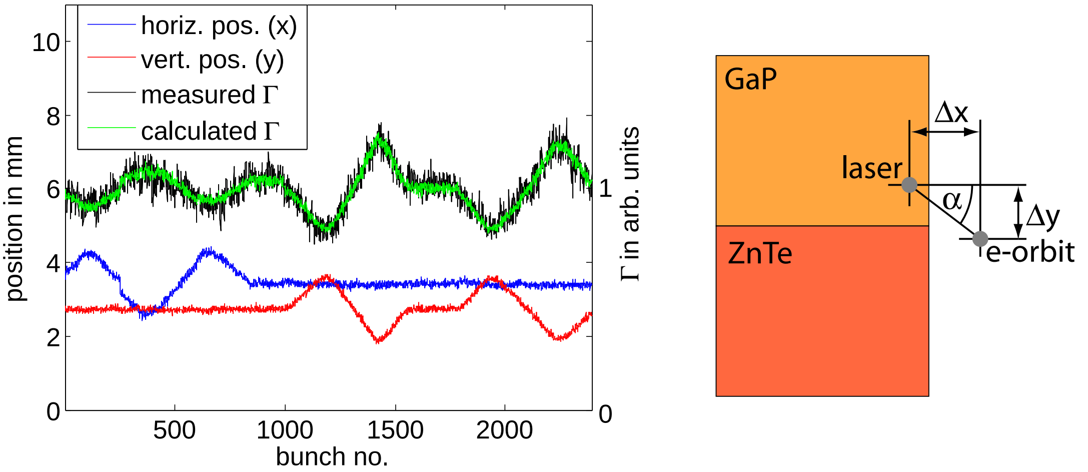

(a) Orbit dependence of the phase retardation. The noise of the phase retardation signal Γ is caused by bunch charge fluctuations.

(b) The geometric set up of the EO crystals inside the beampipe.

Figure 6.32.: Orbit dependence of the phase retardation measured with spectrally resolved detection and the geometric set up inside the beampipe.

Together with equation (2.74) this leads to an orbit dependence of the phase retardation of:

$$\Gamma(\Delta x, \Delta y) \propto \frac{1}{\sqrt{\Delta x^2 + \Delta y^2}} \sqrt{1 + 3\frac{\Delta x^2}{\Delta x^2 + \Delta y^2}} \tag{6.5}$$

Figure 6.32(a) shows the phase retardation parameter measured with spectrally resolved detection, while the electron beam was steered horizontally and vertically by ±1 mm. The beam position was measured by a beam position monitor mounted 0.5 m downstream of the EO setup. The bunch charge was 1 ± 0.03 nC. The phase retardation calculated from the measured orbit and bunch charge agrees well with the measured phase retardation. The EO signals can be corrected for orbit fluctuations using equation (6.5). However, this has not been done for the data presented in this thesis, since the orbit fluctuations are usually small during a series of measurements.

Since the crystal holder can only be moved horizontally, a vertical offset can only be compensated steering the electron beam, which is not always possible during standard accelerator operation. For a large vertical offset as shown in figure 6.32(a) the resulting phase retardation and thus the EO signal is 50% smaller than the phase retardation at zero vertical offset.

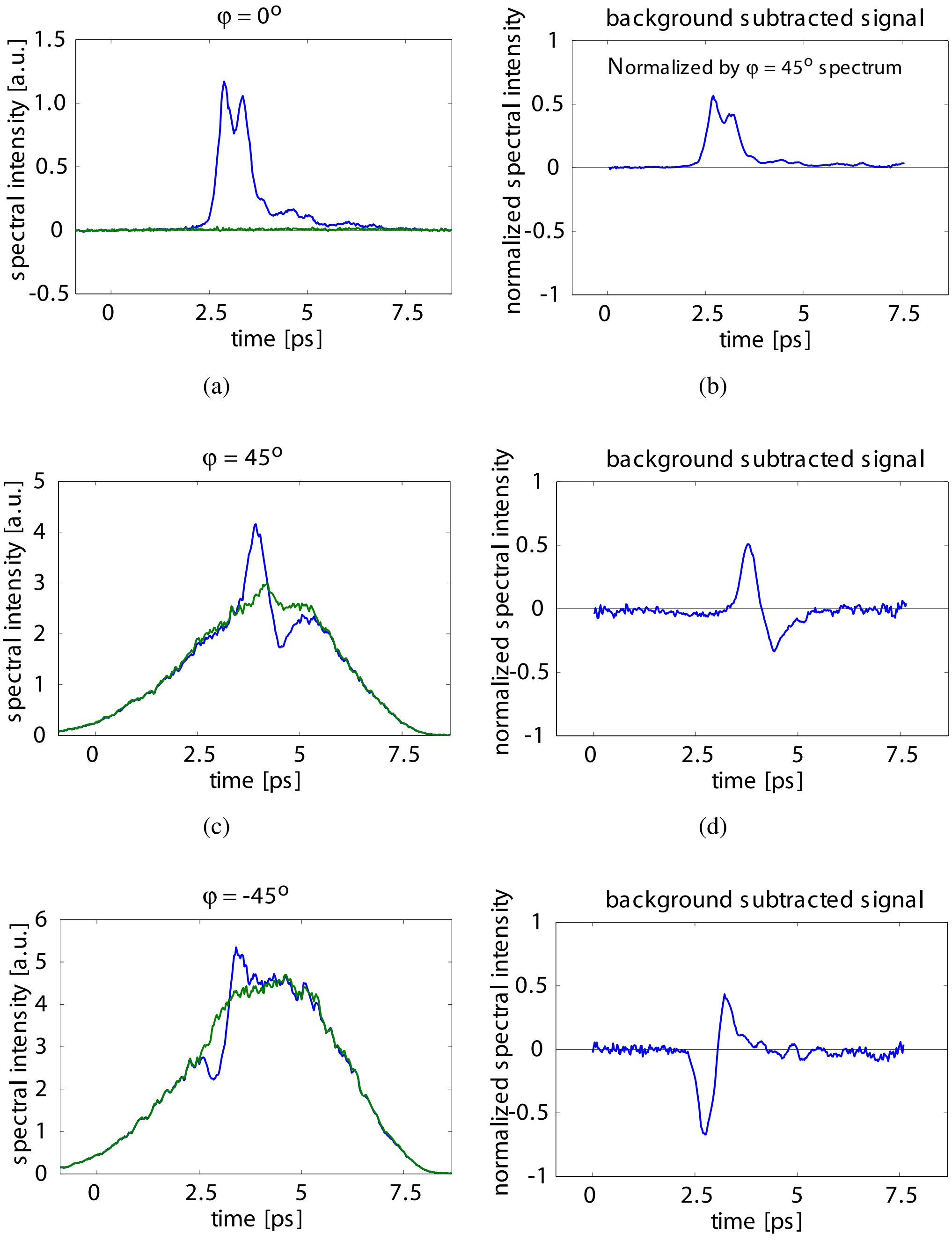

(a) (b) (c) (d) (e) (f)

Figure 6.33.: Single-shot signals obtained at the THz beam line by electro-optic spectral decoding with three different orientation angles of the quarter wave plate. Measured with a 500 μm thick ZnTe crystal. (a),(c),(e): Raw data. Green traces are without CTR radiation, blue traces are with CTR radiation. (b),(d),(f): EO signals after background subtraction and normalization. The leading edge of the CTR pulse is on the left.

6.4.5. Spectrally resolved detection of coherent transition radiation

In a first proof of principle experiment the time structure of CTR pulses at the CTR beam line (cf. 5.3.2) was measured with the spectrally resolved EO technique. For these measurements laser pulses of 30 nm bandwidth chirped to $T_c = 4$ ps from the Ti:Sa amplifier were used and attenuated to a pulse energy of about 1 μJ. A 500 μm thick ZnTe crystal was used. The path length of the CTR radiation trough air was about 1 m from the low-density polyethylene (LDPE) window to the EO crystal.

The EO signals measured with the quarter wave plate rotated by plus or minus 45° show a bipolar structure with a leading peak of 400 fs (FWHM) followed by a broader peak of opposite sign and smaller in amplitude and some small oscillations (Fig. 6.33(d) and (f)). The separation of the two peaks is 490 fs. The signal measured at crossed polarization consists of two peaks separated by 490 fs followed by small oscillations. The width of the double peak is about 800 fs.

The measured pulse width is close to the resolution limit of the EO crystal (about 350 fs for a 500 μm thick ZnTe crystal) and for the used laser parameters significant distortions have to be expected due to frequency mixing according to equation (4.37). It could be proven that the CTR beam line is capable of transporting sub-picosecond THz pulses. However, to determine an accurate time profile of the transported CTR pulse temporally resolved EO measurements using a thin GaP crystal are needed. To avoid absorption of the CTR in humid air and the vacuum window, future measurements will be done in vacuum.

7. Conclusions

An experiment for bunch length measurements using spectrally and temporally resolved electro-optic detection has been carried out at the FLASH accelerator. With temporally resolved detection electro-optic signals as short as 54 fs (rms) can be obtained in a crossed polarizer detection scheme. These are the shortest electro-optic signals measured so far for electron bunch diagnostics. In a detection scheme measuring near crossed polarization, where the electro-optic signal is proportional to the electric field of the electron bunch, the shortest obtained signal width is about 70 fs (rms). The time resolution of these signals is mainly limited by lattice resonances of the electro-optic crystal (gallium phosphide, GaP). The electro-optic signals are compared to electron bunch shapes that are measured simultaneously with a transverse deflecting structure. Numerical simulations using the bunch shapes as determined with the transverse deflecting structure as input data are in excellent agreement with the electro-optic signals measured with GaP, both for temporally and spectrally resolved measurements. In the case of zinc telluride (ZnTe) the observed signals are slightly broader and significantly smaller than expected from simulations. These discrepancies are probably due to the poor optical quality of the available ZnTe crystals or the poor quality the published material properties of ZnTe.

The EO signals obtained with spectrally resolved detection show a lower time resolution than the temporally resolved measurements. The shortest measured signals were about 125 fs (rms), limited by the available spectral bandwidth of the laser pulses. Spectrally resolved EO detection is a capable tool for electron bunch arrival time measurements with a time resolution of about 25 fs. However, the time jitter of 65 fs of the synchronization of the laser to the RF master oscillator of the accelerator has to be improved to benefit from the high time resolution.

8. Future perspectives

The current setup will be redesigned to provide an automated online diagnostic for electron arrival time and bunch shape based on spectrally resolved detection. The proposed optical synchronization system for FLASH [WLL$^+$06] offers the possibility to significantly improve the synchronization of the laser to the master oscillator in order to benefit from the high time resolution of arrival time measurements.

The time resolution of the temporally resolved measurements has almost reached the limits given by the material properties of GaP. For further improvements new electro-optic materials are needed with an electro-optic response function extending to frequencies higher than 8 THz.

A. Abbreviations and mathematical symbols

Table A.1.: Abbreviations used in the text

Abbreviation	Definition
ACC1-5	first to fifth accelerating module of the FLASH accelerator
BBO	β-barium borate
BC	bunch compressor
CDR	coherent diffraction radiation
CSR	coherent synchrotron radiation
CTR	coherent transition radiation
DESY	Deutsches Elektronen-Synchrotron
EO	electro-optic
EOS	electro-optic sampling using a variable delay
EOSD	spectrally resolved electro-optic detection
EOTD	temporally resolved electro-optic detection
FEL	free electron laser
FELIX	Free Electron Laser for Infrared eXperiments at the FOM Institute for Plasma Physics 'Rijnhuizen'
FLASH	free electron laser at Hamburg
FOM	Stichting voor Fundamental Onderzoek der Materie, foundation for fundamental research on matter, The Netherlands
FWHM	full width at half maximum
GaP	gallium phosphide
HOM	higher-order mode
ITO	indium-tin oxide
LDPE	low-density polyethylene
OTR	optical transition radiation

Table A.2.: Abbreviations used in the text (cont.)

Abbreviation	Definition
PETRA	Positron-Elektron-Tandem-Ring-Anlage
RF	radio frequency
SASE	self amplified spontaneous emission
SHG	second-harmonic generation
TDS	transverse deflecting RF structure for long. bunch profile measurements
TEO	timing electro-optic experiment (spatially resolved EO detection for bunch arrival time measurements)
TESLA	teraelectronvolt energy superconducting linear accelerator
Ti:Sa	Titanium-sapphire (laser)
TO	transverse optical (lattice oscillation)
TOPS	Terahertz to Optical Pulse Source at the University of Strathclyde
VUV	Vacuum Ultra Violet light
ZnTe	zinc telluride

Table A.3.: A selection of mathematical symbols

Symbol	Definition
α	angle between the electric field vector $\boldsymbol{E}_{\mathrm{THz}}$ and the [-110]-axis of the EO crystal
$\Delta\omega$	FWHM of the spectral intensity profile $S(\omega)$ of a laser pulse
E_{THz}	Electric field of the THz pulse at the EO crystal
Γ	phase retardation parameter
Γ_{ideal}	phase retardation parameter as expected from an ideal EO material with frequency independent response function
Γ_{TD}, Γ_{SD}	phase retardation parameter as retrieved from the EOTD resp. EOSD signal
$G(f,d)$	response function of an EO crystal
$G(f,d) \cdot r_{41}(f)$	effective response function
$n(f)$, $\kappa(f)$	real and imaginary part of the refractive index
ϕ, θ	angle of the quarter resp. half wave plate with respect to the crossed polarisation setting
ϕ_{ACC1}	RF phase of the first accelerating module
$\psi(\alpha)$	angle between the first principal axis of the refractive index ellipsoid and the [-110]-axis of the EO crystal
Q_0	total bunch change of the electron bunch
r_{41}	electro-optic coefficient
σ	standard deviation
σ_{EO}	rms time jitter of the EO laser to RF synchronization
σ_τ, σ_ω	standard deviation of the electric field distribution of a Gaussian laser pulse in time and frequency domain
σ_{t}	rms width of a Gaussian electron bunch
T_0, T_c	FWHM of the intensity profile $I(t)$ of the compressed and the chirped laser pulse

B. Electro-optical sampling using a variable delay

In conventional THz spectroscopy electro-optical detection is applied in the sampling technique. The first electro-optical sampling data taken at the FLASH linac using a 300 μm thick ZnTe crystal show pulses with a spiky substructure and a width of the envelope of about 1 ps (FWHM) (Fig. B.1(a)). The expected bunch length of less than 250 fs (FWHM) cannot be faithfully reproduced due to jitter in the bunch arrival time at the EO crystal (approx. 150 fs (rms), cf. 6.4.2). One major source of this jitter are energy fluctuations of ≈ 0.03%, which translate into timing fluctuations of ≈ 150 fs (rms) in the magnetic chicane of the first bunch compressor (Fig. 6.23). The overall width of the EOS signal is therefore dominated by the time jitter between the arrival time of the electron bunch and the laser pulse at the EO crystal.

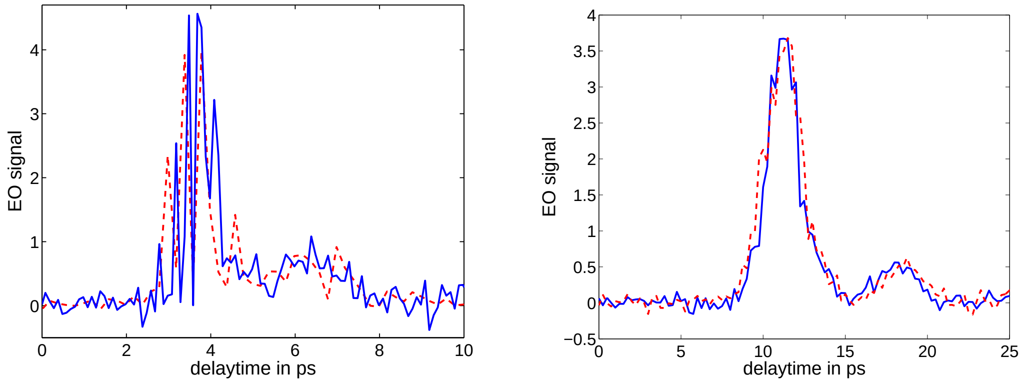

(a) Two EO sampling measurements of bunches with a charge of 1.2 nC. The second measured (dashed) was recorded two minutes after the first one (solid). The pulse length of the laser was <100 fs (FWHM). The delay was changed in steps of 100 fs for the first and 200 fs for the second measurement.

(b) Two EO sampling measurements of bunches with a charge of 0.9 nC. The pulse length of the laser was ≈2 ps. The delay was changed in 250 fs steps.

Figure B.1.: Electro-optic sampling measurements of short electron bunches using a 300 μm thick ZnTe crystal.

Smoother signals are obtained, when the laser pulses after stretched to 2 ps (FWHM, Fig. B.1(b)), but the shape of the signal is now dominated by the laser pulse shape and the arrival time jitter of the electron bunch.

Bibliography

[ADS$^+$06] A. Azima, S. Düsterer, H. Schlarb, J. Feldhaus, A. Cavalieri, D. Fritz, and K. Sengstock. Jitter measurements by spatial electro-optical sampling at the FLASH free electron laser. In *Proceedings of the EPAC 2006*, Edinburgh, Scotland, 2006.

[ALL64] O. H. Altenmueller, R. R. Larson, and G. A. Loew. Investigations of traveling-wave seperators for the stanford two-mile linear accelerator. *Rev. Sci. Instrum.*, 35:438, 1964.

[AS83] D. E. Aspnes and A. A. Studna. Dielectric functions and optical parameters of Si, Ge, GaP, GaAs, GaSb, InP, InAs, and InSb from 1.5 to 6.0 eV. *Phys. Rev. B*, 27:985, 1983.

[Aun00] B. Aune et al. Superconducting TESLA cavities. *Phys. Rev. ST Accel. Beams*, 3(9):092001, Sep 2000.

[Ayv06] V. Ayvazyan et al. First operation of a free-electron laser generating GW power radiation at 32 nm wavelength. *Euro. Phys. J. D*, 37:297–303, 2006.

[Bar64] A. S. Barker Jr. Transverse and longitudinal optic mode study in MgF_2 and ZnF_2. *Phys. Rev.*, 136:A1290, 1964.

[BD00] W. D. Bare and J. N. Demas. Monochromator wavelength calibration standards extending into the near-infrared using second- and third-order emission lines from mercury vapor lamps. *J. Fluorescence*, 10(4):317–324, 2000.

[BGG$^+$03] M. Brunken, H. Genza, P. Göttlicher, C. Hessler, M. Hüning, H. Loos, A. Richter, H. Schlarb, P. Schmüser, S. Simrock, D. Suetterlin, M. Tonutti, and D. Türke. Electro-optic sampling at the TESLA test accelerator: experimental setup and first results. Internal report, DESY, 2003. TESLA Report 2003-11.

[BJM+04] G. Berden, S. P. Jamison, A. M. McLeod, W. A. Gillespie, B. Redlich, and A. F. G. van der Meer. Electro-optic technique with improved time resolution for real-time, nondestructive, single-shot measurements of femtosecond electron bunch profiles. *Phys. Rev. Lett.*, 93:114802, 2004.

[BJS63] D. Berlincourt, H. Jaffe, and L. R. Shiozawa. Electroelastic properties of the sulfides, selenides, and tellurides of zinc and cadmium. *Phys. Rev.*, 129:1009, 1963.

[Bor00] M. Borland. Elegant: A flexible sdds-compliant code for accelerator simulation. Internal Report LS-287, Argonne National Lab., 2000.

[Cav05] A. L. Cavalieri et al. Clocking femtosecond x rays. *Physical Review Letters*, 94(11):114801, 2005.

[CSS+05a] S. Casalbuoni, H. Schlarb, B. Schmidt, B. Steffen, P. Schmüser, and A. Winter. Numerical studies on the electro-optic sampling of relativistic electron bunches. Internal report, DESY, Hamburg, Germany, 2005. TESLA Report 2005-01.

[CSS+05b] S. Casalbuoni, H. Schlarb, B. Schmidt, B. Steffen, P. Schmüser, and A. Winter. Numerical studies on the electro-optic sampling of ultrashort electron bunches. In *Proceedings of the PAC 2005*, Knoxville, Tenessee, USA, 2005.

[CSS05c] S. Casalbuoni, B. Schmidt, and P. Schmüser. Far-infrared transition and diffraction radiation, part I: Production, diffraction effects and optical propagation. Internal report, DESY, Hamburg, Germany, 2005. TESLA Report 2005-15.

[CSSS06] S. Casalbuoni, B. Schmidt, P. Schmüser, and B. Steffen. Far-infrared transition and diffraction radiation, part II: The THz beamline at the VUV-FEL linac. Internal report, DESY, Hamburg, Germany, 2006. TESLA Report 2006-04.

[DES07] DESY. `http://zms.desy.de/e548/e550/e6027/e209/index_eng`, 2007.

[DFK+04] M. Dohlus, K. Flöttmann, O. S. Kozlov, T. Limberg, Ph. Piot, E. L. Saldin, E. A. Schneidmiller, and M. V. Yurkov. Start-to-end simulations of SASE FEL at the TESLA test facility, phase 1. *Nucl. Instr. and Meth. A*, 530:217–233, 2004.

[DGR$^+$05] H. Delsim-Hashemi, O. Grimm, J. Rossbach, H. Schlarb, B. Schmidt, and P. Schmüser anf A. F. G. van der Meer. Broadband single shot spectrometer. In *Proceedings of the FEL 2005*, Stanford, California, USA, 2005.

[DGSS06] H. Delsim-Hashemi, O. Grimm, P. Schmüser, and B. Schmidt. Single-shot longitudinal diagnostic with THz radiation. In *Proceedings of the 37th ICFA Advanced Beam Dynamics Workshop on Future Light Sources*, Hamburg, Germany, 2006.

[DGvdM$^+$06] H. Delsim-Hashemi, O. Grimm, A. F. G. van der Meer, J. Rossbach, H. Schlarb, B. Schmidt, and P. Schmüser. Bunch compression monitor. In *Proceedings of the EPAC 2006*, Edinburgh, UK, 2006.

[Doh06a] M. Dohlus. private communication, 2006. see `http://www.desy.de/xfel-beam/s2e/ttf2_v2.html`.

[Doh06b] M. Dohlus. Modeling of space charge and CSR effects in bunch compression systems. In *Proceedings of the EPAC 2006*, Edinburgh, Scotland, 2006.

[DR95] J.-C. Diels and W. Rudolph. *Ultrashort Laser Pulse Phenomena*. Academic Press, 1995.

[DRS$^+$06] H. Delsim-Hashemi, J. Rossbach, P. Schmüser, O. Grimm, H. Schlarb, B. Schmidt, and A. F. G. van der Meer. Single-shot longitudinal diagnostic with THz radiation at the free-electron laser FLASH. In *Proceedings of the FEL 2006*, Berlin, Germany, 2006.

[EMLP47] F. R. Elder, A. M.Gurewitsch, R. V. Langmuir, and H. C Pollock. Radiation from electrons in a synchrotron. *Physical Review*, 71(11):829–830, 1947.

[FH66] W.L. Faust and C.H. Henry. Mixing of visible and near-resonance infrared light in GaP. *Phys. Rev. Lett.*, 17:1265, 1966.

[Flö04] K. Flöttman. Astra user manual. `http://www.desy.de/~mpyflo/Astra_dokumentation/`, 2004.

[FP99] B. Faatz and J. Pflüger. Magnet sorting for the TTF-FEL undulator using simulated annealing. Internal report, DESY, 1999. TELSA-FEL 1999-01.

[FP02] K. Flöttmann and Ph. Piot. An upgraded injector for the TTF FEL-user facility. In *Proceedings of the EPAC 2002*, Paris, France, 2002.

[Frö05] L. Fröhlich. Bunch length measurements using a Martin-Puplett interferometer at the VUV-FEL. Diploma thesis, University of Hamburg, 2005. DESY-THESIS 2005-011.

[Gri06] O. Grimm. Private communication, 2006.

[GS06] O. Grimm and P. Schmüser. Principles of longitudinal beam diagnostics with coherent radiation. Internal report, DESY, Hamburg, Germany, 2006. TESLA Report 2006-03.

[GSSY04] G. Geloni, E. L. Saldin, E. A. Schneidmiller, and M.V. Yurkov. Application of constrained deconvolution technique for reconstruction of electron bunch profile with strongly non-gaussian shape. *Nucl. Instr. and Meth. A*, 528:330, 2004.

[GZM+99] G. Gallot, Jiangquan Zhang, R. W. McGowan, Tae-In Jeon, and D. Grischkowsky. Measurements of the THz absorption and dispersion of ZnTe and their relevance to the electro-optic detection of THz radiation. *Appl. Phys. Lett.*, 74:3450–3452, 1999.

[HAS06] HASYLAB. `http://www-hasylab.desy.de/facility/fel/userinfo/userfacility`, 2006.

[HBS+05] M. Hüning, A. Bolzmann, H. Schlarb, J. Frisch, D. McCormick, M. Ross, T. Smith, and J. Rossbach. Observation of femtosecond bunch length using a transverse deflecting structure. In *Proceedings of the FEL 2005*, Palo Alto, CA, USA, 2005.

[HHMT73] T. Hattori, Y. Homma, A. Mitsuishi, and M. Tacke. Indeces of refraction of ZnS, ZnSe, ZnSe, CdS and CdTe in the far infrared. *Opt. Comm.*, 7:229–232, 1973.

[HPSS01] K. Honkavaara, P. Piot, S. Schreiber, and D. Setore. Bunch length measurements at the TESLA Test Facility using a streak camera. In *proceedings of PAC 2001*, Chicago, 2001.

[Isc03] R. Ischebeck. *Transverse Coherence of a VUV Free Electron Laser*. PhD thesis, Hamburg University, 2003. DESY-THESIS-2003-033.

[Jac99] J. D. Jackson. *Classical Electrodynamics*. John Wiley and Sons, Inc., 3rd edition, 1999.

[Jar06] D. Jaroszynski. The Strathclyde Terahertz to Optical Pulse Source (TOPS). `http://tops.phys.strath.ac.uk/main.html`, 2006.

[JBM+06] S. P. Jamison, G. Berden, A. M. MacLeod, J. Shen, D. A. Jaroszynski, B. Redlich, A. F. G. van der Meer, and W. A. Gillespie. Temporal limitations of single-shot Electro-Optic THz detection techniques. To be published, 2006.

[JSCZ99] Z. Jiang, F. G. Sun, Q. Chen, and X.-C. Zhang. Electro-optic sampling near zero optical transmission point. *Appl. Phys. Lett.*, 74(9):1191–1193, 1999.

[JSM+03] S. P. Jamison, J. Shen, A. M. MacLeod, W. A. Gillespie, and D. A. Jaroszynski. High-temporal-resolution, single-shot characterization of terahertz pulses. *Optics Letters*, 28(18):1710–1712, September 2003.

[JZ98] Z. Jiang and X.-C. Zhang. Electro-optic measurement of THz field pulses with a chirped optical beam. *Appl. Phys. Lett.*, 72(16):1945–1947, 1998.

[Kam68] I. P. Kaminow. Measurements of the electrooptic effect in CdS, ZnTe, and GaAs at 10.6 microns. *IEEE J. Quantum Electron.*, 4:23, 1968.

[KBC+06] J.-W. Kim, J. Burnham, J. Chen, F. X. Kärtner, F. Ö. Ilday, F. Ludwig, H. Schlarb, A. Winter, M. Ferianis, and D. Cheever. An integrated femtosecond timing distribution system for XFELs. In *Proceedings of the EPAC 2006*, Edinburgh, Scotland, 2006.

[KGHS06] H. Kapitza, P. Göttlicher, N. Heidbrook, and H. Schlarb. FEL disturbance by ambient magnetic field changes. In *Proceedings of the EPAC 2006*, Edinburgh, Scotland, 2006.

[KS60] D. A. Kleinman and W.G. Spitzer. Infrared lattice absorption of GaP. *Phys. Rev.*, 118:110, 1960.

[LBB+03] A. H. Lumpkin, W. J. Berg, M. Borland, J. W. Lewellen, and N. S. Sereno. Initial CTR-based bunch length measurements of the linac beams following the APS bunch compressor. In *Proceedings of the PAC 2003*, page 2420, Portland, Oregon, USA, 2003.

[LHL+06] F. Löhl, K. Hacker, F. Ludwig, H. Schlarb, B. Schmidt, and A. Winter. A sub 100 fs electron bunch arrival-time monitor system for FLASH. In *Proceedings of the EPAC 2006*, Edinburgh, Scotland, 2006.

[LHS+99] A. Leitenstorfer, S. Hunsche, J. Shah, M. C. Nuss, and W. H. Knox. Detectors and sources for ultrabroadband electro-optic sampling: Experiment and theory. *Appl. Phys. Lett.*, 74:1516, 1999.

[Li01] R. Li. Sensitivity of the CSR self-interaction to the local longitudinal charge concentration of an electron bunch. *Nucl. Instr. and. Meth. A*, 475:498, 2001.

[Löh06] F. Löhl. Privat communication, 2006.

[Löh07] F. Löhl. Privat communication, 2007.

[LPS02] T. Limberg, Ph. Piot, and F. Stulle. Design and performance simulations of the TTF-FEL II bunch compression system. In *Proceedings of the EPAC 2002*, Paris, France, 2002.

[Mar64] D. T. Marple. Refractive index of ZnSe, ZnTe and CdTe. *J. Appl. Phys.*, 35:539, 1964.

[Mes04] D. Meschede. *Optics, Light and Lasers*. WILEY-VCH-Verlag, Weinheim, 2004.

[MHB+05] P. Muggli, M. J. Hogan, C. D. Barnes, D. Walz, P. Krajcik, R. H. Siemann, H. Schlarb, and R. Ischebek. Coherent transition radiation to measure the SLAC electron bunch length. In *Proceedings of the PAC 2005*, page 4102, Knoxville, Tenessee, USA, 2005.

[NT68] D. F. Nelson and E. H. Turner. Electro-optic and piezoelectric coefficients and refractive index of gallium phosphide. *J. Appl. Phys.*, 39:3337, 1968.

[OKY+99] D. Oepts, G. M. H. Knippels, X. Yan, A. M. MacLeod, W. A. Gillespie, and A. F. G. van der Meer. Picosecond electronbunch length measurement using an electro-optic sensor. In *Proceedings of the 21st International FEL Conference*, Hamburg, 1999.

[PPY76] A. N. Pikhtin, V. T. Prokopenko, and A. D. Yaskov. Dispersion of the refractive index of light and permittivity of gallium phosphide. *Sov. Phys. Semicond.*, 10:1224, 1976.

[RBH+05] M. Röhrs, A. Bolzmann, M. Hüning, K. Honkavaara, and H. Schlarb. Measurements of slice-emittance using a transverse deflecting structure. In *Proceedings of the FEL 2005*, Palo Alto, CA, USA, 2005.

[RGHS06] M. Röhrs, C. Gerth, M. Hüning, and H. Schlarb. Energy-time correlation measurements using a vertically deflecting rf-structure. In *Proceedings of the EPAC06*, Edinburgh, UK, 2006.

[Rob01] A. L. Robinson. *X-Ray Data Booklet*, chapter History of Synchrotron Radiation. Lawrence Berkeley National Laboratory, 2001.

[Röh06] M. Röhrs. privat communication, 2006.

[RSTW01] F. Richard, J. R. Schneider, D. Trines, and A. Wagner (Editors). TESLA technical design report. Internal report, DESY, March 2001. DESY 2001-011.

[SCG⁺02] S. Schreiber, J.-P. Carneiro, Ch. Gerth, K. Honkavaara, M. Hüning, Ph. Piot, E. Schneidmiller, and M. Yurkov. Improved operation of the TTF photoinjector for FEL operation. In *Proceedings of the EPAC 2002*, Paris, France, 2002.

[Sch05] H. Schlarb. FLASH electronic logbook entry, March 4, 2005, 2005.

[Sch06a] H. Schlarb. Private communication, 2006.

[Sch06b] B. Schmidt. Overview on diagnostics for X- and VUV-FEL. In *Proceedings of the EPAC 2006*, Edinburgh, Scotland, 2006.

[Sch06c] Schott AG, Germany. `http://www.schott.com/optics_devices/english/download`, 2006.

[SG64] A. Savitzky and M. J. E. Golay. Smoothing and differentiation of data by simplified least squares procedures. *Anal. Chem.*, 36:1627–1639, 1964.

[SGRB87] F. Salin, P. Georges, G. Roger, and A. Brun. Single-shot measurement of a 52-fs pulse. *Appl. Opt.*, 26:4528–4531, November 1987.

[SJ66] T. R. Sliker and J. M. Jost. Linear electro-optic effect and refractive indices of cubic ZnTe. *J. Opt. Soc Am.*, 56:130, 1966.

[SJZ98] F. G. Sun, Z. Jiang, and X.-C. Zhang. Analysis of terahertz pulse measurements with a chirped probe beam. *Appl. Phys. Lett.*, 73(16):2233–2235, 1998.

[SSY04] E. L. Saldin, E. A. Schneidmiller, and M. V. Yurkov. Expected properties of the radiation from VUV-FEL at DESY (femtosecond mode of operation). Internal report, DESY, 2004. TELSA-FEL 2004-06.

[SVC85] K. Strössner, S. Ves, and M. Cardona. Refractive index of GaP and its pressure dependence. *Phys. Rev. B*, 32:6614, 1985.

[SWJ01] M. Schall, M. Walther, and P. Uhd Jepsen. Fundamental and second-order phonon processes in CdTe and ZnTe. *Phys. Rev. B*, 64:094301, 2001.

[SWK+00] J. Shan, A. S. Weling, E. Knoesel, L. Bartels, M. Bonn, A. Nahata, G. A. Reider, and T. F. Heinz. Single-shot measurements of terahertz electromagnetic pulses by the use of electro-optic sampling. *Optics Letters*, 25(6):436–428, 2000.

[TA71] K. Tada and M. Aoki. Linear electrooptic properties of ZnTe at 10.6 microns. *Jap. J. Appl. Phys.*, 10:998, 1971.

[TES02] The TESLA Test Facility FEL team. SASE FEL at the TESLA Test Facility, Phase 2. Internal report, DESY, 2002. TELSA-FEL 2002-01.

[UUKK98] M. Uesaka, T. Ueda, T. Kozawa, and T. Kobayashi. Precise measurement of a subpicosecond electron single bunch by the femtosecond streak camera. *Nuclear Instruments and Methods in Physics Research A*, 406(3):371–379, 1998.

[vdB05] F. van den Berghe. Adaptive dispersion compensation of a fiber for the timing electro optical sampling experiment at TTF2. Diploma thesis, University of Hamburg, 2005. DESY-THESIS-2005-014.

[vdBDF+04] F. van den Berghe, S. Düsterer, J. Feldhaus, R. Ischebeck, K. Ludwig, J. Hauschildt, H. Schlarb, P. Schmüser B. Schmidt, S. Simrock, B. Steffen, A. Winter, P. H. Bucksbaum, A. L. Cavalieri, D. M. Fritz, S.-H. Lee, and D. A. Reis. Proposal for a sub-100 fs electron bunch arrival-time monitor for the VUV-FEL at DESY. In *Proceedings of the EPAC 2004*, Lucerne, Switzerland, 2004.

[War91] L. Ward. *Handbook of Optical Constants of Solids II*, chapter Zinc Selenide (ZnSe) Zinc Telluride (ZnTe), page 737. Handbook of Optical Constants of Solids II. Academic Press, Boston, 1991.

[WCI+06] A. Winter, J. Chen, F. Ö. Ilday, F. X. Kärtner, F. Ludwig, H. Schlarb, and P. Schmüser. High-precision laser master oscillators for optical timing distribution systems in future light sources. In *Proceedings of the EPAC 2006*, Edinburgh, Scotland, 2006.

[WIK+05] A. Winter, N. Ignachine, E.-A. Knabbe, A. Simonov, S. Simrock, B. Steffen, and S. Sytov. Femtosecond synchronisation of an ultrashort pulse laser to a microwave rf clock. In *Proceedings of the PAC 2005*, Knoxville, Tenessee, USA, 2005.

[Wil02] I. Wilke et al. Single-shot electron-beam bunch length measurements. *Phys. Rev. Lett.*, 88:124801–1, 2002.

[Win04] A. Winter. Bunch length measurements using electro-optical sampling at the SLS linac. Diploma thesis, RTWH Aachen, 2004. DESY-THESIS-2004-027.

[WLL+06] A. Winter, F. Löhl, F. Ludwig, H. Schlarb, B. Schmidt, and P. Schmüser. Layout of the optical synchronization system for FLASH. In *Proceedings of the EPAC 2006*, Edinburgh, Scotland, 2006.

[WZ95] Q. Wu and X.-C. Zhang. Free-space electro-optic sampling of terahertz beams. *Appl. Phys. Lett.*, 67:3523, 1995.

[WZ97] Q. Wu and X.-C. Zhang. 7 terahertz broadband GaP electro-optic sensor. *Appl. Phys. Lett.*, 70:14, 1997.

[YMG+00] X. Yan, A. M. MacLeod, W. A. Gillespie, G. M. H. Knippels, D. Oepts, A. F. G. van der Meer, and W. Seidel. Subpicosecond electro-optic measurement of relativistic electron pulses. *Phys. Rev. Lett.*, 85(16):3404–3407, Oct 2000.

[YY84] A. Yariv and P. Yeh. *Optical Waves in Crystals - Propagation and Control of Laser Radiation*. John Wiley & Sons, New York, 1984.

[ZWD04] I. Zagorodnov, T. Weiland, and M. Dohlus. Wake fields gererated by the LOLA-IV structure and the 3rd harmonic section in TTF-II. Internal report, DESY, 2004. TESLA Report 2004-01.

Acknowledgments

I would like to thank all my colleagues at DESY, the University of Hamburg, FELIX, the Daresbury Lab, the University of Strathclyde, the Paul-Scherrer-Institute, and elsewhere, who contributed to the electro-optical experiment at FLASH. This work would not have been possible without their alacrity to share their time, experience, and equipment with me.

First of all I would like to thank my advisor *Prof. Dr. Peter Schmüser* for his immense support throughout the last years, from teaching me the basics of electro-optic detection to straighten my line of thoughts writing this thesis. Without the many fruitful discussions and constructive ideas the experiment would not have been as successful as it was.

I owe very special thanks to *Dr. Giel Berden*, *Dr. Steve P. Jamison*, and *Dr. P. Jonathan Phillips* for sharing their knowledge and experience on temporally resolved electro-optic detection and ultrafast lasers with me. The time they spent at DESY was indispensable for the success of the project. The setup for EOTD would not have been possible without the support from FELIX and the Universities of Strathclyde, Dundee and Abertay, providing a considerable part of the equipment for the measurements. I am grateful to *Prof. Dr. Dino Jaroszynski* for his support during the crystal characterization at the Strathclyde Terahertz to Optical Pulse Source (TOPS).

Many thanks to my group leader *Dr. Bernhard Schmidt* and *Hossein Delsim-Hashemi* for the helpful discussions on longitudinal bunch diagnostics with CTR and the help with the EO measurement at the CTR beamline.

I am grateful to *Prof. Dr. Manfred Tonutti*, who supported me whenever he was at DESY with his knowledge on measurements techniques and his experience in scientific writing.

I have spent a wonderful time in the FLA group and want to thank my current and former colleagues and fellow PhD students for the always friendly and inspiring atmosphere in the group. *Dr. Rasmus Ischebeck* introduced the FLASH accelerator to me, when I first came to DESY as summerstudent. *Axel Winter* designed and built the laser synchronization during his diploma work and we spent many shifts together for electro-optical measurements at the SLS in Switzerland. *Dr. Sara Casalbuoni* spent a lot of work on the numerical description of the electro-optic sampling with ZnTe and GaP crystals, preparing the basis for the numerical simulation of temporally and spec-

trally resolved detection presented in this thesis. *Dr. Ernst-Axel Knabbe*'s efforts to improve the infrastructure of the EO laboratory, from the reduction of electromagnetic noise to the surveillance of the laser safety, were a great support, as well as the hours he spent with me in the lab and the stimulating discussions. I am grateful to *Florian Löhl* for the parallel measurements of the bunch arrival time with the BPhM and EOSD, giving us the opportunity to compare the techniques. *Dr. Vladimir Arsov* joined our group lately to participate in the research on electro-optic detection. His questions helped me a lot to clarify the description of the electro-optic detection schemes and techniques. From *Dr. Holger Schlarb* I learned very much about the FLASH accelerator, especially about bunch compression and beam instabilities. Together with *Michael Röhrs*, he helped me a lot with the TDS measurements and the interpretation of the results.

The discussions with my fellow PhD student *Armin Azima* on the TEO experiment and the exchange of experience from the work on the two different electro-optic experiments at FLASH were always helpful and inspiring. I want to thank *Dr. Harald Redlin* and *Dr. Stefan Düsterer* for their help with the Ti:Sa laser system and many questions they answered on ultrafast lasers.

I'm very grateful to *Prof. Dr. Jörg Roßbach*, *Dr. Siggi Schreiber*, all FLASH operators, and the whole FLASH team, who made the successful operation of the accelerator and the FEL possible and gave me the opportunity to perform these measurements. I enjoyed being part of a great team. Special thanks to *Gerhard Grygiel*, *Dr. Vitali Kocharyan*, and *Dr. Vladimir Rybnikov* for the ICCD camera server and the numerous discussions on the data acquisition system; to *Jörg Thomas* for the motor control server; to *Helmut Remde*, *Dirk Ahrent*, and the MVP vacuum team for fitting last minute crystal changes into the time schedule; and to *Burghard Sparr* for containers, concrete blocks and other solutions to space problems. To *Dr. Martin Dohlus* I owe thanks for providing me with the simulation data of the longitudinal electron bunch profile.

Bernd Beyer, *Mattias Böttcher*, *Jens Hansen*, *Mattias Hoffmann*, *Kai Ludwig*, *Otto Peters*, *Wolfgang Reinsch* and *Albert Schleiermacher* did a great job in the mechanical design, engineering, and technical support of the laser laboratory and the experimental setup. Thanks also to *Alexander Titze*, who mounted the fragile crystals with patience and never-shaking hands. Many special thanks also to *Ingrid Nikodem* for her support in all areas of the DESY administration.

A very special thanks to my friends and my family for their tremendous support during the last years and apologize for the negligence you had to experience lately. Last but not least, I thank *Anja Heins* for reminding me once in a while that life is more than electrons and lasers alone and for being there whenever she is needed.